TISSUE BIOMECHANICS OF THE URINARY BLADDER WALL

by

Dorothy Claire Gloeckner

Bachelor of Science, University of Miami, 1996

Master of Science, University of Miami, 1998

Submitted to the Graduate Faculty of
the School of Engineering in partial fulfillment
of the requirements for the degree of
Doctor of Philosophy

University of Pittsburgh

2003

UNIVERSITY OF PITTSBURGH

SCHOOL OF ENGINEERING

This dissertation was presented

by

Dorothy Claire Gloeckner

It was defended on

January 22, 2003

and approved by

Michael B. Chancellor, Professor and Surgeon, Department of Urology

William C. de Groat, Professor, Department of Pharmacology

Sanjeev G. Shroff, Professor, Department of Bioengineering

George D. Stetten, Assistant Professor, Department of Bioengineering

Dissertation Director: Michael S. Sacks, Associate Professor, Department of Bioengineering

ABSTRACT

TISSUE BIOMECHANICS OF THE URINARY BLADDER WALL

Dorothy Claire Gloeckner, Ph.D.

University of Pittsburgh, 2003

The urinary bladder stores urine and permits proper micturition, both functions that are inherently mechanical. Bladder research to date has been limited to whole-organ testing and simple uniaxial study, both of which are inadequate for comprehensive modeling and rigorous analysis of the mechanical properties of the bladder wall. In this work, we studied the quasi-static and time-dependent properties of the bladder wall to further understand bladder function. To obtain the requisite multiaxial data we utilized biaxial testing techniques, which allow for a more realistic physiological loading state. The goal of the study was to develop a comprehensive understanding of bladder wall biomechanics to provide insight into tissue-level bladder function. This information can be compared against other ongoing and future studies of pathologies to aid in the design of clinical treatments.

The results indicated that bladder tissue 10 days after spinal cord injury was more compliant than normal bladder when referenced to the preconditioned state. However, the preconditioned state itself was different between normal and spinal-cord-injured groups, indicating large rapid changes in structure. There was a fundamental change in material behavior after spinal cord injury that indicates structural rearrangement on a microstructural fiber level. Unlike other soft tissues, there was no difference in mechanical response over three orders of magnitude of loading strain rate, most likely due to the large range of bladder function, including fast emptying and very slow filling. The time-dependent stress relaxation tests indicated that bladder behavior was dependent on stress level, with less relaxation occurring at higher stress levels. This may be because the massive structural rearrangements during normal function cause more collagen to bear load at higher stress levels as protection from over distention.

This study provided the first mechanically rigorous information regarding the tissue properties of the normal bladder wall, including comparisons to a diseased state. This information can be used to understand how differences in structure caused by disease alter the tissue behavior, and hence the biological function, of the urinary bladder.

PREFACE

Thanks foremost to the National Institutes of Health for funding part of my doctoral work through their Training Grant: Genes and Proteins (5T32 GM08540) and the rest through the Program Project Center for Urologic Research Excellence-Spinal Cord Injury HD39768-01A1.

This thesis would not be complete without constant encouragement from my wonderful husband, Cesar Manuel Valencia. Special thanks also to my mother, a terrific technical editor, and my nuclear physicist father for providing organization assistance.

Thanks to the many students in the Tissue Mechanics Lab of both Miami and Pittsburgh. My very special thanks to Kristen Billiar, Ph.D. and David Smith, Ph.D., for their varied assistance toward my education. Thanks, Wei Sun, soon to be Ph.D., for being an excellent sounding board for research ideas and dragging me out of the lab for lunch so many times. Also, my appreciation to Hiroatsu (Brent) Sugimoto for his constant comic relief.

For my academic survival, thanks to the past and present members of the Department of Bioengineering. Thanks very much, Lynette Spataro, for always having the answers to my class and graduation questions, or else knowing where I could get them. Thanks to Joan Williamson for all those rushed orders and seeing I got my stipend every month.

Many of the beautiful images in section 4.0 were produced using Resolution Sciences' ResVIEW program (www.resolve3d.com). My thanks to Russell Kerschmann, M.D., President and CEO, for all his assistance. Some of the other images I obtained using the research facilities at the Center for Biologic Imaging (www.cbi.pitt.edu/) directed by Dr. Simon Watkins. Thanks to Dr. Donna Stolz for her assistance on SEM and her always cheerful and “buggy” temperament. Special thanks to my TEM and SEM professor, Ana Bursick.

The rest of the images I obtained on the microscope at the CURE-SCI lab in the Department of Urology, directed by Naoki Yoshimura, M.D., PhD. Many thanks to Vickie and Kris Erickson for showing me how to use it. I owe a great deal of thanks to many people in the Urology lab for obtaining rat bladder specimens for me, very often after they had finished their own testing late at night. Foremost among this group are Dr. Matt Fraser, Ph.D. now an adjunct assistant professor at Duke University and Dr. John Kim, still at UPitt. Also from Urology, Drs. ShingHwa (Henry) Lu, Izumi Kamo, and Kazumasa Torimoto are also part of the reason this thesis finally reached its end. Finally, thanks to Rachelle Prantil and Ron Jankowski, my fellow Bioengineering doctoral students for not only sectioning bladder specimens for me after they harvested urethras, but also being in the same position as me, begging for tissues to complete their own studies and dissertations.

My greatest appreciation to my doctoral committee members, William de Groat, Ph.D., Michael Chancellor, M.D., George Stetten, Ph.D., M.D, and Sanjeev Shroff, Ph.D. for their valuable time and effort spent serving on my doctoral committee. Finally, I thank Dr. Michael Sacks for all the training and financial support he’s given me over the last seven years. I have no doubt I learned more than most students in my position.

It is my learned opinion that the urinary bladder is one of the more fascinating organs in the body and I look forward to seeing many theses and publications come out of its future study. I wish a final good luck to Dr. Jiro Nagatomi, Jonathan Grashow, and Amy Graveline, who will be continuing to work on the wonders of the bladder.

TABLE OF CONTENTS

LIST OF TABLES

LIST OF FIGURES

1.0 INTRODUCTION

The function of the urinary bladder is to store large volumes of urine at low pressures and to allow for proper micturition. Therefore, the bladder is inherently a mechanical organ, yet few rigorous studies have quantified its mechanical function. These studies were limited to *in situ* and simple uniaxial tests that cannot be used for predictive modeling. For example, while there have been many investigations using cystometrograms or whole-organ bladder preparations, these studies do not consider the unknown effects of heterogeneous external loading of the other abdominal organs, variations in tissue properties, and irregular bladder shape.(1-3) In addition, the results of these studies are restricted to basic pressure-volume relationships.

To conduct a rigorous study, biomechanics at the tissue level must first be investigated. Simple models created from bladder wall strip testing data are also available in the literature.(4-6) However, these uniaxial testing methods leave the lateral edges stress-free, a condition that never occurs *in vivo*, and are therefore non-physiologic. More importantly, mechanical data generated from uniaxial studies cannot be utilized in constitutive modeling. This is true even if the bladder wall properties are isotropic as the functional form requires information on how the material directions interact, which requires multiple loading protocols. More sophisticated approaches are required to provide information necessary for a detailed study of the bladder wall tissue behavior.

The long-term goal is to develop a comprehensive understanding and awareness of bladder biomechanics to provide insight into bladder pathologies and to aid in the design of repair materials for bladder wall. To obtain adequate data for comprehensive modeling and rigorous analysis, a multi-axial testing modality is required. Biaxial mechanical testing, which controls stress or strain in two planar directions, ensures physiological boundary conditions and provides the requisite data for constitutive modeling. The immediate goal is to perform rigorous biaxial mechanical evaluation of the bladder wall. These data will be used to construct a quasi-static model to describe tissue properties independently of time-dependent effects. However, as the bladder has been demonstrated to have significant viscoelastic behavior,(7-9) there will also be a study of viscoelastic behavior, with emphasis on determining if stress-level dependence exists. This information will aid in deciding what conditions must exist to obtain the necessary information for a time-independent quasi-static model of the bladder wall.

1.1 Physiology and Anatomy

The urinary bladder is located just above the pelvis in the lower abdomen. It differs slightly in the male and female because of the presence of the prostate in the male (Figure 1-1, Figure 1-2). The thickness of the bladder wall is composed of the primary layers urothelium, submucosa, and three muscle layers (Figure 1-3).(10) It is composed of collagen, elastin, and bundles of smooth muscle cells. The normal human bladder wall is several millimeters thick and the maximum volume is 400-500 ml. Voiding, or micturition, occurs several times per day. Details of the bladder morphology are presented in section 4.0.

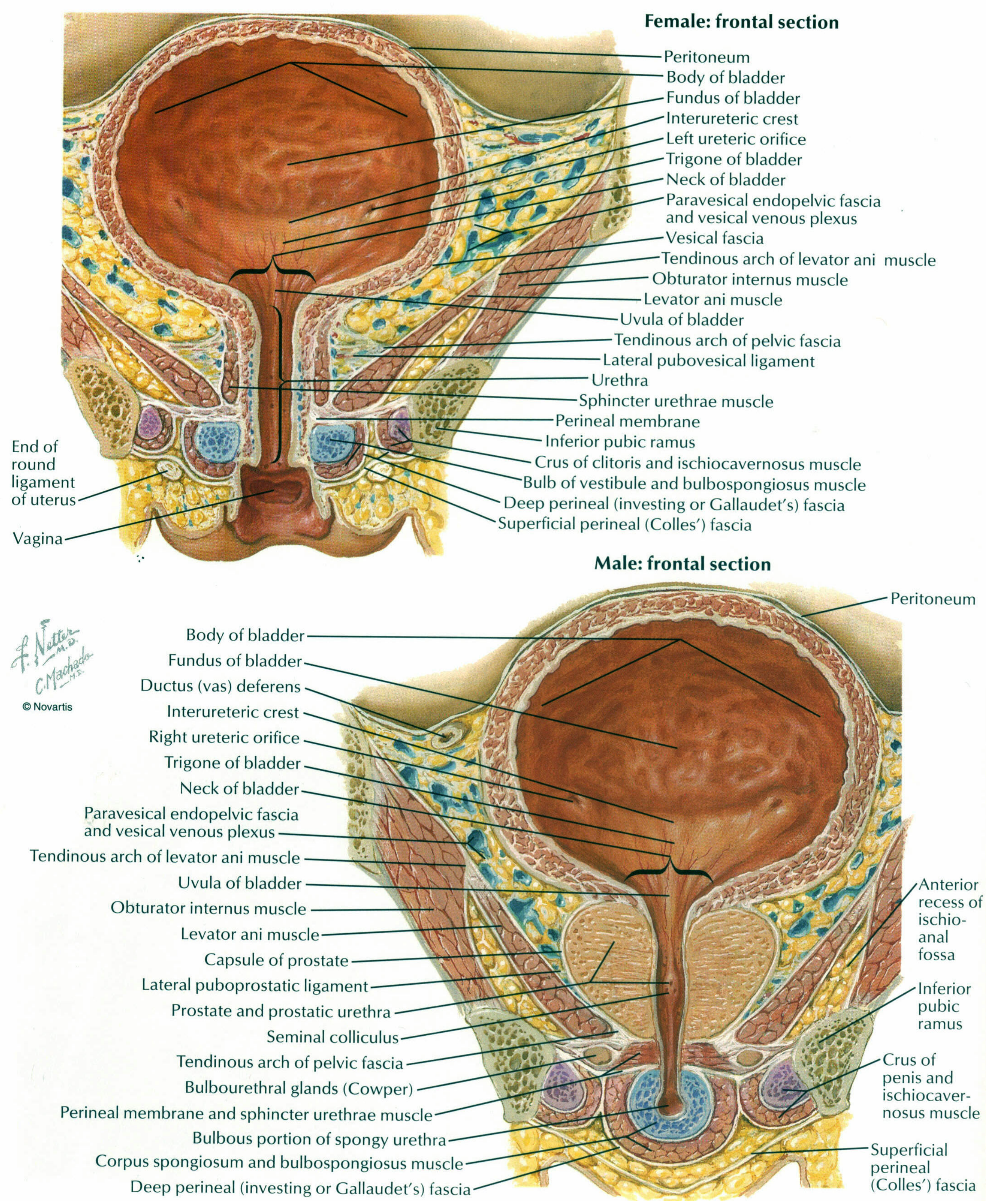

Figure 1-1 Frontal cross section schematic of a human urinary bladder as in female (upper right) and male (lower left). Reproduced from Netter, Atlas of Human Physiology, 1997.[11]

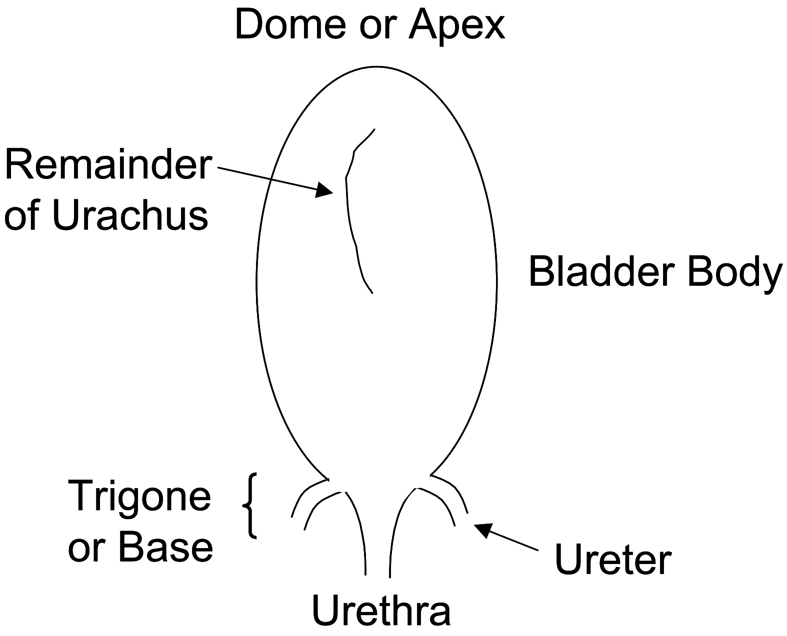

Figure 1-2 Schematic of the bladder in ventral view.

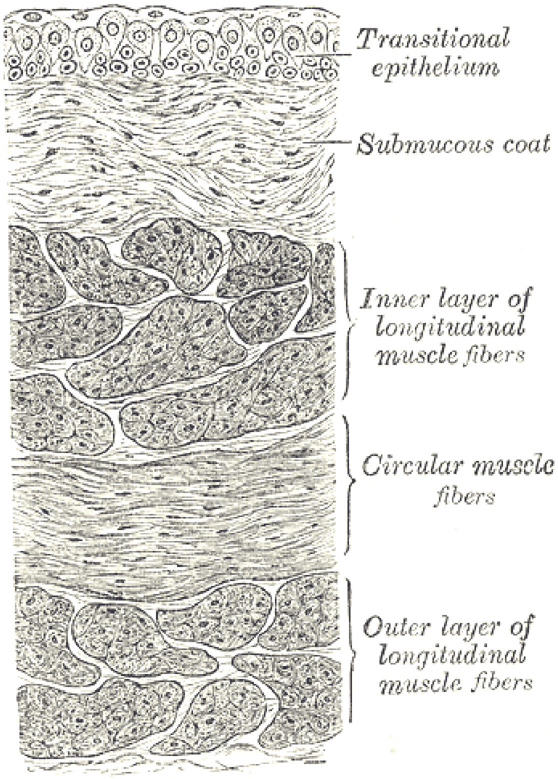

Figure 1-3 Structure of the bladder wall. Reproduced with permission from Bartleby, Inc.[10]

1.2 Neuropathic Disease

Neuropathic disease or trauma such as spinal cord injury (SCI) are known to cause significant alterations in the neural control of voiding. Loss of neural control with SCI(12) can lead to substantial functional changes in the urinary bladder, including significant alterations in bladder compliance, function,(13,14) and thickness.(15) In neurogenic disorders, obstruction is secondary to detrusor-sphincter dyssynergia caused by disruption of the neural pathways between the micturition center in the brain and the bladder. In this etiology, the urethral sphincter does not relax simultaneously with the contraction of the bladder detrusor, resulting in detrusor contraction against a closed outlet and thus obstruction. If left unmanaged, this may lead to a clinical decrease in the ability of the bladder to hold urine, termed bladder compliance, from a normal of 20 ml/cm H_2O to less than 10 ml/cm H_2O. The decrease in compliance is caused by thickening of the bladder wall, including hypertrophy of smooth muscle cells and an increase in connective tissue quantity.(16)

1.3 Aims of the Present Study

In addition to structure and cellular phenomena, knowledge of bladder function at the tissue and organ levels is critical to our understanding of its physiological function during filling.(17) The bladder pressure-volume filling relation is dependent on all aspects of bladder mechanical response as well as the behavior of the surrounding tissue. Fundamental mechanical properties include the stress-strain relationship, viscoelasticity, and non-recoverable (plastic) deformation of bladder tissue. Whole bladder properties include bladder shape, mass, and distension. Organ-level pressure-volume assessment is usually achieved through the cystometrogram. Although an essential tool for the urologist, the cystometrogram alone cannot rigorously distinguish between the effects of changes in tissue compliance and the shape and wall stress distribution of the whole organ. For example, changes in the cystometrogram in a pathological state could be due to any number of reasons, including alterations in bladder shape,(15) tissue properties, other abdominal organ properties, and many other physiological changes. Thus, in order to assess intrinsic changes in bladder wall properties independently, proper assessment of the changes in bladder function requires a thorough understanding of bladder wall biomechanical properties. This includes a rigorous mechanical characterization obtained through multiaxial mechanical tests.

To understand how the tissue-level mechanical properties work with the structure of the bladder wall to produce the bladder function, the structure-function relationship must be determined. Unlike the structure of the heart, (18) which has been thoroughly characterized to develop structure-function models, there are no quantitative studies of fiber orientation or arrangement. This information is critical to understand how the loads on the bladder wall are distributed among connective tissue and muscle fibers. The amount of loading and the strain level at which the loading occurs in each of the types of fibers are unknown. Formulation of a structural model requires the determination of the density, orientation, alignment and size of the constituent fibers and their interactions. Additionally, study of these characteristics under active contraction along with information of the accompanying molecular and cellular events are required for a complete representation of the bladder function. A model of this intricacy is of tremendous importance in determining the differences in function due to pathology. The knowledge that one type of tissue component is supporting more of the pressure in pathology can lead to improvements in pharmacological and surgical treatments for the disease.

Specifically, the aims of this study are to obtain the basic multiaxial tissue-level mechanical behavior for the normal urinary bladder wall in the passive inactivated state. Quasi-static tests to understand the mechanical response to loading under time-independent conditions will be conducted. Examination of the effects of temperature, oxygenation, and strain rate will be studied. Basic time-dependent stress relaxation tests will be carried out to determine if the bladder tissue properties are stress-level independent. In addition, a brief structural analysis will be performed to obtain some preliminary information on the quantitative arrangement of the fibers within the bladder.

2.0 LITERATURE REVIEW

As already discussed, the urinary bladder is a complex and important organ. It must distend to hold volumes of 400-500 ml of urine at low pressures and must release its contents voluntarily with no leakage.(19) The bladder wall's unique structure allows for the large distensions required during filling and storage of urine (section 2.1.3). To accomplish this, it is composed primarily of several layers of collagen, elastin, and smooth muscle cells (Figure 2-1).

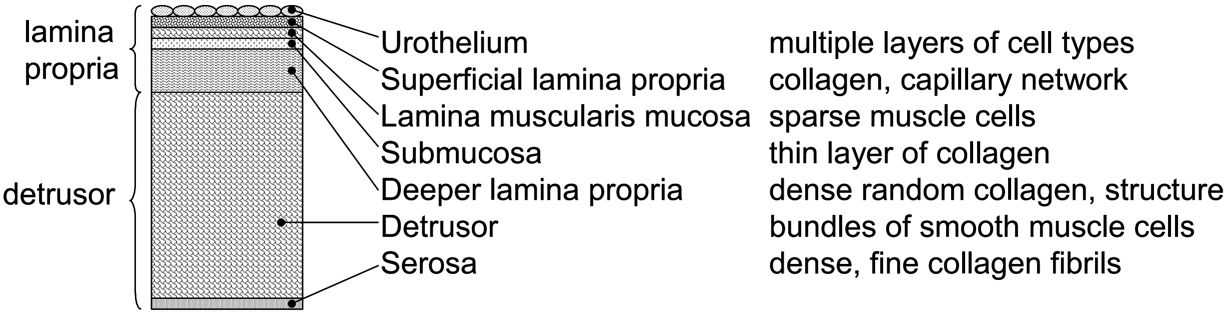

Figure 2-1 Schematic of bladder layers and constituent components. The scale of the components is approximately correct for normal bladder wall.

Bladder muscles go through phases of relaxation and contraction throughout the filling and emptying phases, respectively. During filling the bladder contents are maintained against the weight of the abdominal contents and abdominal pressure increases (caused by conditions such as pregnancy and events such as coughing) via two sets of sphincter muscles around the urethra at the base of the bladder, one skeletal (voluntary) and the other smooth muscle (autonomic). In a healthy individual, the sphincter muscles are contracted while the detrusor muscle of the bladder is relaxed. That is, when the bladder is filling sphincter muscles keep the urethra closed and the bladder contents from leaking. During voiding, the sphincter muscles relax as the detrusor muscles contract simultaneously through neural control. Proper neural control is essential for proper bladder function. Neural disruption, not structural injury, is usually the cause of bladder dysfunction.

2.1 Morphology of the Urinary Bladder Wall

The urinary bladder consists of two major layers, each comprised of several sublayers: the lamina propria near the lumen and the detrusor on the exterior of the bladder (Figure 2-2).(16) A healthy human bladder contains a lamina propria that is approximately 1.3 mm thick and a detrusor layer about 4.4 mm thick.(20) The lamina propria is composed of the urothelium, the superficial lamina propria, and the deep layers of the lamina propria. The normal urothelium is several cell layers thick and is composed of umbrella cells. These cells provide the barrier that isolates the toxic urine from the bloodstream and the rest of the body. Directly beneath the urothelium is the capillary network of the bladder embedded in the superficial portion of the lamina propria.(16,21,22) This layer is a dense weave of randomly oriented collagen fibers.(21) The deeper lamina propria, a thick layer of collagen (more than 300 μm in the human adult)(21) maintains the shape of the bladder wall.

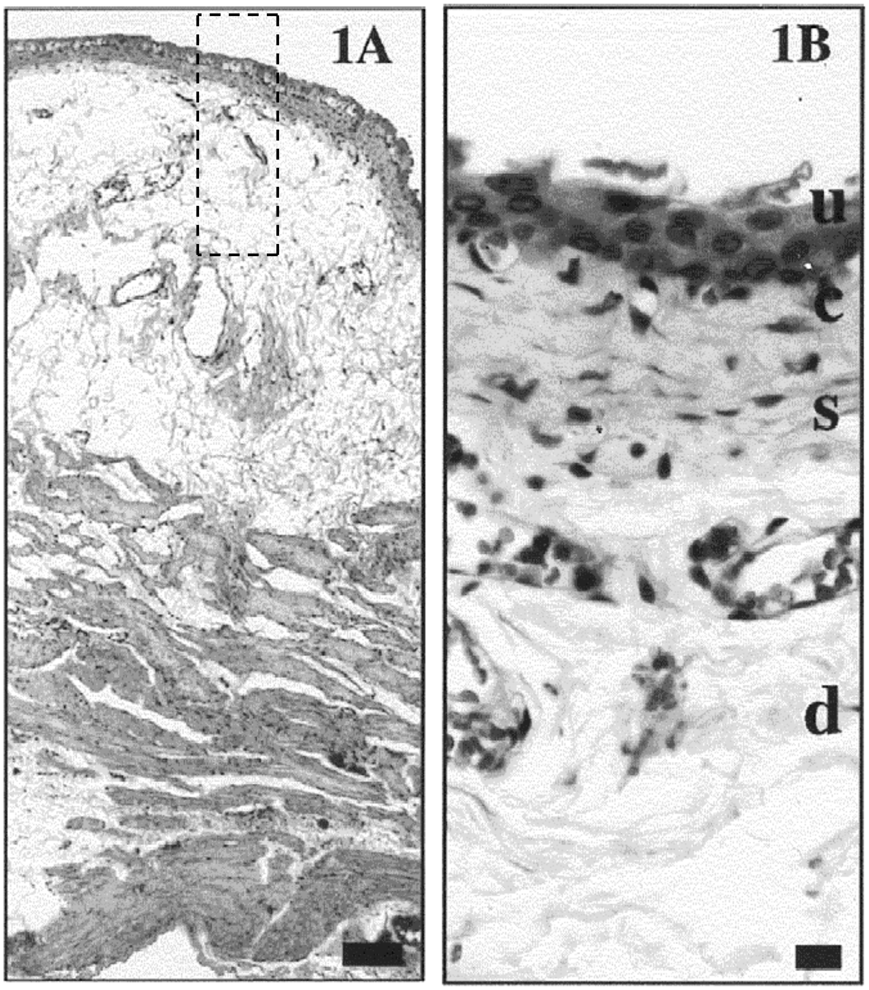

Figure 2-2 Histology of the normal rat bladder wall. **1A** is full thickness bladder wall, stained with hematoxylin and eosin. Scale bar is 100 µm. **1B** Urothelium (u), capillary plexus (c), superficial lamina propria (s), and the deeper lamina propria (d). Scale bar is 20 µm. Reproduced with permission from Elsevier Science.(21)

One function of the lamina propria is to limit the overall compliance (ratio of maximum volume divided by pressure), or distension, of the bladder; when it is removed, the remaining bladder wall distends significantly under normal bladder pressures.(16,23) Lining the lumen side of the lamina propria are urothelial cells and fibroblast-like cells responsible for building and maintaining the connective tissue matrix in this layer both during development and during remodeling in disease.(20,24) Directly beneath the urothelial cell layer is a collagen layer called the superficial lamina propria. Adjacent to this layer is a thin sparse layer of muscle cells, the lamina muscularis mucosa.(21) Beneath this layer is a thin layer of collagen called the submucosa, followed by the remaining and majority of the lamina propria called the deeper lamina propria.(25) The next layer from the lumen is the muscular detrusor of the bladder which contracts during emptying. The major smooth muscle layer of the detrusor is composed of muscle bundles or fascicles (groups of muscle cells) of diameter 50 to 150 μm in various orientations. These fascicles are interconnected with collagen bundles of diameter 3 to 8 μm in the rat.(21) Significant amounts of perimysial connective tissue connects the muscle fascicles and minimal endomysial connective tissue matrix surrounds individual muscle cells.(20) The detrusor layer also contains fibroblast-like cells that, along with the smooth muscle cells, secrete proteins that make up the connective tissue matrix that surrounds and lies within the smooth muscle fascicles.(24) Finally, the outer serosal or adventitial layer covering the external surface of the bladder is a dense layer of fine collagen fibrils of diameter 1-3 μm and about ten microns thick.(20,21) In addition a network of nerves, including myelinated fibers, is found in all layers of the bladder and these nerves are sheathed in connective tissue.(26)

2.1.1 Collagen Types in the Urinary Bladder Wall

The human urinary bladder is approximately 30-60% collagen dry weight.(20,27,28) This percentage content depends on the age and health of the bladder; collagen content tends to increase with development and may change in the presence of disease. In human fetal bladders, the percentage is near 30%,(28) while in human adults, it is 53% - 68%, with higher percentages in women over fifty years of age.(29) In addition, the trigone, or base, has a higher percentage of collagen than the body and dome of the bladder.(29)

Types I, III, VI, and V collagen are the major collagen components of the bladder, with type I the most plentiful.(19) Types I and III together make up 80-99% of total collagen in the body(30) and more than 98% of the collagen in the bladder, as heterotypic fibrils.(19,31) In children, normal bladders contain 76.3% type I and 23.8% type III collagen.(16,32)

In a study of human bladder, Kim and colleagues found that thick collagen fibers, classified as type I collagen, were predominant in the intermuscular bundle space; thin collagen fibers (type III collagen) were abundant between individual muscle cells within the muscle fascicles.(28) Type III has also been found coating the exterior of fascicles(33) and connecting neighboring fascicles in cattle and rats.(21,31) Both types I and III are coiled structures within detrusor and associated with perimysial connective tissue around muscle fascicles.(34) Type III collagen also exists in a coiled configuration in the urinary bladder to allow for large strains,(16,22,31) as is discussed in a following section (2.1.3).

The other types of collagens contribute only 1-2 % of the total dry weight collagen in the bladder. Type IV forms a cocoon-like sheath that surrounds each individual smooth muscle cell in the bladder wall.(31) Collagen types XII and XIV connect collagen fibrils to other extracellular matrix components associated with the surface of fibrillar collagens, and may mediate interaction between collagen fibrils and extracellular matrix proteins or the cell surface.(35) Type XII collagen has been found in the lamina propria and in the endomysium in the detrusor.(35) Type XIV collagen has been found in the submucosa and in the serosa as well as in the perimysial tissues between the smooth muscle fascicles in small amounts in rats.(35) Other collagen types are present in negligible amounts.

2.1.2 Smooth Muscle Bundles

Within the detrusor, the fascicles are 20-50 μm apart.(21) The majority of them are directional in certain areas of the bladder, including a large component of circumferential muscle on the dorsal side of the rat.(26) Collagen fibers of 30-170 nm diameters and small elastic fibers are between muscle cells within fascicles.(26)

2.1.3 Large Deformations in the Bladder and Presence of Elastin

The urinary bladder has the remarkable ability to distend to several times the original surface area and then return quickly to its original size and shape. This deformation energy is stored in a distensible protein called elastin. The amount of elastin present in any connective tissue depends on the function of the tissue. For example, elastin composes only 2-4% dry weight in skin, but more than 50% in some large arteries.(36) Although the structure of elastin is less understood than that of collagen, the elastin fibers are thought to be composed of several glycoproteins.(37) In the urinary bladder, elastin has been found in the urothelium and adjoining lamina propria,(36) around individual smooth muscle cells, (22,33,38,39) within the connective tissue connecting the fascicles(36), in the interfascicular space, and in the outermost layer of the serosa.(39) Although no study attempting to quantify elastin content in the urinary bladder could be found in the literature, its presence in any amount indicates that it plays a role in the ability of the bladder to undergo large recoverable deformations.

Macarak and colleagues have determined that collagen has a specific role in the unique distention abilities of the bladder. They examined the fetal bladder wall distended to different volumes using confocal microscopy (Figure 2-3). The type III fibrils were kinked and coiled when the bladder was fixed in an empty state. When the bladder was distended to 25% of its maximum volume during fixation the fibers were stretched parallel to the urothelial layer. Fibers were more organized near the lumen, but became progressively more disorganized through the thickness from the lumen to the serosa. The fibers coiled in bundles around the fascicles, connecting them to adjacent fascicles. At 50% volume the collagen fibrils were extended parallel to the muscle fibers, but not tightly compressed. At maximum volume, there were extended cells parallel to the urothelium and all cells were stretched or extended, but the fibers were not tightly compressed. The fibers were tightly packed and parallel to the muscle bundles that they surrounded.(19) That type III collagen fibers are kinked and coiled when the urinary bladder is empty and they straighten out during filling has also been demonstrated by Murakumo *et al.*.(22)

Comparing the relative thickness of the bladder layers during filling provides useful information about how the various layers support tension in the bladder wall as the process continues. From 0 to 25% volume the thickness of the lamina propria decreases more rapidly than that of the detrusor.(16) From 25-50%, there is a reversal in tension-bearing and the detrusor layer thins more rapidly.(16) From 50 to 100% volume the lamina propria again thins more rapidly than the detrusor layer. These changes in the rate at which the two layers thin throughout filling indicate that the major load-bearing layer of the bladder changes throughout filling.(16)

Throughout the filling cycle, the lamina propria layer decreases from 40% to only 10% of the total thickness.(16,32)

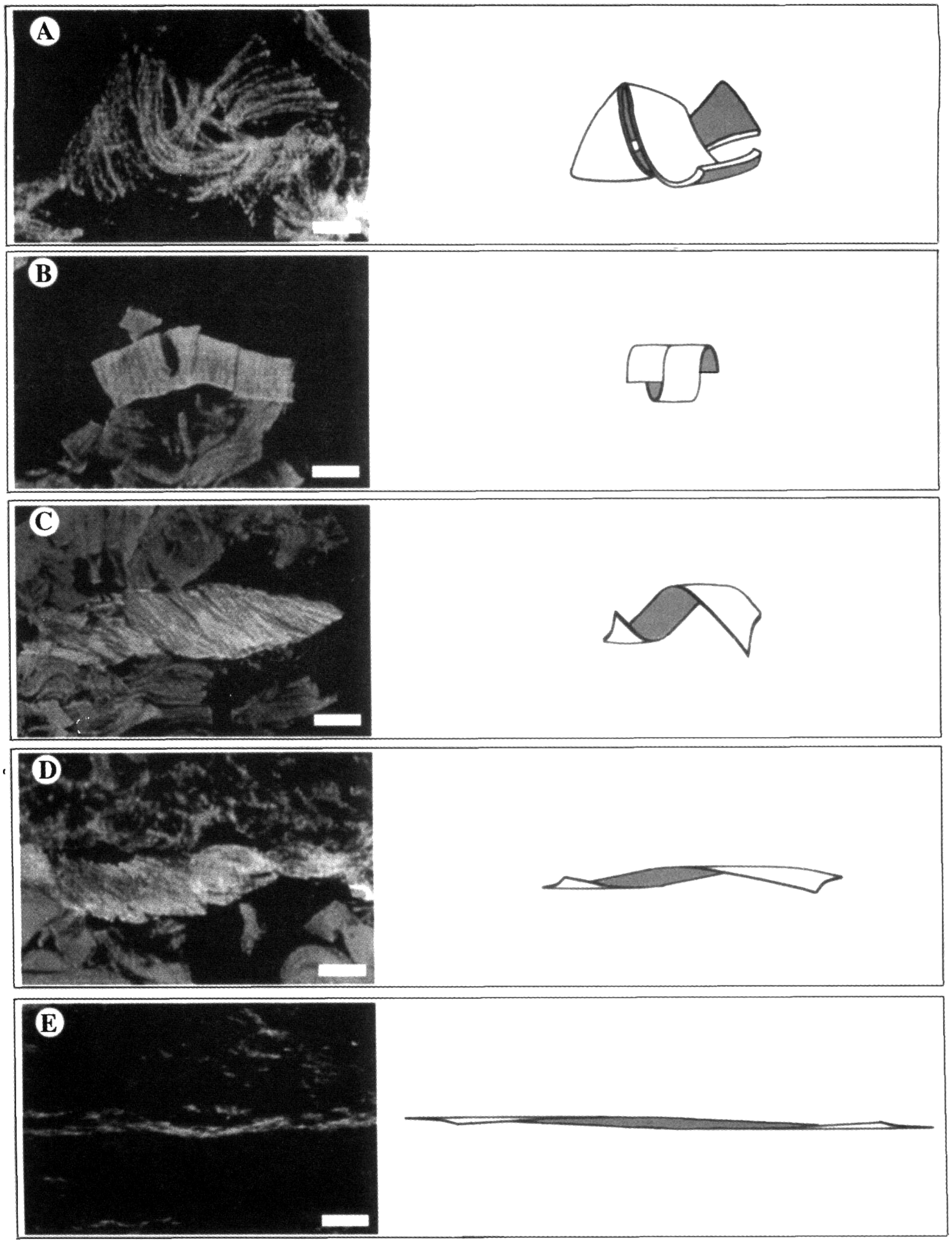

Figure 2-3 Confocal micrographs and corresponding schematic of hypothesized bladder distension mechanism during filling from A (empty) to E (completely full). Reproduced with permission from Kluwer/Plenum Publishers.(32)

2.1.4 Development of the Urinary Bladder

Development is often used as a model of the healing and remodeling process as well as in the study of congenital disorders. During gestation, the fetal kidneys and bladder remove toxin from the blood. During the earliest stage of gestation, fetal urine is not emptied through the urethra but instead through the urachus, a soft tissue tube emanating from the dorsal part of the dome of the bladder. Fetal urine leaves the developing fetus through the umbilical cord. The urachus contains smooth muscle; experiments in fetal sheep have demonstrated muscle tone and contraction within it.(38) In the bovine and ovine species, the urachus closes off just before birth, while in humans this happens at about 4 months into gestation. It is likely that the closing of the urachus, which requires the bladder to start functioning as a storage vessel, may trigger the final development.(38)

In cattle, bladder wall thickness increases through development to adulthood; the total dry weight of collagen does not change after the second trimester of gestation.(40) Cystometrograms measuring the bladder compliance (pressure to volume ratio) demonstrate an increase in the maximum volume during development followed by a decrease during early adulthood.(40-42) This increase and then decrease indicate concomitant changes in structural makeup. In addition, it has been discovered that the removal of the detrusor layer of the bladder results in increased compliance throughout fetal developmental, but compliance increases most in the second trimester and least in the third trimester.(41) Throughout development in the human, the total collagen-to-smooth-muscle ratio decreases from 1.1 to 0.65, indicating more smooth muscle cell growth than deposition of collagen.(28)

One measure of how much a specific protein is being produced at a particular time and in a particular location is to measure the amount of messenger RNA (mRNA). Messenger RNA is created during the transcription of DNA and the relative amounts indicate how much of the specific protein, or protein segment, are being manufactured by the cells. The relative amounts of type I collagen, made of two protein segments, α1(I) and α2(I), and type III collagen, α1(III) that are deposited at any point in gestation can be determined.

The expression of the mRNA of the two chains composing collagen type I, α1(I) and α2(I), is higher during bovine fetal gestation by three to six times compared with the adult state.(34) In the second trimester, type I collagen was localized to the lamina propria while in the third trimester the localization of type I collagen was plentiful within the central region of the lamina propria.(34) The peak expression of type I during the early third trimester is an indication that the bladder is strengthening since this is when the bladder first begins to function properly at low pressure and empty completely because the urachus has closed.(34)

Type III collagen predominates in newly formed fetal structures, including the bladder and in early wound healing, so it is often called fetal or embryonic collagen.(34) At the earliest stages of bovine gestation, the amount of collagen type III is high in the fetal bladder, composing up to 40% of the collagen in the bladder; by birth, it drops to 19%. It increases slightly during growth and development to 25% in the adult animal.(40)

The levels of α1(III) mRNA in a whole bladder preparation peaked in the youngest bovine gestational stages in the detrusor of the bladder and gradually declined throughout gestation.(19,34) In the second trimester, type III collagen was localized to the lamina propria and around the muscle fascicles.(34) Changes in the collagen I: collagen III ratio differed between studies. For example, one study showed that the absolute amount of type III collagen decreases by greater than half from the beginning of the second trimester to newborn in the calf,(31,40) yet human and bovine studies have demonstrated a decrease in the ratio through gestation.(28,31)

The three known elastin proteins (elastin, fibrillin-1, and MAGP) were found throughout all bovine developmental stages.(38) Levels of fibrillin-1 and MAGP were higher in the fetal period compared to postnatal.(38) In the human, the size, thickness, and number of elastic fibers increased during human gestation as the organ developed.(28) Elastin mRNA levels were highest in the second trimester, the earliest stage measured, and decreased until birth.(38) In both the second and third trimesters, fibrillin-1 and MAGP localized to the fine fibers in the lamina propria and the basal cells of the urothelium, and elastin was found in similar locations but in lower concentrations.(38) In the third trimester and at term, all three proteins measured localized to the lamina propria.(38) Elastin levels increased through gestation and higher levels were found in the third trimester, but there was decreased expression in the calf at full term.(36) The peak of microfibrillar mRNA occurred in the early third trimester, coinciding with peak expression of type I collagen.(38) After birth there was no change in the detrusor layer elastin expression but an increase in the urothelial-lamina propria layer in both young and adult animals, similar to type III collagen, which is highest early in development and then decreases as the fetus matures.(38) It is possible that steady-state mRNA levels of elastin in post-natal bladders are related to the requirement for increased bladder volume as the animal grows.(38) The accumulation of elastin declines rapidly by end of first year followed by little or no new production after the first decade. Also, the turnover rates of insoluble elastin are very low, with half-life protein measurements ranging in years.(43)

2.2 Function and Mechanical Properties

Since the bladder is a pressure vessel, subject to significant stresses during filling and voiding, the mechanical tissue properties of the bladder wall have been the subject of numerous studies. Evaluation of mechanical properties has included quasi-static uniaxial tests,(4,44-46) *in situ* studies,(46-48) and uniaxial viscoelasticity studies.(46,49-51)

2.2.1 Current Clinical Functional Evaluation: Cystometry and Urodynamics

Urodynamics studies are performed in a clinical setting to evaluate the health of the bladder. The cystometrogram is an organ-level test in which the functional pressure-volume curve is recorded. A double-lumen catheter inserted through the urethra into the bladder is used to fill the bladder and to measure intravesical pressure. This pressure-volume curve is compared against a standard and used to diagnose bladders that are noncompliant due to a variety of maladies. Variations on cystometry include natural cystometry or controlled slow cystometry (CSC), which use a filling rate closer to physiological urine output, one much slower than conventional cystometry.(52,53) On the other end of the scale, rapid filling and step filling instead of constant rate filling have been used to obtain viscoelastic constants of the bladder wall.(2,8,9,54,55) In addition, attempts have been made to quantify urinary bladder fiber strength(3) and the amount of work done by the bladder(1) using the pressure-volume relationship obtained from cystometry. To isolate the effects of nerve impulses on bladder function, sacral nerve roots have been identified and stimulated.(56) Studies have also been performed to optimize the size of the catheter to reduce interference of the test method on the measurements obtained.(57)

Another minimally invasive urologic test is the measure of bladder impedance correlated to bladder fullness is used in patients who have lost the ability to sense urinary fullness.(58) Echo planar imaging and Doppler sonography of the bladder emptying have been used to view the velocity of urine exiting the bladder.(59-61) More complete studies include measurements of bladder wall thickness to normalize the pressure-volume data;(56) however this cannot be used clinically as it involves removal of the bladder after cystometry.

Cystometrograms cannot directly determine bladder wall tissue properties, because these tissues have thickness and regional differences that cannot be reliably measured *in vivo*. Further, *in vivo* studies may be affected by neural influences and are always affected by intrinsic muscle activity, neither of which can be controlled. In general, *in vivo* evaluation is a function of the mechanical properties of the bladder wall, the non-uniform wall stress distribution, and external loading by the pelvic organs.

2.2.2 Intact Organ Testing *In Vitro*

In *in vitro* whole-organ testing, the intact bladder is removed to isolate it from nervous stimulation and external loading. As in cystometry, the bladder is filled with a fluid and the resulting pressure-volume curve is examined.(8,62) This test allows the researcher to control the environment of the bladder by introducing specific electrical impulses that affect muscle contraction.(63) Since the bladder is maintained as a three-dimensional fluid-containing sac as *in vivo*, the recorded parameters can be directly related to bladder function and its ability of the bladder to hold and void urine under specified conditions.

Although *in vitro* testing is more physiological and not confounded by the interaction of the other abdominal contents as are cystometry measurements, it still has the disadvantage of variations and errors due to wall thickness and bladder shape, and the inability to apply a simple loading pattern or know with precision the loading pattern applied. Additionally, only a single control of either pressure or volume is available to the experimentalist. Rigorous mechanical analysis requires better control of the material and the ability to load the material in multiple dimensions.

2.2.3 Uniaxial Testing

A complete analysis of the mechanical properties of the bladder wall tissue can be conducted only when the tissue is isolated and all forces applied are known. This requires either knowledge of the exact shape and regional thickness of the intact bladder, both of which are invariably different from animal to animal, or isolation of sections of bladder wall in known and specific configurations. Many investigators have carried out controlled-force studies on isolated tissue using bladder strips.

Alexander has used bladder strips to study the rat bladder in detail, applying load to a transverse strip of tissue.(4,46,64) Van Mastrigt and coworkers have studied human and guinea-pig bladder in an isolated strip preparation.(2,54) Much useful information has been gathered through strip uniaxial testing. Alexander found that when a high pressure is rapidly removed, there is a corresponding rapid decrease in length, indicating an elastic element in urinary bladder mechanics.(46) Macarak and others have found that after the detrusor layers were surgically removed, both in bladder strips and in intact bladders, the tissue samples became more compliant, indicating that the components of the muscle layers may serve to limit the total volume of the bladder, contributing to stiffness.(31,47) The numerical results of these tests are maximum tensions and other stress-strain relationship quantities. However, uniaxial testing cannot be used to fully describe the properties of the bladder, since the muscle bundles are not homogenous nor always of a predictable orientation.(26) In addition, to allow dissipation of the uneven stress concentrations at the gripped sample edges, deformation measurements are done in the center of the tissue and the specimen dimensions are typically 1:5 to 1:10 (width: length), resulting in a long, thin specimen. Cutting the tissue results in a reorganization of the fibers at the edges, yet due to the small width of the sample, measurements often need to be taken near the edge, resulting in large errors. Nevertheless, data obtained from uniaxial strip tests have been used to develop predictive models of bladder behavior. These models have been largely empirical, constructed to meet the criteria that the model fit the given data well. Most have been based on the classic spring (elastic) and dashpot (viscous) elements, incorporating three or four elastic and three or four viscous elements in each model.(2,7,46,54,64) The models may fit the data well, but the parameters that result can only be compared to those of other tissues tested and fit in the same manner, to the same model. As in all phenomenological models, the parameters do not describe the intrinsic properties of the tissue and therefore cannot be used to learn anything about the tissue function or, more importantly, differences in tissue function due to abnormal states.

Baskin and coworkers devised a novel two-dimensional test in which a strip of material was sandwiched between two plates with a circular hole cut out of them. A pressure gradient was then applied across the cutout so the specimen bulged. The maximum pressure applied and the resulting deflection were then used to compute the stresses.(40) Although this test did remove the effects of the specimen geometry from the tissue testing, it still allowed only a single test. To obtain a complete description of the mechanical properties, multiple stress states with different stresses in both anatomical directions is required.

Uniaxial testing has revealed that the bladder is similar to other biological tissues. It undergoes a reduction in stress when held at constant deformation (stress relaxation). The behavior stabilizes after the first few cycles so that the first cycle is different from the subsequent stable cycles (preconditioning). There is measurable energy loss during each cycle (hysteresis). In addition, it has been shown that the rate of stretch does not affect the magnitude of tension developed.(5)

2.2.4 Effects of Pharmaceuticals and the Media Environment

Short of surgical removal, augmentation, or alteration of the bladder wall, the most convenient treatment for incompliant bladders is pharmaceutical intervention. As the bladder lumen is accessible through minimally invasive procedures, much study has focused on how intravesical pharmaceuticals affect it. In animal sacrifice studies, this is easily accomplished by adding the pharmaceutical agents with the intended action to the tissue media during testing.

Studies using dogs have demonstrated that intravesical egtazic acid (EGTA) causes a decrease in pressure and therefore an increase in volume during rapid-fill cystometry.(55) Rat bladder strips also become stiffer with higher concentrations of bethanechol chloride (a contractile agent) and more compliant with EGTA.(4) Interestingly, bethanechol chloride, EGTA, and control solutions all yielded the same relationship between series elastic stiffness and tissue tension in rat bladder strips.(4,46) Only the initial stress changed between conditions, demonstrating that neither inhibition nor activation of the contractile apparatus changed the elasticity of the tissue. Additionally, although EGTA chelates the calcium available in solution, the residual calcium left in storage in the muscle cells still allows some muscle contraction, possibly in the intrinsic bladder tone. Any leftover muscle contraction is also removed with the further addition of sodium azide, which inhibits oxidative phosphorylation, the process that supplies energy to muscle contraction.(65)

Other environmental aspects of the tissue media such as temperature and oxygenation also affect bladder behavior. Alexander showed an almost two-fold increase in relative deformation of a rat bladder tissue ring when the temperature was raised from room temperature (23° C) to body temperature (37° C) under long-term conditions.(64) Both rat and guinea pig uniaxial strips showed no difference in peak force when subjected to displacement rates ranging from 0.5 to 3 cm/hr, indicating a lack of a perceivable loading-rate effect.(5) Finkbeiner also found that the rate of relaxation of the bladder strips was greater with faster loading rates. Immersing bladder tissue in oxygen-free media results in behavior similar to those resulting from EGTA.(48)

2.3 Spinal Cord Injury and Obstruction

Neurogenic disorder spinal cord injury (SCI) is a devastating condition, resulting in both mobility limitations and potentially fatal organ failures. Historically, urologic complications have been partially responsible for early mortality in SCI patients. Lifelong urologic care is central to the wellness of the SCI patient. SCI occurs at an incidence of about 32 new injuries per million population (3-3.2 per 100,000) in the United States and has a prevalence of approximately 906 per million population.(66,67) The level of injury determines the severity of neurogenic control loss. Fifty-five percent of such injuries result in quadriplegia and 45% result in paraplegia.(67)

Initially after injury, no voiding occurs due to the presence of detrusor-external sphincter dyssynergia (DESD) and patients must be catheterized.(13) This neurogenic disorder is a disruption of the usual coordinated relaxation of the external urinary sphincter with the contraction of the detrusor. Instead of relaxing, the external sphincter often contracts further in response to a detrusor contraction. The detrusor then contracts against a closed sphincter so that no urine can exit. This obstruction results in many alterations to bladder structure and function (Table 2-1).

Two to twelve weeks after trauma, a reflex bladder response returns that restores at least involuntary bladder emptying. This response may result from collateral sprouting of new neural pathways, loss of an inhibitory influence of the injury, or emergence of more primitive alternative pathways.(13,68) However, return of the reflex response does not mean normal bladder control. Intervention is often required.

Bladder dysfunction caused by spinal cord injury does not improve through time. In fact, it usually gets worse and requires continuing, vigilant medical supervision and patient compliance with the prescribed routine. After many years of poor or no medical management, the urinary bladder can deform into an elongated ellipsoid in the cranio-caudal direction.(15) Additionally, the bladder neck can hypertrophy and enlarge.(69)

Table 2-1 General effects of spinal cord injury on urinary bladder.

Initial (2-12 weeks) shock phase no voiding; urinary retention
Increase in bladder weight throughout remainder of life
Increase in bladder capacity throughout remainder of life
Hypertrophy of bladder smooth muscle cells throughout remainder of life
Resulting clinical conditions, any or all, (12 weeks – end of life)
    Detrusor hyperreflexia (DH): overactive bladder
    Detrusor-external sphincter dyssynergia (DESD)
    Decreased bladder compliance (volume/pressure during cystometry)

2.3.1 Urinary Bladder Obstruction

Chronic obstruction at the urethra is a common bladder disorder. Obstruction can result from many different pathologies. The most common of these are benign prostatic hyperplasia (BPH), posterior urethral valves (PUV), and neurogenic disorders. Benign prostatic hyperplasia, common in men over the age of 40,(32) is an overgrowth of the cells in the prostate, and results in an increasingly narrowed urethra lumen, increasing the resistance to flow through the urethra. Posterior urethral valves is a congenital condition, a result of incomplete urinary tract development. It causes an obstruction at the outlet of the bladder and opening of the urethra. In severe cases, PUV can affect the developing fetus, causing increased bladder and kidney size and decreased lung capacity. In neurogenic disorders, the obstruction is secondary to detrusor-sphincter dyssynergia caused by disruption of the neural communication network within the bladder. In this etiology, the urethral sphincter does not relax simultaneously with the contraction of the bladder detrusor, resulting in detrusor contraction against a closed outlet. All three of these conditions, if left unmanaged, lead to a clinical decrease in the ability to store large amounts of volume at low pressures, called bladder compliance. The normal adult has bladder compliance of 20 ml/cm H_2O and the bladder is considered incompliant if it drops to less than 10 ml/cm H_2O. The decrease in compliance is caused by thickening of the bladder wall, including hypertrophy of smooth muscle cells and an increase in the amount of connective tissue.(16)

In the early stages of obstruction, most of the increase in overall mass in the bladder wall is due to edema, primarily in the lamina propria and serosa, not because of muscle hypertrophy or connective tissue deposition. This swelling occurs rapidly, after only one or two days obstruction in rabbits(70) and over a similar time period in humans as measured by dry/wet weight comparison.(20) As time passes, however, the increase from edema is less significant than the increase from protein deposition.(70) In addition, some studies find no change in the thickness of the lamina propria layer in both neurogenic and non-neurogenic noncompliant bladders, identifying the increase in the detrusor layer only.(20,31)

Research suggests that the hypertrophy of smooth muscle cells and the edema caused by obstruction can be reversed if the obstruction is removed early on.(71) For example, experiments using rats in which a ligature was tied around the urethra for six weeks resulted in an increase in the wet weight of the bladder, with a return to normal weight six weeks after the ligature was removed.(71) Similarly, in the guinea pig, bladders obstructed for four weeks and then relieved of obstruction returned to a normal weight in 16 weeks; animals kept obstructed for eight weeks did not return to normal 16 weeks later.(72)

2.3.2 Structure and Morphology Changes

One of the most obvious results of obstruction is smooth muscle hypertrophy. This causes a rapid increase in wet weight of the urinary bladder to two to three times as much as the control in only 7 days.(73) The detrusor layer thickness increases from 100-120 μm in normal to 250-300 microns in obstructed bladders.(26) In one study, after 10 weeks with obstruction there was a 15-fold increase in muscle growth.(26)

Interestingly, upon microscopic analysis of SCI patient tissue, not all smooth muscle cells are found to be hypertrophied, as would be expected if this phenomenon were only an effect of pressure.(73) One explanation for this phenomenon is that the hypertrophy is caused by an alteration or lack of stimuli from peripheral autonomic nerves and that only smooth muscle cells with nerve receptors are affected(74), leaving the cells that receive their nerve signals from adjacent cells unaffected. Other investigators, however, have found that all muscle cells are directly innervated in the bladder.(26)

In general, the pathological change caused by obstruction was first evident in the superficial detrusor layer next to the lamina propria, and then occurred deeper within the muscle layer, and finally resulted in the fibrotic effect over the full transmural thickness in noncompliant bladders.(33) This widespread fibrosis may result in an outward shift of the capacitance layer in the noncompliant bladder from the lamina propria to the infiltrated smooth muscle layer.(33)

Changes in collagen content after obstruction have also been discovered. The relative amounts of type III and type I collagen have been found to change after spinal cord injury. One study found that while normal rat bladder collagen type III and type I contents are 25% and 75%, respectively, in the obstructed bladder, progressive fibrotic changes increased the percentage of type III to 33%.(31,32) This change is also associated with alterations in mechanical compliance in bovine studies.(16) Throughout this change, however, the distribution of the connective tissue components (collagens I and III and elastin) in the lamina propria did not change in noncompliant bladders,(33) suggesting that most of the alterations were within the detrusor layer.

It is interesting to note that in most tissues, fibrosis is characterized by overproduction of collagen type I, not type III as is seen in the urinary bladder. This holds true even for tissues that have a high type III content in their normal state, such as the heart. The fibrotic process within a noncompliant urinary bladder due to obstruction is therefore very unusual, at least within the detrusor.(33)

Results of studies investigating changes in collagen content in humans differ. Some studies have found no significant difference in the total collagen content between normal and non-neurogenic obstructed bladders in persons from 3 months to 68 years of age.(27) However, Deveaud and colleagues found a significant increase in collagen type III in both neurogenic and non-neurogenic noncompliant bladders but no significant change in type I.(20) Within the areas of neurogenic bladders classified as relatively normal, there were increased collagen levels but not elastin levels, indicating that elastin might be localized to damaged regions but collagen deposition is more uniform throughout the bladder wall.(75) In comparisons of neuropathic and non-neuropathic disorders, both collagen and elastin levels increased, but the increases were higher in neuropathic bladders (Figure 2-4).(75)

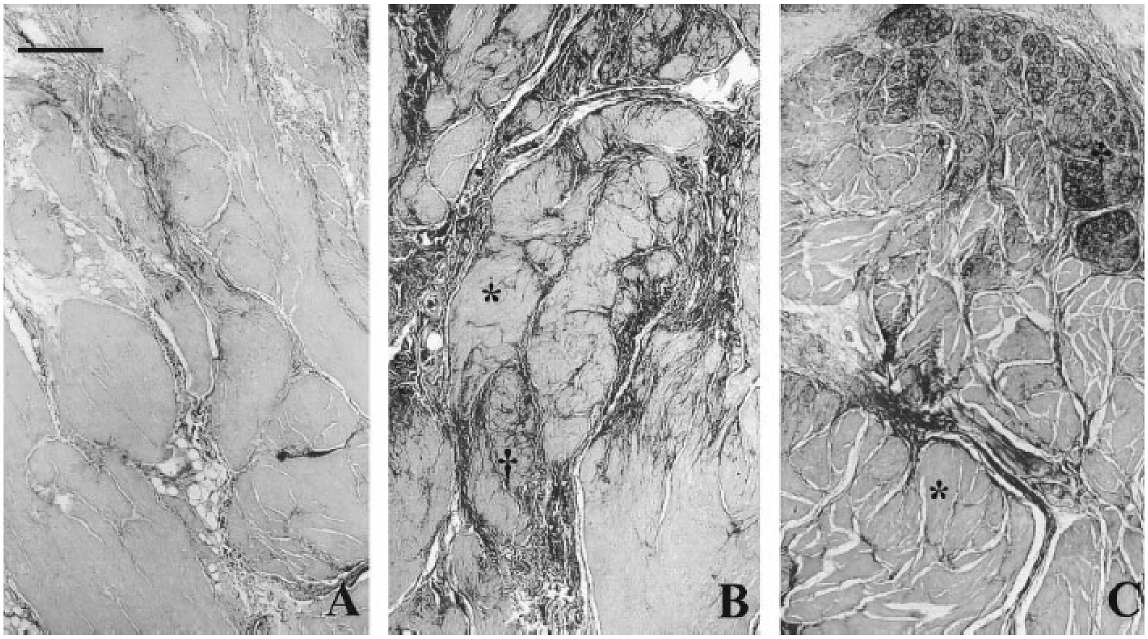

Figure 2-4 Photomicrographs of human detrusor bladder tissue from control (**A**), idiopathic (**B**), and neuropathic bladders (**C**). The Elastic van Gieson stain shows collagen, muscle, and elastin in red, yellow, and black, respectively. Normal areas are signified by * and † indicates a severely affected area in B. The scale bar is 200 μm. Reproduced with permission from Blackwell Publishing Limited.(75)

There are some differences in structural changes between neurogenic and non-neurogenic causes of non-compliant, obstructed bladders in the human according to a study by Deveaud and coworkers. Neurogenic bladders tend to have higher dry weight compared to non-neurogenic etiologies, indicating more smooth muscle cell hypertrophy and/or connective tissue deposition due to lack of nerve input alone. There is an increase in the ratio of type III to type I mRNA levels in neurogenic bladders compared to normal, but no increase for non-neurogenic bladders.(20)

Over longer times, noncompliant human bladders demonstrate a thickening of the perimysial collagen in the tissue and an endomysial infiltration of the connective tissue(20,33) resulting in smooth muscle bundles encased in thick collagen fibers.(76) In mild pathological conditions, there is type III collagen, elastin, and pericellular infiltration but no definite increase in collagen type I within muscle fascicles in either human or bovine samples.(31,33) However, in normal rat bladders, types I and III collagen localized to the lamina propria, but after obstruction were more prominent in the detrusor.(71) Collagen within fascicles in noncompliant bladders does not normally occur.(28,32,75) Overall, the ratio of collagen to muscle decreases in obstructed bladders.(76)

Analysis of large sections of human neurogenic bladders has demonstrated localization of altered connective tissue morphology.(75) Unfortunately, since diagnosis of bladder wall pathology is based on punch biopsies of only a few millimeters in diameter, such diagnoses can be difficult. The differences in connective tissue include deposition of type III collagen in the endomysium of the smooth muscle bundles of noncompliant bladders (neurogenic or non-neurogenic) compared to controls, accompanied by a 48% increase in collagen III.(16,20)

The number of elastin fibers in obstructed bladders increased compared to control bladders in human(27,76) and in a guinea pig model.(72) Specifically, this increase occurred within the detrusor layer in obstructed human tissues.(27) Elastin within fascicles in noncompliant bladders does not normally occur.(28,32,75) In more severe cases the deposition of elastin is localized to the exterior of the smooth muscle cells.(33)

2.3.3 Mechanical Changes

Most of the analysis of SCI tissue samples, both in human and animal studies, has focused on structural changes. However, some mechanical strength studies have been performed. Both spinal cord injury, which results in outlet obstruction, and outlet obstruction have been induced in animal models, then cystometry and *in vitro* experiments have been performed to quantify the outcome. It has been shown that the compliance of the obstructed bladder decreases through time. The compliance is further decreased in cases where the patient empties his or her bladder using intermittent catheterization(77) and even more so with a permanent indwelling catheter.(78)

Outlet obstruction in rabbits induced by surgically placing a part of a polyethylene tube around the urethra caused a decrease in active force generation, but a significant increase in passive force during stretching of a bladder ring.(6) Regional differences were found in mechanical behavior between the upper body, lower body, and base of the bladder.(6) Reversed obstruction, or de-obstruction, as already discussed, has been shown to reverse the bladder weight gain.(71,72) The mechanical properties approach normal as well.(17)

In time-independent (quasi-static) testing, there were only small increases in tension in noncompliant bladder strips compared to normal.(12) In time-dependent viscoelastic tests, it has been shown that the amount of relaxation is decreased in human muscle strips after obstruction.(79)

2.4 Limitation of Previous Studies and Current Rationale

Previous evaluations of the mechanical properties of bladder wall tissue have focused on testing strips of bladder tissue where a load is applied in one direction only, i.e., uniaxial testing.(4,44-46) Uniaxial testing is attractive in that it isolates the tissue and subjects it to controlled stress states. However, a uniaxial stress state is non-physiologic since it leaves the edges completely stress-free, a state that never occurs *in vivo*. Physiological loading of the bladder wall includes components in all three dimensions; tensile tissue loads are in the plane of the tissue and compressive loads oriented perpendicular to the bladder surface are induced by urine and surrounding pelvic structures.

For thin (thickness an order of magnitude less than next larger dimension), incompressible membranes like the bladder, a planar biaxial state of stress is sufficient to fully describe the three-dimensional tissue mechanical properties.(80) Biaxial mechanical testing thus allows for a more realistic physiological loading state. Further, by varying the loads along each axis the complete mechanical behavior of the bladder wall over the entire normal and pathological physiologic functional range can be determined.

3.0 MECHANICAL CHARACTERIZATION

This section is devoted to the development of techniques, methods, and experimental protocols needed to characterize soft tissue mechanical behavior. Tissue and organ level mechanical behavior affect the function of the bladder as it fills.(17) The bladder pressure-volume filling relation is dependent on both the fundamental mechanical properties of bladder tissue, which include the stress-strain relationship from both quasi-static and time-dependent viscoelastic responses and whole bladder properties which include bladder shape, mass, and distension.

Organ-level pressure-volume assessment is measured with the cystometrogram. Although it is an essential tool for the urologist, the cystometrogram alone cannot meticulously distinguish between the effects of changes in intrinsic tissue compliance, the distribution of wall stress, and alterations in external loading. Assessment of intrinsic changes in bladder wall properties independently requires a thorough understanding of bladder wall biomechanical properties. This includes a thorough mechanical characterization obtained through multi-axial mechanical tests which best approximate the three-dimensional behavior under physiological loading.

This section contains the development of testing methods to obtain basic quasi-static (section 3.3) and viscoelastic properties (section 3.4) of normal tissue in order to provide a rigorous mechanical characterization of bladder. Passive biaxial mechanical properties of spinal cord injured rat bladder wall (section 3.5) were quantified as a first step in understanding the basic mechanical properties of the bladder wall and how these properties are altered in a neurogenic bladder disorder, but the complete investigation of the spinal-cord-injured bladder is left to later research.

3.1 Background of Biaxial Mechanical Testing

Previous evaluations of the mechanical properties of bladder wall tissue have focused on testing strips of bladder tissue where a load is applied in one direction only, i.e., uniaxial testing.(4,44-46) Uniaxial testing isolates the tissue and subjects it to controlled stress states, but it is non-physiologic since it leaves the edges completely stress-free, a state that never occurs *in vivo*. Physiological loading of the bladder wall is both tensile and compressive, and includes components in all three dimensions. Tensile tissue loads are in the plane of the tissue while compressive loads oriented perpendicular to the bladder surface are induced by urine and surrounding pelvic structures.

For thin, virtually incompressible membranes like the bladder, a planar biaxial state of stress is sufficient to fully describe the three-dimensional tissue mechanical properties.(81) In biaxial testing, the thickness must be significantly smaller than the lateral dimensions (Figure 3-1). Biaxial mechanical testing therefore allows for a more realistic physiological loading state. Further, by varying the loads in each orthogonal axis the complete mechanical behavior of the bladder wall over the entire normal and pathological range of function can be determined.

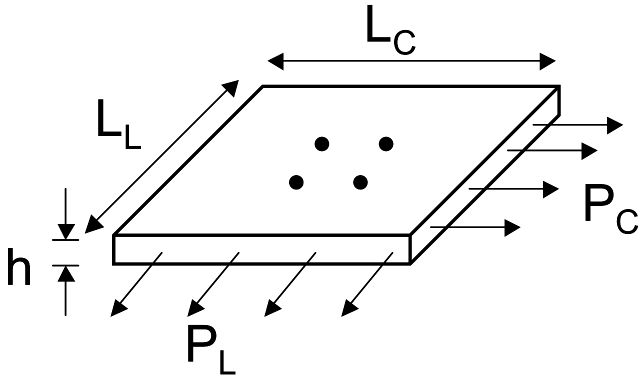

Figure 3-1 Schematic of biaxial specimen dimensions. The subscripts C and L represent the two orthogonal directions, circumferential and longitudinal, respectively, as described in Figure 3-3. The length (L) and axial load (P) are measured in both material directions. The thickness, h, is usually averaged over the entire area of the sample. See equation (3.8) for calculations.

Square biaxial testing samples are mounted in a trampoline style using point attachments. This mounting method allows the edges to expand freely in the lateral directions (Figure 3-2). Testing is performed with the specimen completely submerged in an appropriate physiologic solution. Stretch in the specimen is typically measured optically via markers in the central region to avoid edge effects. Generally, the stress and stretch fields in the center target region are considered homogenous, so that the components of the deformation (displacement) gradient, **F**, are independent of position. Following is the brief general introduction to the details of biaxial analysis. Full details are available in the literature.(81)

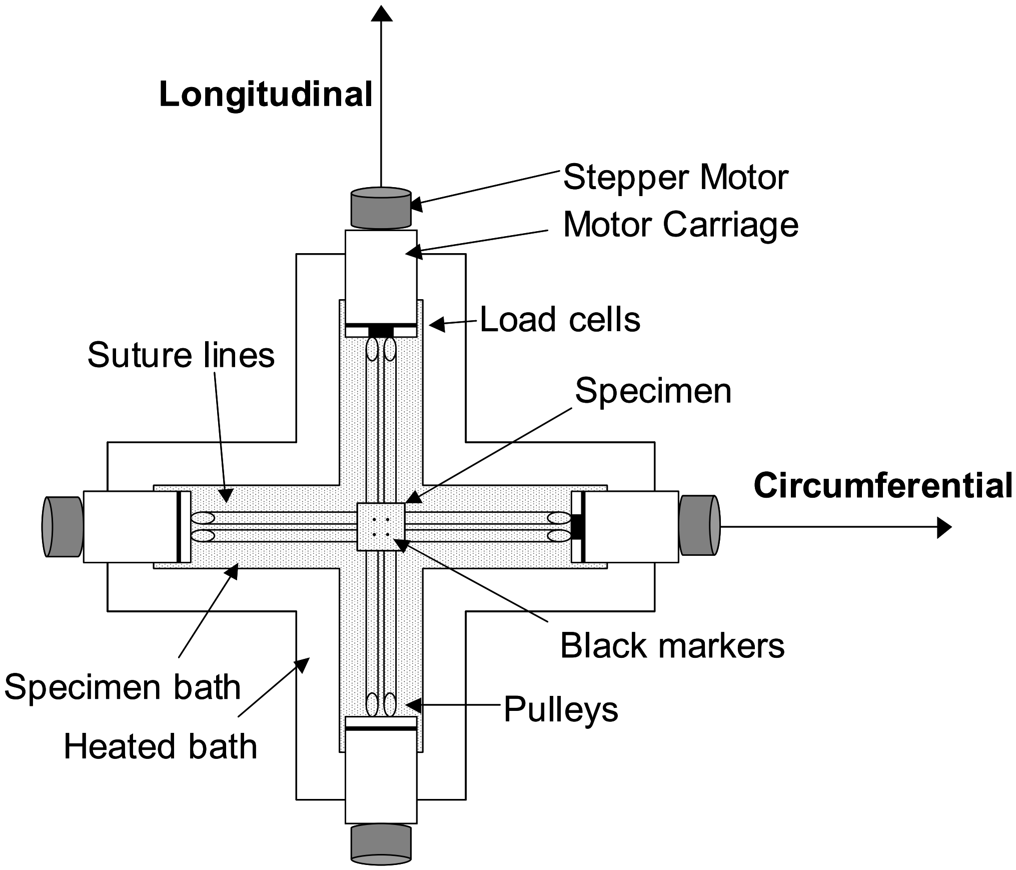

Figure 3-2 Sample biaxial testing setup. The sample is marked with four black graphite particles (markers) and attached to the device via four hooks at each side.

3.1.1 Biaxial Mechanical Testing Analysis(81)

The deformed positions **x** and the initial positions **X** of the node markers are used to calculate the stretch ratios, λ_i, and the in-plane shear components, κ_i, cumulatively the deformation gradient, **F**.

$$\begin{aligned} x_C &= \lambda_C X_C + \kappa_C X_L \\ x_L &= \lambda_L X_L + \kappa_L X_C \\ x_h &= \lambda_h X_h \end{aligned} \tag{3.1}$$

The shear components, κ_i, are a measure of the two angles with respect to the orthogonal axes and the subscripts C, L, and h represent the three dimensions circumferential, longitudinal, and the thickness dimension, respectively. Stretch, λ, is defined as follows.

$$\lambda = \frac{\text{current length}}{\text{original length}} \tag{3.2}$$

The deformation here is assumed to be homogenous between the markers. Soft tissues have negligible permeability$^{(82)}$ and are thus modeled as incompressible, so that λ_h, although not measured, can be calculated from det $\mathbf{F} = 1$.

The locations of the markers in the target region of the specimen are tracked and two-dimensional coordinates of each marker are recorded throughout testing. The absolute local coordinates are often mapped to a finite element to obtain the components of the **F**. The displacement field comprised of the components of **F**, $\mathbf{u}=\mathbf{x}-\mathbf{X}$ for each data point is mapped to the finite element through

$$\mathbf{u}(r,s) = \sum_{n=1}^{m} f_n(r,s)\mathbf{u}_n \tag{3.3}$$

where f_n is the shape function of that marker (henceforth termed node), n is the node number index, m is the number of nodes, and r and s the two-dimensional finite element isoparametric coordinates. The derivatives of u_i are calculated from the sum of the shape functions across all nodes with the following equation:

$$\begin{aligned} \frac{\partial \mathbf{u}}{\partial r} &= \sum_{n=1}^{m} \frac{\partial f_n}{\partial r}\mathbf{u}_n \\ \frac{\partial \mathbf{u}}{\partial s} &= \sum_{n=1}^{m} \frac{\partial f_n}{\partial s}\mathbf{u}_n \end{aligned} \tag{3.4}$$

Using shape functions that are bilinear in a four-node, two-dimensional element allows easy computation of the displacements in the two orthogonal dimensions within the element using equations (3.4). Then the displacements (**u**) in real space - mathematically the derivatives with respect to the C (circumferential) and L (longitudinal) directions - are calculated via numerical inversion of the following relation:

$$\begin{bmatrix} \dfrac{\partial}{\partial r} \\ \dfrac{\partial}{\partial s} \end{bmatrix} = \begin{bmatrix} \dfrac{\partial u_C}{\partial r} & \dfrac{\partial u_L}{\partial r} \\ \dfrac{\partial u_C}{\partial s} & \dfrac{\partial u_L}{\partial s} \end{bmatrix} \begin{bmatrix} \dfrac{\partial}{\partial x_C} \\ \dfrac{\partial}{\partial x_L} \end{bmatrix} \tag{3.5}$$

Using these derivatives, the deformation gradient is calculated at each point by differentiating with respect to the reference positions via

$$\mathbf{F} = \frac{\partial \mathbf{u}}{\partial \mathbf{X}} + \mathbf{I} = \begin{bmatrix} \dfrac{\partial u_C}{\partial X_C} & \dfrac{\partial u_C}{\partial X_L} \\ \dfrac{\partial u_L}{\partial X_C} & \dfrac{\partial u_L}{\partial X_L} \end{bmatrix} + \begin{bmatrix} 1 & 0 \\ 0 & 1 \end{bmatrix} = \begin{bmatrix} \lambda_C & \kappa_C \\ \kappa_L & \lambda_L \end{bmatrix} \tag{3.6}$$

For constitutive modeling in strain-energy models, these measurements are converted into the equivalent in-plane Green's strain tensor **E** using

$$\begin{aligned} E_C &= \frac{1}{2}\left(\lambda_C^2 + \kappa_L^2 - 1\right) \\ E_L &= \frac{1}{2}\left(\lambda_L^2 + \kappa_C^2 - 1\right) \\ E_{CL} &= \frac{1}{2}\left(\lambda_C \kappa_C + \lambda_L \kappa_L\right) \end{aligned} \tag{3.7}$$

Stress is calculated from the loads (P), lengths (L), and thickness (h) measurements shown in Figure 3-1 using equation (3.8). It is assumed that the tissue is in a state of plane stress so that only the components t_{ii} where i=C,L are nonzero. Lagrangian stresses, **T**, the force per unit original cross-sectional area, are usually computed in real-time during testing. The components of **T** are computed by from g=9.8 m/s^2. Here the subscripts C and L represent circumferential and longitudinal specimen dimensions, as shown in Figure 3-1.

$$\begin{aligned} T_{CC} &= \frac{gP_C}{hL_L} \\ T_{LL} &= \frac{gL_L}{hL_C} \end{aligned} \tag{3.8}$$

For modeling purposes, these Lagrangian stresses are converted to the second Piola-Kirchhoff stress tensor $\mathbf{S}$ via

$$\mathbf{S} = \frac{\mathbf{T}}{\mathbf{F}} \tag{3.9}$$

3.2 Setup and Preparation

3.2.1 Tissue Preparation

All bladders used in the studies presented in this section are from female Sprague-Dawley rats 250-300g and four to five months of age. They were devoid of disease unless otherwise stated. Before testing, the intact bladders were refrigerated at least overnight (12+ hours) but not longer than two nights (<48 hours) in a modified Krebs solution containing 113 mM NaCl, 4.7 mM KCl, 1.2 mM $MgSO_4 \cdot 7H_2O$, 25 mM $NaHCO_3$, 1.2 mM KH_2PO_4, 11.5 mM glucose, and 1 mM egtazic acid (EGTA). No calcium was present in this solution, helping to ensure that the bladder was in an inactivated state. Other researchers have verified that the addition of EGTA to the bath media both immediately before testing(4) and overnight(65) was sufficient to remove bladder muscle tone and prevent spontaneous and stretch-induced contractions during testing. The bladders were opened along the urachus, and the trigone and apex were removed. The tissue was trimmed to a square with the edges parallel to the anatomical and orthogonal longitudinal (apex-urethra, or cranio-caudal direction) and circumferential directions (Figure 3-3). Although the final sample represented the majority of the entire bladder, there was little, if any, curvature present, so curvature was not a factor in testing or analysis.

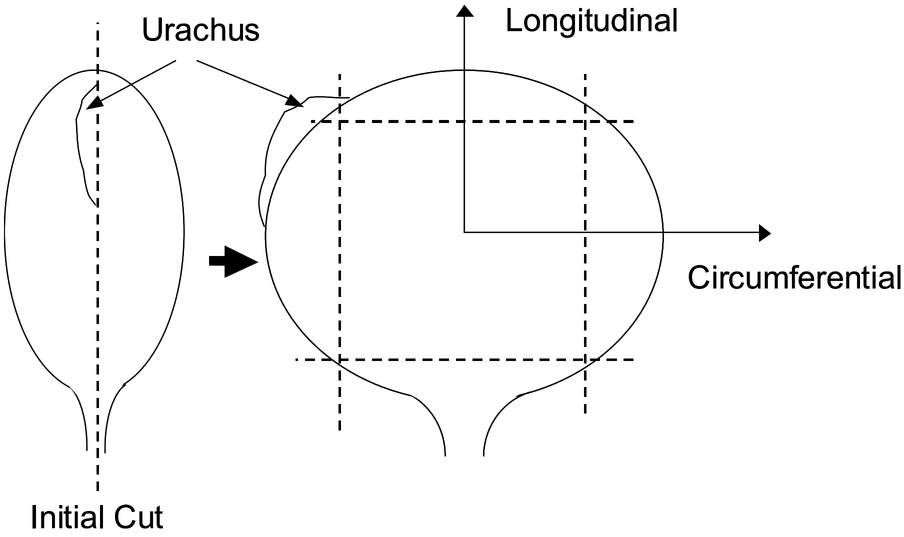

Figure 3-3 Preparation of biaxial test sample from intact rat bladder. The organ is trimmed to a square.

The thickness and lengths were measured with a dial caliper and a ruler, respectively. The sample was trimmed until the lengths of the sides were equal so these measurements were always identical. The average thickness was calculated from four measurements of the thickness at four evenly-spaced locations in the square. Mean measurements are shown in Table 3-1.

Table 3-1 Mean and (SEM) measurements of all biaxial sample groups. See Table 3-3 for a listing of how many samples were in each group.

Group	Sides (mm)	Thickness (μm)
Normal room temperature biaxial	8.42 (0.19)	359.63 (16.8)
Normal physiologic environment biaxial	8.22 (0.30)	341.95 (13.7)
Normal slow-loading testing biaxial	8.44 (0.55)	345.54 (26.6)
Normal viscoelastic biaxial	9.17 (0.32)	385.74 (15.9)
Spinal cord injured biaxial	12.38 (0.54)	620.71 (64.3)

3.2.2 Validation of Absence of Muscle Activity

The specimen preparation, bath medium, and protocol were developed to ensure that no spontaneous contractions would occur during testing but to otherwise maintain live, intact tissue. To verify that this resulted in the desired tissue condition, two rat bladders were placed in the refrigerated modified Krebs solution described above for two nights before testing. From each, a 1 mm wide strip of tissue was cut about 2 mm from the apex of the dome, then the ring was cut open and the specimen was mounted in a testing apparatus equipped with a field stimulator and force transducers. Each sample was tested twice. In the first test, the bathing solution was the same as the storage solution, and at room temperature. The solution was not bubbled with 95% O_2 5% CO_2, identical to the first set of planned quasi-static biaxial mechanical testing runs. The electrical stimulation consisted of a train of 100 rectangular wave pulses at 20 Hz of magnitude 100 volts every 100 seconds. Following several cycles of field stimulation, stimulation was halted and 1 μM carbamylcholine chloride was administered, followed by a washout, and then 50 μM α,β methylene ATP (α,β methyleneadenosine 5'-triphosphate), a purinergic receptor agonist, was administered. After the test in calcium-free Krebs, the bathing solution was changed to a calcium-enriched solution (the solution above minus EGTA plus 2.5 mM $CaCl_2 \cdot 2H_2O$), heated to 37 °C and bubbled with 95%O_2 5%CO_2. Then the testing was repeated.

There was no tissue response to either electrical or chemical stimulation in the calcium-free EGTA solution during the first 2,000 seconds (Figure 3-4). When the solution was changed to one without EGTA and with calcium at 2,000 seconds into testing, small contractions began and were enhanced by heating and gas bubbling at 3,000 seconds. In a calcium-enriched solution, both carbamylcholine chloride and α,β methylene ATP produced normal responses at times 4,200 and 4,800 seconds, respectively.

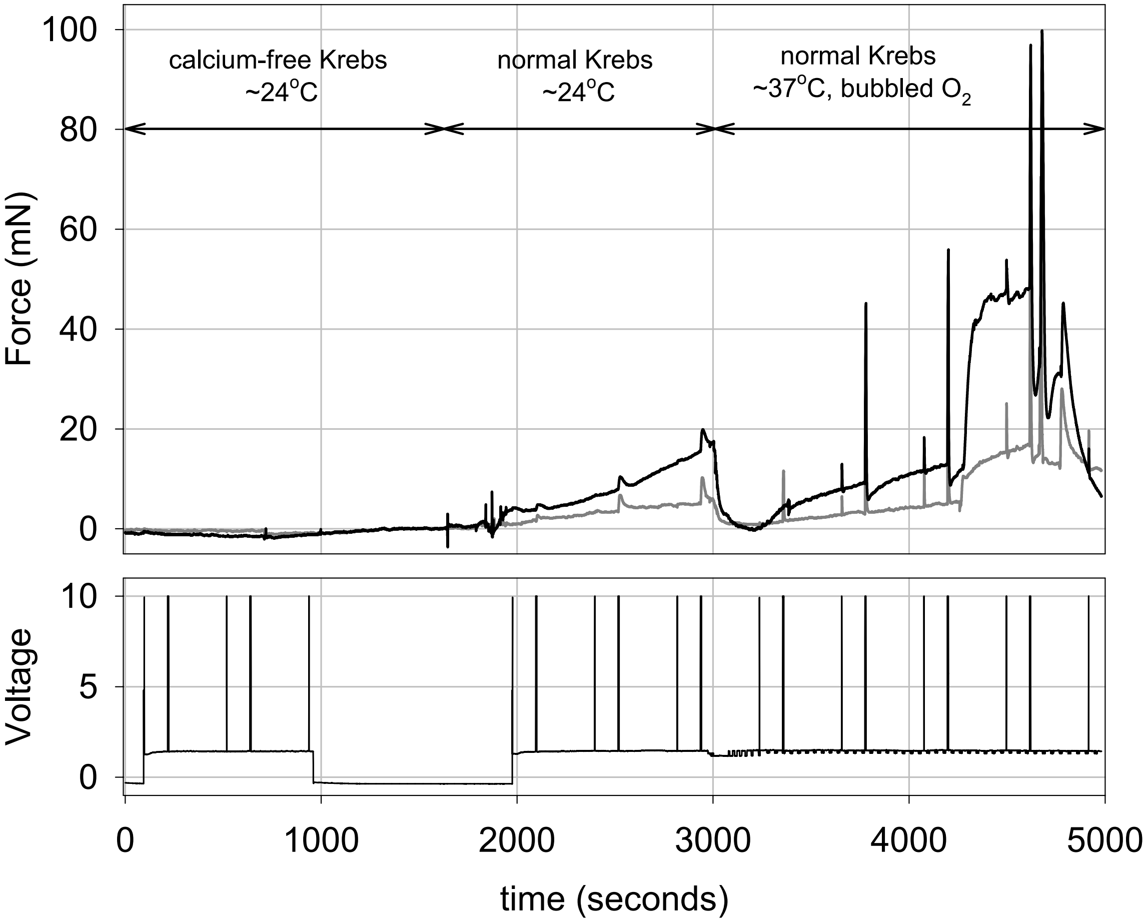

Figure 3-4 Electrical stimulation of bladder wall. The top trace shows the force generated by two specimens that were kept in the calcium-free Krebs solution described above, while the bottom trace illustrates the times of electrical stimulation of the muscle contraction. 0-1,000 seconds: Electrical stimulation was applied to the strips of bladder in a room temperature, with no gas bubbling. No force response was seen. 1,000-1,600 seconds: The stimulation was turned off and the following pharmaceuticals were administered to evoke a response: 10 μM carbachol, 50 μM carbachol, and 50 μM α-β mATP. None of these evoked a response. 2,000-3,000 seconds: At 2,000 seconds, the solutions were exchanged for a solution containing calcium and without EGTA to allow for contractions. Contractions started almost immediately. 3,000-4,200 seconds: In a heated, bubbled solution, the contractions were strong. 4,200-5,000 seconds: 50 μM carbachol, and 50 μM α-β mATP both caused large contractions (washout between).

3.2.3 Biaxial Testing Methods

Details of biaxial testing procedures in our laboratory have been thoroughly described in the literature for other studies.(80,81,83,84) In the present study, as in those, the procedure was as follows: Each side of the square test specimen was attached to motor carriages with a surgical staple at each end of two nylon thread lines (Figure 3-2 and Figure 3-5). Opposite the staples, the two loops encircled small pulleys on each side of a common horizontal axle, the axle connected in turn to a vertical pivoting rod, permitting near-frictionless rotation in three dimensions. Each pulley ensured that the force in each line was equivalent and the pivoting rod ensured that the forces were the same in each pair of suture lines. All specimens were tested in the modified Krebs solution described above, at either room temperature with no bubbling, or in the same solution heated to 37 °C and bubbled with 95%$O_2$5%CO_2. Load was monitored in the two orthogonal axes by two load cells. Stresses along the longitudinal and circumferential axes (T_L and T_C, respectively) were defined in the Lagrangian sense as force/unloaded cross-sectional area (Figure 3-1). Further, by varying the loads in each orthogonal axis the complete mechanical behavior of the bladder wall over the entire normal and pathological physiologic functional range could be determined (Figure 3-6, Table 3-2). An example of a 12-cycle run is shown in Figure 3-7.

The in-plane axial stretch (λ=current distance/initial distance) was determined during testing from the displacements of four black graphite markers affixed to the surface of the specimen (Figure 3-2). These marker positions were used later during post-processing in a finite element interpolation procedure to determine the true stretches (section 3.1.1).(85) During testing, both the load and deformation in each axis were continuously recorded at 12-15 Hz.

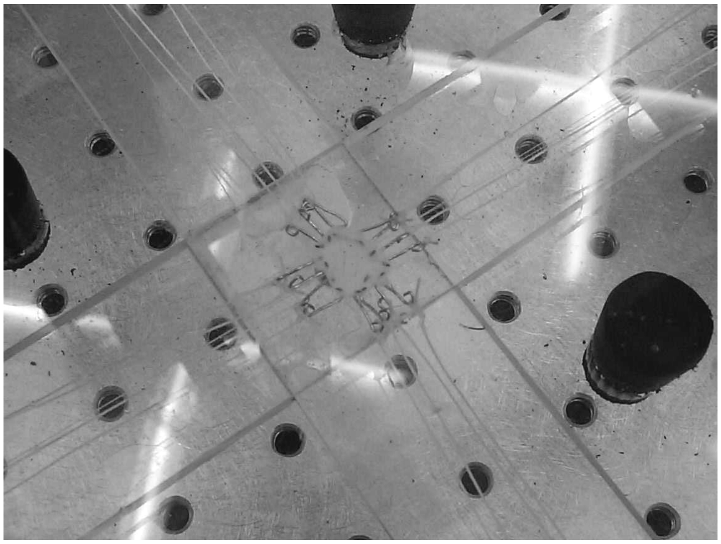

Figure 3-5 Image of sample attached to biaxial testing device. For schematic, see Figure 3-2.

Table 3-2 Protocol for all specimens. See Figure 3-6 for graphical representation.

Protocol	Ratio (T_C:T_L)	Maximum Stresses (kPa)	
		Circumferential, T_C	Longitudinal, T_L
1	1:1	100	100
2	0.5:1	50	100
3	0.75:1	75	100
4	1:1	100	100
5	1:0.75	100	75
6	1:0.5	100	50
7	1:1	100	100

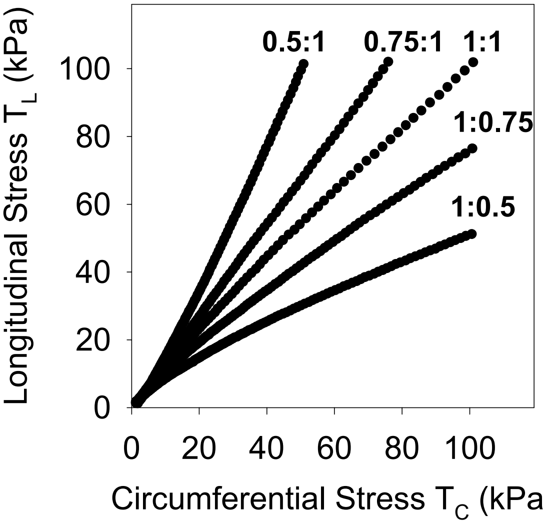

Figure 3-6 Example of the stress control for all test protocols for a normal bladder specimen along with the protocol ratio (see Table 3-2). See Figure 3-3 for direction definitions.

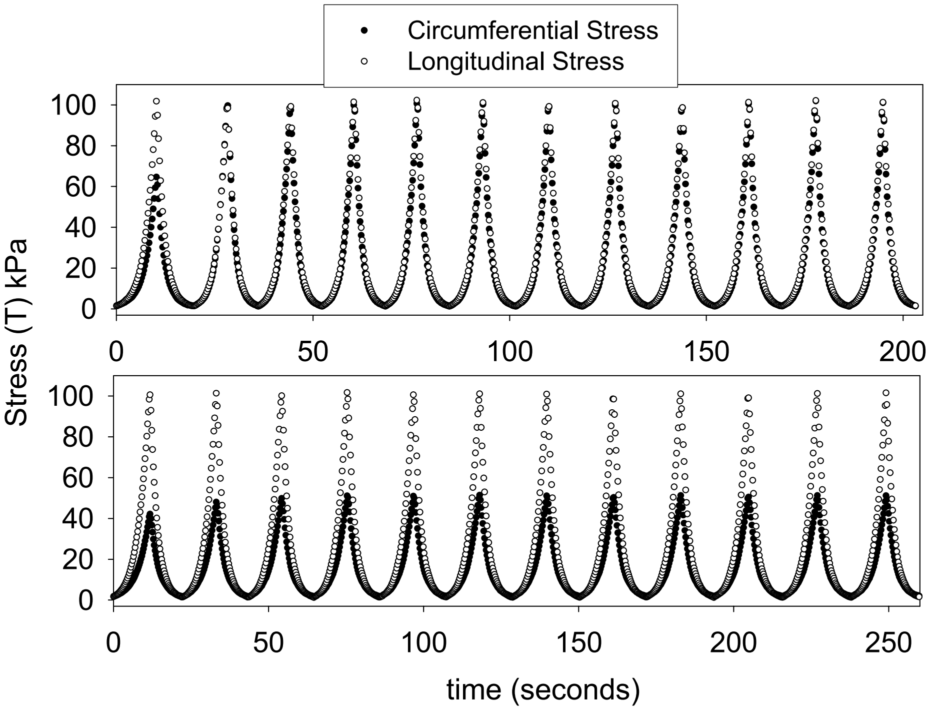

Figure 3-7 Loading and unloading test runs for protocol 4, equibiaxial stress (top) and protocol 2, maximum 50 kPa circumferential: 100 kPa longitudinal stress (bottom).

3.2.4 Load and Strain Synchronization

The biaxial testing components were controlled through a custom-written C++ program. In this program, the measurement of time, load, and the frame grabbing were triggered in series through functions within the program. To ensure that the three measurements were synchronized, the load and time were taken first as both were completed very quickly. Obtaining the subsequent single image to the memory of the frame grabber was somewhat slower. The longest computation time was that of calculating the actual marker positions from the image, which included functions to call small subimages of data from the frame grabber memory. Using this successive acquisition of these three data types allowed for the data to be out of synchronization no more than the time it took to call the functions, measured as at least an order of magnitude less than the limiting time resolution, as discussed below.

3.2.5 Spatial, Load, and Temporal Resolutions

The spatial resolution was different for each sample because it depended on the magnification of the lens, which in turn depended on the size of the sample. The resolution was determined for each sample by saving an image of the sample in the same field as a millimeter ruler at the beginning of every test. Later, the image coordinates of points on two successive millimeter lines were recorded and the distance between the points calculated. Of the 43 normal rat bladder biaxial samples (see section 3.2.6 for table of samples) the mean spatial resolution was 13.67 microns per pixel, with a standard deviation of 1.461 (range: 10.87-17.54). The spatial resolution of the eight spinal-cord-injured samples (these tissue samples were larger) had a mean of 18.17 microns/pixel and standard deviation of 1.45 (range 15.62-19.22). Repeating the measurement on the same sample 20 times checked the repeatability of this measurement and calculation technique. The standard deviation of the mean of these verification measurements was 1.10% of the mean, indicating high repeatability.

For these experiments, the load was acquired through a 12-bit A/D computer data acquisition card at 5000 kHz. For each load value, 50 samples were recorded and averaged to remove high frequency jitter. To obtain the most precise load as possible for each test two different load cells were used during the course of these studies. For all quasi-static tests, including room temperature (section 3.3), physiologic environment (section 3.3.2), and slow-loading tests (section 3.3.3), the normal specimens were tested using a 50-gram full-scale load cell. For all stress relaxation tests (section 3.4) and all spinal-cord-injured animal testing (section 3.5), a 250 gram maximum load cell was used. The load cells used were calibrated with a known weight at the beginning of every test. The resolutions for these two load cells are shown below. Note that these resolutions are the theoretical resolutions, and that due to noise and other factors the practical resolution is generally slightly less. This is one reason for the acquisition and averaging of 50 points for every datapoint.

$$\begin{aligned} \text{50 gram cell} &= \frac{50}{2^{12}} = \frac{50}{4096} = 0.0122 \text{ grams} \\ \text{250 gram cell} &= \frac{250}{2^{12}} = \frac{250}{4096} = 0.0610 \text{ grams} \end{aligned} \tag{3.10}$$

The marker positions used to calculate stretch in all experiments were obtained via images captured by a standard camera attached to a frame grabber. The number of pixels was 480x640, and a maximum of 15 frames per second (30 interlaced frames) could be obtained. In most experiments, the simultaneous calculations required that the framing rate be reduced to 12 or 13 frames per second during runtime. Since the load and time acquisition had to be synchronized with the stretch calculations, the framing rate dictated the temporal resolution.

3.2.6 Statistical Significance and Number of Samples

In general, statistical significance was assessed with the unpaired Student-t test, with significance at values of $p<0.05$, unless otherwise stated. Unless otherwise specified, all error bars are standard error of the mean (SEM), which is defined as the standard deviation divided by the square root of the number of samples. Where possible, significant differences between data in vertical bar charts are represented by a barbell line (●———●), indicating statistical differences between the populations represented by the bars under the dots at each end of the barbell line.

In total, 109 rat bladders were used to study the mechanical behavior of rat urinary bladder wall (Table 3-3). Each bladder was used for one experiment only and one sample only was sectioned from each intact bladder. Wherever possible, bladders were obtained from rats that were used for other purposes. To limit the number of animals used experiments were well-planned and carefully considered before experimentation. In some cases, the urethra was also harvested for investigations by another researcher. Other organs were also harvested for other purposes. In almost all cases, the spinal-cord-injured (SCI) animals were used also for cystometry studies in other research.

The 30 samples listed below next to "Normal, other" were used for preliminary experiments, to validate removal of contraction by EGTA (see section 3.2.2), for active contraction experimentation (not discussed here), and for experiments which, for various reasons, were not successful. Almost all samples of the SCI "other" group were part of a study investigating the effects of systemic capsaicin on the quasi-static mechanical properties of the SCI bladder from 1 to 6 weeks after injury (not reported here).

Table 3-3 Number of samples used for mechanical property studies of rat bladder wall.

Group	Number of Samples	See section
Normal room temperature biaxial	12	3.3
Normal physiologic environment biaxial	8	3.3.2
Normal slow-loading testing biaxial	8	3.3.3
Normal viscoelastic biaxial	15	3.4
Normal whole organ filling	7	3.3.5
Spinal cord injured biaxial	8	3.5
Normal, other	30	Not shown
Spinal cord injury, other	21	Not shown
TOTAL	**109**	

3.3 Quasi-static Testing(86)

Each test consisted of 12 contiguous cycles (see examples in Figure 3-7) with a period of 15 to 25 seconds, with a total of seven test runs (Figure 3-6 and Table 3-2). This period was chosen because during preliminary testing it was repeatable and stable between specimens and it resulted in enough data for all the analyses planned. Multiple cycles per protocol were utilized to allow for mechanical preconditioning. Mechanical preconditioning is inherent in soft tissue testing: the first few contiguous cycles (approximately five) are needed to stabilize mechanical behavior.(82) As in previous studies, the loading curve of either the last or next-to-last cycle was chosen as representative of the preconditioned mechanical response.(84) During all tests, the maximum stress level was 100 kPa on one or both axes. This maximum stress level was based on rat cystometrogram data and the Law of Laplace which relates pressure in a sphere to the tension in the wall of the vessel (Figure 3-8).

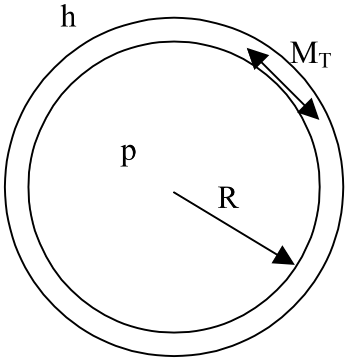

Figure 3-8 The law of Laplace describes the tension (M_T) in the wall of a sphere of radius (R) as a function of the pressure (p). A requirement of application of this law is that the thickness of the wall is much less than the radius ($h \ll R$).

$$M_T = \frac{pR}{2} \tag{3.11}$$

where M_T is the membrane tension (force/length) in a sphere, p is the internal pressure (force/area) and R is the radius of the sphere (length). Maximum Lagrangian stress is then computed by

$$T_{\max} = \frac{M_T}{h} \tag{3.12}$$

In these equations, the internal radius of the normal bladder was 6 mm, the thickness was 0.4 mm, and the pressure was the maximum in rat cystometry studies of 45 mmHg(46) or 75 cmH_2O.(87) These computations yield a stress of about 50 kPa. We used 100 kPa to gather extra physiologic mechanical data. Preliminary testing indicated that this stress level did not induce tissue damage, as evidenced by a stable mechanical response throughout the test protocol. Further, 100 kPa is well below the ultimate stress of 720 kPa for normal tissue reported by Dahms *et al.*(44) The maximum stress level for the SCI group was kept at 100 kPa to allow comparison to the control group.

All test protocols maintained a constant ratio of the axial stress, T_C:T_L throughout cycling. Testing began with an equibiaxial protocol of T_C:T_L = 100 kPa : 100 kPa. Next, five consecutive tests were performed with T_C:T_L: 100:50, 100:75, 100:100, 75:100, 50:100 (Figure 3-6 and Table 3-2). These ratios were chosen to cover a wide range of stress states. A final equibiaxial test (run 7) was performed to confirm that the mechanical behavior had not changed during the experiment. Total testing time was approximately an hour and a half for each specimen. In addition to the stress and strain data, we also computed the areal strain = $\lambda_L\lambda_C$-1, the change in area between the reference and deformed states. Areal strain is a physically meaningful parameter that represents the net compliance of the tissue, incorporating stretch effects from both axes. Finally, hysteresis was computed as a percentage of the difference between the unloading area and the loading areas underneath the stress-strain curves.

$$\text{Percent area hysteresis} = \frac{(\text{loading area - unloading area})}{\text{loading area}} \times 100 \qquad (3.13)$$

Before each test, the stretches were normalized to the present marker coordinates so that the stretches always began at one. After testing, all specimens were analyzed to the preconditioned marker position (section 3.6). However, to record the changes of stretch between the test runs, the resting marker positions were recorded periodically throughout testing. These regular intervals are shown in Table 3-4.

Table 3-4 Marker positions taken between testing runs.

Marker Filename	Description
Floating	After graphite markers applied, sutures not attached
Mounted	Suture lines attached, but not loaded
0.5 grams	Suture lines attached to device and loaded to 0.5 grams
Preconditioned	After initial preconditioning run, protocol 1 in Table 3-2
Final	After final equibiaxial test, protocol 7 in Table 3-2

3.3.1 Equibiaxial Results

Stress levels were controlled well for all samples for all stress protocols (Figure 3-6 and Figure 3-7). The preconditioned reference state, used for analysis, was about 80% above the floating (unloaded) condition. There was a statistical difference in areal strain (Tukey's test) between the first (1) and last (7) 1:1 protocol tests, but neither of the other comparisons (1-4 or 4-7) was statistically different (see Table 3-2, Figure 3-10). This is an indication of the stretch increase over the entire test. In addition, creep is observed in individual samples (Figure 3-11). The mean equibiaxial response for both circumferential and longitudinal directions was approximately isotropic with a maximum stretch of ~1.12 above the preconditioned stretches (Figure 3-9). Additionally, shear and rotation were less than 3 degrees at all times during testing, resulting in small shear stresses and strains. Therefore, the shear values were considered insignificant and were not computed in the analysis.

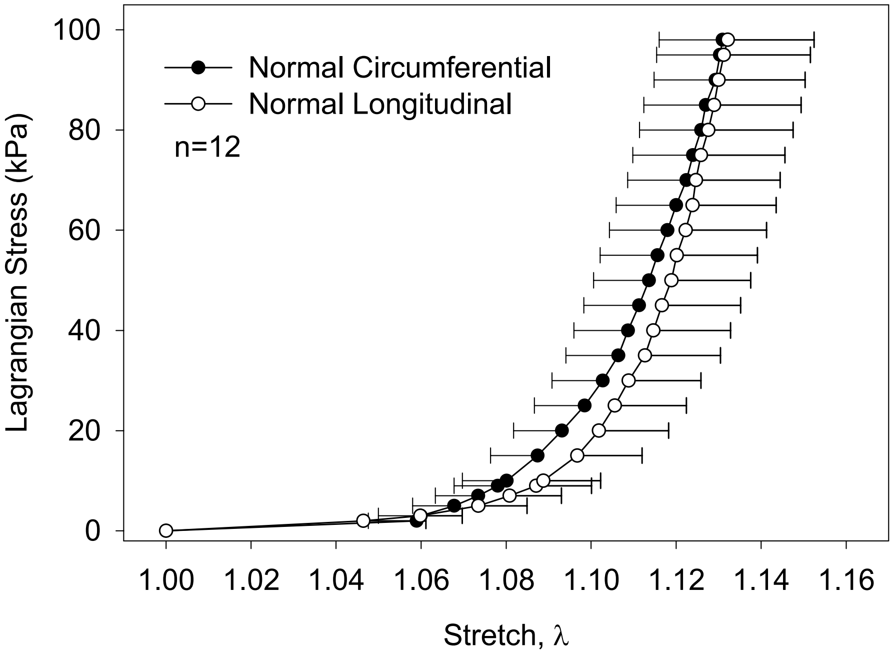

Figure 3-9 Mean and SEM of the mechanical response to equibiaxial loading in the circumferential (filled circles) and longitudinal (open circles) directions. The circumferential stresses have negative error bars and longitudinal stresses have positive error bars.

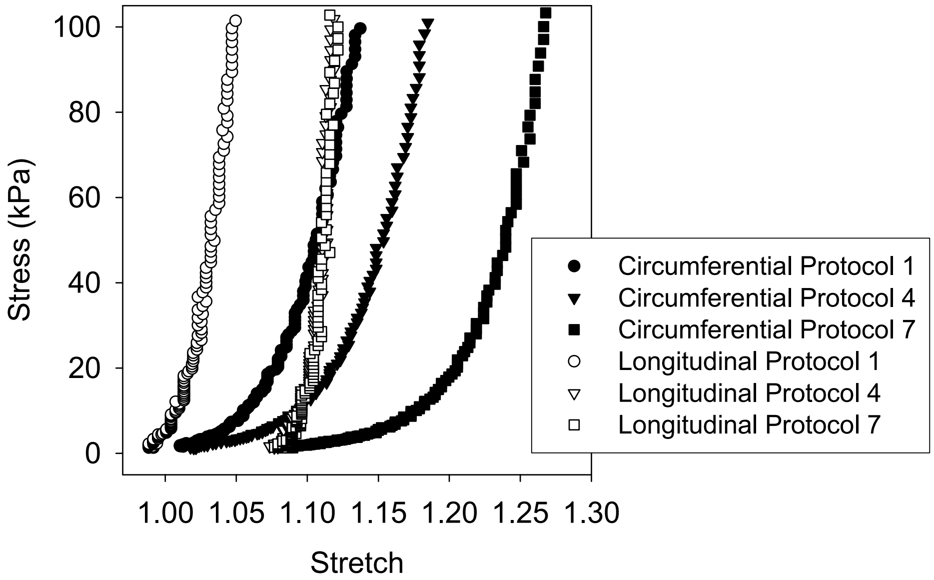

Figure 3-10 Stress-stretch curves for protocols 1, 4, and 7 for a representative sample.

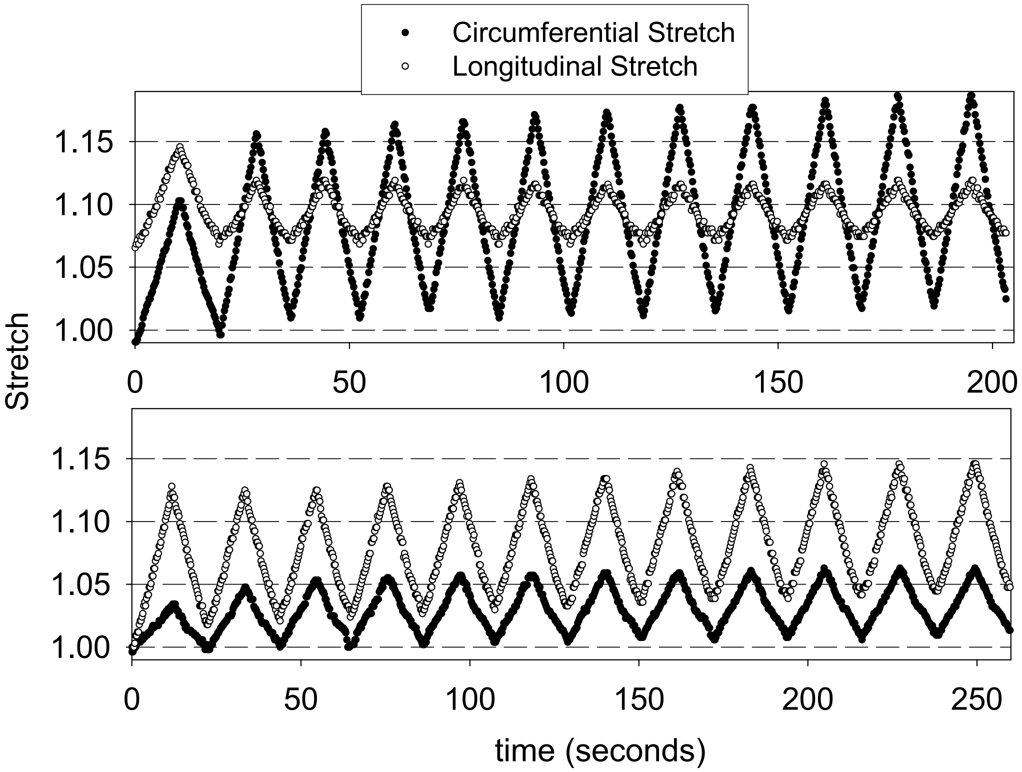

Figure 3-11 Stretch during one protocol. This stretch corresponds to the stress in the sample of Figure 3-7.

The stress-strain response for normal bladder is shown in Figure 3-12. There are several important differences between the circumferential and longitudinal responses. The spread of the curves (i.e. differences between the equibiaxial and non-equibiaxial responses) and the circumferential plot is much greater than for the longitudinal direction. The run 6 curve (T_C:T_L of 1:0.5) goes to the left in the longitudinal direction, indicating that the tissue becomes shorter in the longitudinal direction during this test. This was not an active contraction effect (the tissue has been inactivated) but a decrease in passive tissue dimensions and is evidence of "asymmetric" mechanical cross-coupling, indicating that the longitudinal direction was more affected by the circumferential stress state than the circumferential direction was affected by the longitudinal stress state. Eight out of the 12 normal samples demonstrated this asymmetric cross coupling.

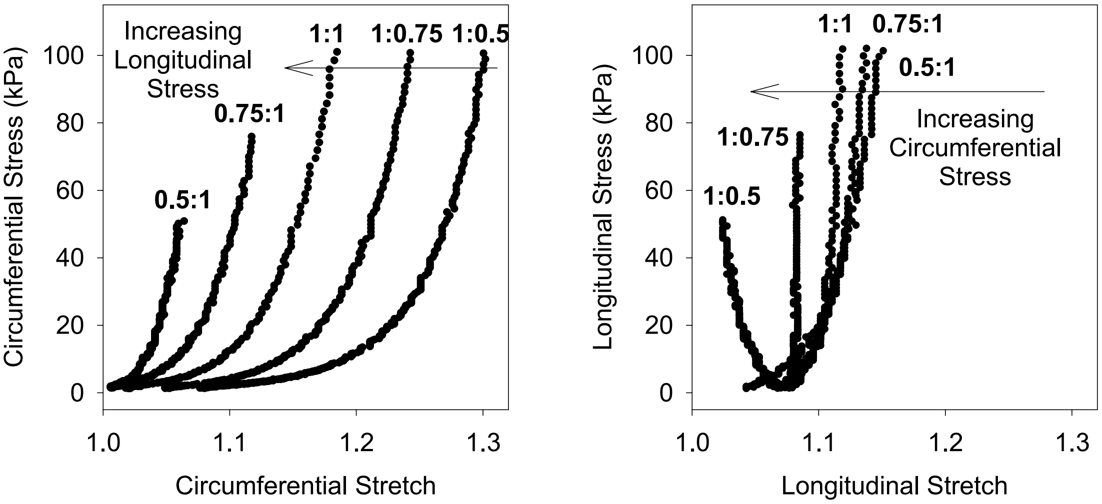

Figure 3-12 Stress-strain response to protocols listed in Table 3-2 for one normal specimen

3.3.2 Physiological Environment

The equibiaxial protocol was repeated in an environment with oxygenation and body temperature (37 ^{o}C) after the addition of a water jacket and heater to the device. In addition, an air cylinder, regulator, and tubing system were obtained so 95%$O_2$5%CO_2 could be bubbled through the testing media. This setup was not available previously, but all subsequent tests, including slow-loading tests and all stress relaxation protocols, were performed within this environment. The data from these heated and bubbled tests are presented against the room temperature and slow-loading data in Figure 3-15 and Figure 3-20 through Figure 3-25 in the following sections.

3.3.3 Slow-Loading Tests

As previously mentioned, Finkbeiner demonstrated that bladder wall strips subjected to different deformation rates had the same tension-deformation relationship.(5) However, the range of deformation rates used in his study was small, only 0.5 to 3 cm/hr, to a maximum stretch of about 1.50. Since the rat bladder function requires it to undergo the change from full to empty in ~30 seconds and from empty to full in one to two hours, the mechanical behavior over both states must be ascertained. For these experiments, a target cycle time of 1 hour was used, which allowed for comparisons over three orders of magnitude.

The tissue preparation was identical to that previously summarized, but the protocol was limited to equibiaxial tests because of the length of time required for each cycle. First, preconditioning was performed with the same 20-30 second cycle as previously described. Next, five cycles were run with the stepper motors at a much slower speed so that the complete loading and unloading cycle was about one hour (Figure 3-13). Some deformation that did not disappear at the end of the run (creep) was observed in these runs, and the fourth cycle was chosen for analysis in each sample (Figure 3-14). Due to the lack of perfect specimen control, an exact cycle time could not be specified. The real cycle times are shown in Figure 3-15. The mean cycle time was 22.63 minutes, with a SEM (n=8) of 2.36 minutes. This mean of 1,358 seconds is three orders of magnitude greater than the loading time previously described (20-30 seconds), indicating significant difference in loading times.(64) Both rats and guinea pigs uniaxial strips showed no difference in tension when subjected to strain rates ranging from 0.5 to 3 cm/hr, indicating a lack of a perceivable strain-rate effect.(5)

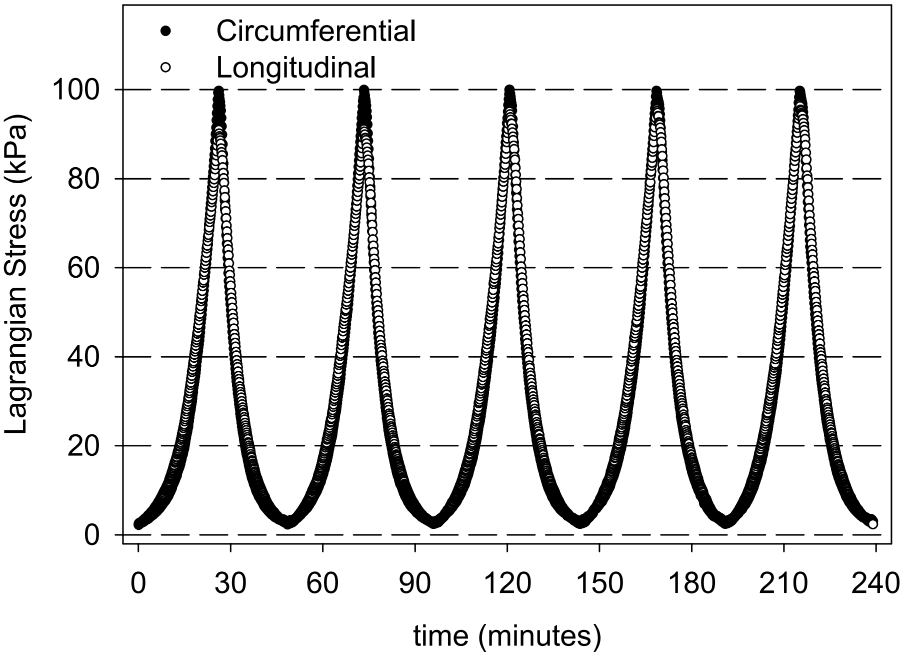

Figure 3-13 Complete five cycle loading and unloading curves in slow-loading protocol.

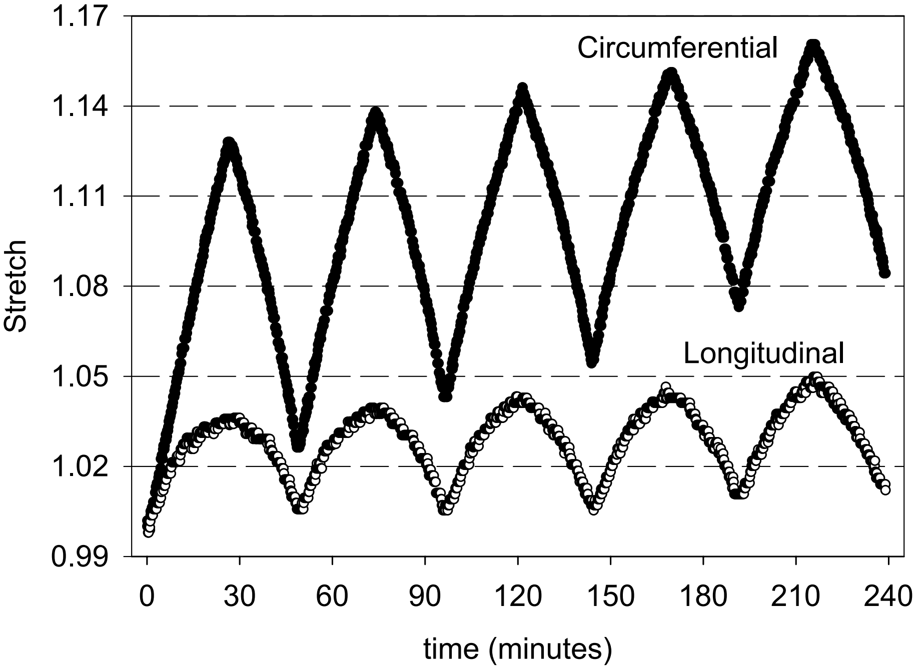

Figure 3-14 Resulting stretch from complete five cycle loading and unloading curves in slow-loading protocol (see Figure 3-13).

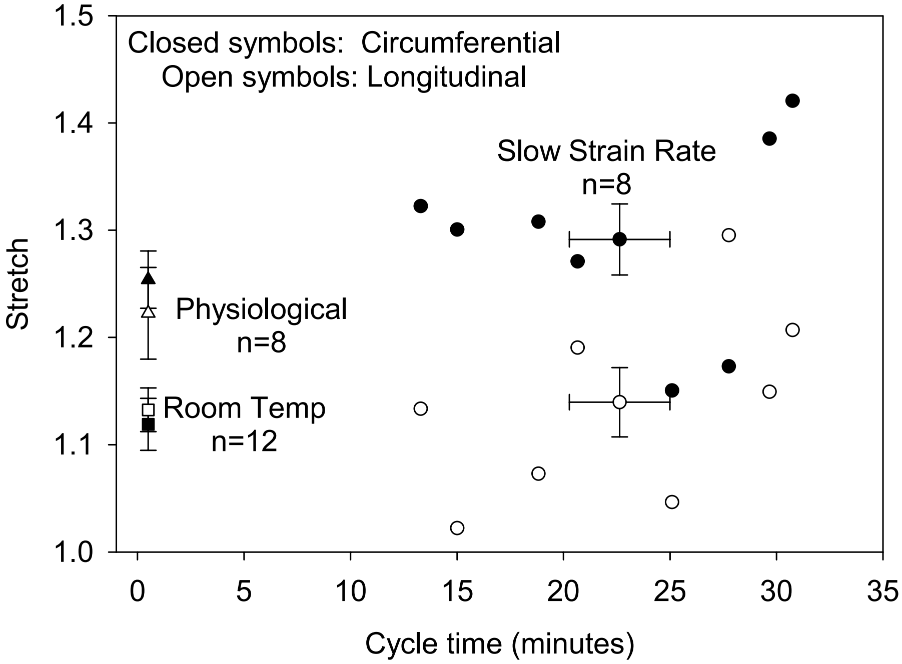

Figure 3-15 Maximum stretches in the 1:1 protocol in the circumferential and longitudinal directions for the three groups, showing comparison between cycle time and stretch. The circles demonstrate the range of cycle times tested. The means only are shown in Figure 3-20. Mean and SEM shown.

During these tests, data acquisition was slowed considerably because of computer memory constraints. Approximately the same number of data points was taken as during the 20-30 second cycles; however, the length of time between saved data points was increased. The rate of acquisition of data remained as high as possible for the best control of the test, but not all points were recorded. The peak stresses of many of the samples were lost when the peak occurred at a time point different than the recorded data point time (Figure 3-16). For discussion of the possible limitations and difficulties this restriction may have caused, see section 3.3.6

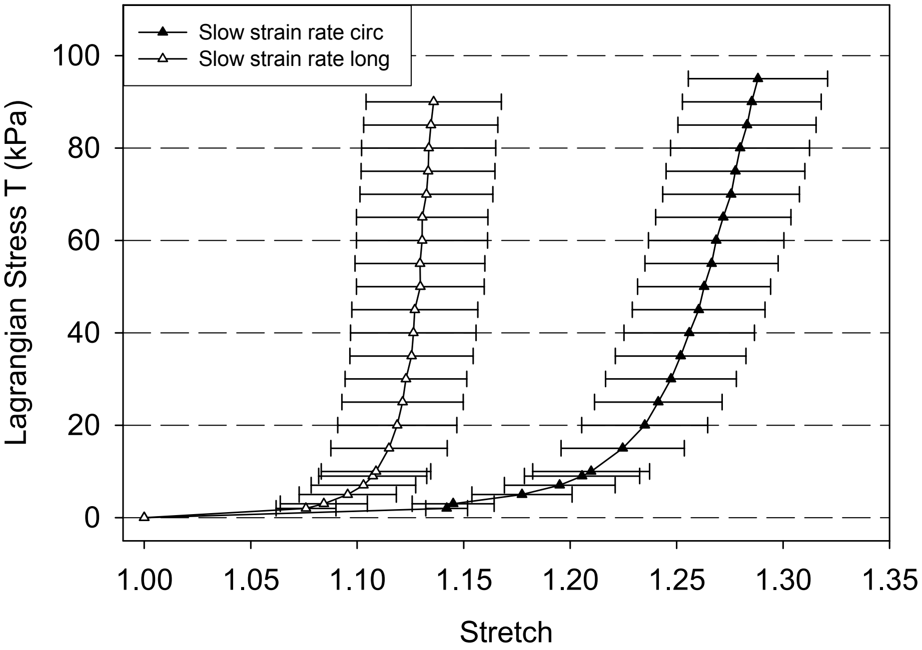

Figure 3-16 Mean and SEM curves from the slow-loading rate equibiaxial protocol. Note that the highest strain symbols are missing because of the method of acquiring the data (see text).

The protocol used in these tests also allowed comparisons between the results due to usual 20-30 second loading time and the slow-loading cycles. The test protocol used on each specimen involved running a preconditioning equibiaxial test with 12 cycles at the normal loading rate, which was then used for individual calibration of each specimen slow-loading tests. Thus, the differences in rate of stretch, maximum stretch, and hysteresis could be directly compared for each specimen.

The rate of stretch was two orders of magnitude lower in the slow-loading test than in the preconditioning test (Figure 3-17). The rate of stretch in the orthogonal directions in the slow-loading test were found to be statistically different due to the difference in stretch magnitude. Although the slow-loading test was three orders of magnitude slower than the preconditioning test, the stretch was generally higher in the slow-loading test (Figure 3-18). Additionally, the hysteresis values were different between the two axes in both tests (Figure 3-19).

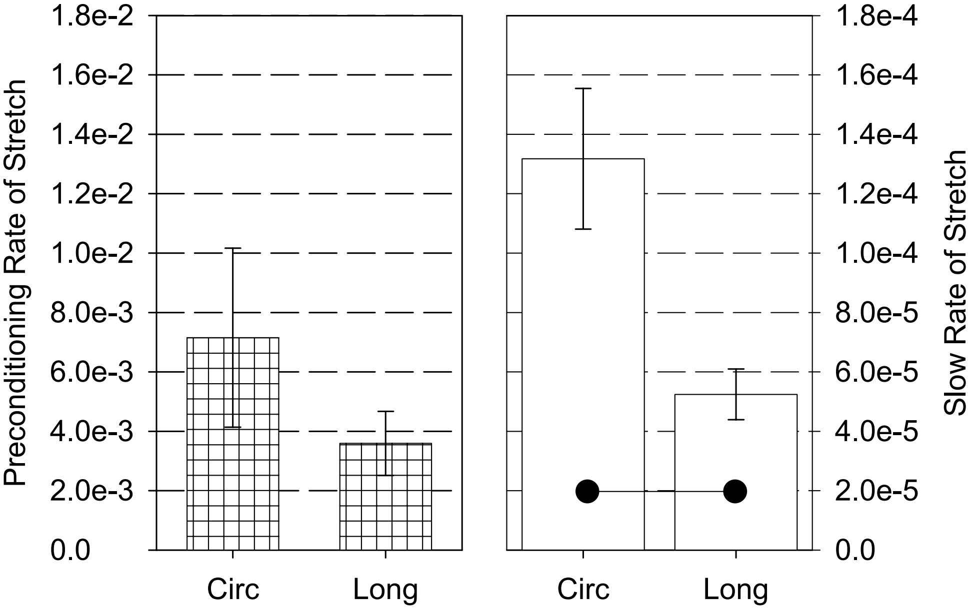

Figure 3-17 Mean and SEM rate of stretch for both preconditioning and slow-loading runs for circumferential (Circ) and Longitudinal (Long) samples. The preconditioning stretch rates in the two directions are not statistically different, but the rates in the slow-loading test are (p= 0.0083).

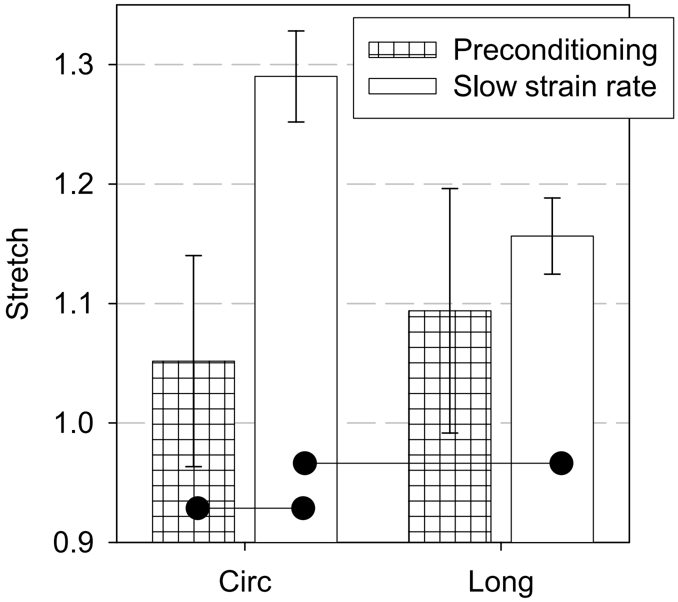

Figure 3-18 Maximum stretch values for both preconditioning and slow-loading runs in the same samples. The two anatomical axes are different in the slow-loading test (p=0.0196) and the circumferential direction is statistically different in the two protocols (p=0.0291).

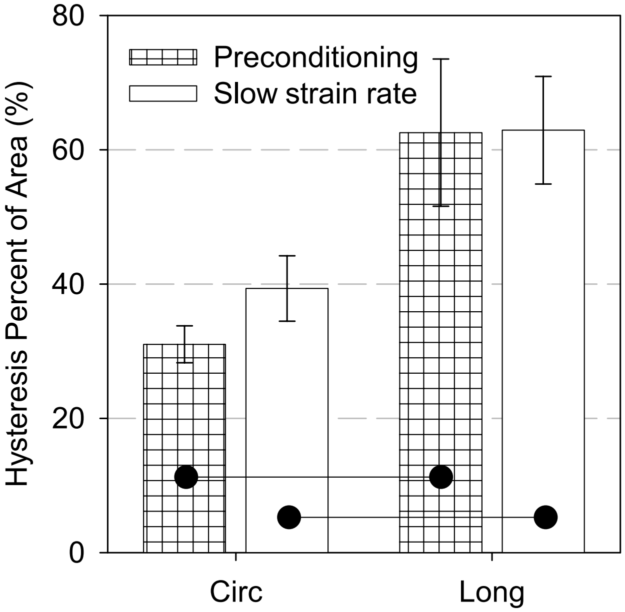

Figure 3-19 Hysteresis area for both preconditioning and slow-loading runs. In this group of samples, the hysteresis values are different between directions, with p-values of 0.0236 for preconditioning and 0.0363 for the slow-loading test.

3.3.4 Differences Between the Three Quasi-static Tests

As previously reported, the maximum stretches between the two anatomical directions in the room-temperature equibiaxial tests were not significantly different.(86) Also, the same test protocol performed under physiological conditions did not show significant differences between the two anatomical directions. However, within the two anatomical directions, there was a significant difference between those two testing environments as the stretch increased in both directions (Figure 3-20). The same effect was found by Alexander under long-term creep conditions.(64) This indicates that the mechanical behavior is different between the two environments, but that the two directions still behaved equally under equibiaxial loading.

The slow-loading protocol, however, did induce a difference between the circumferential and longitudinal directions. The stretch in the circumferential direction increased compared to the faster loading test in a physiologic environment, resulting in a significant difference between the room-temperature test and the slow-loading test. In the longitudinal direction, the stretch was lower, at a level similar to that of the room-temperature test, but not different from either of the other tests in that direction. This indicates that the behavior due to slow-loading may be fundamentally different from that due to faster loading, at least within the structure of the circumferential direction. As this slow-loading test may involve more time-dependent, viscoelastic effects, it is reasonable to assume that the viscoelastic behavior may be different between the two axes. Finkbeiner found an increase in maximum tension when the strain rates were slower.(5) Interestingly, here there was no statistical difference between the groups.

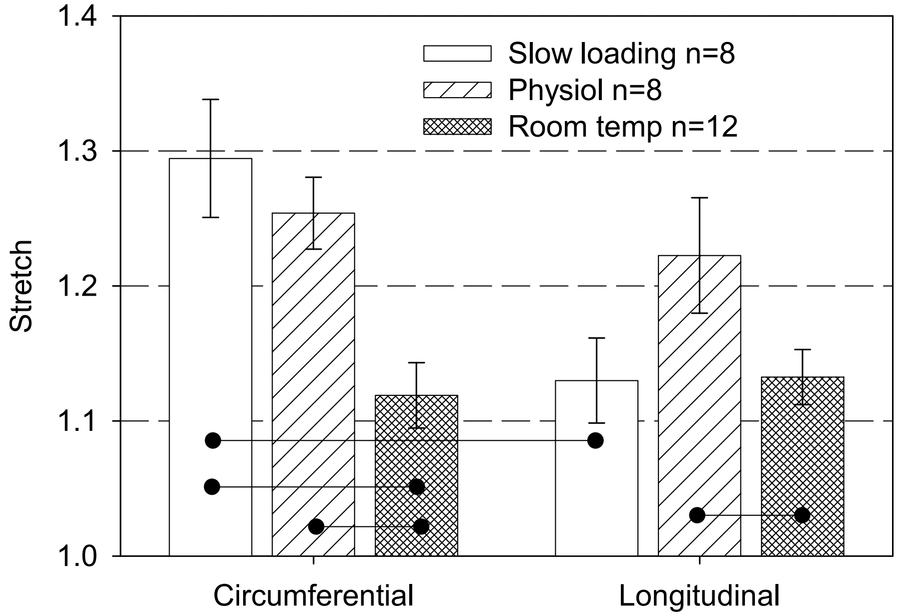

Figure 3-20 Comparison of stretch, λ, between the three sets of quasi-static data. The dotted lines indicate statistical difference with Student t-test and $p<0.05$. Circumferential physiological to room temperature: $p=0.0002$, circumferential slow-loading rate to room temperature: $p=0.0001$. Slow-loading circumferential to longitudinal: $p=0.0129$. Longitudinal physiological to room temperature: $p=0.0259$. Mean and SEM shown.

The differences in percent area hysteresis were similar to the differences between maximum equibiaxial stretches (Figure 3-21). The hysteresis was not different between orthogonal axes for any of the three protocols; however, the slow-loading hysteresis values were larger than the physiological environment values and the physiological environment hysteresis values were larger than the room-temperature testing values. There was a significant difference in both anatomical directions between the room-temperature group and both of the other groups, but not between the two tests performed under physiological environment. The difference is due only to the environment, not to the rate of loading, and the increase is equivalent in both orthogonal directions.

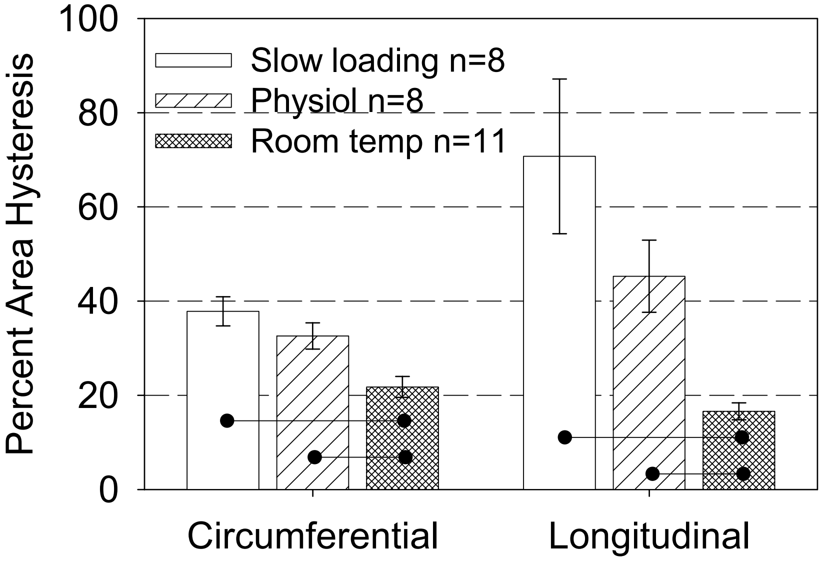

Figure 3-21 Percent area hysteresis for three groups. The barbells (●———●) indicate statistical difference with Student t-test and $p<0.05$. Circumferential physiological to room temperature: $p=0.0066$, circumferential slow-loading tests to room temperature: $p=0.00046$. Longitudinal physiological to room temperature: $p=0.00085$. Longitudinal slow strain rate to room temperature: $p=0.00076$. Slow-loading tests in the circumferential to longitudinal directions were almost significant at $p=0.0552$. Mean and SEM shown.

The following four figures show the circumferential (Figure 3-22) and longitudinal (Figure 3-23) stretch , the shear (alpha, Figure 3-24), and rotation (theta, Figure 3-25) in each of the three quasi-static testing protocols. As explained in section 3.3, the marker positions were recorded at various times during mounting and testing. In these plots, the number of samples is less than the total because the graphite markers fell off during mounting or the specimen stretched more than expected and the markers went out of the field of view during testing. In either case, the specimen was omitted from this analysis. Total group specimens were: Slow-loading test, 8; Physiological testing, 8; Room temperature, 12.

Both stretches increased most following the application of the 0.5 gram load (Figure 3-22 and Figure 3-23). This is typical of soft tissues and represents significant movement into the "toe" region of the exponential stress-strain curve describing the general tensile behavior of all soft tissues. These values demonstrate a preconditioning response, which is most likely recoverable some time after testing. The circumferential stretches were higher than the longitudinal stretches. Corresponding to the response curves previously described, the room-temperature values were generally lower than the tests in heated and bubbled media.

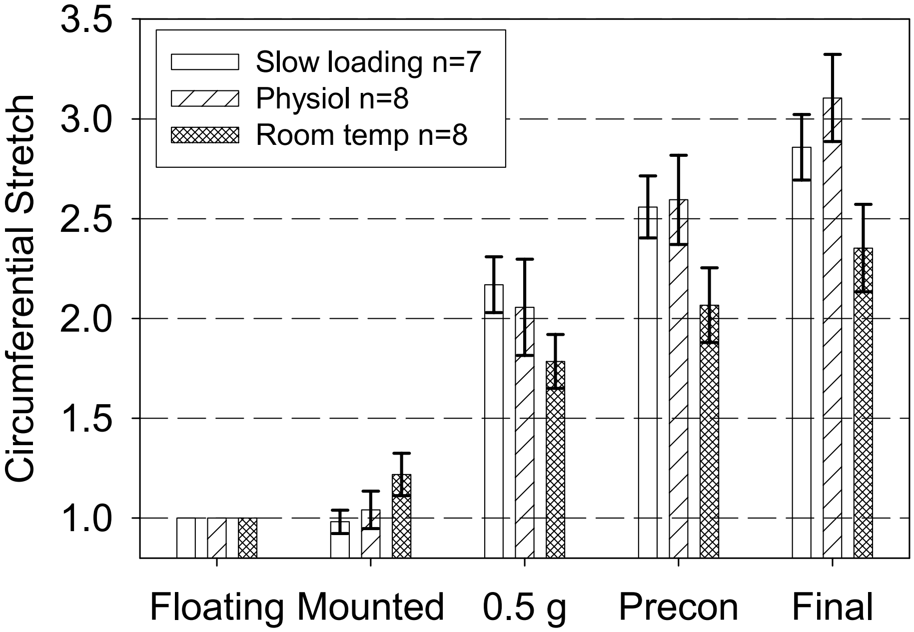

Figure 3-22 Stretch in the circumferential direction in each of the marker files shown. Floating is shown for reference. Mean and SEM are shown.

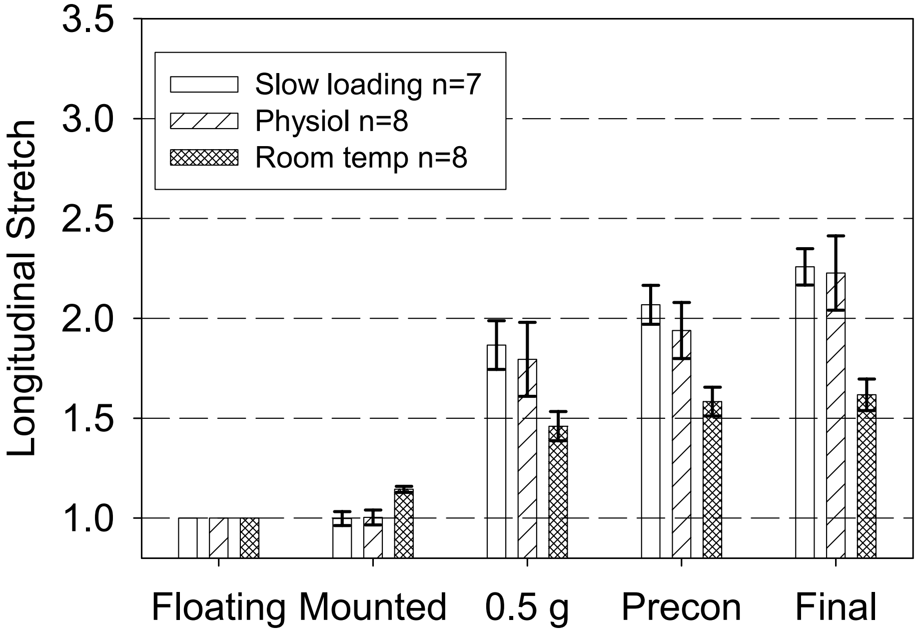

Figure 3-23 Stretch in the longitudinal direction in each of the marker files (Table 3-4) shown. Floating is shown for reference. Mean and SEM are shown.

Neither shear (Figure 3-24) nor rotation (Figure 3-25) significantly changed once mounted, indicating the stability of the tissue in the device. This stability is a good indication of the success of the device design, which allows the specimen to rotate and shear freely to mitigate rotations and shears caused by imprecise placement of suture attachments and markers, and minor discrepancies between suture lengths. Note that although the shears and rotations are relatively high, these are stabilized, preconditioned, changes, not the rotations or shears that occur during testing. As reported in section 3.3.1, the shears and rotations from the beginning to the end of the test were small and were therefore ignored.

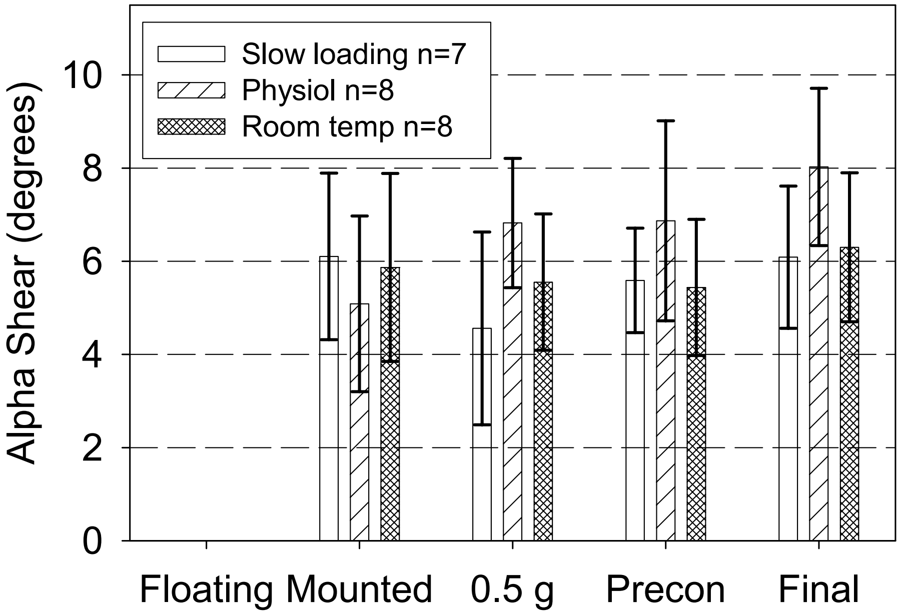

Figure 3-24 Shear in degrees in each of the marker files shown. Mean and SEM are shown.

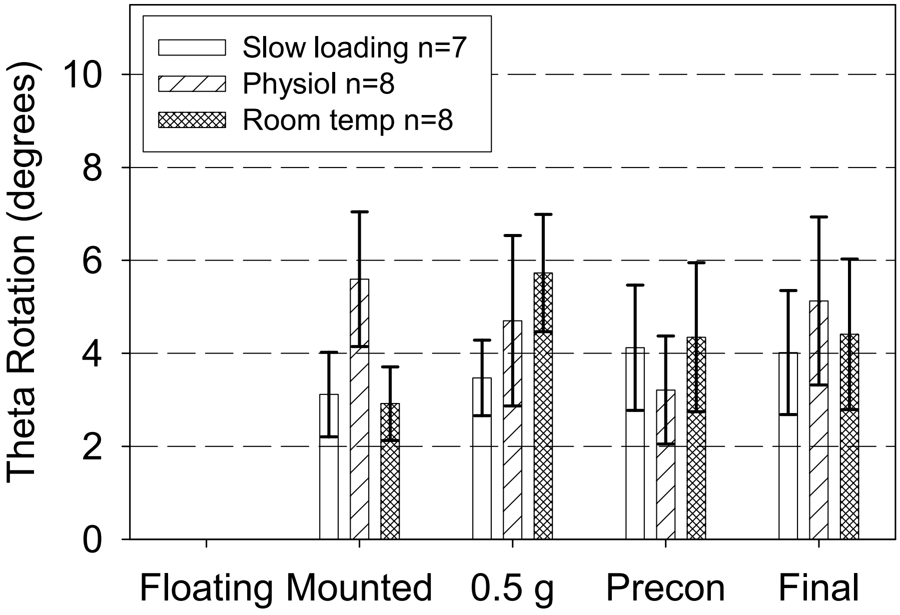

Figure 3-25 Rotation, in degrees, in each of the marker files shown. Mean and SEM are shown.

3.3.5 Whole Organ Filling

The tests described to this point were performed, as described, with sections of bladder wall. Although the stress-control protocol and stress magnitude used during the experimental protocols were carefully selected (section 3.3), proof was needed that this method was physiological. To provide this proof, a simple set of experiments with seven intact whole bladders was performed. These bladders were obtained with both partial urethra and ureters intact.

The bladders were from the same sources as those used previously, of the same species, gender, and age. Before testing they were left overnight in a refrigerated Krebs solution containing EGTA. Instead of opening the bladder and removing a square section, however, the entire intact organ was used during testing. First, the ureters were tied off with suture line. Four small graphite particles were affixed to the exterior of the mid-body of the bladder to form the corners of a square, as with the quasi-static experiments previously described. The marker coordinates were obtained by imaging and the initial distances recorded. A catheter was inserted into the bladder and the urethra was tied off around it. The samples were placed in a bath filled with Krebs solution with EGTA at room temperature and without bubbling. Subsequently, a 1 ml syringe was connected to the catheter and the bladder. The marker positions and stretches from the earlier state were recorded and calculated. Then the bladder was filled in 0.1 ml increments to 0.7 ml during approximately one minute. The volume of 0.7 ml is the maximum that a rat will hold before voiding under normal conditions as used by many investigators and our group.(88) At each increment, the marker positions were taken again and the stretch from the empty state obtained. Calculated spatial resolution for this setup was 0.01 stretch (see section 3.2.4).

The raw stretches are shown in Figure 3-26 and Figure 3-27. In these figures the empty state, before the catheter was inserted, was used as reference demonstrating very little change in stretch at the 0.0 ml mark from attaching the catheter. There was a significant difference in the elastic behavior of the bladder wall between the circumferential and longitudinal anatomic directions as shown in the means of the seven samples (Figure 3-28). The difference between the circumferential and longitudinal directions become significant with $p<0.05$ at only 0.1 ml instillation. At 0.7 ml, the bladder wall stretched 2.10 (0.08 SEM) past the empty state in the circumferential direction and 1.75 (0.06 SEM) from the empty state in the longitudinal. The shear and rotation values (Figure 3-29) at each milliliter instillation were higher than those experienced by the planar specimens (Figure 3-24 and Figure 3-25), perhaps because of the increased complexity of the deformation in a three-dimensional structure compared to that in two-dimensional biaxial samples.

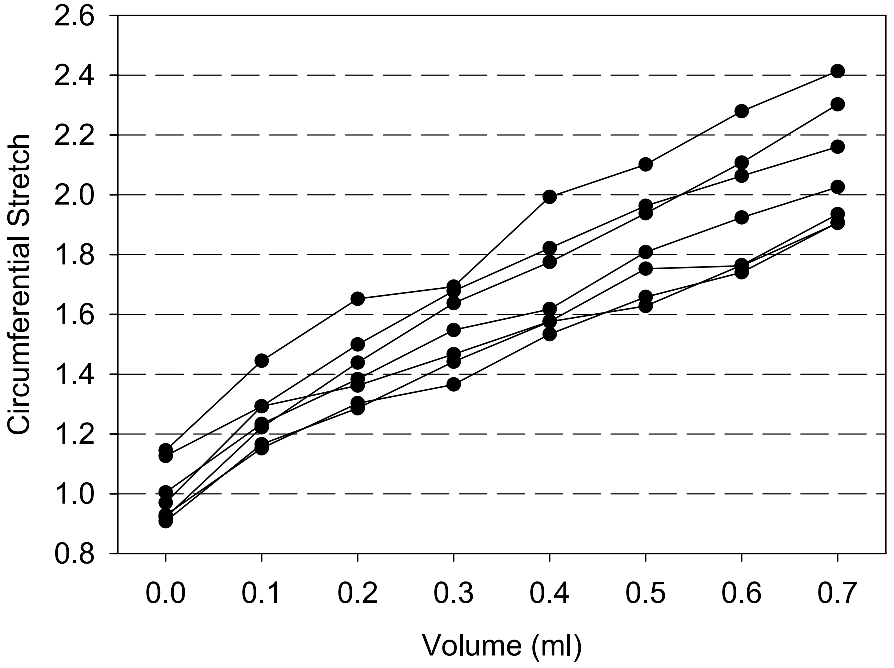

Figure 3-26 Circumferential stretch at each increment of filling for each sample. The stretch was calculated referenced to the stretch before the catheter was inserted.

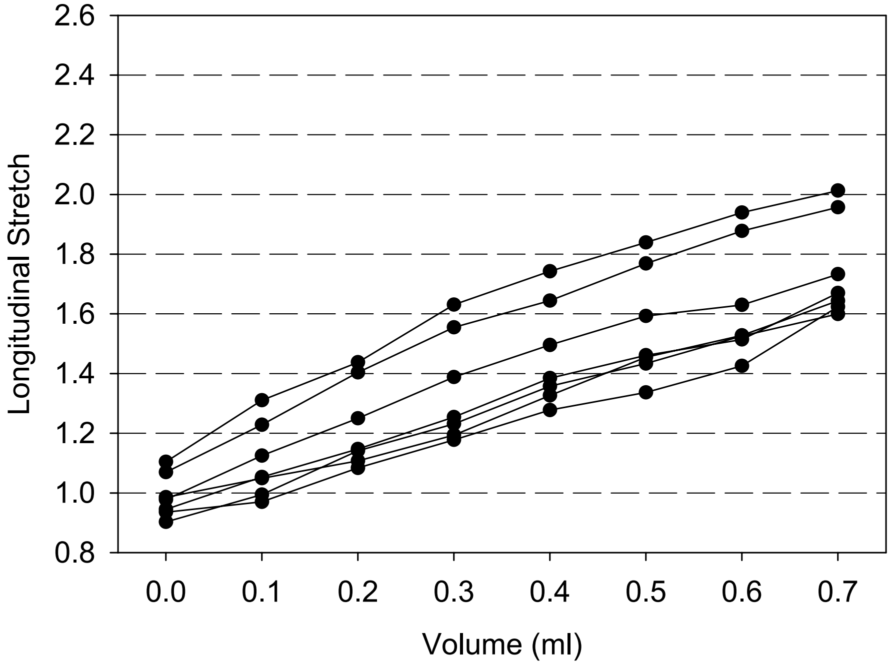

Figure 3-27 Longitudinal stretch at each increment of filling for each sample. The stretch was calculated referenced to the stretch before the catheter was inserted.

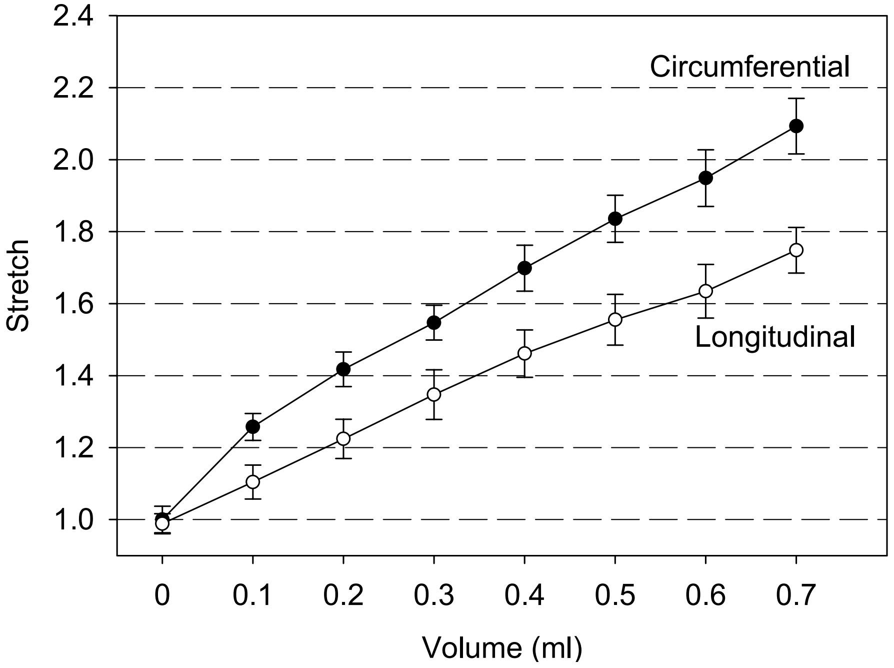

Figure 3-28 Mean circumferential and longitudinal stretches at each increment of filling. Mean and SEM are shown.

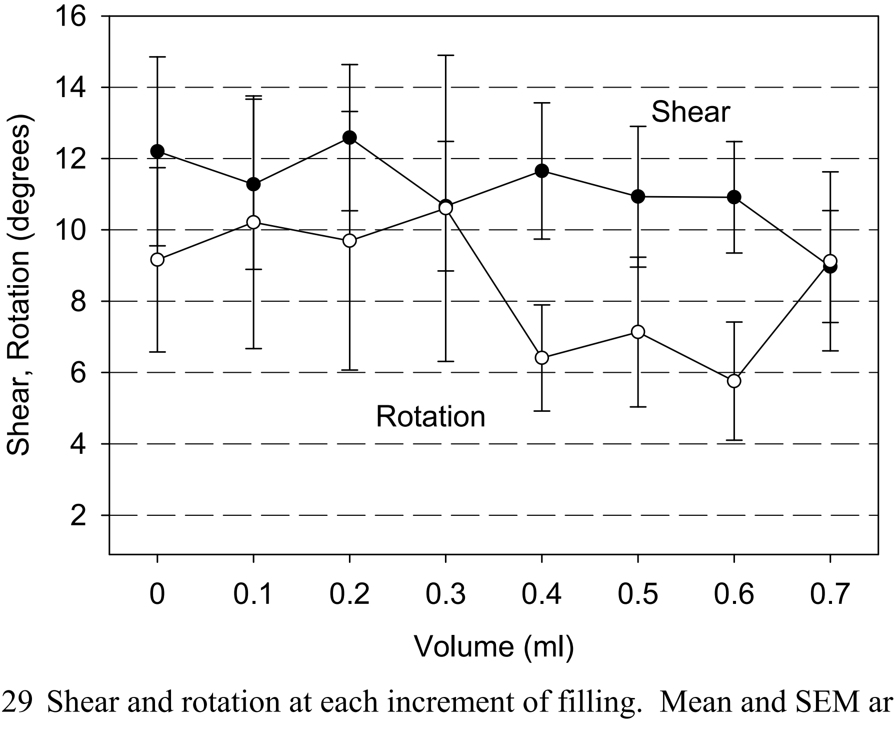

Figure 3-29 Shear and rotation at each increment of filling. Mean and SEM are shown.

The stretches found in this filling study were also compared to the stretches in the planar quasi-static testing protocol in room-temperature media (Figure 3-30). The stretches of the room-temperature equibiaxial data were computed using the floating marker position as the reference marker position to allow a direct comparison to the empty reference state in this filling study (section 3.3). The comparison shows no significant difference in the maximum stretches between the two tests in the two directions. There was a significant difference between the directions in the whole organ filling experiment, but not in the room-temperature experiment, using a paired Student t test. This is most likely caused by a difference in the preconditioning between the two axes (section 3.6). In conclusion, this study shows that the stretches resulting from a 100 kPa maximum stress protocol are the same as the stretches present in the intact organ when filled to the physiological maximum.

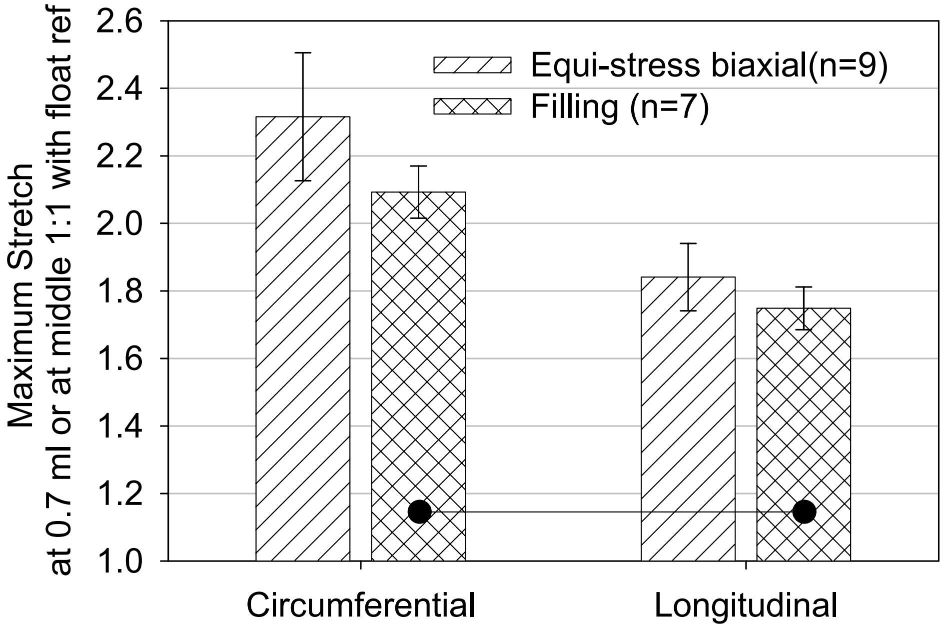

Figure 3-30 Comparison of room-temperature mechanical tests to whole organ filling surface stretches. Mean and SEM are shown. The statistical significance shown is p=0.001 using a paired Student t-test. The difference between the room-temperature directions is almost significant at p=0.078 with a paired Student t-test.

3.3.6 Limitations and Difficulties

All the limitations and resolution issues discussed in section 3.2.4 apply to these experiments.

The limitations of the device require large sample sizes relative to the size of the rat urinary bladder. Preliminary tests have been performed using cat bladder and have found a difference in mechanical properties between the dorsal and ventral sections. Mechanical studies on rabbit bladder have shown regional differences between the upper body, lower body, and base of the bladder, including the passive force generated by deformation and active force induced by electrical stimulation.(6)

Oxygenation of the media was performed only between cycles because the bubbles disrupted the surface of the media and affected the imaging of the sample marker positions. Therefore, in all physiologic experimental setups, bubbling was allowed for 5 minutes between all protocols in each test. Although oxygenation levels of the media were not checked, this limitation most likely did not affect the relatively fast cycles of the quasi-static cycling that continued for only 2-3 minutes; however, it may have affected the slow-loading protocol.

As previously discussed, the acquisition of data in the slow-loading tests was the same as for the other tests, around 12 to 13 points per second. However, to conserve memory, the data were thinned during run time and only every ~50th data point was recorded. This resulted in the possible loss of the highest and lowest data points at the top and bottom of the cycles. When the duration of the cycles (Figure 3-15) is divided by the number of data points recorded for that cycle, the average time between data points is 5.38 seconds (0.38 SEM). Therefore, the real maximum and minimum points could occur as much as half that, or 2.69 seconds, from the measured maximum and minimum points. The cycles were very slow so it is unlikely that the real peak and valley points occurred very far from the measured points, although more discrepancy is to be expected in some measures. For example, while the majority of the stretch occurs in the toe region and less occurs when the stress reaches its maximum, the opposite is true of stress. Indeed, the maximum stress that every sample reached was around 96 kPa, 4kPa from the target stress of 100 kPa (Figure 3-16).

The filling experiments caused a fully three-dimensional stretch to occur in the bladder wall. Although bladder wall is very thin, and becomes thinner under stretch, the exact stretch values on the inner and outer surfaces are different. By necessity, the stretch was measured on the outside of the bladder wall for these experiments. For the planar experiments, however, the graphite markers were placed on the lumen side of the bladder surface because the urothelium was lighter in color and provided a better contrast with the black graphite particles. The difference due to this disparity between the two testing methods is most likely small.

Although the volume used during the filling experiments was physiological, the pressure within the bladders was not measured in this setup. A further validation of this method would be to introduce a pressure sensor into the bladder during filling to verify that the tension within the wall is close to the tension experienced *in vivo*.

3.4 Viscoelastic Methods

In the experiments of the prior section it was assumed that the bladder wall mechanical behavior was completely independent of time. These experiments are technically simpler than time-dependent tests and therefore make ideal preliminary testing methods. The assumption of time independence allows more thorough testing and more complex loading conditions than are available when time is a factor. However, it well known through a variety of experiments available in the literature that the bladder wall mechanical behavior is time dependent, and that viscoelasticity is an important part of bladder function.(79)

Viscoelastic analysis can be complicated, involving many different experiments including stress relaxation, a decrease in stress under constant stretch; creep, an increase in stretch under constant stress; recovery; and preconditioning phenomena, all of which may occur simultaneously under certain conditions. As viscoelastic analysis is by definition time-intensive, only some basic preliminary analyses were performed in this study. The goal was to answer a simple question: are the viscoelastic properties strain-level dependent? To provide an answer, stress relaxation experiments were performed. The data from these studies were used in a quasi-linear viscoelastic model presented in section 5.3.

Stress relaxation is a time-dependent phenomenon that occurs when a material is held stretched. The stress within the material increases with deformation and then decreases through time. The decrease in stress is called stress relaxation or simply relaxation. Depending on the material and deformation, stress relaxation may continue virtually indefinitely or it may reach an asymptote. In materials that are highly viscoelastic, stress relaxation may occur at all times, even under relatively rapid loading. For this reason, the true relaxation behavior of a material can be obtained only if the material is loaded instantaneously, a technically impossible task. Realistically, loading rates of 0.1 to 0.25 seconds are common in stress relaxation experiments.

3.4.1 Protocol

Because it was difficult technically to obtain marker positions while the samples were undergoing very rapid (<0.1 sec) deformations, we performed stress relaxation to a maximum stress instead of maximum stretch. Based on the quasi-static data already presented, the stretches in the tissue were expected to be roughly equal in the two orthogonal directions while under equibiaxial stress. The maximum equibiaxial stress levels chosen were based upon the calculations of section 3.3 using the Law of Laplace: 25, 50, and 100 kPa. There were five samples in each group, each of which underwent only one of the three protocols, for a total of 15 samples. The duration of the experiment made it impractical to perform several protocols of ratios of the two stresses. Only equibiaxial ramp loading was used. Due to the length of testing, only one equibiaxial run was performed on each specimen.

All stress relaxation tests were performed in the modified Krebs-plus-EGTA solution described previously, bubbled with 95%$O_2$5%CO_2, and maintained at a constant 37^o C temperature. All samples were preconditioned prior to ramp loading with 12 equibiaxial cycles of 20-30 seconds duration each, then the preconditioned marker positions were recorded. One more equibiaxial run was completed for the testing program to prepare for the rapid movement of ramp loading. The biaxial device was programmed to complete the ramp loading in 0.05 seconds; however, all samples reached the maximum stress approximately 0.06 seconds from the initiation of loading.

The data were recorded as rapidly as possible for the first 300 points, including the ramp loading. The rate of data acquisition was decreased through the test as relaxation resulted in smaller changes of stress. During the first 10 seconds, load and time data were acquired more rapidly than was possible for the frame grabber, so stretch values were not recorded. After 10 seconds, data acquisition was decreased to ~3 Hz and the sample was imaged and stretch calculated and recorded for the remainder of the test. (See Figure 3-31 for a graphical representation of the complete data acquisition rate over the length of the experiment.) All specimens were allowed to relax for 10,000 seconds and had identical data acquisition rates throughout the length of relaxation.

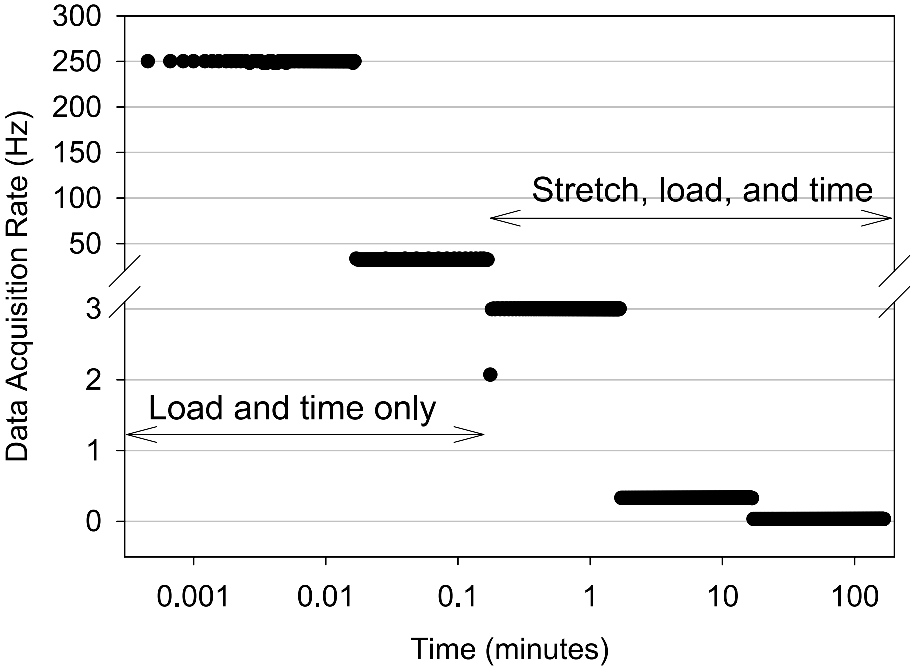

Figure 3-31 Rate of data acquisition for stress relaxation experiments of all samples. Load and time only were recorded until 10 seconds (including loading), at acquisition rates of ~250 Hz for 1 second, then at ~30 Hz until 10 seconds had elapsed. After 10 seconds, strain, load, and time were recorded at 3 Hz until 100 seconds, then at 0.3 Hz until 1,000 seconds, then at 0.03 Hz until 10,000 seconds.

3.4.2 Ramp Loading Compared to Quasi-static Loading

The maximum stretch values of the last loading cycle and at the first stretch value available at 10 seconds after the ramp loading during stress relaxation were examined to determine whether the rapid ramp loading alone caused different stretches from those observed during slow-loading. This comparison is particularly important because stress relaxation requires deformation to a constant stretch; yet here, due to device limitations, a constant stress level was used. We had previously found that the tissue response was equibiaxial (section 3.3.1) so we hypothesized that this restriction was inconsequential and the two techniques are equivalent for this tissue. We found that there was indeed no significant difference with a

Student-t unpaired test at $p<0.05$ between any stretch values (Figure 3-32). In most cases, the ramp loading caused the same equibiaxial stretches as the quasi-static loading.

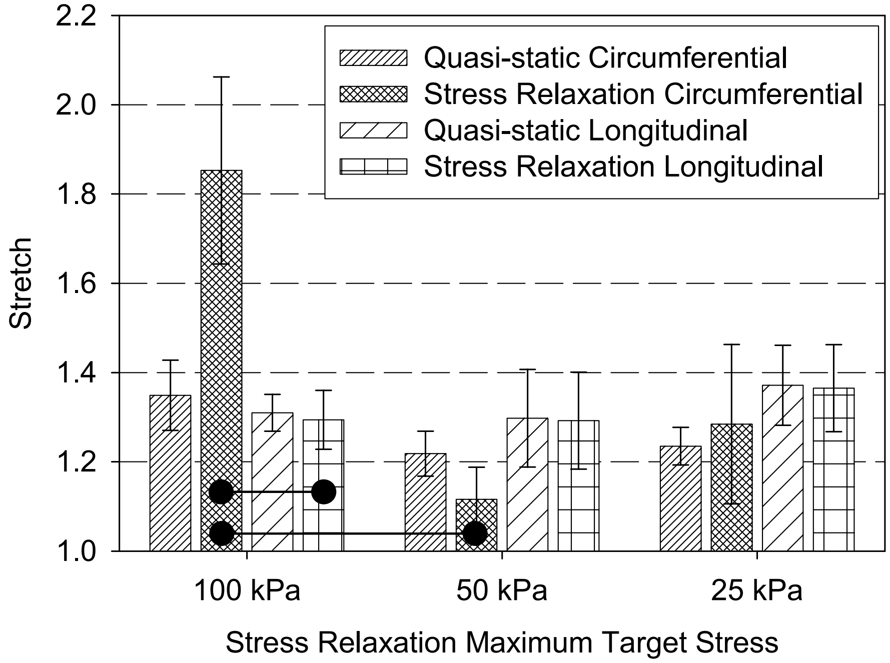

Figure 3-32 Stretches in the last cycle of equibiaxial quasi-static preconditioning and the initial stretch caused by the ramp loading of stress relaxation.

The strain rates within all quasi-static groups were not statistically different (Figure 3-33). In the stress relaxation group, however, the difference between circumferential and longitudinal directions in the 100 kPa group was different with $p=0.0463$. However, this was due to one outlier sample with a value of ~41, more than two times the SEM higher than the mean. When the sample is removed from the group, the difference becomes insignificant at $p=0.08$. This one sample may be only a case of biologic variability and may not represent a true difference; more testing would be necessary to prove this hypothesis. Although a decrease in stress level would be expected to result in lower stretches, the lack of a statistical difference between stretches in the three different stress levels demonstrates the stability of this tissue through changes in testing protocol.

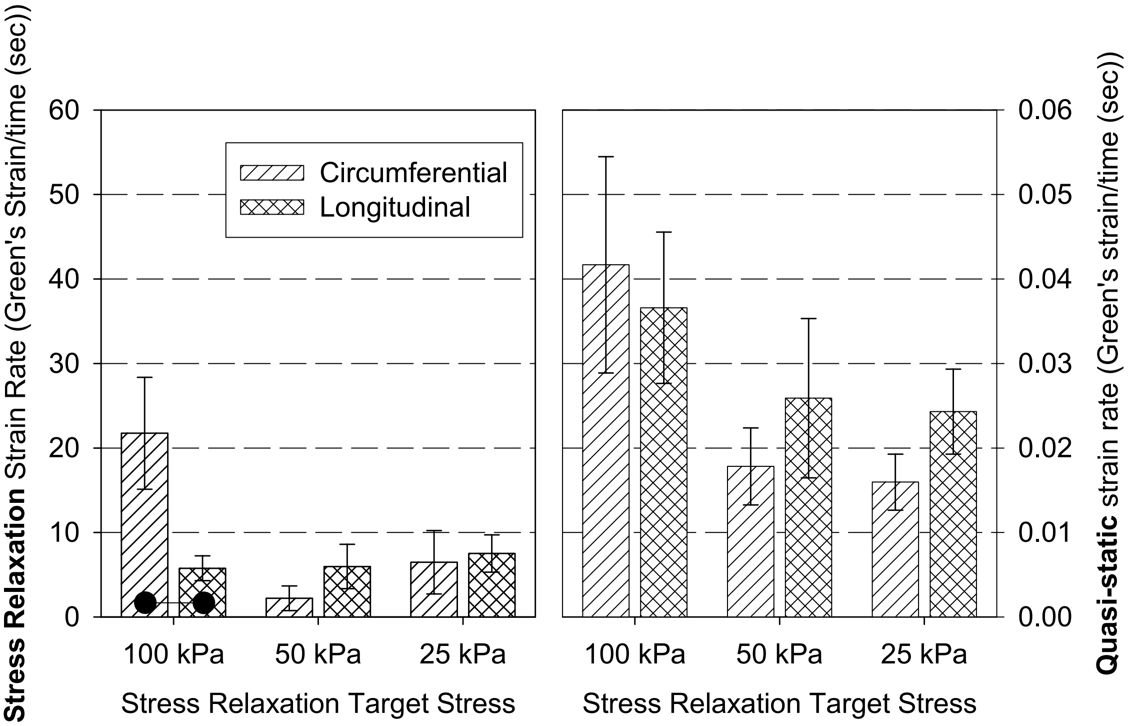

Figure 3-33 Strain rates in last loading cycle of preconditioning and loading strain rate of stress relaxation protocols. The only statistical difference is between circumferential and longitudinal in the 100 kPa group during stress relaxation (p= 0.0463), however, there is one specimen in the circumferential group with a strain rate of ~41, more than 2 standard deviations higher than the mean, which probably causes this statistical difference. When this specimen is removed, leaving n=4, there is no significant difference (p>0.08).

The preconditioning quasi-static loading protocol was controlled well, with maximum stresses within 1% of the target stresses. However, in the stress relaxation ramp-loading protocol every sample reached a maximum stress that was generally two to three times greater than the target stress (Figure 3-34, Figure 3-35). The mean maximum measured stresses were about 150% higher at each stress level in each direction (Figure 3-36). This overshoot was due primarily to oscillations caused by the biaxial device response to the rapid loading (section 3.4.3). This issue has been reported in other studies.(89,90) Since this overshoot was similar in all stress levels and in both directions, it did not prohibit comparisons between groups.

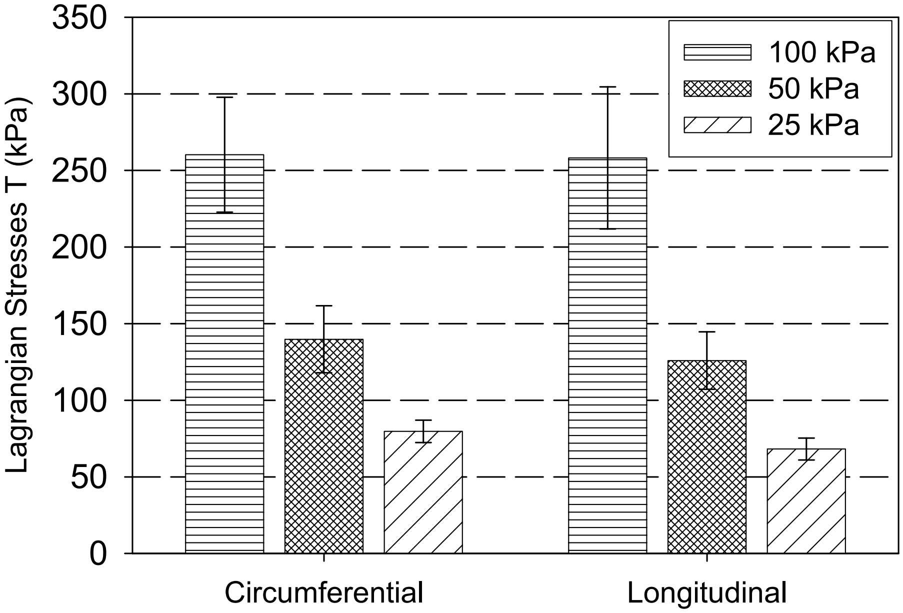

Figure 3-34 Measured maximum stresses in the stress relaxation protocols. Mean and SEM shown. No statistical differences between circumferential and longitudinal within the same stress level were found.

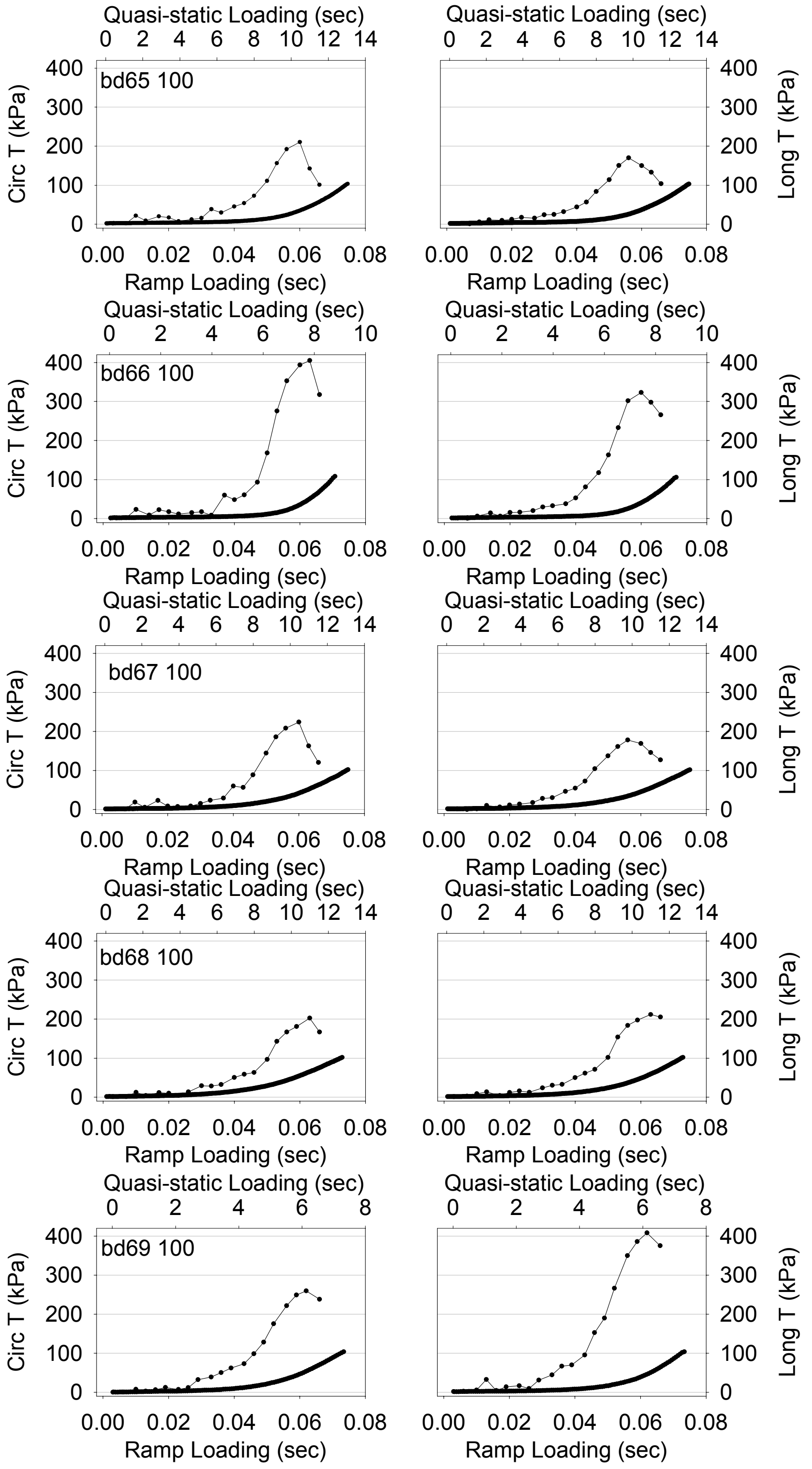

Figure 3-35 Raw data for quasi-static loading (thick line) and ramp loading (symbols and line) for 100 kPa group. The other two groups (50 kPa and 25 kPa,) were similar.

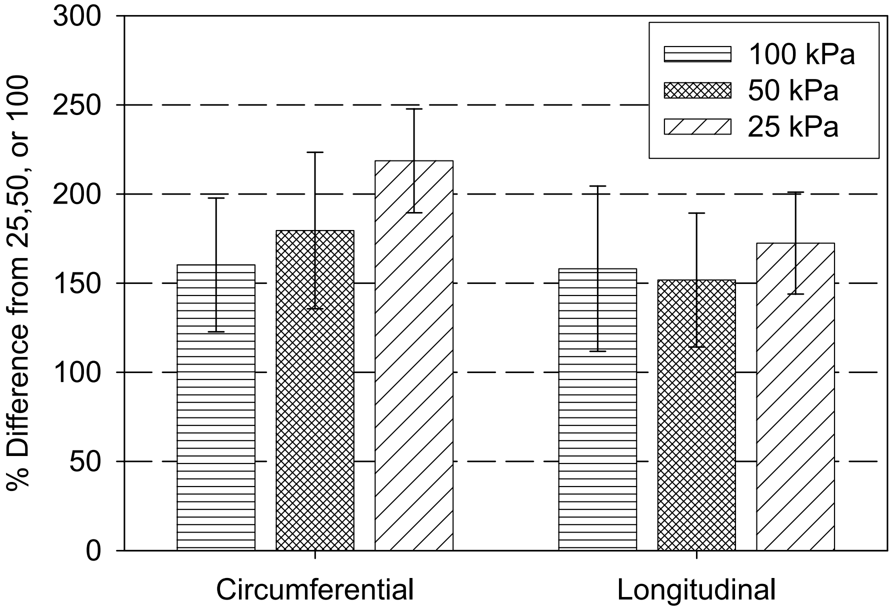

Figure 3-36 Percent difference of measured maximum stress from the target stress level as shown in Figure 3-34. Mean and SEM shown. No statistical differences found.

3.4.3 Stretch During Relaxation

Ideally, stress relaxation involves holding the tissue at a certain stretch and allowing the stress to relax. As mentioned previously, due to the inability to calculate the stretch fast enough to adjust the motor displacements in the early parts of the test, the samples were ramped to a certain stress and then the displacement motors were turned off. Although stretches were not calculated during the first 10 seconds, the stretches were recorded from then through the end of the experiment. This was to verify that the stretches did not change radically. We did see a small increase in the stretches during this period as shown in Figure 3-37.

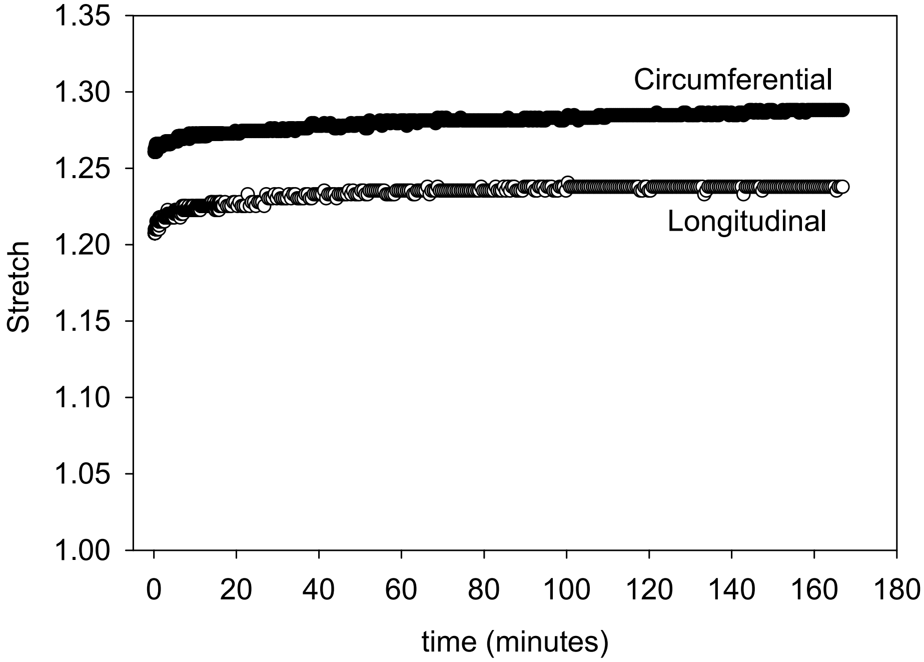

Figure 3-37 Typical stretch profile during a stress relaxation test from 10 seconds to the end of the test. This particular sample was one of the 100 kPa group.

3.4.4 Oscillations

Another complicating factor in the analysis of the stress relaxation data was the occurrence of oscillations during the first 0.2 seconds after the maximum load. These oscillations occurred in both the circumferential and longitudinal directions and were in phase with each other (Figure 3-38, Figure 3-39). They were of similar magnitude (relative to stress level) and frequency throughout all samples. All oscillations damped out within 0.3 seconds.

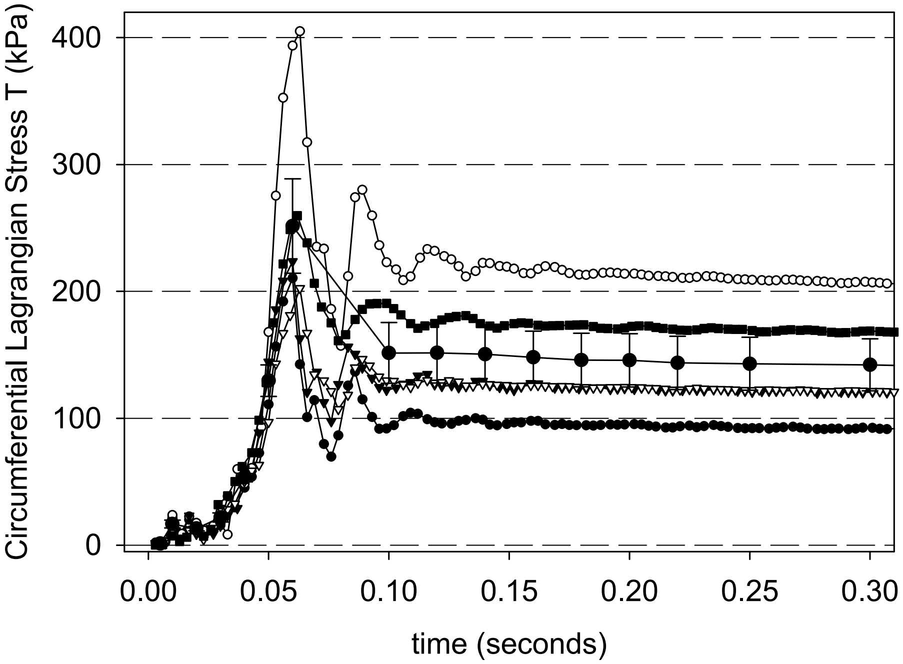

Figure 3-38 Oscillations evident in first 0.2 seconds of circumferential stress after ramp loading. All five samples in the 100 kPa group shown as symbols with lines. Mean and SEM for these samples also shown.

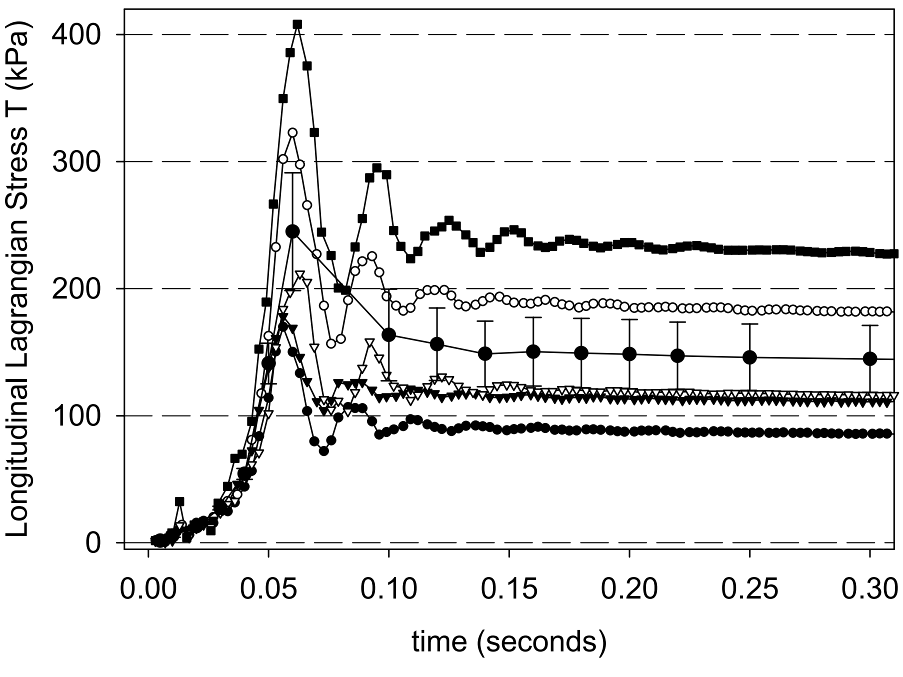

Figure 3-39 Oscillations evident in first 0.2 seconds of longitudinal stress after ramp loading. All five samples in the 100 kPa group shown as symbols with lines. Mean and SEM for these samples also shown.

As the final goal in this viscoelastic analysis was to perform modeling (section 5.3) and it was conceivable that the oscillations were not a result of the specimen response, the source of the oscillations needed to be determined. There were four possible primary sources:

1. A natural rapid viscoelastic response of the tissue. This was unlikely. The bladder would not be expected to undergo such a response *in vivo*.
2. A result of standing waves (vibration) in the sample due to rapid movement of the bath media when the carriages rapidly moved through the media during ramping.
3. A viscoelastic property of the suture material used to attach the specimen to the device.
4. A response of the biaxial device system parts that are in series with the specimen, the motor carriages.

Possibilities two, three, and four were checked by two additional validation experiments. In the first, the sample was replaced with a section of a stiff plastic. This setup was tested with and without the bath media. The stiff plastic removed the possibility of significant force waves in the sample, and the comparison of wet to dry was used to evaluate whether the media alone had any effect. Dimensions of the plastic weigh boat section were measured identically to the bladder wall measurements. The 100 kPa stress relaxation protocol was followed. Distilled water was used instead of Krebs solution and the solution was not oxygenated. The test was conducted at room temperature because temperature would have a different effect on the plastic than the bladder wall tissue, and temperature was not a suspect for the cause of oscillations.

The resultant stress was roughly equivalent in both directions; only one direction is shown here (Figure 3-40). The oscillations were present in both environments, demonstrating that the media alone did not cause the oscillations. On the contrary, it appeared that the water aided in damping the oscillations more rapidly in the submerged test. The difference in stress shown represents different magnitudes of overshoot between the two runs. For this reason, stress relaxation data is typically analyzed normalized to the maximum stress (section 3.4.5).

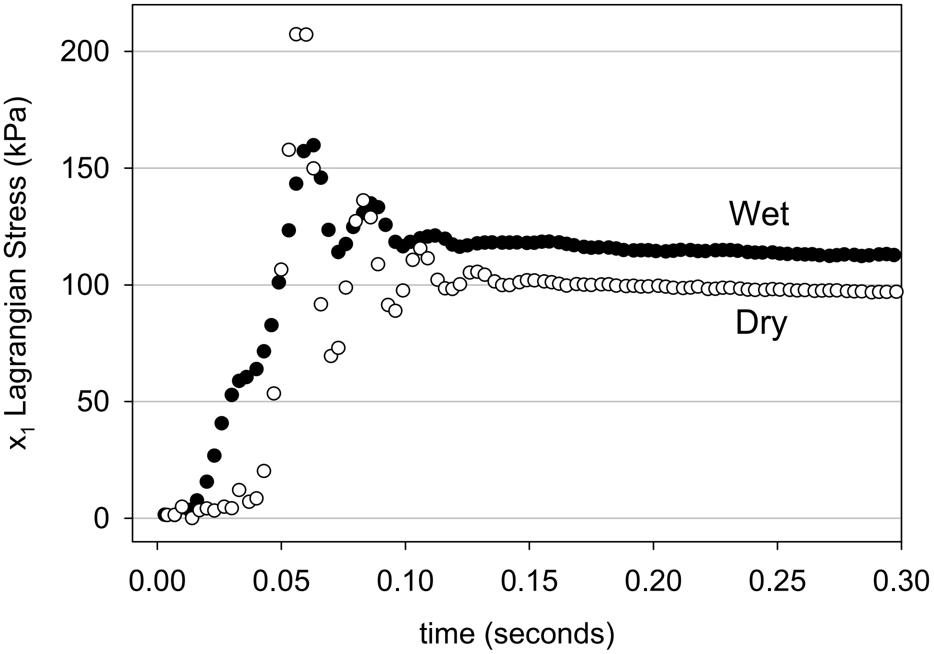

Figure 3-40 Oscillations in wet and dry bath using a stiff plastic weigh boat as a sample. Only one axis shown.

The second experiment replaced the regular suture lines and sample with stiff stainless steel wires. This experiment was done in a dry bath. Because the steel wires had a very small diameter (0.018 mm), the load required to achieve a 100 kPa stress was calculated at less than 1 gram. The load resolution of the device is 0.0610 grams when no noise is present (section 3.2.4), resulting in only 16 steps to 1 gram and hence a very noisy signal. Therefore, a 20-gram load was used for these experiments.

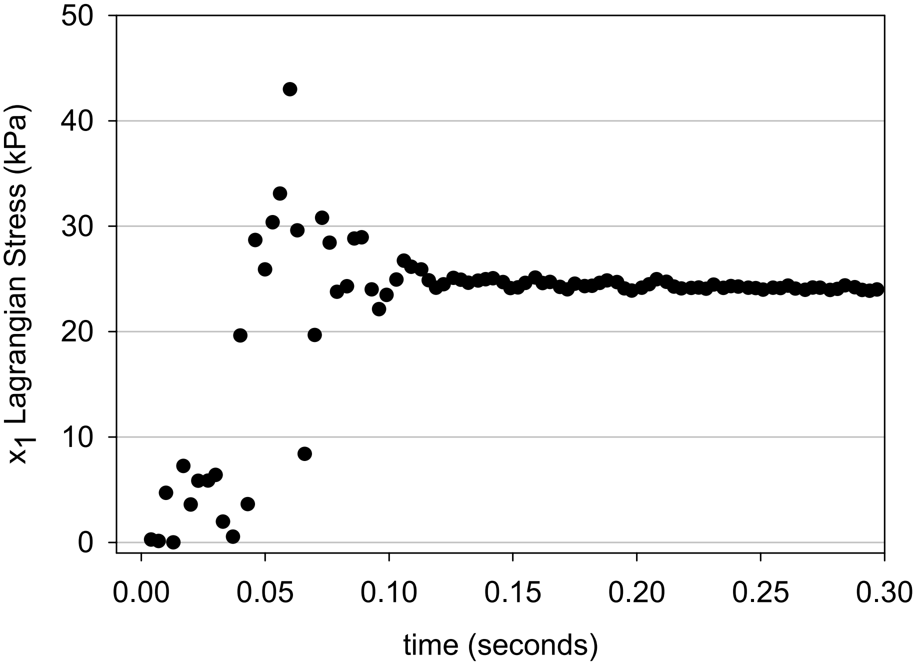

Figure 3-41 Oscillations of stainless steel wire in dry bath. Only one axis shown.

This test (Figure 3-41) also yielded oscillations of the same magnitude as the wet bath test (Figure 3-40). Thus we concluded that these oscillations were not a part of the sample response intrinsic to bladder wall and they must be removed from the response before extensive analysis could begin. This result was not surprising as the device was designed for quasi-static experiments, not stress relaxation experiments. Some of the components in series with the specimen in the motor carriages are polymer and are most likely viscoelastic to some extent. This source of error has also been noted in several viscoelastic experimental setups in the literature.(89,91)

The power frequency components were analyzed with a Fast Fourier Transform and it was verified that there was a ~40 Hz noise in all bladder wall samples and in the plastic and stainless steel experiments (Figure 3-42), probably the device response to loading in 0.05 seconds. This ~40 Hz noise could be removed with digital filters applied to the data (not shown), but the associated attenuation of other components of the response was not acceptable;

hence, an extrapolation procedure was adopted from similar methods found in the viscoelastic literature.(89,90)

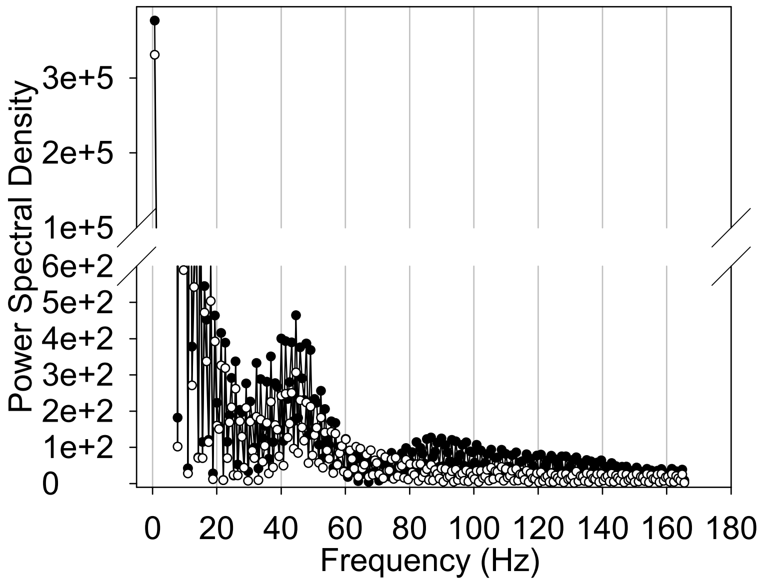

Figure 3-42 Power spectrum in the first 0.23 seconds of a sample subjected to a stress relaxation experiment. All samples showed a peak in power at ~40 Hz.

In the extrapolation procedure, the data recorded during the oscillatory period was replaced by values generated from a linear regression fit to a small section of data. For these samples, almost all of the oscillations were damped by 0.15 seconds. The stress values between time 0.15 seconds and 0.35 seconds were fit to a straight line. The fitted slope and intercept with the actual time values were then used to generate stress values back to the first time point when the real stress was greater than the extrapolated stress (i.e. the intersection of real and extrapolated). In all cases, this first time point was 0.05, the original programmed ramp loading time. Finally, the first time point was set to zero time and all times were adjusted accordingly (Figure 3-43).

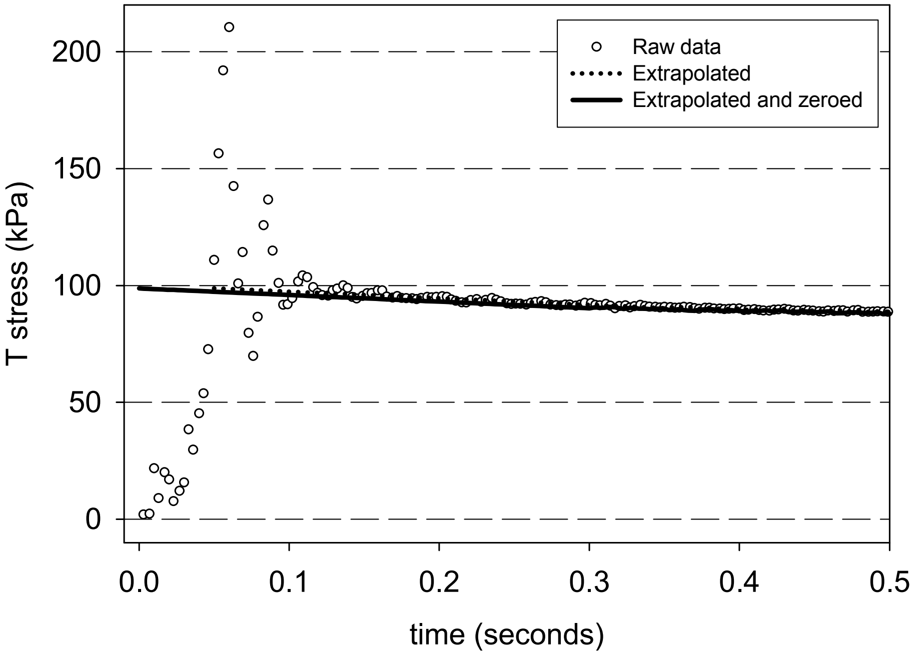

Figure 3-43 Extrapolation procedure. Data are shown as circles. The extrapolation process generated the dotted line from a fit through the data (see text). Then the time points for the extrapolated line were zeroed to begin at time=0 (solid line).

The extrapolation resulted in a significant decrease in maximum stress in all specimens (Figure 3-44). Comparison of the decrease to the original measured maximum stresses reveals that although the percent difference was still not different between the circumferential and longitudinal directions within the three groups, there were significant differences within the directions when comparing 100 kPa and 50 kPa to the 25 kPa group (Figure 3-45). The percent difference from the target stress was not significantly different among groups (Figure 3-46).

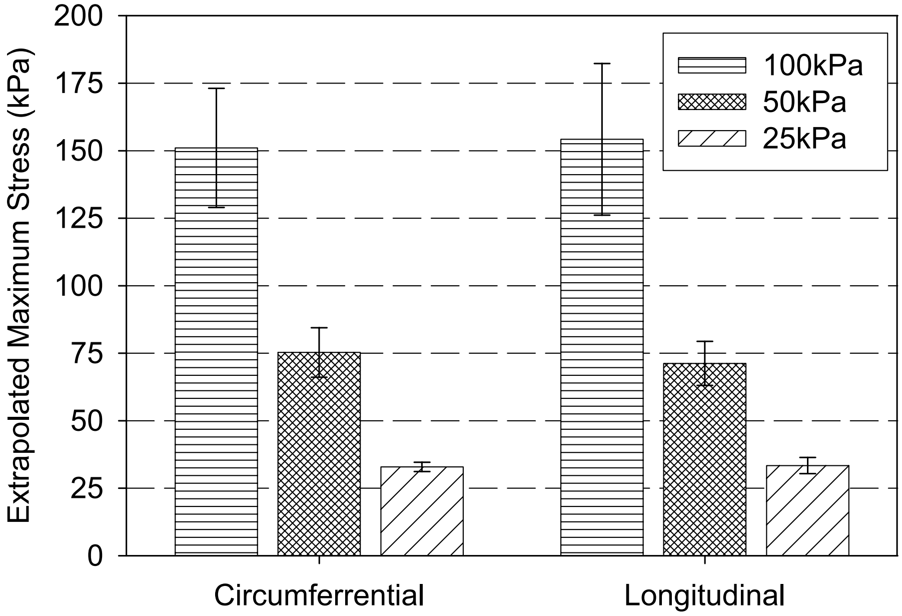

Figure 3-44 Mean and SEM maximum stresses after extrapolation.

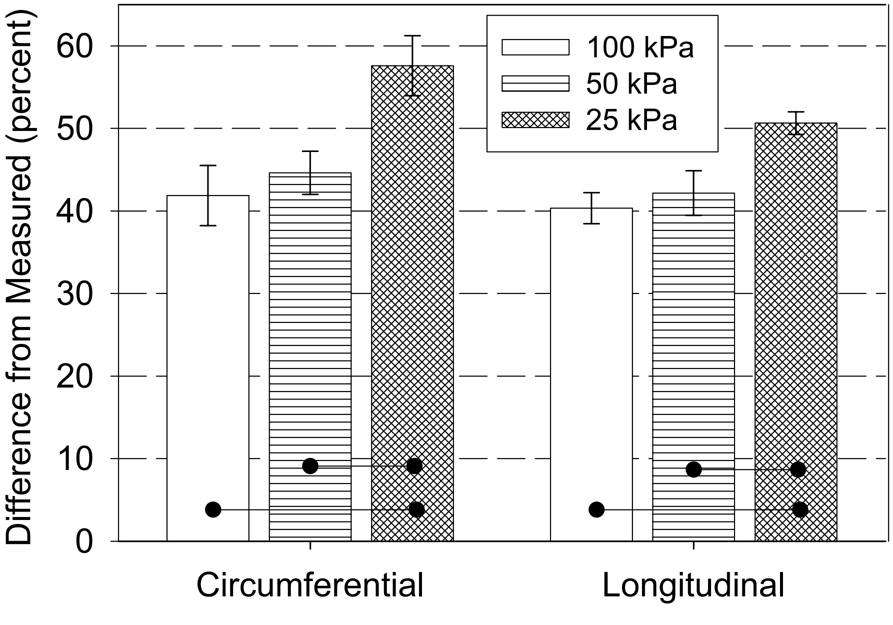

Figure 3-45 Difference between original measured maximum stresses and extrapolated maximum stresses. There were no significant differences between circumferential and longitudinal in any of the three groups, but there were differences in the circumferential group: 100 kPa-25 kPa (p=0.0157) and 50 kPa-25 kPa (p=0.0200) and longitudinal group: 100 kPa-25 kPa (p=0.0022)and 50 kPa-25 kPa (p= 0.0231).

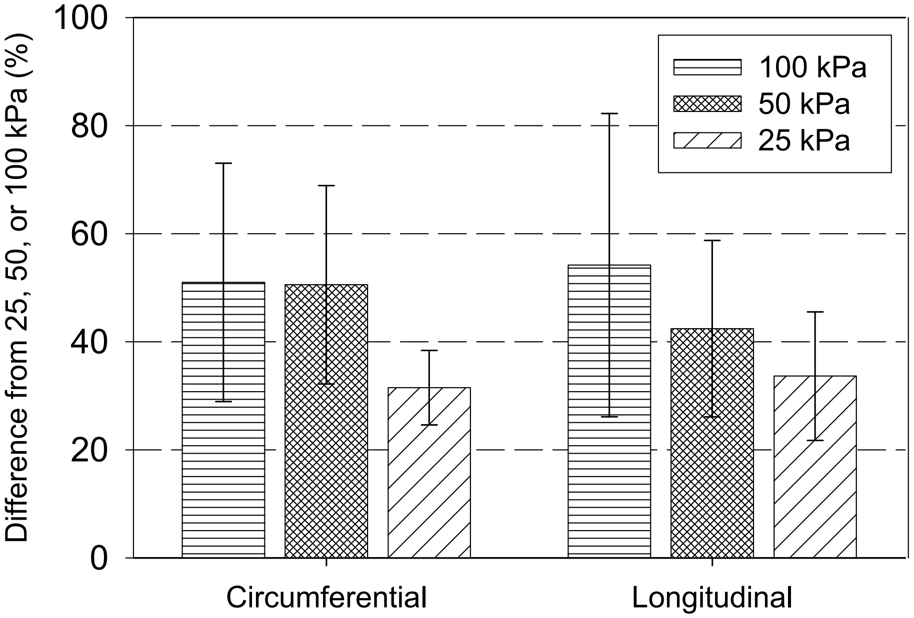

Figure 3-46 Percent difference of measured maximum stress from the target stress level. Mean and SEM shown.

3.4.5 Results

The final extrapolated data still exhibits variations in the maximum stress (Figure 3-44), and differences from the target stress (Figure 3-46). For this reason, the data are traditionally normalized to the maximum stress. The resulting curve is called the reduced relaxation function, G(t), by Fung in his quasi-linear viscoelasticity (QLV) theory.(82) This data was fit to a QLV model (section 5.3). Here, the extrapolated G(t) data are as shown in Figure 3-47 through Figure 3-49. From this raw data, it is evident that the longitudinal data in the 100 kPa and 50 kPa groups have much less inter-specimen variability than do the circumferential values, whereas in the 25 kPa group the opposite is true. In all three groups there are at least two definite slopes in the relaxation function, with an altered slope at 0.1 seconds. In the 100 kPa group, there is an additional change in slope just past 100 seconds. The 50 kPa group data have a more consistent curve over time 0.1 to 10,000 seconds, and the 25 kPa group appears to have a decreasing slope near 10,000 seconds.

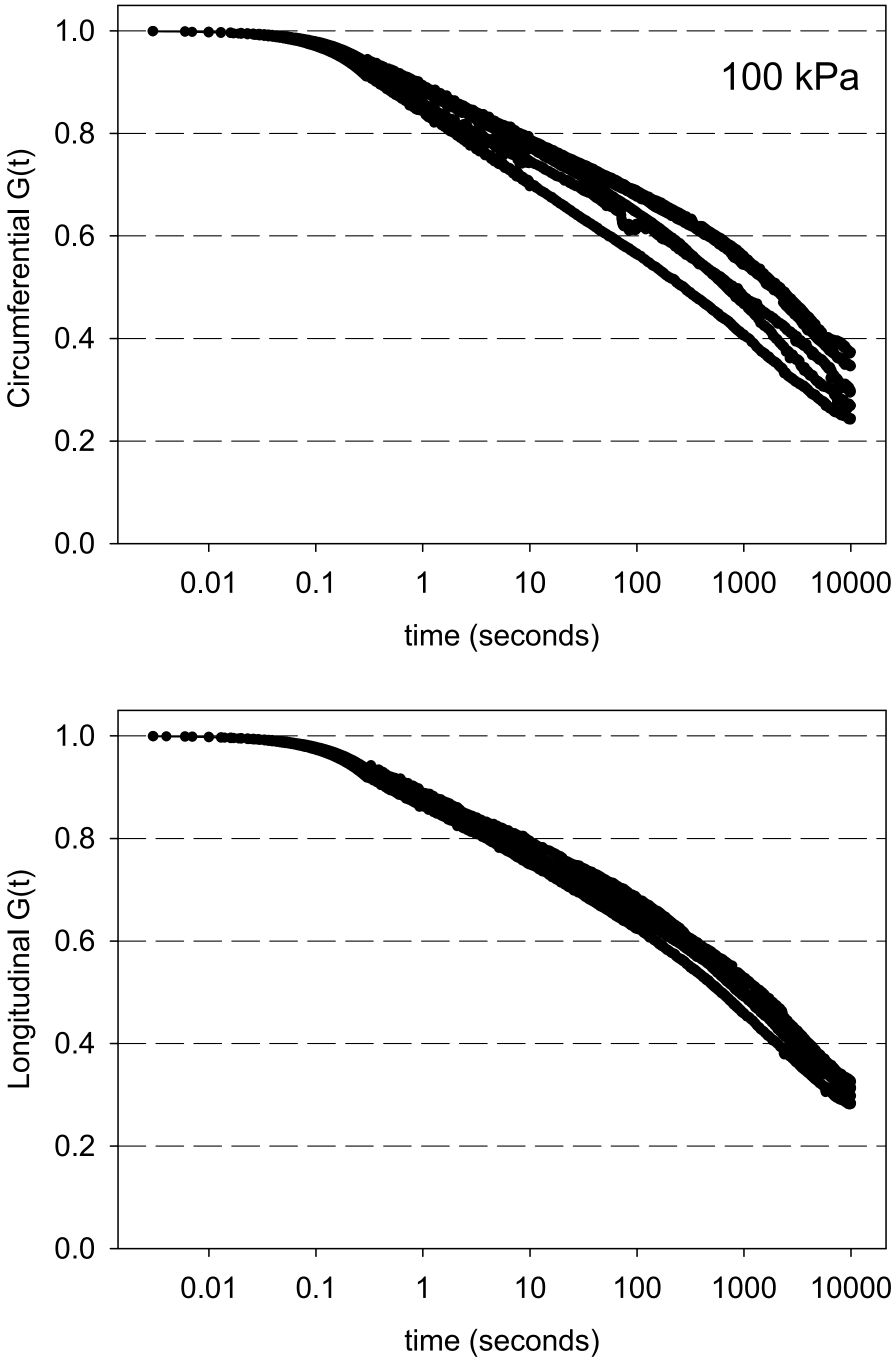

Figure 3-47 Stress relaxation 100 kPa stresses after extrapolation.

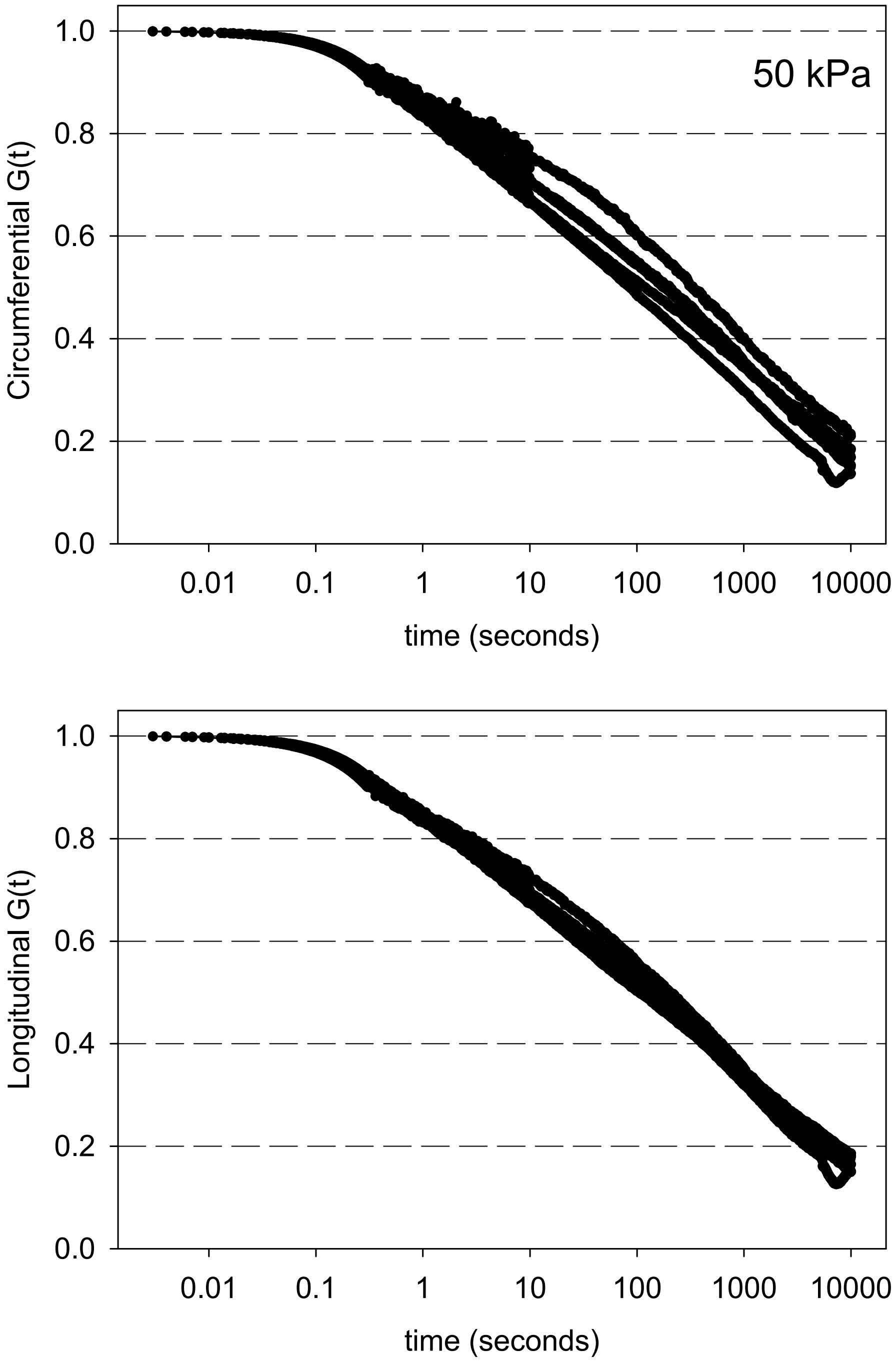

Figure 3-48 Stress relaxation 50 kPa group stresses after extrapolation.

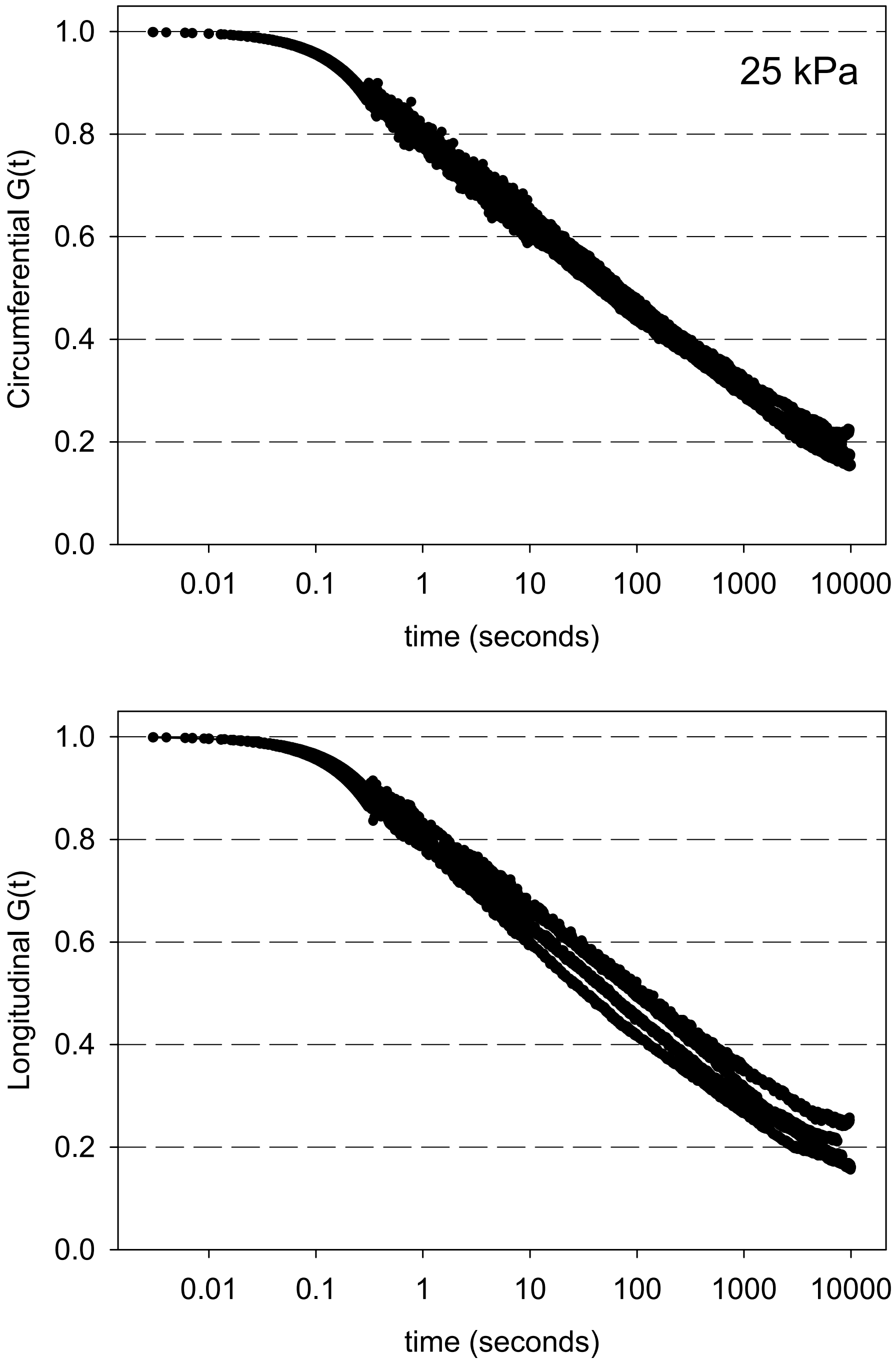

Figure 3-49 Stress relaxation 25 kPa group stresses after extrapolation.

Mean curves for these data are shown in Figure 3-50. These plots show that the 50 kPa and 25 kPa groups undergo more relaxation than does the 100 kPa group, but they take different paths to the minimum. The same phenomenon is demonstrated by the different slopes seen in the raw extrapolated data. In fact, the mean and SEM curves of the 25 and 50 kPa groups shown are statistically different beginning at time point 0.0122 seconds. The difference in final G(t) values, which is the fraction of relaxation occurring in the tissue, are shown in Figure 3-51. There are no differences between directions in any of the three groups, but the 25 kPa and 50 kPa are both different from 100 kPa in both directions.

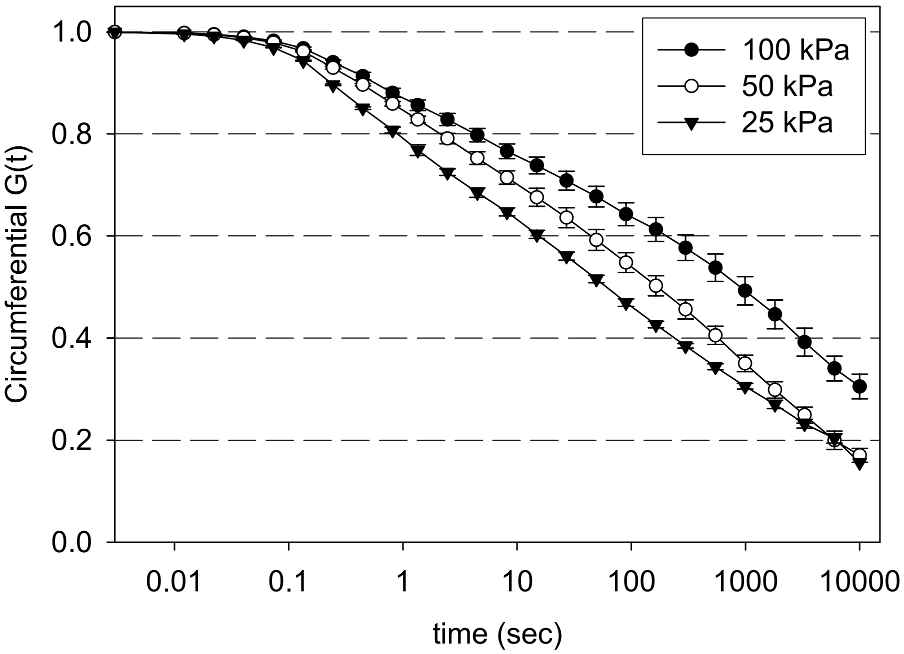

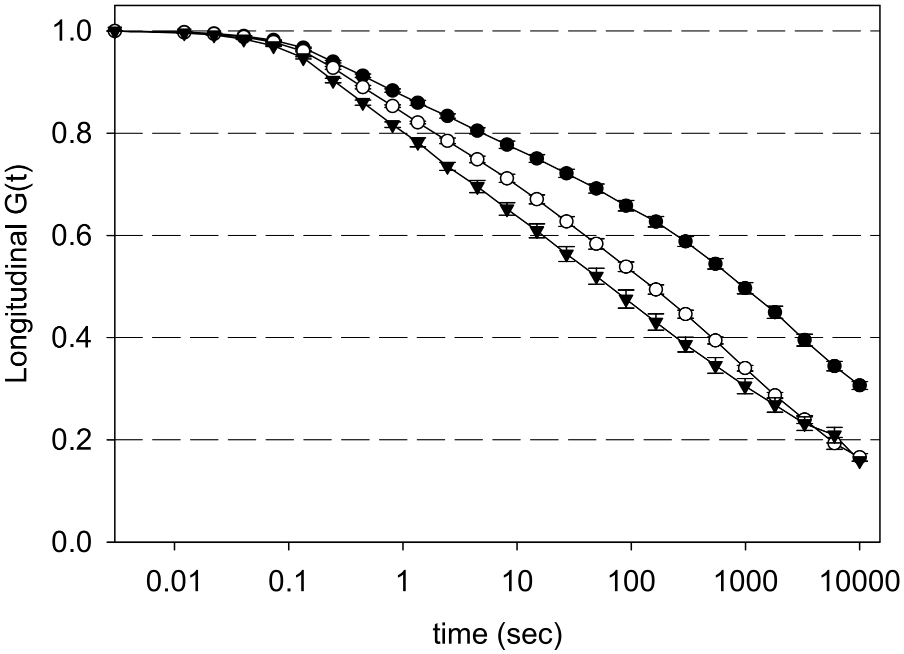

Figure 3-50 Stress relaxation G(t) curves mean and SEM after extrapolation.

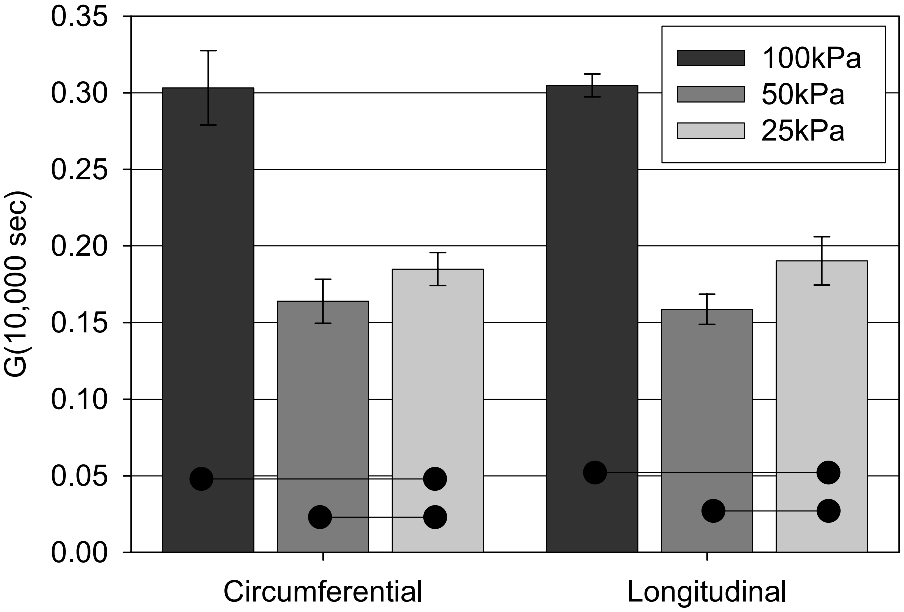

Figure 3-51 Minimum G(t) values, representing the amount of relaxation in each group. There is a significant difference ($p<0.01$) between 100 kPa and both 25 kPa and 50 kPa in both directions. Mean and SEM shown.

3.4.6 Marker Position Changes

Although the floating, mounted, and 0.5-gram marker positions should be identical for the three protocols, the preconditioned and final marker positions could be different if the different stress levels were causing different preconditioned stretches. To explore this possibility, the circumferential and longitudinal stretches are compared in Figure 3-52 and Figure 3-53. In these plots, it is evident that the circumferential stretches are generally higher than the longitudinal stretches, but the preconditioned and final stretches are not different between groups. From these observations, we can conclude that the preconditioned behavior is identical between stress levels. Further, the stress relaxation did not cause a significant increase in stretch in either direction. Comparison of these preconditioning to final stretches in the marker files is shown in section 3.6.1.

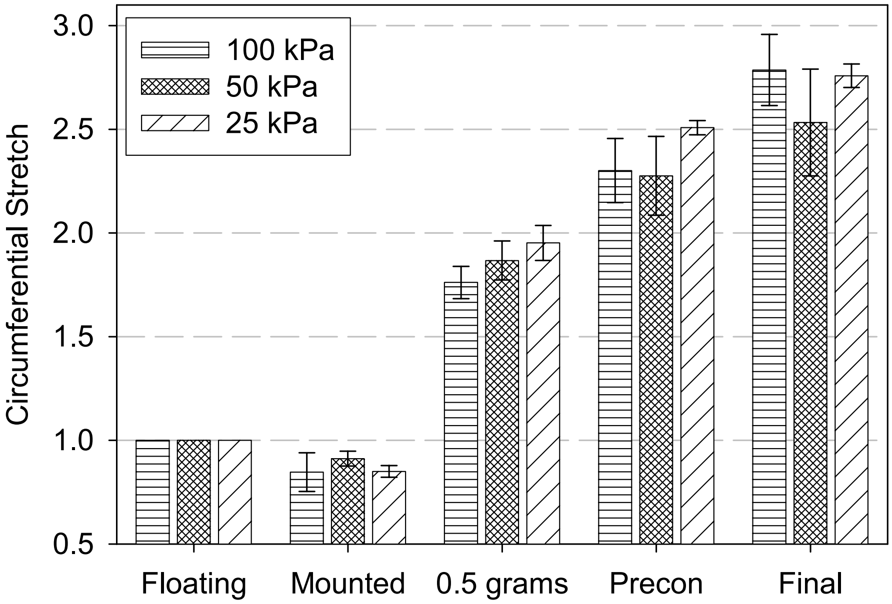

Figure 3-52 Circumferential stretch in the five marker position files (Table 3-4) of the three viscoelastic protocols. Mean and SEM shown.

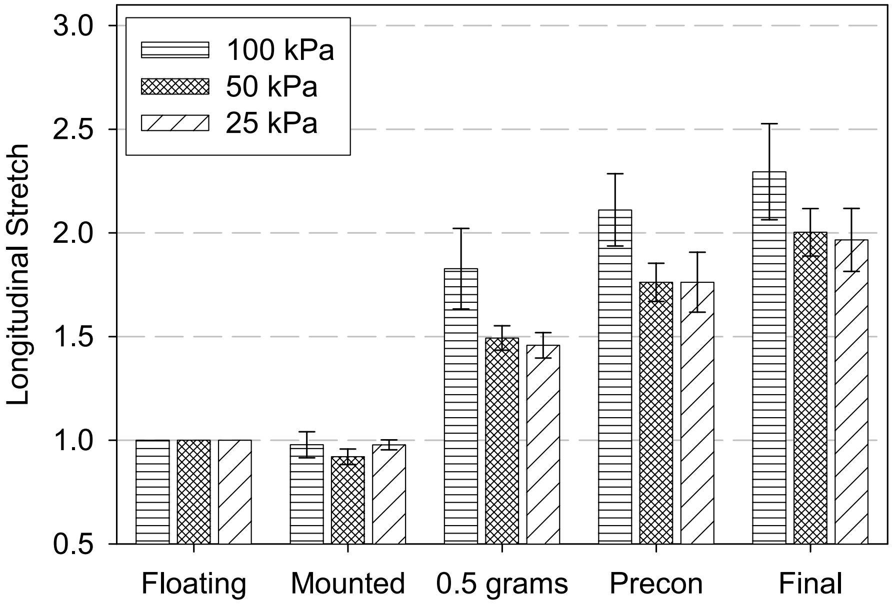

Figure 3-53 Longitudinal stretch in the five marker position files (Table 3-4) of the three viscoelastic protocols. Mean SEM shown.

The shear and rotation in the samples throughout testing are on the order of that observed in the quasi-static tests of section 3.3.4 (Figure 3-24 and Figure 3-25), and none are statistically different between groups in any of the marker files (Figure 3-54 and Figure 3-55). The magnitude of shear and rotation, like the stretch, does not seem to depend on the stress level.

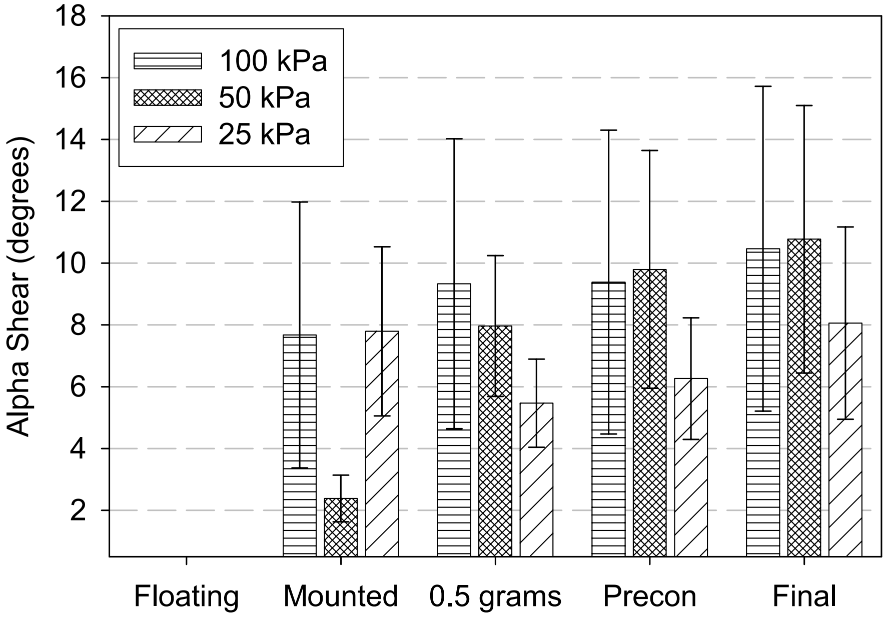

Figure 3-54 Shear in the five marker position files of the three viscoelastic protocols. Mean and SEM shown.

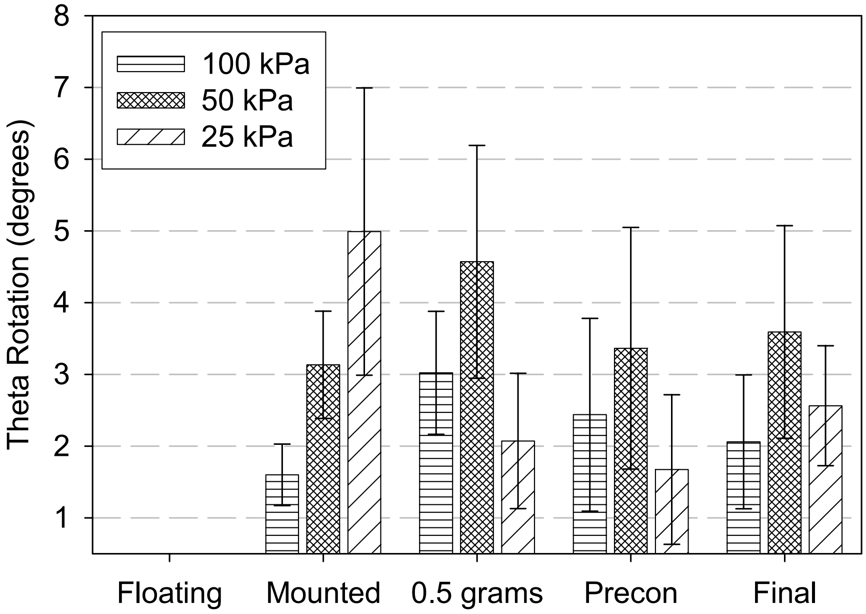

Figure 3-55 Rotation in the five marker position files of the three viscoelastic protocols. Mean and SEM shown.

3.4.7 Limitations and Difficulties

There are several additional limitations to those previously reported, including spatial and load resolution, and the lack of oxygenation during 2.8 hours of testing. One of the largest is the limitation on the data acquisition rate. As previously mentioned, the stretch cannot be acquired any faster than 15 Hz using this hardware, which is not fast enough to observe the stretch changes during the ramp loading and initial relaxation during a stress relaxation test. Additionally, the maximum load acquisition of 250 Hz was limiting at the very early times. The software can be changed to acquire at a faster rate, but the result would include increased noise in the present setup. Shielding that better insulates the signal-carrying cables from the power cables should be developed to eliminate this effect.

The impact of the device viscoelastic response upon the measured sample response is definitely evident in the results. Although the method developed to remove the oscillations and reduce the stress overshoot performs both these functions, it is unknown how much of the real response is also being removed. A rigorous analysis of the viscoelastic response of the device is required for any complete analysis of the viscoelastic properties of any soft tissue.

3.4.8 Summary

Stress relaxation experiments were simple to perform on rat urinary bladder wall and the results of different protocols are significantly different, demonstrating the ability of the device to measure small differences. It is interesting that although a significant difference was found between the three stress levels, no difference was found between the anatomical directions. Although the last data points acquired at 10,000 seconds revealed no difference between the 25 and 50 kPa groups, there are significant differences in the relaxation of the samples in these two groups between the beginning and end of relaxation, an intriguing contrast. Not only does the amount of relaxation change between stress levels, but also a change is seen in the path to the greatest relaxation.

The stress relaxation experiments performed here constitute very little of the available experimental protocols. Ratios of stresses between the two directions may help further elucidate the differences between axes, as no differences were observed in the equibiaxial tests. Only one loading rate was used for all samples, and other loading rates may very well result in different relaxation curves. Additional stress levels may also indicate where the qualitative differences between the directions begin.

In addition to stress relaxation experiments, the issues of preconditioning and recovery are very important in tissues that function like the bladder, tissues that undergo large stretches and must remain structurally stable through large, slow changes as well as large, rapid changes. The study of creep, the measurement of the increase in stretch due to a constant stress, is also directly related to the function of the bladder as an organ that fills and remains distended for long periods. In summary, the study of the viscoelastic behaviors of the normal urinary bladder is a long way from completed, even before the study of disease and abnormalities can begin in earnest.

3.5 Spinal Cord Injury Comparisons(86)

In conjunction with our studies on normal rat bladder, we conducted some parallel studies on rat bladder wall tissue from spinal-cord-injured (SCI) rats for comparison. The primary reason for the characterization of the normal rat bladder wall was to compare it to abnormal conditions. Many aspects of spinal cord injury (SCI) are studied in the Departments of Urology and Pharmacology at this university, making spinal cord injury the obvious choice for such a study. As in the normal studies of normal bladder tissue, whole urinary bladders from female Sprague-Dawley rats 250-300g and four months of age were used.

Characterization of mechanical behavior of normal tissue was the focus of this study, so only one series of tests was performed with SCI samples. The test protocol was identical to the room-temperature quasi-static testing protocol described in section 3.3.

3.5.1 Method of Spinal Cord Injury

The protocol for creating spinal cord defects was identical to that used in prior studies in the urology and pharmacology laboratories.(88,92) In the test group, spinal cord injury was surgically created at the T9-T10 level at 10 days (n=10) and two weeks (n=3) prior to sacrifice. Under anesthesia, at the T9-T10 level the dura and spinal cord were cut with scissors and a sterile sponge was placed between the severed ends of the spinal cord. The bladders were emptied manually two to three times a day and general animal care was given.(93) Although neither the bladders nor rats were weighed before testing, it has been demonstrated that properly cared for SCI animals weigh the same as control and sham SCI animals.(88) The transection was verified visually at the time of creation of the surgical defect and upon removal of the bladder after sacrifice. If the bladder appeared abnormal from expected after SCI, it was discarded from the study. Details of the samples thus discarded from general analysis are discussed in section 3.5.3.

Differences between groups were compared using an ANOVA analysis followed by a post hoc test of either Tukey's test (where normality exists) or Dunn's procedure (when sample sizes were not equal). Since the three 14-day samples were tested early in the study and to only about half of the maximum stress of the other samples, this group is largely excluded from statistical comparisons. Data are presented as mean ± SEM.

3.5.2 Quasi-static Results

The mean equibiaxial behavior of SCI tissues was also approximately isotropic, but was significantly more compliant than the normal tissues (Figure 3-56). The strain at the maximum stress was significantly different from normal in both the circumferential direction ($p<0.001$) and in the longitudinal direction ($p<0.017$). Statistical comparison between normal, SCI 10 days and SCI 14 days with ANOVA followed by Dunn's procedure indicated a continuous increase in areal strain with time after SCI (Figure 3-57).

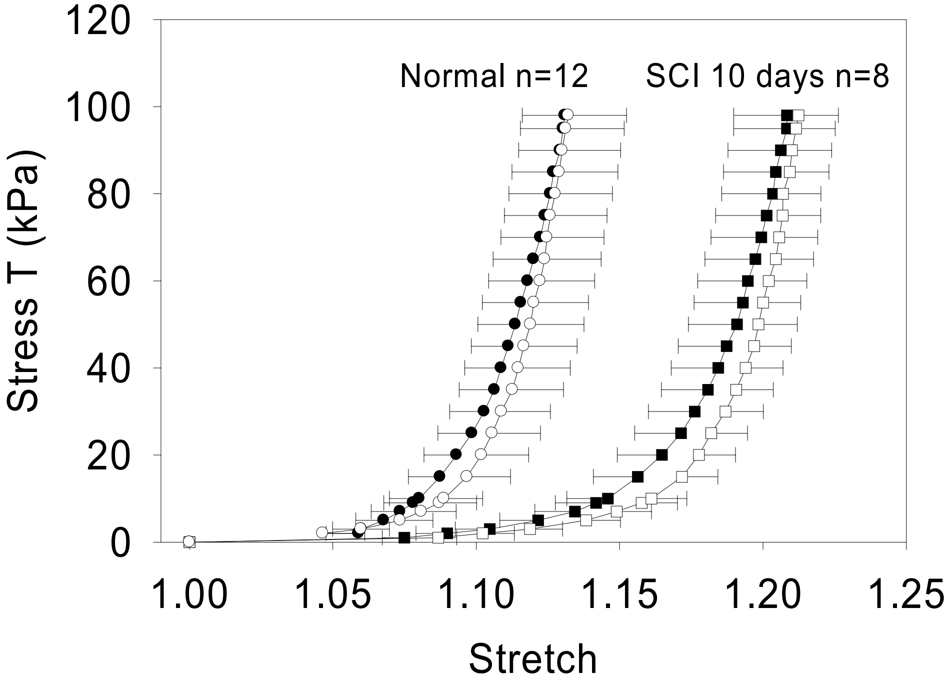

Figure 3-56 Mean and SEM equibiaxial (protocol 4) plots for normal (circles) and SCI 10 day (squares) samples. Filled symbols are circumferential, open are longitudinal direction. Both circumferential and longitudinal curves are statistically different at the maximum stress between the two groups, with $p<0.001$ and $p<0.017$, respectively. Note that the circumferential stresses have negative error bars and longitudinal stresses have positive error bars.

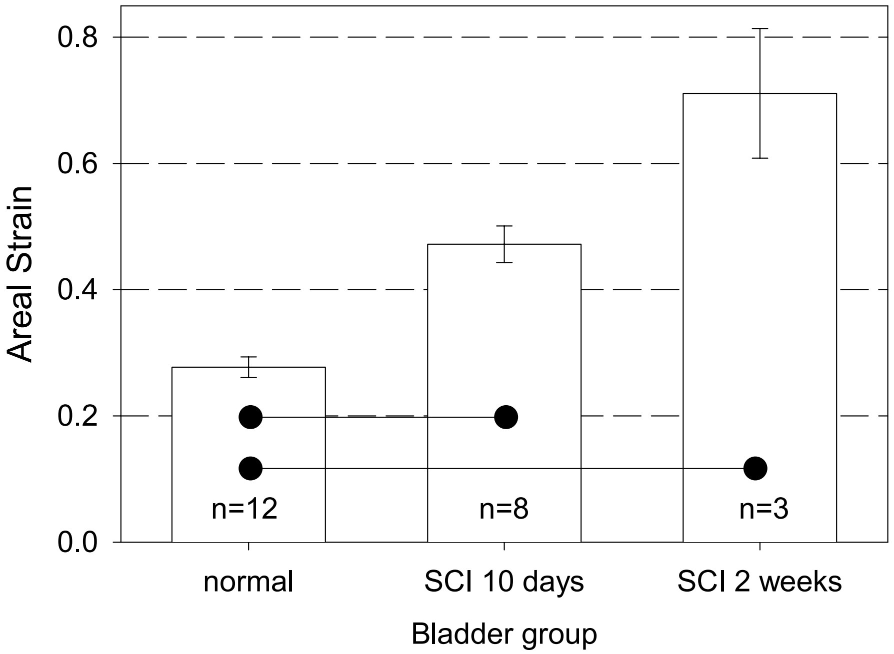

Figure 3-57 Maximum areal strain comparisons between normal, SCI at 10 days, and SCI at 14 days. The steady increase indicates that there are still changes occurring at 14 days. Both are significantly different from normal using Dunn's procedure.

The right column of Figure 3-58 shows the stretch responses of an SCI sample to the extreme and middle runs of Table 3-2. It can be seen that the SCI specimens are not isotropic, since all the curves in the circumferential and longitudinal graphs are not equal, although they are more similar than those of the normal specimens. The shortening seen in test protocol 6 of the longitudinal direction in the normal specimens is not present in the SCI sample presented. Most of the control group specimens exhibited this shortening behavior (8 of 12 specimens), but only one SCI specimen demonstrated it (1 of 8 specimens).

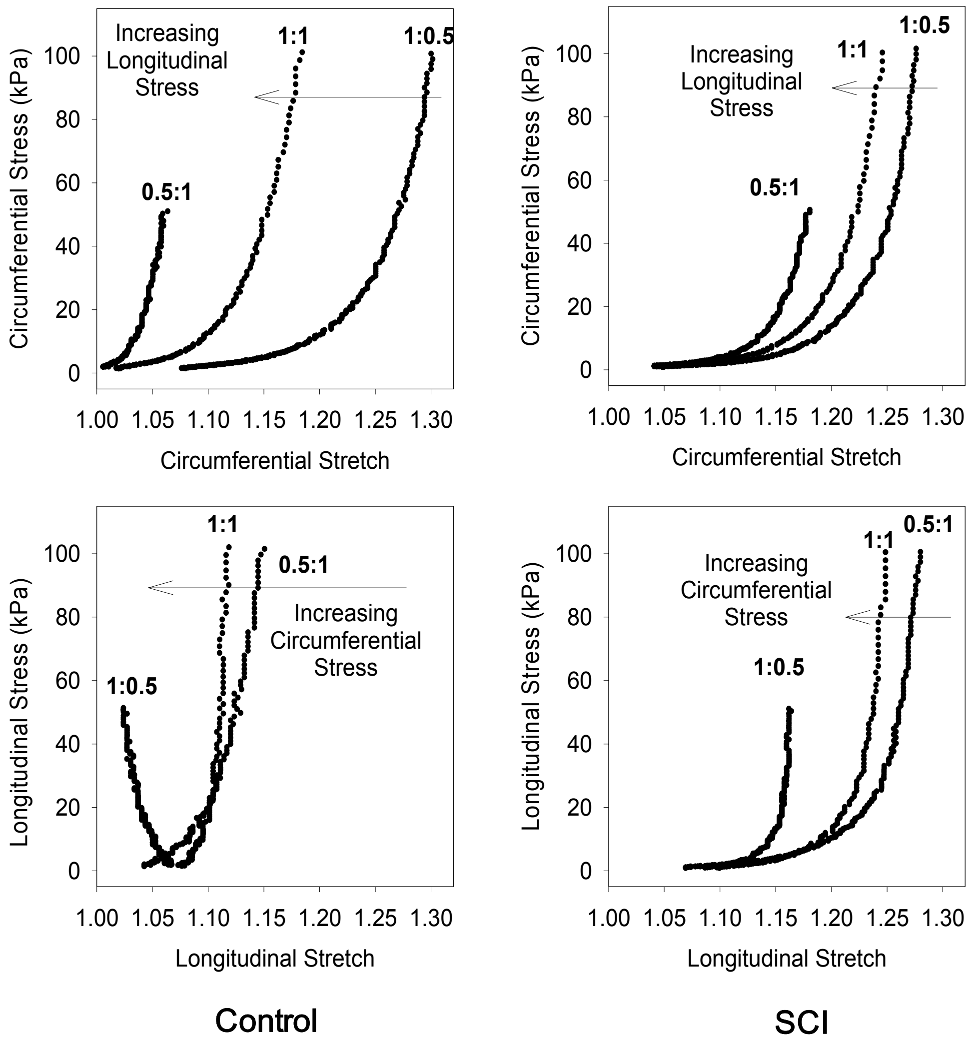

Figure 3-58 Example figures for one normal and one SCI sample showing equibiaxial and extreme protocols. Note that in the normal specimen the longitudinal normal axis shows stretch reversal but the circumferential direction does not, while the SCI samples show no stretch reversal, and the three protocols for which the stress is increasing in the opposite direction are similar to each other.

The hysteresis values of the 1:1 protocols have also been compared between normal and SCI (10 day) groups (Figure 3-59). The hysteresis mean absolute values were slightly higher for the SCI group as compared to the normal group, and the increase was higher in the longitudinal direction, although none of the differences were statistically significant.

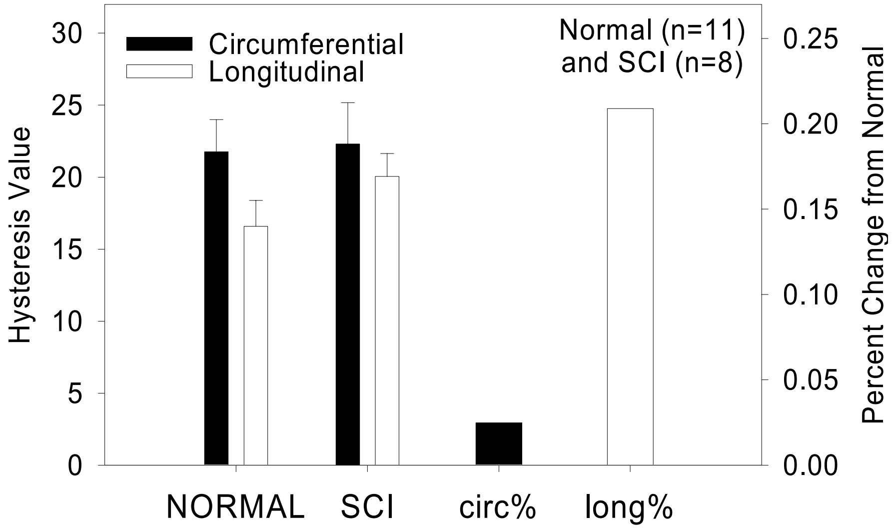

Figure 3-59 Absolute values of hysteresis comparisons between groups in both longitudinal and circumferential axes. Notice the larger shift from normal to SCI 10 day in the longitudinal direction. Mean and SEM presented.

3.5.3 Abnormal SCI Bladders

Two samples in the SCI group were not included in the mean plots of Figure 3-56 and Figure 3-57. One rat had balance difficulties, believed to be due to an inner ear infection, which prevented her from obtaining adequate nutrition and hydration from the overhead bins in her cage. When removed, her bladder was found to be smaller than those of the others in the group. Another bladder was morphologically normal when excised; it was subsequently determined that the spinal cord had not been completely severed. Both demonstrated a lower compliance than the other SCI specimens (Figure 3-60). No histology was done to determine the extent of the spinal cord lesion, nor is any additional information available about the infection.

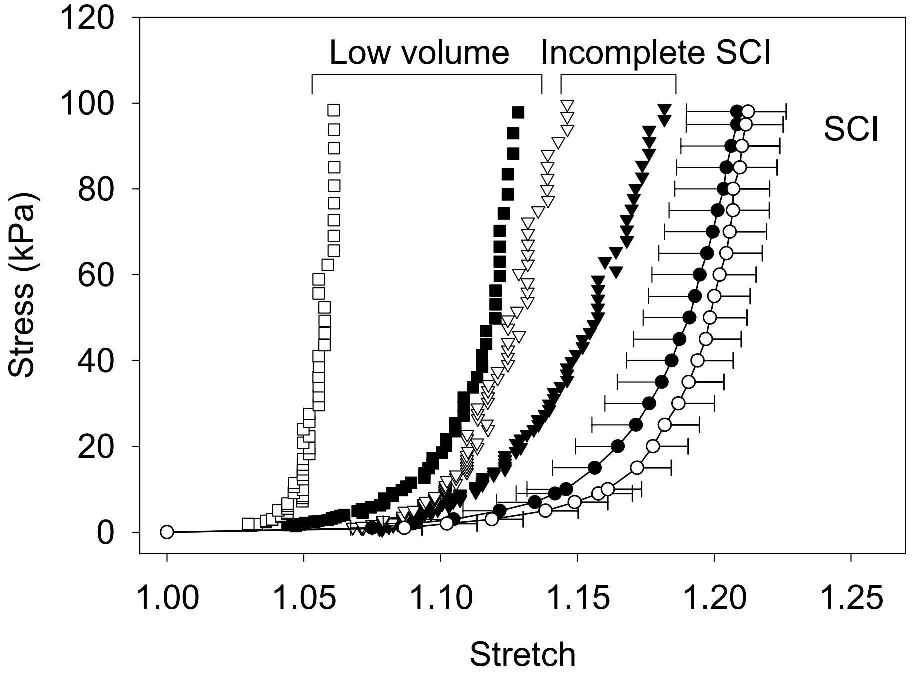

Figure 3-60 Equibiaxial data mean and SEM for accepted SCI data (n=8) and two specific cases. One rat acquired an infection (squares). The other rat bladder shown was morphologically normal when excised due to incomplete spinal sever (triangles). Filled symbols represent the circumferential direction stress and open symbols represent longitudinal stress. Note that the circumferential stresses have negative error bars and longitudinal stress have positive error bars.

3.6 Reference States

The choice of reference state is critical in soft tissue biomechanics because it can significantly change the final results. Unfortunately, it is often unknown what state is "stress-free" and physiologically relevant to the properties under study. The occurrence of residual stretches and stresses is known in many soft tissues.(94,95) In bladder tissue, the intrinsic tone most likely causes some residual stresses and stretches within the wall that may vary with disease. In this study, the tone was eliminated to remove that variable, and for other reasons already discussed.

During preliminary testing, many stretch reference states were recorded (Table 3-4). As these tests were stress controlled, any state could then later be used to observe the effect of the reference state on the stretch data. All the testing analysis in the studies described herein were with reference to the preconditioned reference state unless otherwise stated. It was determined that the preconditioned reference state after the first run produced the most stable stress-strain response after testing. It is also usually considered the most physiological-like state.(96)

3.6.1 Normal

The amount of stretch increase due to preconditioning through the marker files was different between circumferential and longitudinal directions in the experiments presented. This includes the three study groups, the quasi-static tests (Figure 3-22 and Figure 3-23), the intact organ-filling study (Figure 3-26 and Figure 3-27), and the viscoelastic tests (Figure 3-52 and Figure 3-53). With the exception of the filling study, the experiments began with a equibiaxial preconditioning cycling run. In the viscoelastic tests, the maximum stress level was varied in the three groups. The slow-loading and physiologic environment tests differed from the room-temperature quasi-static studies by the addition of $95\%O_2 5\%CO_2$ bubbling and constant 37 ^{o}C temperature media in the former two groups. The measurement of the preconditioned marker positions allowed direct comparison of level of stress and the effects of physiological environment on the preconditioned stretches. Surprisingly, there were few differences, including the difference between room temperature and the 25 kPa stress relaxation test, slow-loading and physiological tests (Figure 3-61 and Figure 3-62). In addition, the only significant difference between preconditioned and final states was in the circumferential direction of the 25 kPa stress relaxation test.

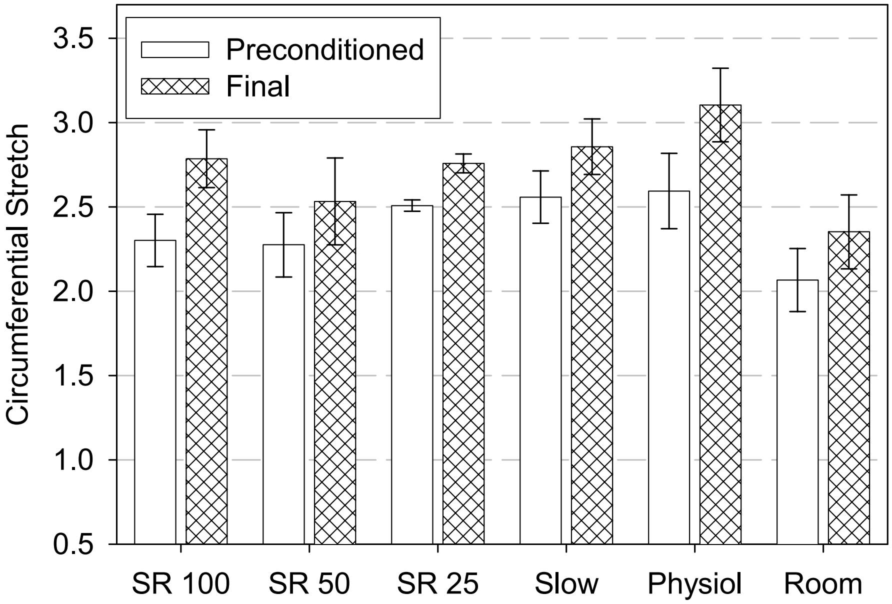

Figure 3-61 Comparison of circumferential stretch referenced to the floating marker position between preconditioned and final marker files for all biaxial mechanical studies. SR stands for stress relaxation, of maximum target stress 100, 50, or 25 kPa. The only statistically different pair is the SR 25 by unpaired Student t-test with $p<0.05$. Mean and SEM shown.

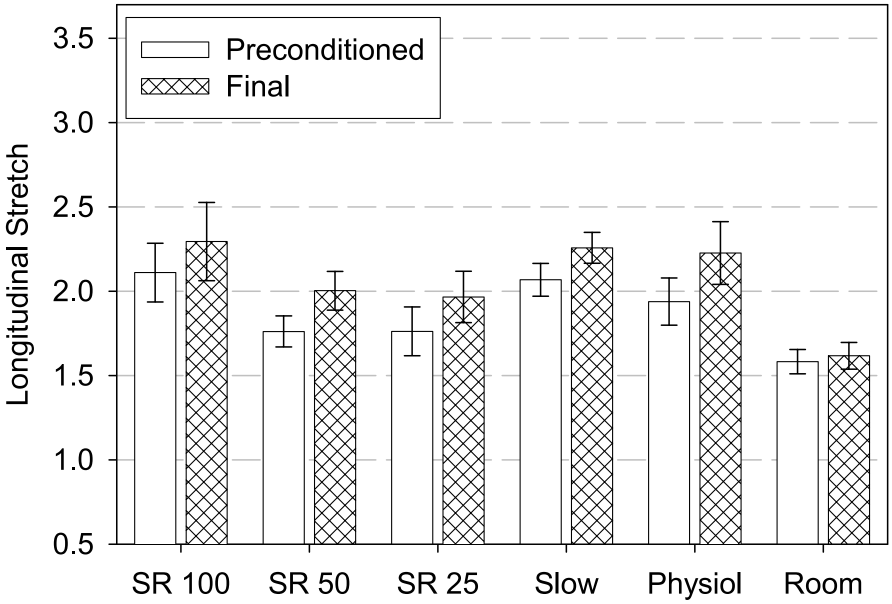

Figure 3-62 Comparison of longitudinal stretch differences between preconditioned and final marker files for all biaxial mechanical studies. SR ## represents stress relaxation of maximum target stress 100, 50, or 25 kPa. Mean and SEM shown.

3.6.2 Spinal Cord Injury

The magnitudes of preconditioned stretch in the two directions in the spinal cord injured (SCI) bladder wall are closer to each other than the stretches in the normal samples (Figure 3-63). This indicates structural changes occurred within only 10 days after SCI. Additionally, analysis using the free floating, original marker positions as reference gave a different result in both normal and SCI samples (Figure 3-64). The variability is clearly higher in both the normal and SCI groups when referenced to the floating reference position. Also, the floating marker position made the specimen appear more anisotropic. This was due to the asymmetric changes in the preconditioned stretch (Figure 3-63). The circumferential direction preconditions to a higher stretch level than the longitudinal direction. Whether this difference indicates that the specimen preconditions to an isotropic state and is anisotropic initially is unknown, although it is possible.

Also, the preconditioned stretches of the SCI specimens are closer to equivalent than the normal specimens, which may be indicative of the structural changes occurring within the SCI tissue.

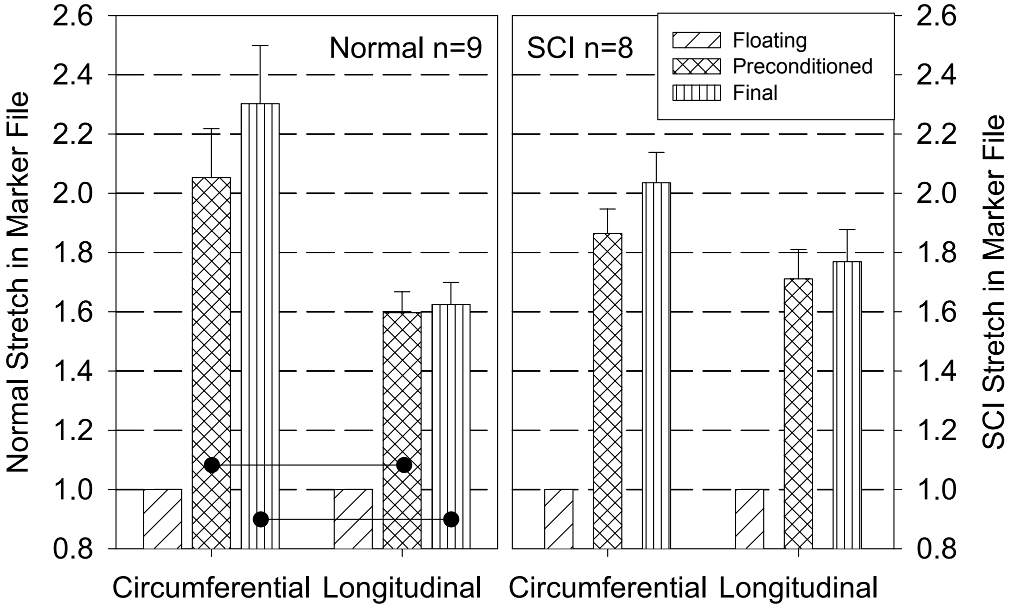

Figure 3-63 Change in stretch due to marker position reference used. There are significant differences between the marker files in between the two directions in normal preconditioned and normal final ($p<0.022$), but no significant differences in the SCI group. Therefore the SCI specimens show preconditioning stretches that are closer to symmetric than normal preconditioning stretches. Mean and SEM shown.

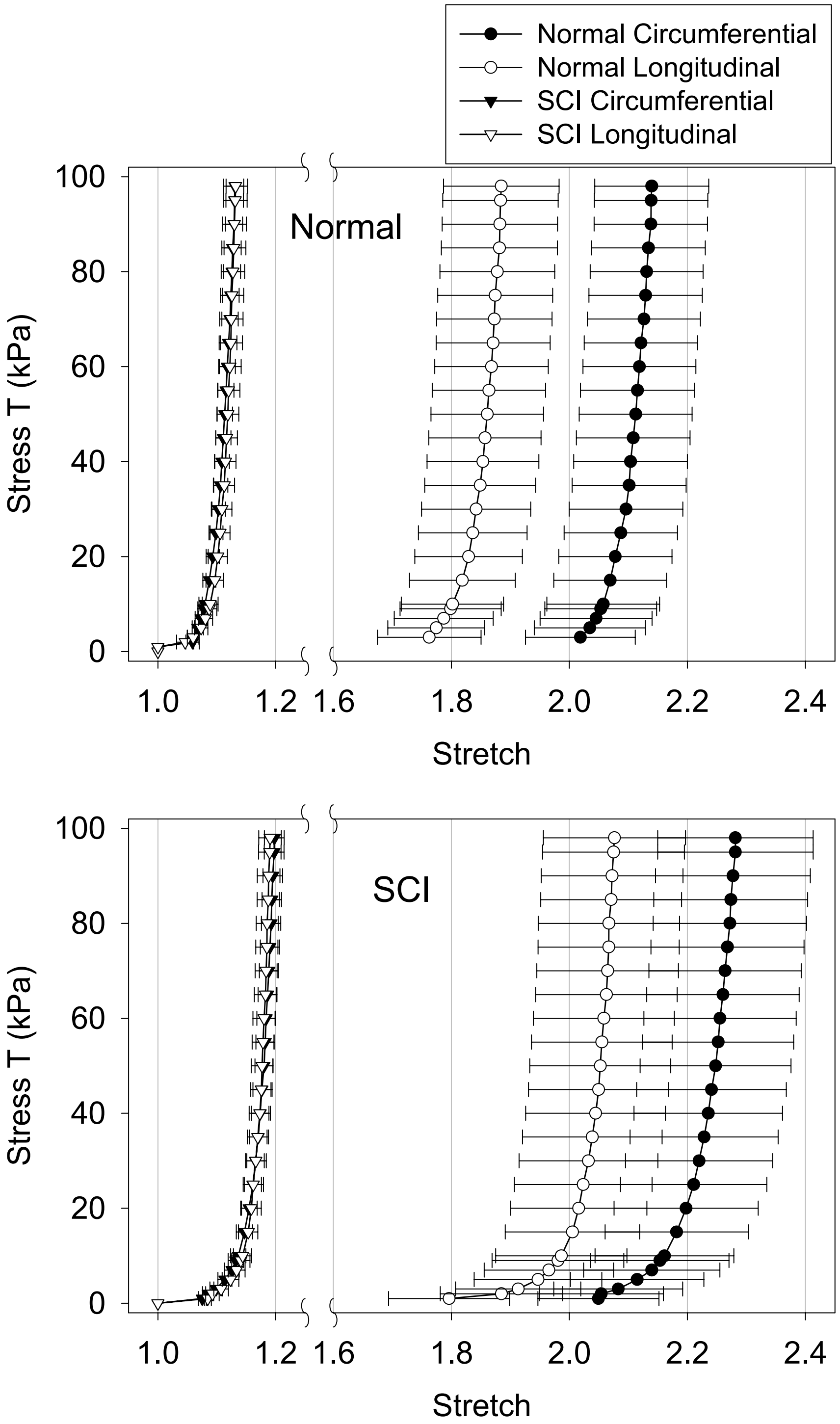

Figure 3-64 Comparisons of the analysis of normal specimens with respect to the preconditioned (left curves) and free floating reference states (right curves) for bladder wall samples from normal (top, n=11) and SCI (bottom, n=8). The error bars are SEM. The preconditioned reference state gives a less variable response than the floating state. In addition, the floating data appears more anisotropic due to the preconditioned marker states.

4.0 MORPHOLOGY ASSESSMENT

As discussed in section 2.0, much is known about the structure of the bladder wall, including cell and connective tissue components, the amounts of muscle in them, and their arrangements on a microscopic level. However, little information is available to relate these sub-cellular structures to mechanical behavior at a tissue level. Why does bladder tissue behave as it does? How can we predict changes in functional behavior when structural components are changed, such as during disease states? To answer these questions, quantitative bulk tissue-level information is required, such as the type, volume, organization, and orientation of tissue components.

There are several methods of obtaining this information, including conventional histology and microscopy, electron microscopy, and digital imaging systems. Each can contribute some information and can be used to verify others.

4.1 Volumetric Digital Imaging

Conventional microscopy is performed by embedding a tissue sample in a hard substance, creating a tissue block, and then sectioning it into thin slices that are placed on transparent glass. The sections are then examined individually under a microscope. Since the advent of sophisticated digital imaging and automated computer processing, the microscope is often connected to a digital camera that transfers the images to a computer for objective digital analysis and storage. A logical next step is to bypass digitizing the microscope slides by imaging the sample block directly (Figure 4-1). This has many advantages, including reduced analysis time (the slides do not need to be imaged manually), registration of all slices of a tissue block, removal of sectioning artifacts (since the block is imaged before sectioning), and simpler distribution and sharing of data (for example, via FTP instantly instead of by regular mail). The volumetric service used for this study was purchased from Resolution Sciences Corporation (RSC) based in Corte Madero, CA.

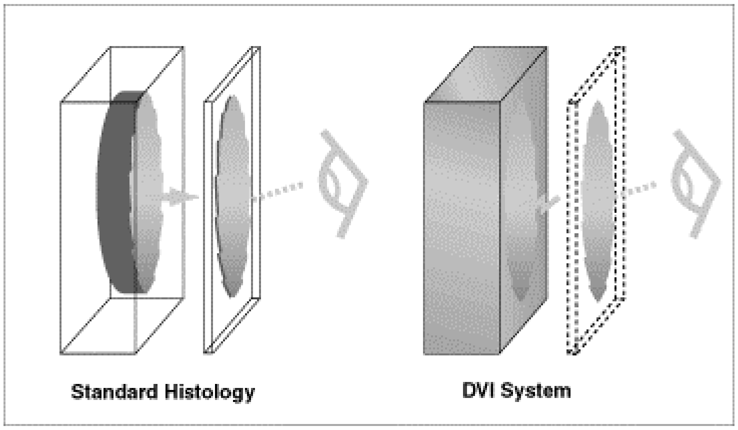

Figure 4-1 Comparison of conventional microscopy and digital volumetric imaging, also called surface imaging microscopy. Reproduced with permission from Resolution Sciences Corporation (www.resolve3d.com).

4.1.1 Method

Upon receipt at RSC by express mail, each of the samples was fluorescently stained. Then the sample was embedded in an opaque polymer which was then mounted in the automated sectioning system (Figure 4-2). Each sample was sectioned by a diamond blade from MicroStar (Huntsville, TX) in a robotically controlled microtome from Olympus (Melville, NY). A personal computer controlled a DCX-AT2000 motion-control board from Precision (Carlsbad, CA) that positioned the microtome to cut sections off the sample.

The exposed cut face was positioned in front of a microscope objective of 4x, 10x, 20x, or 40x magnification attached to a computer-controlled surface-imaging microscope. An arc lamp and computer-controlled excitation and analysis filters provided stimulation and filtering for fluorescence of the stain. The image from each fluorescent stain filled one channel of the final data set. The images were captured to computer memory using a PCI-DVK digital camera interface from Engineering Design Team (Beaverton, OR). The digital camera used was a 2029 x 2044-pixel MegaPlus: 4.21 CCD camera from Redlake MASD (San Diego, CA) with 200-mm-focal-length lenses from Nikon (Melville, NY). The block face was sectioned and imaged 1000 times or more per sample, creating a digital three-dimensional virtual replica of the original.

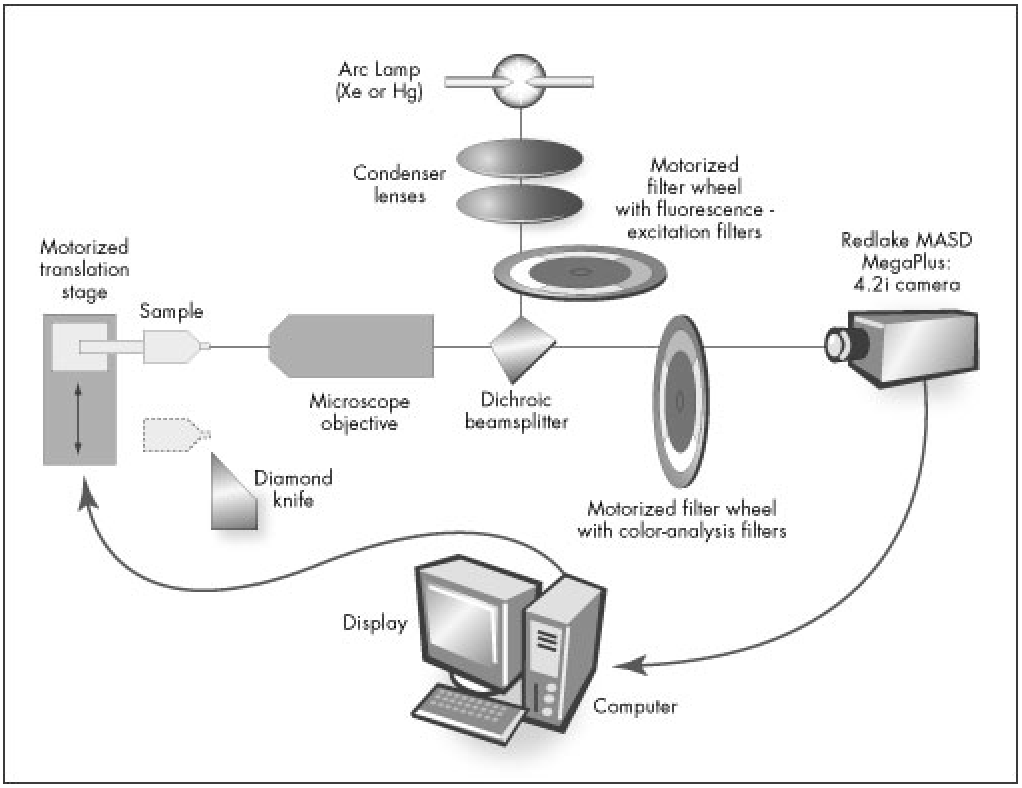

Figure 4-2 Process and hardware of sectioning a sample using digital volumetric imaging. Reproduced with permission from Resolution Sciences Corporation (www.resolve3d.com).

At capture time, the data were reduced from the camera's 2k by 2k to 1k by 1k output images. The digital volumetric imaging (DVI) datasets were recorded on DVD and shipped to the University of Pittsburgh or served over the Internet by FTP. The data were then displayed, manipulated, and extracted using visualization and analysis software, RESView 3.2, produced by RSC.

The method utilized by RSC offers four spatial resolutions: 0.4, 0.8, 1.8, and 4.5 microns/voxel. Due to the number of CCD elements on the digital camera, an increased sample size dictates a lower resolution, and vice versa. Each voxel of the final volumetric dataset consists of three bytes, or channels, of information, in RGB (red-green-blue) format. Each byte consists of 256 intensity levels. Therefore, for a 1k by 1k by 1k image with 3 bytes per image, the raw data alone would sum to 3.1 GB. The proprietary file format serves also as a compression program, reducing the size of the final file. For these studies, only two channels were used, one for the connective tissue and one for cellular matter.

4.1.2 Samples

For these studies, three bladder samples were imaged, including one taken four weeks after spinal cord injury (SCI) (Table 4-1). All were imaged with the standard connective tissue stain which stains cells in the red channel and the connective tissue in the green channel. Samples 1 and 2 were each fixed as an intact bladder, to volumes of 0.1 and 0.7 ml, respectively. Sample 3 was prepared as a biaxial specimen (section 3.2) and chemically crosslinked at 4 ^{o}C overnight with a ~2g load applied to the planar surface to keep it flat ("flat-fixed").

Table 4-1 Bladder samples submitted for digital volumetric imaging.

Sample #	**Tissue Type**	**Condition**	**Linear Resolution**
1	Normal	Filled to 0.1 ml	0.44 microns
2	Normal	Filled to 0.7 ml	0.44 microns
3	Four weeks post SCI	Flat-fixed	0.88 microns

4.1.3 DVI Images

After the first DVI was taken of sample 1 (Table 4-1), it was determined that all subsequent samples would have to be fixed in a flat or distended state to prevent tissue warping. The first sample was so distorted it was impossible to identify the directions (Figure 4-3). Although the lumen and serosa could definitely be located, quantitative analysis of any kind was impossible by, so sample 2 was used for all normal bladder analyses (Figure 4-4). The SCI sample demonstrated an obvious increase in muscle and more collagen integrated into the muscle, as opposed to the clear muscle sections in the normal ones (Figure 4-5).

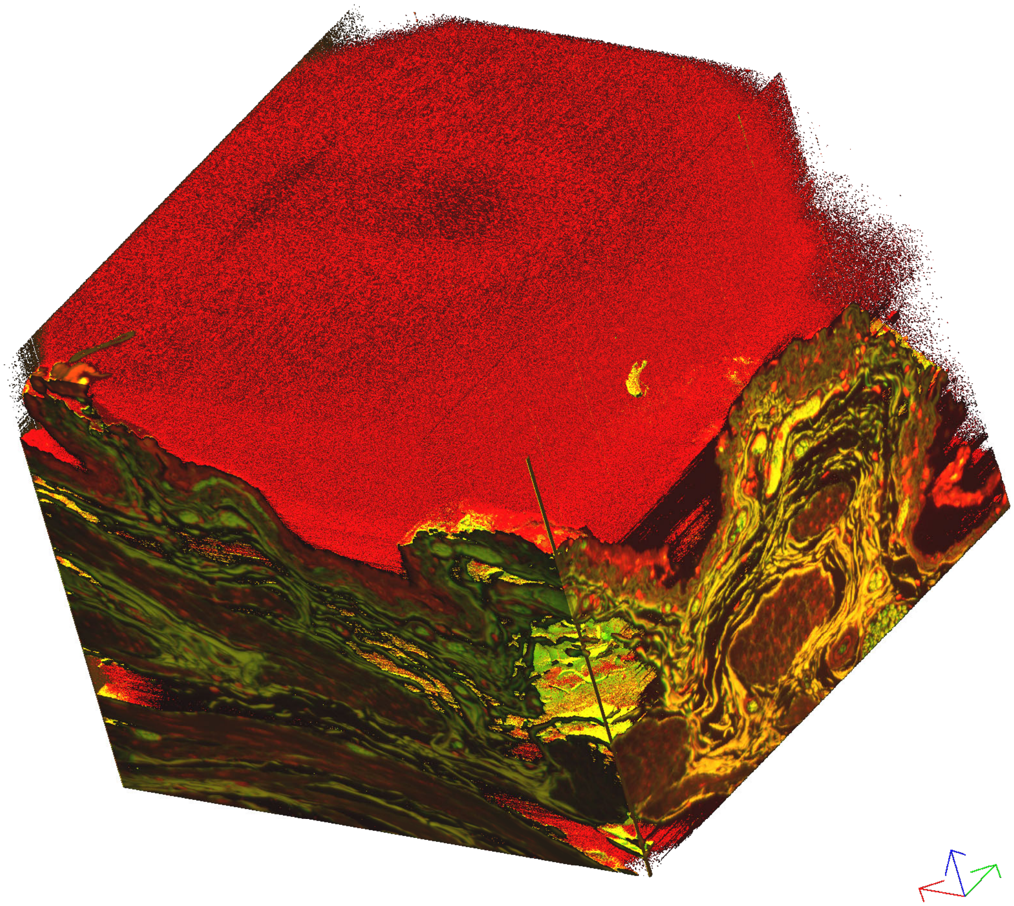

Figure 4-3 DVI of normal rat bladder, sample 1 in Table 4-1. Green is connective tissue and red/orange is cellular material.

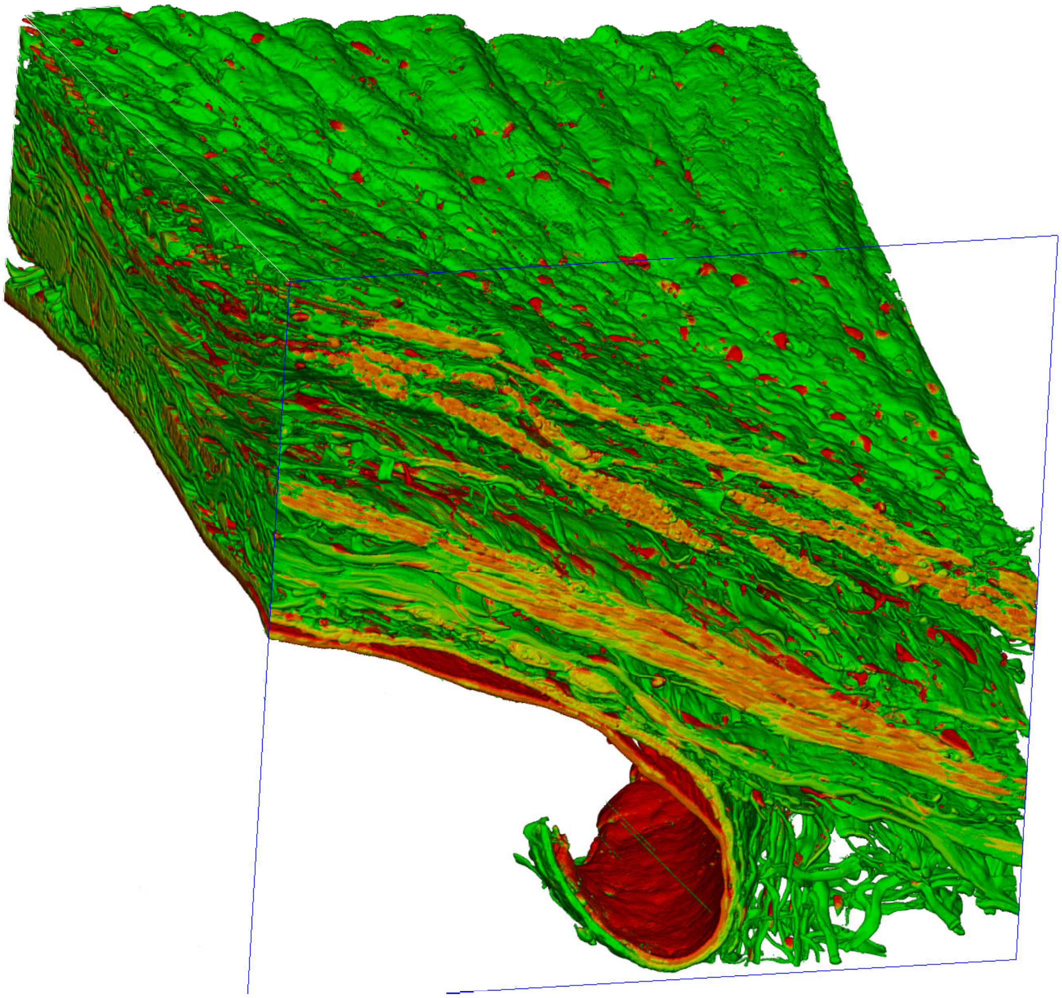

Figure 4-4 DVI of normal rat bladder, fixed as intact bladder filled to 0.7 ml, sample 2 in Table 4-1. Green is connective tissue and red/orange is cellular material. The urothelial lining is clearly visible at the bottom, as are muscle layers in the interior.

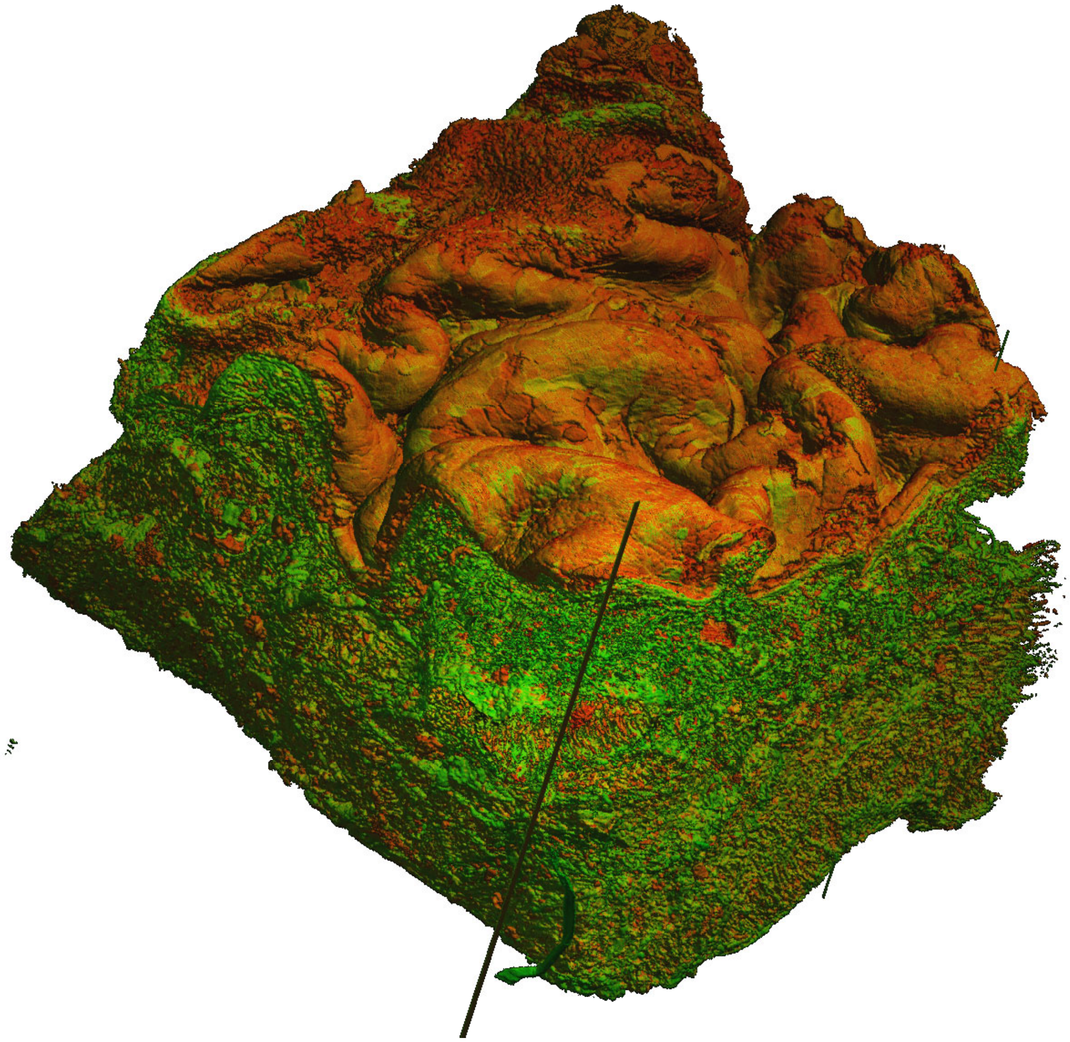

Figure 4-5 DVI of spinal cord injured rat bladder, four weeks after injury, sample 3 from Table 4-1. Green is connective tissue and red/orange is cellular material. Note the increase in green dispersed throughout the muscle, and the convolutions in the urothelial surface (top).

4.1.4 Limitations

Although an excellent system for the information it supplies, this system is limited in several ways. First, the technology is new and therefore expensive. Most budgets will allow for only a few samples so extensive variability, pharmacology, or treatment studies cannot be performed.

The best resolution is not adequate for many applications. For example, collagen fibers in connective tissue are typically on the order of a few to 10 microns in diameter. To obtain clear images of these collagen fibers, the resolution must be several times the maximum diameter to be clearly distinguished. Normal samples were thin enough to be sectioned at a resolution of 0.44 microns. This allows relatively clear imaging of the larger collagen fibers (Figure 4-4). However, the spinal cord injured samples were thicker than 0.9 mm so they were sectioned at the next-best resolution level (Figure 4-5). At this resolution, the structure appears more homogeneous. Additionally, the resolution can never be changed. The advantage of conventional slides is that they can be re-imaged as equipment improves, for no additional direct cost.

The available stains were limited, and as the process was proprietary, the specific stains used and their properties were not disclosed to the users. This lack of information leaves questions regarding the specificity of the staining and other related issues.

Although the RESView program was very versatile, it had some limitations. The user could move through the sample in all three orthogonal planes, cutting into the virtual tissue, but at the time of this study no oblique sections could be made, so analysis dependent on the specific orientation of the tissue was more difficult. Additionally, the only way to extract the data for other client uses was to export it as a series of tiff images; the user was not granted direct access to the intact dataset.

4.2 Fiber Directions

Tension in the bladder wall is supported by the components of the tissue, including the smooth muscle cells and the connective tissue. Mechanical behavior under stress is therefore dictated by the organization and alignment of the constituent fibers of collagen, elastin, and smooth muscle. To determine the orientation of these constituents, a stack of images was obtained from samples 2 and 3 of the DVI bladder sample datasets. These images were used to obtain quantitative values of fiber directions and strength of alignment through the thickness of the bladder sample. The goal was to determine the orientations of these components through the entire thickness of the bladder wall.

4.2.1 Methods

The image processing analytical methods used to visualize the orientations were adapted from a technique developed by Chaudhuri and coworkers for characterization of directions in textures.(97) This method was modified by Karlon and coworkers to detect myofiber alignment.(98) The analysis was implemented in MatLAB. The code functions and scripts are available in Appendix B: Fiber Orientation Analysis.

Local orientation of the images was determined in subregions of each image through the thickness. The orientations of the smooth muscle cell bundles and the connective tissue (almost entirely collagen) were determined separately by using two different sized subregions, 120 microns for muscle and 2 microns for connective tissue. To further focus the analysis on only one type, the RGB images were converted into two grayscale images comprising the red and green channels separately. Other than the size of the subregions, the analyses on the two images were identical. The size of the original tiff stacks (1k by 1k) was reduced to 600 by 600 during this analysis.

First two filters, or masks, of size 7x7 pixels were defined by the following equations.

$$\begin{aligned} h_x(i,j) &= \frac{2i}{\sigma^2}\exp\left[\frac{-\left(i^2+j^2\right)}{\sigma^2}\right] \\ h_y(i,j) &= \frac{2j}{\sigma^2}\exp\left[\frac{-\left(i^2+j^2\right)}{\sigma^2}\right] \end{aligned} \tag{4.1}$$

Here i and j are the integer image coordinates in the horizontal and vertical directions and lie within the range $-3<i, j<3$. The determination of 7x7 pixels as the optimal size for the filter has been previously demonstrated.(97) This particular filter is a Gaussian filter, with a mean of zero and a variance of σ^2. The determination of $\sigma^2=100$ was made through preliminary analyses using values in the range of 4 to 100 as suggested in the literature by other researchers.(99)

Next, these filters were combined (via image convolution) with the subimages (I) (the size of the collagen and muscle bundle fibers as outlined above) to obtain horizontal (x) and vertical (y) edge images.

$$\begin{aligned} G_x &= h_x * I \\ G_y &= h_y * I \end{aligned} \tag{4.2}$$

where I is a 7x7 element pixel array section of the original image.

Then the magnitude (G) and angle (φ) of the edges were computed as

$$G = \left(G_x^2 + G_y^2\right) \text{ and } \varphi = \tan^{-1}\left(\frac{G_y}{G_x}\right) \tag{4.3}$$

The direction was computed in 1 degree increments. For each subimage, an array, A_θ, of 180 accumulator bins was defined. Contribution of the pixels within the subimage to each of the discrete θ=1 to 180 degree angles was summed with the accumulating function below.

$$A_\theta = \sum_{(i,j)} G(i,j)\cos^2\left(\theta - \varphi(i,j)\right) \tag{4.4}$$

The result was a bell-shaped curve over the 180 degree interval with intensity values at each degree, for every subimage in the image and for each image in the image stack.

The preferred fiber direction was calculated as the angle of the maximum intensity of the subimage. The final result was a grid of preferred fiber direction angles overlying the original image. The mean and standard deviation of all the preferred directions in the image were determined for each image through the thickness of the material. This procedure was implemented on bladder samples two and three listed in Table 4-1.

4.2.2 Results

Representations of the fiber orientations of muscle bundles and connective tissue are shown in Figure 4-6 and Figure 4-7, respectively. The analysis was successful in determining the fiber directions in both the normal and SCI samples. Computational time was less than 10 minutes per each image for cells and connective tissue.

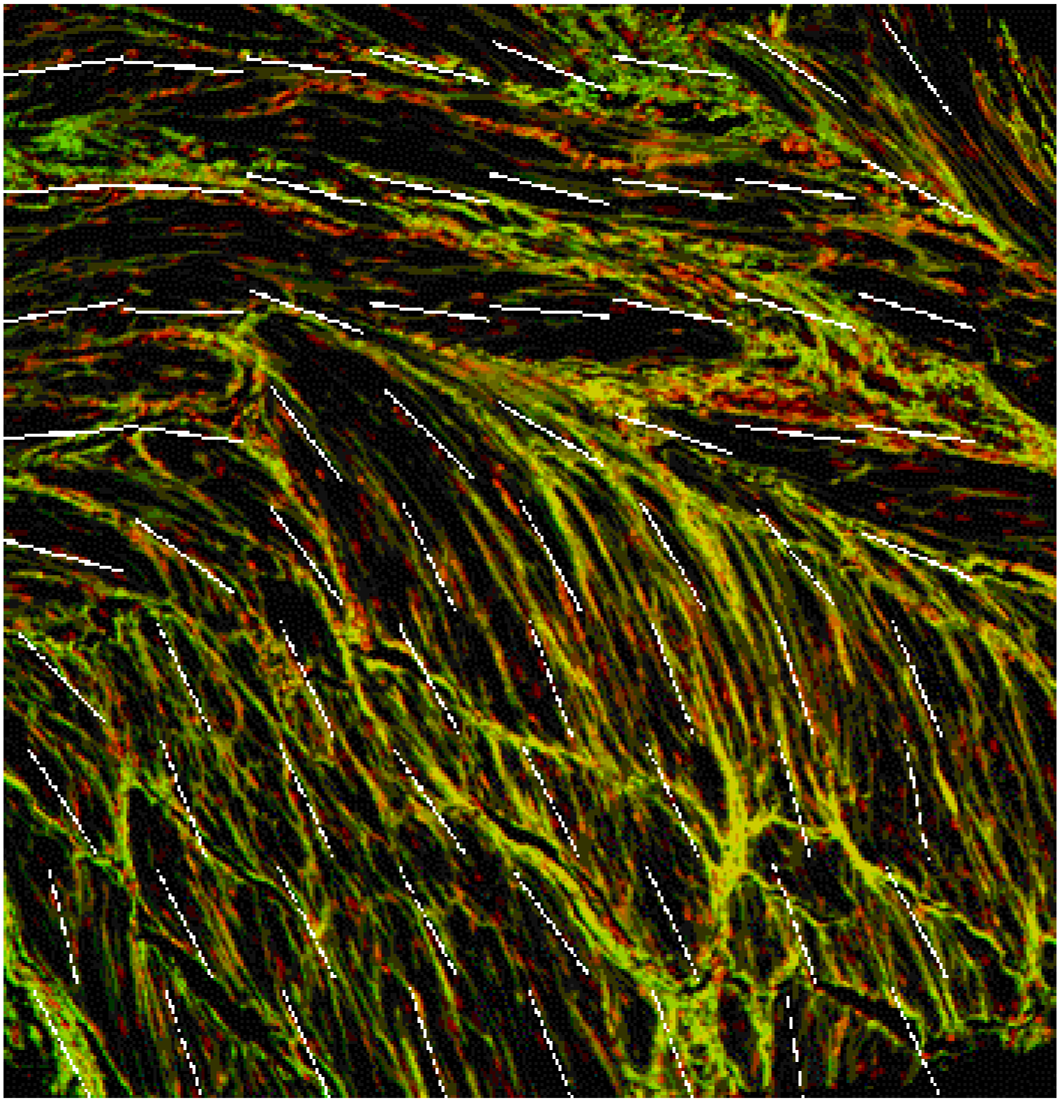

Figure 4-6 An image slide of an SCI sample overlaid with the fiber orientation of muscle bundles, shown as white lines. The direction of the lines is the computed direction of muscle bundles in that region. The length and width of each box represented by the line is representative of the approximate size of a muscle bundle. The size of this image is approximately 0.5 mm each side.

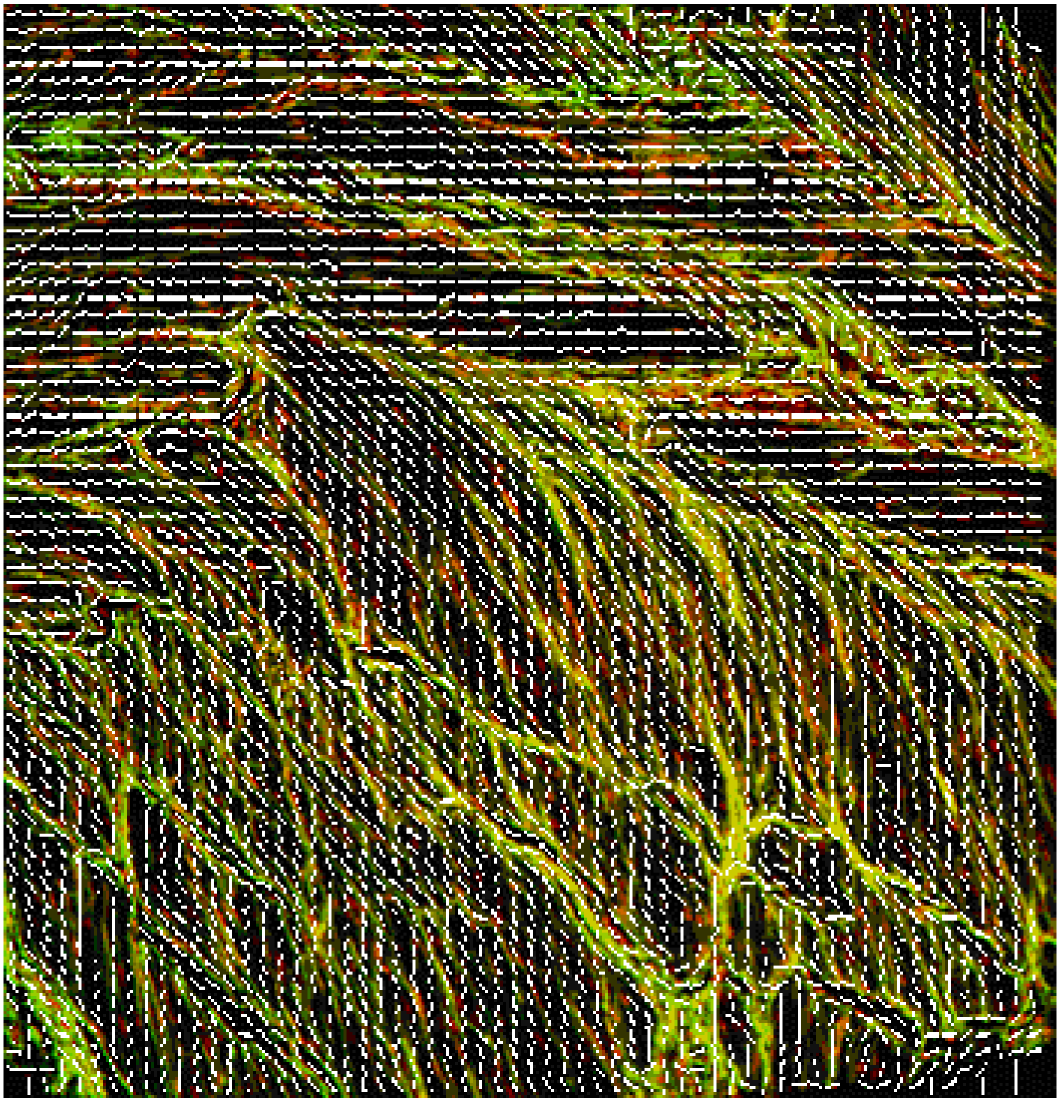

Figure 4-7 The image slide of the SCI sample in Figure 4-6 overlaid with the fiber orientation of connective tissue, shown as white lines. The direction of the lines is the computed direction of connective tissue (mainly collagen) in that region. The size of this image is approximately 0.5 mm each side.

In both normal and SCI samples, both muscle bundle and connective tissue orientation vary through the tissue thickness. The fibers of the SCI sample are oriented in one direction at the lumen, then become oriented in the other direction, then return to the original orientation near the serosa (Figure 4-8). The fiber directions of the normal bladder are less clear, but there is an orientation change near the serosa. It is possible that the hypertrophy of smooth muscle dominates the thickness in the SCI sample and therefore the muscle dominates the response, whereas the muscle layer is much thinner in the normal specimen and only exhibits a small change in direction.

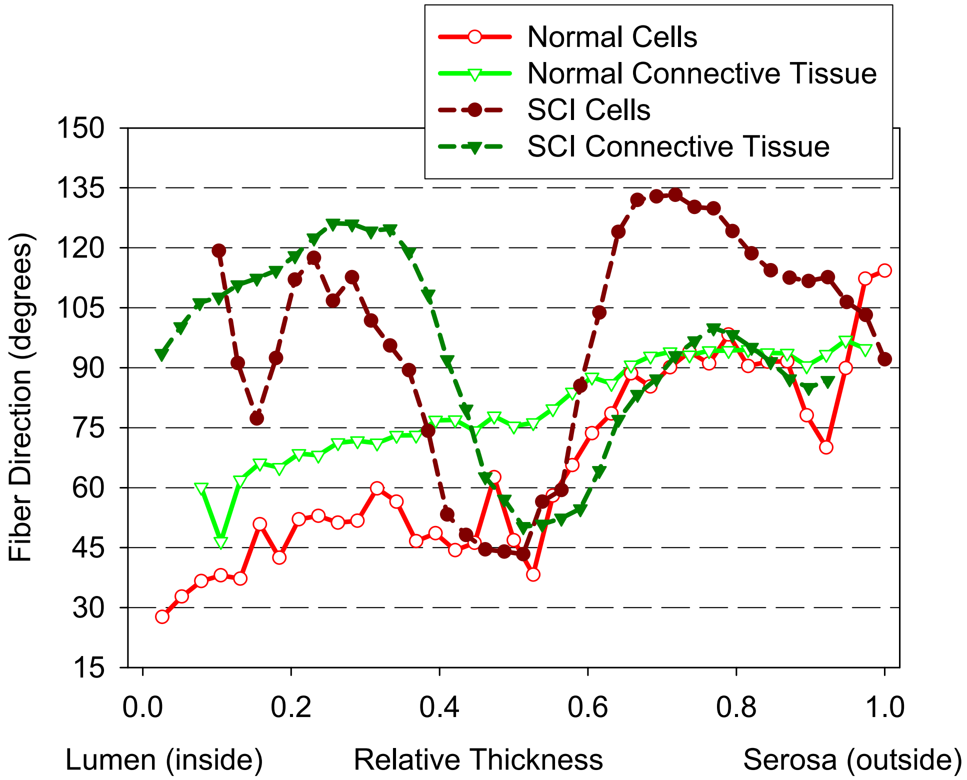

Figure 4-8 Orientation of normal and SCI bladder components muscle and connective tissue through the thickness.

4.2.3 Limitations and Difficulties

The spatial resolution of the camera and the sectioning thickness are two physical values. For optimum accuracy, these values should be equal. In this setup, the opacity of the sample block polymer is adjusted slightly to allow light to pass only as far as the spatial resolution of the camera, so that the sections can't be imaged any farther through the thickness of the section. Additionally, the microtome is adjusted to a sectioning thickness equal to the spatial resolution.(100) Therefore, the three-dimensional resolution is very close to isotropic in all three dimensions. However, given all these variables, the exact resolution of the third sectioning dimension may not be equal to the spatial resolution of the optical camera setup.

Additionally, the samples were not processed perfectly planar to the camera. Therefore, the images were not perfectly orthogonal to the planes of the virtually sectioned blocks. Figure 4-4, for example, shows the normal tissue section positioned at a slight diagonal. By comparison, the diagonal slant of the SCI sample was minimal. Fortunately, both samples were also fairly flat. The normal images were rotated to make them flat within MatLAB using a bilinear method to interpolate between pixels.

The two images analyzed, samples 2 and 3, were imaged differently. The SCI sample was imaged in the plane of the tissue, called *en face* in traditional histology. The normal sample, however, was imaged in cross section. As the output image stacks were generated from the actual camera images, the SCI images were ready for analyses immediately, but the normal samples had to be processed to obtain images that were perpendicular to the image plane. This was done by taking the same row from all the images to form a new image, a process completed for the entire image stack. This procedure added significant time to the sample analysis.

The thickness of each of the samples changed through the block. The thickness of the tissue was analyzed in the four extremes (corners) of the sample block. The maximum difference between any two of these four measurements was about 10%. Also the normal sample had a significant angle in only one of the two axes parallel to the tissue. However, it would be impossible to section the sample perfectly flat, or perfectly planar. The resulting angles affect the analysis to some degree.

As reported in section 2.1.2, collagen fibers surround the muscle cell bundles. Therefore, the results for the muscle and collagen fibers are similar, as they are oriented identically. Information regarding the collagen fiber direction independent of muscle bundles is essential for determining the force transmission within and between muscle bundles, but cannot be readily measured by this method. It is likely that these structures change after spinal cord injury, giving rise to changes in behavior such as anisotropic coupling (section 3.5).

Additionally, this technique is difficult to verify, as the muscle bundles are variable and are affected by regional differences throughout the bladder. The sample size available is very small relative to the size of the organ. Section 4.4.1 supplies some validation using conventional microscopy.

4.3 Tissue Type Volume Components

Also important is the amount of structural components in each layer through the thickness of the bladder. The DVI images are ideal for this analysis. They offer perfect registration, a large number of slices through the thickness, and easy separation into cell and connective tissue components because the dual fluorescent staining classifies the intensities of these two components into two channels.

4.3.1 Methods

The same images used for the fiber direction analysis in the previous section were utilized. Every pixel in each image was examined and classified as connective tissue or cells (muscle or urothelium) or both by comparing the intensity values of the red and green channels in the tiff image. If the red intensity was larger, the pixel was classified as cellular material, and the cell volume counter was incremented by one for that image. If the green intensity was larger, then the pixel was classified as connective tissue. If the red and green intensities were equal, a third counter was incremented to record the number of unclassifiable pixels. The total number of unclassifiable pixels was less than 1% of the total pixels for each image analyzed.

This component analysis was implemented in MatLAB code. See Appendix C: Volume Component Analysis.

4.3.2 Results

The results showed that the normal sample was 38.4% cells and 61.6% connective tissue. The sample four weeks after SCI was 56.5% cells and 43.5% connective tissue. This represented an increase of 47.2% of the cells and 29.4% decrease in connective tissue (Figure 4-9), clearly a result of the hypertrophy of the SCI sample.

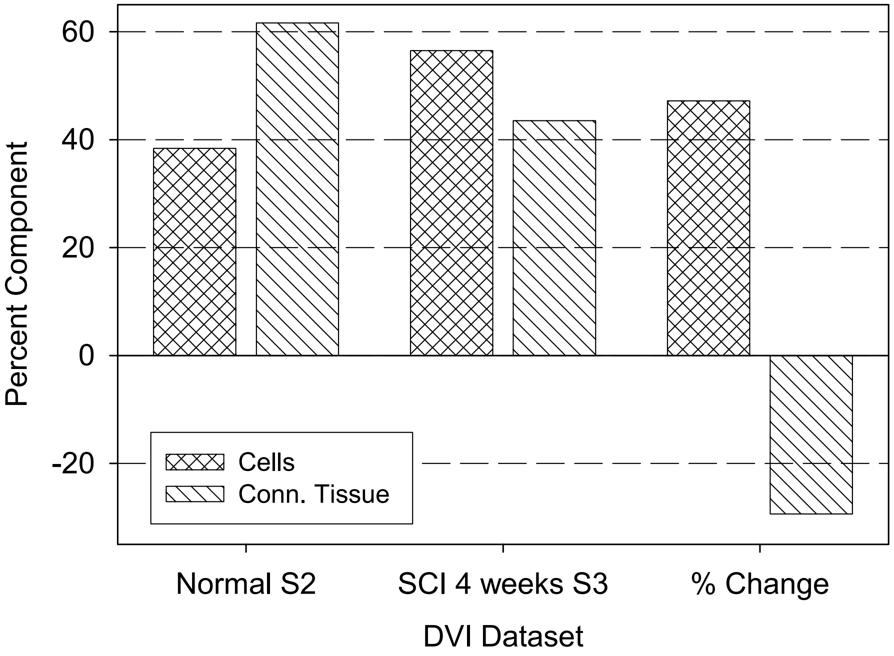

Figure 4-9 Percent volume of cells and connective tissue in the DVI datasets. Normal S2 is sample 2 and SCI 4 week is sample 3 in Table 4-1.

The changes in tissue type through the thickness are shown in Figure 4-10. In this figure the thickness has been normalized from 0 (lumen) to 1 (serosa) for comparison purposes. The predominant component types through the thickness alternate in both samples. In the normal sample, cells predominate for the first 15% of the thickness from the lumen (presumably the urothelium), then connective tissue predominates through the rest of the thickness. There is a peak of connective tissue at 40% (deep lamina propria) and a leveling off of both connective tissue and muscle from 45% to 80% (detrusor). In the SCI sample, collagen is predominant until only 5% into the wall, then roughly equal amounts of connective tissue and muscle exist until about 60%, where muscle becomes predominant for the remainder of the thickness. This clearly represents the increase in cells, due primarily to smooth muscle hypertrophy (Figure 4-10, Figure 4-11).

Layers of the lamina propria are observed in the first few microns of the SCI sample but not in the normal sample (Figure 4-11). It is likely that the increase in cells is due to either the lamina muscularis mucosa or the capillaries present in the submucosa. The next layer is the deeper laminar propria and is primarily collagen, followed by the layers of the detrusor, containing both collagen and muscle cells.

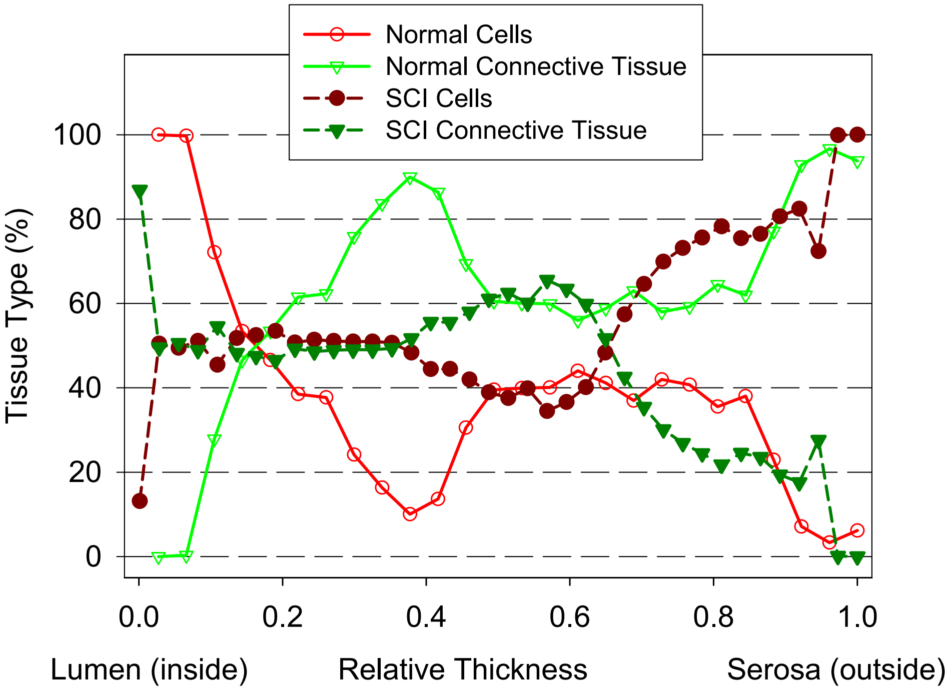

Figure 4-10 Percentage of cells and connective tissues through the thickness of one normal (sample 2 in Table 4-1) and SCI sample (sample 5 in Table 4-1). The data here have been thinned slightly for clarity. See Figure 4-11 for details of component information near the lumen.

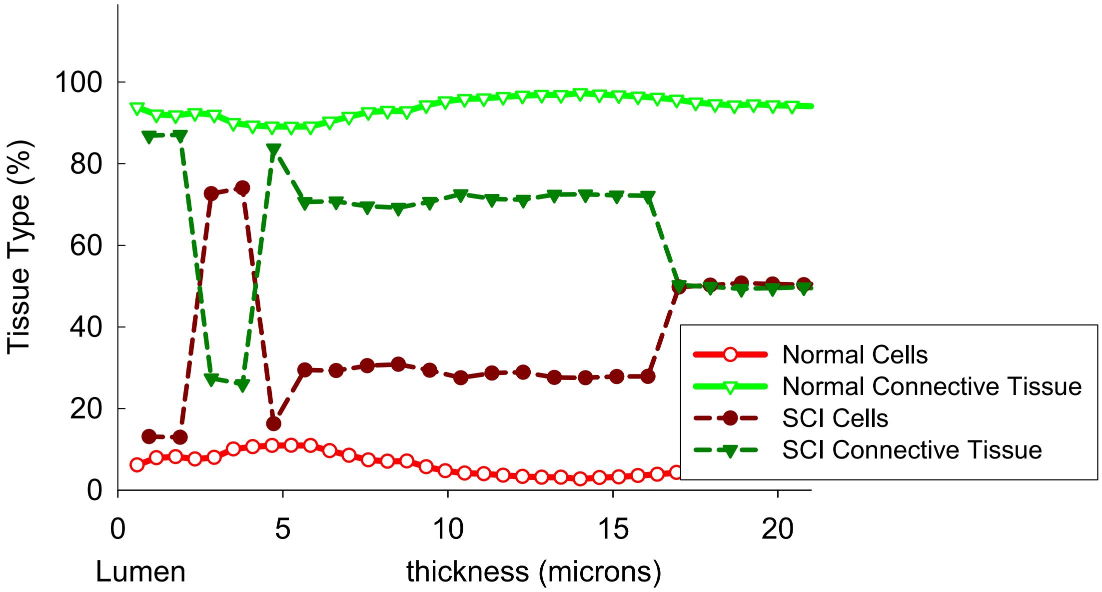

Figure 4-11 Percentage cells and connective tissue near the lumen surface of one normal bladder wall (sample 2 in Table 4-1) and SCI (sample 3 in Table 4-1).

4.3.3 Limitations and Difficulties

All the limitations and difficulties listed in section 4.2.3 apply.

The increased thickness of all layers in the SCI sample provided sufficient thickness increase to view the lamina muscularis mucosa/capillary layer, but since the normal was much thinner, the spatial resolution was not adequate for this purpose.

4.4 Conventional Microscopy

Microscopic imaging was performed in addition to the DVI analyses. Both Movat's Pentochrome stain (cells, connective tissue, and elastin), and pico sirius red (collagen) were used in separate bladder sections. Standard histological protocol was observed. All images were taken under relatively low magnification.

Three normal bladders were chemically crosslinked while filled to 25%, 50%, and 100% of maximum normal bladder volume, 0.7 ml. Sections were taken from each in cross section and stained with pico sirius red, in which collagen appears red (

Figure 4-12). The 25% filled sample had the largest thickness, while the 100% sample was the thinnest, clearly demonstrating the thinning that occurs during large stretches due to filling (3.3.5). The coiling of the collagen fibers previously documented in the literature is also seen in all three samples.(32) At 25% the collagen is densely coiled and therefore dark in color. Individual collagen coils are difficult to identify. At half-full (50%), most of the collagen coils are lengthened and therefore visible in a coiled configuration. Finally, at 100% filled, the collagen fiber coils are very elongated, and individual fibers are visible within the coils. The overall images become lighter in color from 25% to 50% to 100% filled due a decrease in staining of the stretched coils.

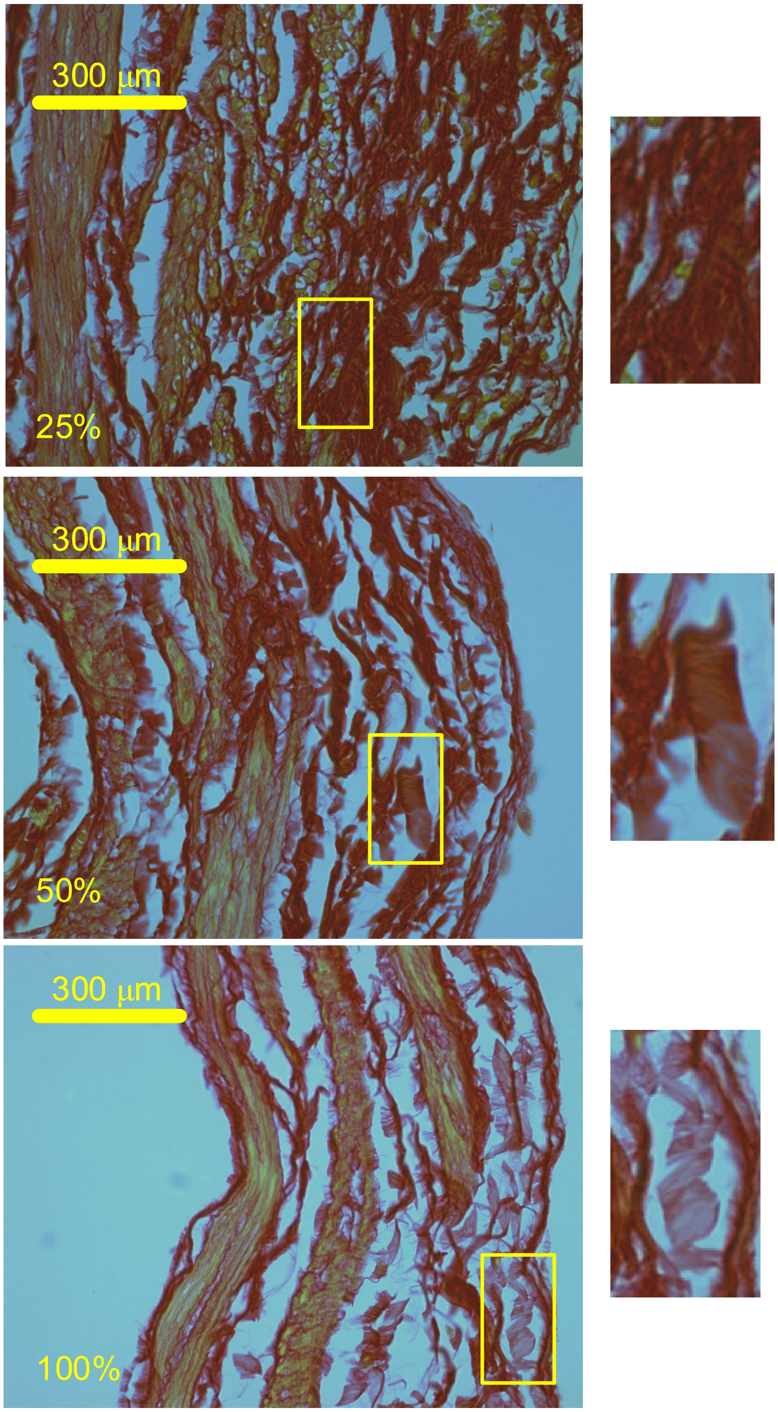

Figure 4-12 Cross section micrographs of bladder filled to 25%, 50% and 100% of 0.7 ml and stained with pico sirius red. Boxes indicate collagen fiber coils at different states of uncoiling through filling and these regions are enlarged on the right.

4.4.1 Validation of Fiber Direction

Validation of the fiber direction obtained from processed DVI images was performed using normal rat bladder wall histology samples stained with pico sirius red. The entire thickness of a normal bladder wall was serially sectioned to obtain 120 sections *en face*. Forty equally-spaced sections were imaged at the lowest resolution available on the microscope. The imaged field of view was approximately 2.5 mm, approximately five times the DVI field of view. Images taken of sections near the serosa and the lumen demonstrated a predominantly circumferential muscle direction while sections near the center of the bladder wall were generally longitudinally oriented (Figure 4-13).

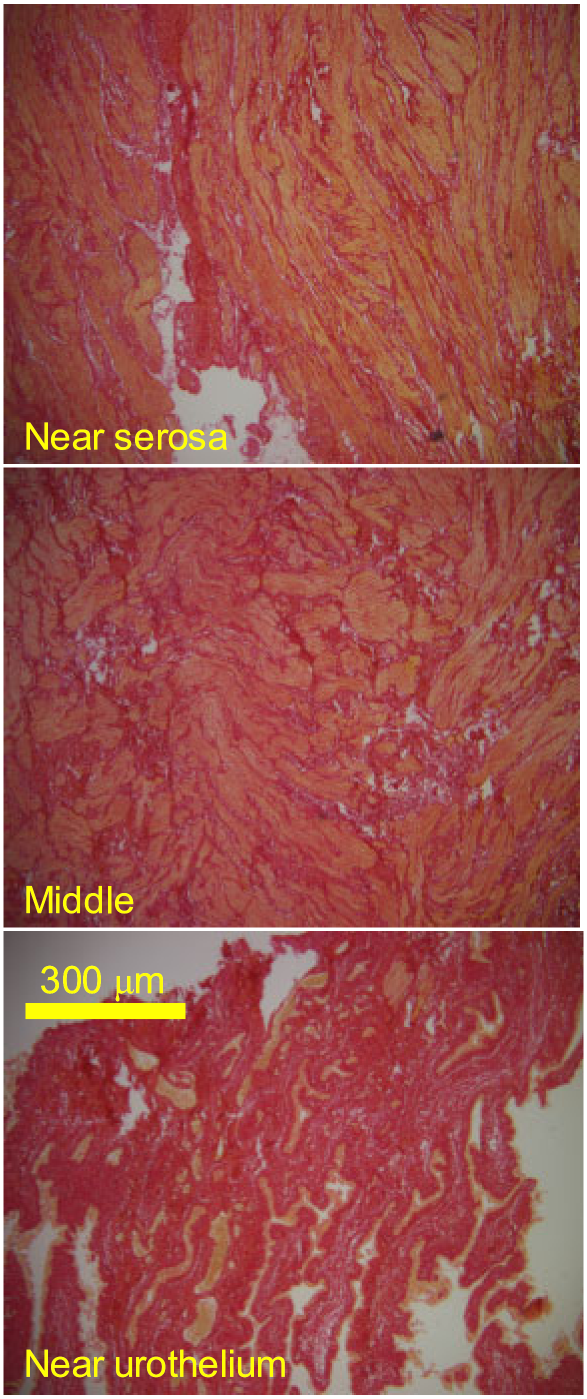

Figure 4-13 Outer, middle, and inner (lumen) images of the bladder *en face* obtained from standard histology sections stained with pico sirius red. Scale is identical in all images.

4.5 Scanning Electron Microscopy

SEM was performed on normal bladder. The sample was chemically crosslinked in 2.5% glutaraldehyde for 1 hour followed by three rinses in phosphate-buffered saline (PBS). The sample was then immersed in 1% osmium tetraoxide (OsO_4) for 1 hour, followed by three rinses in phosphate buffered saline (PBS). Then the sample was dehydrated in ethyl alcohol (EtOH) gradations of 30%, 50%, 70%, and 90% for 15 minutes each. Finally, the sample was rinsed in 100% EtOH three times before drying under CO_2, sputter coated with gold, loaded into the SEM machine and imaged at 10 kV.

The bladder is a interconnected layered structure (Figure 4-14) with a expansive network of collagen fibers (Figure 4-15).

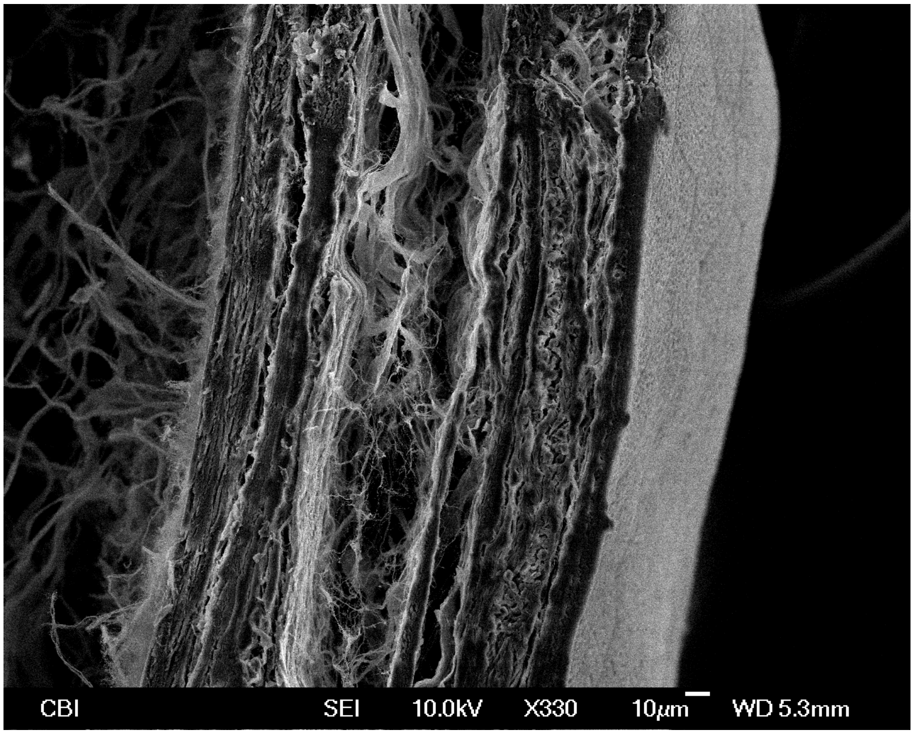

Figure 4-14 Scanning electron microscopy of the thickness of normal bladder sample (sample 2 in Table 4-1). The urothelium is on the right, and the long strands on the left are adhesive used to affix the sample to the platen. The layered structure is evident.

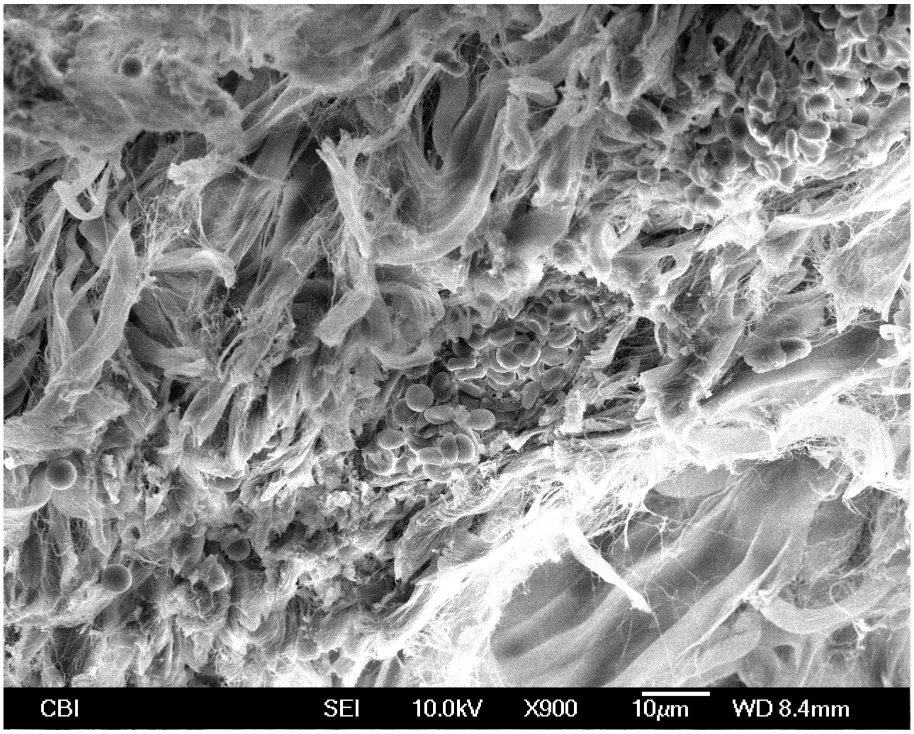

Figure 4-15 Scanning electron microscopy of the normal bladder sample (sample 2 in Table 4-1).

4.6 Summary

Digital volumetric analysis was performed on the bladder wall to obtain a stack of images through the thickness. These images were used to determine the orientation of cells and connective tissue through the bladder wall. In addition, the cell and connective tissue component types through the bladder wall were determined for both a normal bladder wall specimen and four weeks after spinal cord injury. This quantitative information is the first step towards the structural information needed to compose a structure-based model of bladder tissue behavior.

5.0 MODELING

In this section, the mechanical data obtained in section 3.0 is used in constitutive models. The quasi-static data is analyzed using a response function technique and the results used to determine the best phenomenological model for normal and spinal-cord-injured (SCI) bladder wall tissue to highlight the differences in material classification between the two. The stress relaxation data was fit to the Quasi-linear Viscoelastic model proposed by Y.C. Fung. To avoid local minima, a genetic algorithm technique was used for fitting.

5.1 Genetic Algorithm

Traditionally, all methods used in nonlinear curve fitting procedures are fairly complex. The goal is to find the value of parameters that fit an equation that is as close to the data as possible. All are iterative procedures and use the sum-of-squares (sum of the square of the difference between the real data and the computed value) to measure the quality of fit. The smaller this distance, the better the fit. In each procedure fit parameters are changed at each iteration to best minimize the sum-of-squares. Many are commonly used, but the three most frequently cited are the method of linear descent, Gauss-Newton, and Levenberg-Marquardt. The method of linear descent changes each parameter a set small amount, and checks the resulting sum-of-squares for decreases to determine whether to continue in that direction in each iteration. The Gauss-Newton method is similar, but it calculates the rate of change (derivative or slope) of the sum-of-squares to determine the size of future iteration steps. The Levenberg-Marquardt uses a combination of the two; it uses the method of descent to get close to the minimum, then the Gauss-Newton method of rate of change to pinpoint the absolute bottom.

The drawback to these and other methods is that they can all get drawn into local minima (with limited predictive ability) when the initial values are far away from the best minimum parameters. In practice, there is often not a good basis to estimate the initial parameter values. The complexity of the function dictates how close the initial values must be to avoid this pitfall. For simple models, or those with few parameters, these methods can be adequate and optimal. However, for highly complex functions and functions with many parameters, the possibility of minimization to a local minimum instead of a global minimum increases.

An alternative to this dilemma is the method of the genetic algorithm, also called differential evolution. It also uses an iterative, sum-of-squares procedure, but utilizes an altogether different method of optimizing the parameters. A group of parameters sets is maintained instead of just one working solution set. Based on how well each set fits the data, it is either used to produce better candidate solutions or thrown out. The Darwinian survival of the fittest concept is used to find the best solution possible.

First, 5 to 10 sets of parameters are initialized. In the language of the genetic algorithm, each set, or individual, constitutes a chromosome vector that contains the genes (parameters) to be optimized. These initial values are usually calculated from a range of values for each parameter using a random-number generator to make each unique. Then each set is used to generate the sum-of-squares. Several different methods of evolution can be used to determine which of the candidate sets are kept for the subsequent iteration. Reproduction involves keeping only the highly fit individuals (sets of parameters) that have a low sum-of-squares. Crossover involves the combination of two or more individuals. Mutation changes each of the individuals slightly. After some number of generations, all the individuals will be the same and the genetic algorithm will terminate. Standardized numbers for the amount of crossover and mutation are added in each generation, and these values are almost always successful in convergence at the same time as the population loses its diversity, but these values can be often optimized to speed convergence for a given function or data set.

As the initial parameter ranges can be several orders of magnitude, the necessity of an exact initial value is avoided. The disadvantage of this method is that the sum-of-squares must be calculated several times in each iteration, so the method is very slow. However, with today's fast desktop computers, this requirement is not very limiting.

All the nonlinear fitting performed in the remainder of this section was done with the genetic algorithm. Implementation for the genetic algorithm was in MatLAB R12 (MathWorks, Inc). All fits were performed 20 times for each sample to allow for different initial values for each of the 20 runs; however, the parameters never differed from the mean by more than 0.1%, so analysis of the variability of these 20 fits was not necessary. For more details on the genetic algorithm, see the work of Kenneth Price and Rainer Storn.(101) Appendix A: Genetic Algorithm supplies more details on this implementation.

5.2 Quasi-static Constitutive Modeling(102)

The data was obtained from quasi-static biaxial tests of normal and post-spinal cord injured rat urinary bladder wall as reported in sections, 3.3, and 3.5. Test specimens were aligned to the circumferential and longitudinal directions of the bladder, and tests were performed under stress control. Increased compliance was observed in both stretch directions at ten days after spinal cord injury compared to the normal group. In both groups, the mean equibiaxial stress responses in both anatomical directions were equivalent (Figure 3-56), suggesting an isotropic mechanical response. However, the responses to the non-equibiaxial protocols were different in the two material directions, indicating the response was not truly isotropic (Figure 3-58). This "quasi-isotropic" response was more prevalent in the normal specimens than in the SCI specimens, suggesting a change in material class due to disease.

The choice of a particular constitutive model requires an a priori assumption of the material classification. An incorrect choice can lead to difficulties with quality of fit, lack of convergence, and parameter significance. Choosing the correct model and fitting the data can therefore be time consuming if an appropriate model is difficult to identify. Further, alterations due to growth or pathology may induce unknown changes that are difficult to predict before an extensive experimental study is undertaken. Thus, it is desirable to evaluate biaxial mechanical properties independent of any specific constitutive model form. This is particularly the case when using stress-based biaxial mechanical protocols, which, although more convenient for quantifying the biaxial response within the physiological range, cannot be readily used to determine optimal constitutive model forms. In the present study, strain-energy interpolation functions were utilized in combination with stress-based biaxial testing data to determine changes in the material class and changes in degree and direction of mechanical anisotropy in the rat bladder wall pre- and post spinal cord injury.

5.2.1 Response Functions

The bladder wall was modeled with a biosolid mechanics approach. The material was assumed to be hyperelastic, incompressible, and pseudoelastic.(82) Thus, the in-plane 2nd Piola-Kirchhoff stresses $\mathbf{S}$ were derived from a two-dimensional strain energy function W using

$$\mathbf{S} = \frac{\partial \mathrm{W}}{\partial \mathbf{E}} \tag{5.1}$$

Although both load and unloading data were recorded, only loading data were utilized for the fit. Further, as the data demonstrated very low values of shear, shear strains and stresses were neglected.

To estimate the stress response to an arbitrary loading path within the experimental range, data obtained from all test protocols were fit to interpolation functions. Next, the highest maximum and lowest minimum value of the E_{11} and E_{22} for the middle five protocols were determined, and a 26 x 26 equally-spaced mesh was created within this range (Figure 5-1).

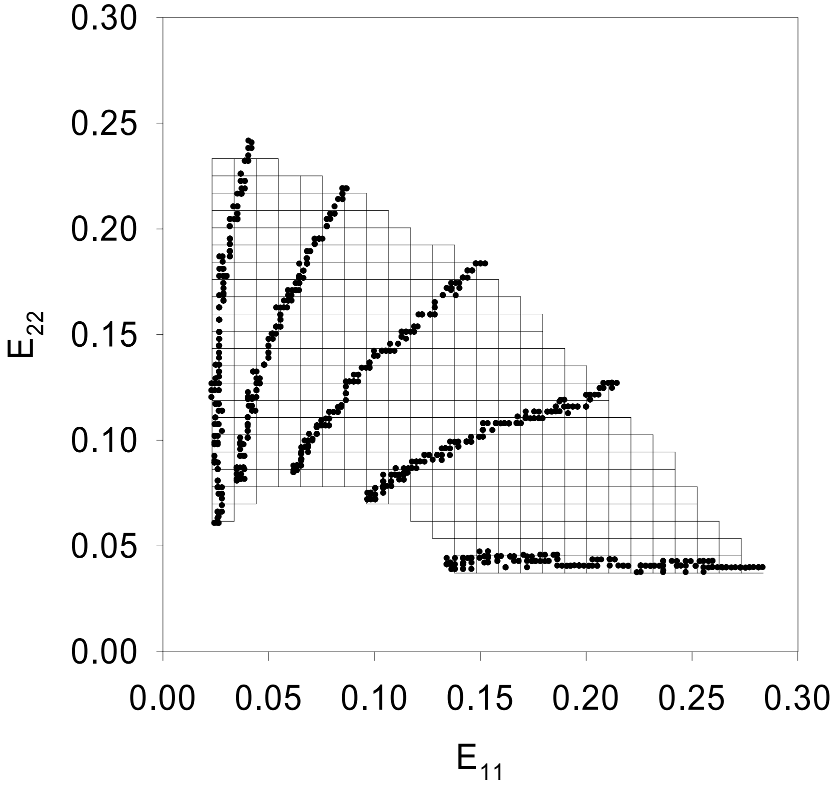

Figure 5-1 Strain values from a representative bladder biaxial experiment, overlaid with grid of 26 equally-spaced strain values. Interpolated stress values were calculated at the vertices of the horizontal and vertical lines. Units of strain on both axes are length/length.

At each vertex, both stress components were computed using the following interpolation functions.

$$\begin{gathered} S_{11} = \frac{c_{10}}{2}\left(2c_{11}E_{11} + 2c_{13}E_{22} + 2c_{14}E_{11}E_{22} + c_{15}E_{22}^2 + 2c_{16}E_{11}E_{22}^2 + 4c_{17}E_{11}^3\right)\exp P_1 \\ \text{with} \\ P_1 = c_{11}E_{11}^2 + c_{12}E_{22}^2 + 2c_{13}E_{11}E_{22} + c_{14}E_{11}^2E_{22} + c_{15}E_{22}^2E_{11} + c_{16}E_{11}^2E_{22}^2 + c_{17}E_{11}^4 + c_{18}E_{22}^4 \end{gathered} \tag{5.2}$$

$$\begin{gathered} S_{22} = \frac{c_{20}}{2}\left(2c_{22}E_{22} + 2c_{23}E_{11} + c_{24}E_{11}^2 + 2c_{25}E_{22}E_{11} + 2c_{26}E_{11}^2E_{22} + 4c_{28}E_{22}^3\right)\exp P_2 \\ \text{with} \\ P_2 = c_{21}E_{11}^2 + c_{22}E_{22}^2 + 2c_{23}E_{11}E_{22} + c_{24}E_{11}^2E_{22} + c_{25}E_{22}^2E_{11} + c_{26}E_{11}^2E_{22}^2 + c_{27}E_{11}^4 + c_{28}E_{22}^4 \end{gathered} \tag{5.3}$$

where c_{ij} are fitted parameters and E_{ii} are the axial strains.

Note that each stress component was fit with a different parameter set with an excellent fit. In all cases the biaxial protocols were fit simultaneously so that a wide region of strain states was included in the fit to avoid multiple colinearities. Stress component contours over the experimental strain plane were generated to allow direct examination of material symmetries and stress contours and to evaluate the material classification.

The results of the response function analyses were used to determine which material class (e.g. isotropic, orthotropic, transverse orthotropic) was most applicable by examining the intricacies of the contour plots. Symmetry across the $E_{11}=E_{22}$ line in a contour plot indicates isotropy, which may be modeled most efficiently with an isotropic function. Asymmetric plots, requiring an orthotropic function, were examined to determine the larger strain axis, indicated by the majority of the strain region lying to one side of the line of symmetry and larger contour gradients. The most appropriate model choice for each group was determined by examining the contour plots of each specimen and determining the dominant response.

The response functions proved useful for visualizing the stress response over a region of strain and were used for comparisons between the groups regardless of the particular strain values. Functions and data were viewed both as a three-dimensional surface plots (Figure 5-2) and as two-dimensional contour plots (Figure 5-3). In particular, the existence and direction of material axes were most apparent in the contour gradients plots, which were remarkably similar between specimens within the same group.

The goodness-of-fit was measured by the calculation of the coefficient of determination, r^2 from the regression and total sums-of-squares. It represents the fraction of variability in the data that is explained by the regression.

$$r^2 = \frac{SS_{Regression}}{SS_{Total}} = \frac{\sum_{i=1}^{n}\left(\hat{y}_i - \bar{y}\right)^2}{\sum_{i=1}^{n}\left(y_i - \bar{y}\right)^2} \tag{5.4}$$

Student t-test was used to determine differences between groups, with significance taken at $p<0.05$.

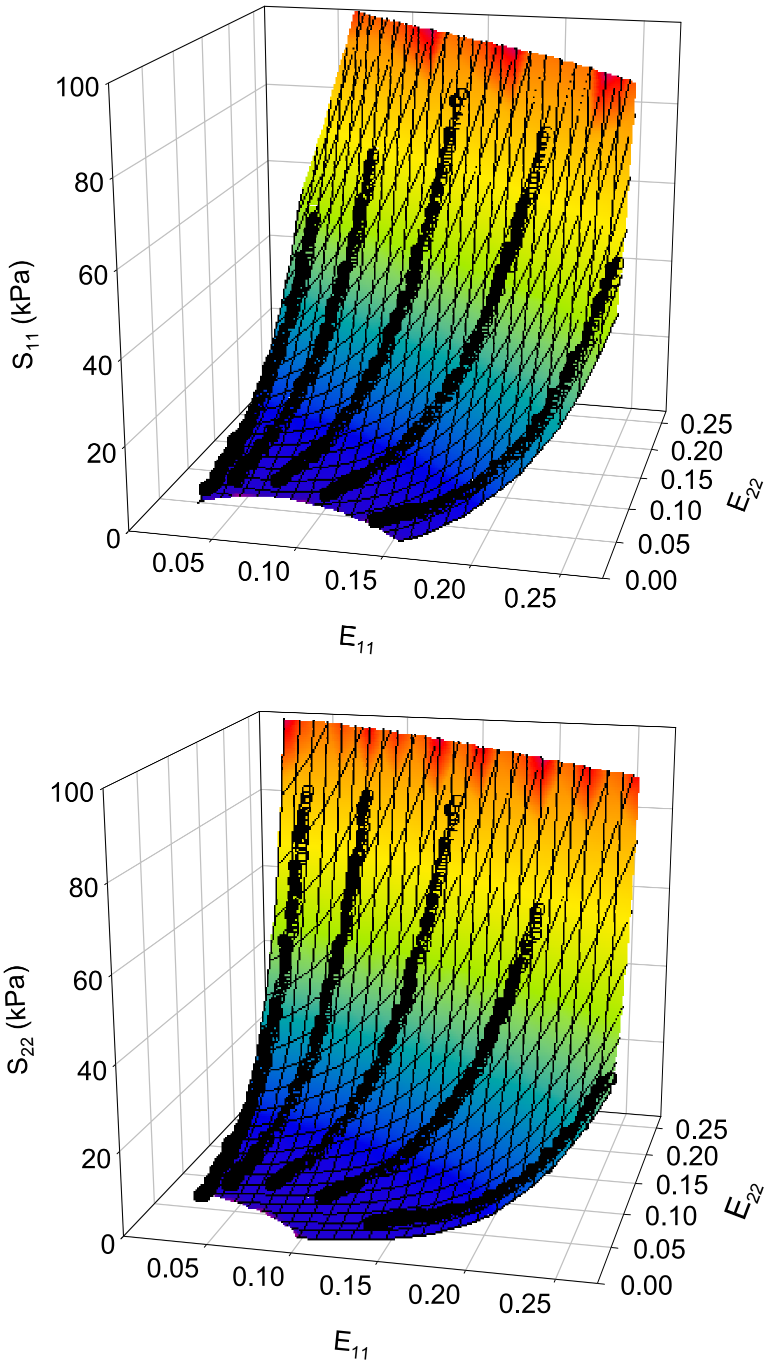

Figure 5-2 Surface plots of the interpolated stress components for the normal bladder wall, demonstrating the fidelity of the 18-parameter interpolation function set. Circles represent the actual, unsmoothed data while the interpolation is represented by the surface. Filled circles represent data just above the surface, unfilled circles are data below the surface, and partially filled circles represent data on the surface. Units of strain are length/length.

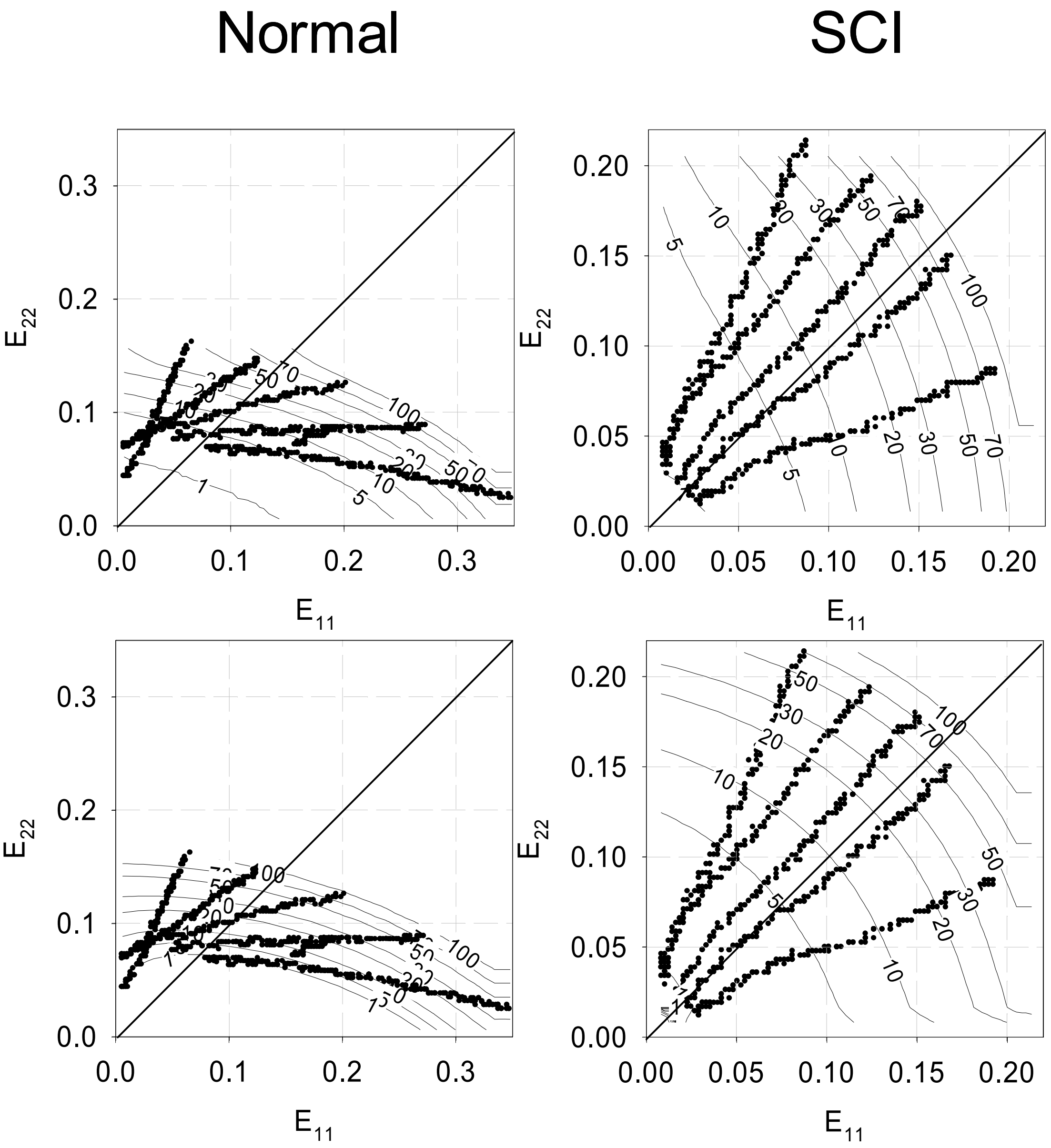

Figure 5-3 Stress contours for normal (left) and spinal cord injured (right) rat bladder wall, along with the actual strain values. Solid diagonal lines are the $E_{11}=E_{22}$ identity, which is shown for visual reference. Strain units are length/length.

For the normal specimens, there was marked lack of symmetry across the $E_{11}=E_{22}$ line, with the material axes strongly aligned to the x_1 stretch axes (Figure 5-3). Further, the distance between the contours was narrowed near the E_{11} axis compared to the E_{22} axis, indicating a strong dependence of W on E_{11}. Conversely, the SCI samples exhibited a weak dependence or no dependence, with symmetry at the equi-strain line in seven out of eight samples. It was determined that the SCI group belongs to an isotropic material classification and normal bladder wall is orthotropic. These results were used to guide the form of the constitutive model, as described in the following

5.2.2 Constitutive Model

Validation of the observed material classes was performed by fitting the biaxial mechanical data from both groups to isotropic and orthotropic models. The first model was an isotropic exponential function of the first strain invariant I_1 of the strain tensor **C.**

$$W = c_0\left[\exp\left(c_1(I_1 - 3)\right) - 1\right] \tag{5.5}$$

where c_i are constants, W is the strain energy, and I_1 is the first strain invariant.

A Fung-type second-order orthotropic model composed the second model.

$$W = \frac{c_0}{2}\exp Q \tag{5.6}$$

$$Q = c_1E_{11}^2 + c_2E_{22}^2 + 2c_3E_{11}E_{22} \tag{5.7}$$

where E_{ii} are the axial strains and c_i are the parameters.

5.2.3 Normal Bladder Wall Model Fit

Not surprisingly, normal bladder wall was not fit well to the isotropic model (mean individual fit r^2=0.496, Table 5-1). In addition, parameters displayed no statistical significance when the goodness of fit was low. In contrast, the normal samples attained an adequate fit (mean r^2=0.836) for the orthotropic model (Table 5-2). Graphically, the normal bladder wall fit poorly to the isotropic model and well to the orthotropic model (Figure 5-3). As expected, the orthotropic fit appeared graphically worse in the protocols with the higher E_{11} stress, 100 kPa : 50 kPa and 100 kPa : 75 kPa.

Table 5-1 Parameters and r^2 values from all data to all normal samples, showing individual sample fits for the isotropic model. All parameters for all specimens are significantly different from zero with a p-value of less than 0.05 are marked with an asterisk (*).

	Isotropic Fit (Equation (5.5))		
Sample	**c_0**	**c_1**	**r^2**
1	*0.297	*12.455	0.836
2	*1.372	*8.115	0.565
3	*0.819	*8.336	0.707
4	*2.900	*9.411	0.567
5	38.691	0.933	0.132
6	*0.218	*9.546	0.791
7	*2.291	*4.948	0.444
8	*1.169	*8.941	0.459
9	12.704	*1.660	0.147
10	*3.524	*4.503	0.312
Mean	6.398	6.885	**0.496**
SEM	3.770	1.176	**0.078**

Table 5-2 Parameters and r^2 values from all data to all normal samples, showing individual sample fits for the orthotropic model. All parameters for all specimens are significantly different from zero with a p-value of less than 0.05 are marked with an asterisk (*).

	Orthotropic Fit (Equations (5.6) and (5.7))					
Sample	c_0	c_1	c_2	c_3	c_1/c_2	r^2
1	*1.172	*28.998	*39.912	*16.071	0.727	0.943
	*2.867	*89.086	*23.612	*28.898	3.773	0.936
3	*2.266	*19.453	*36.022	*14.076	0.540	0.931
4	*1.806	*50.311	*109.024	*48.564	0.461	0.918
5	*2.425	*33.676	*253.774	*62.527	0.133	0.824
6	*1.001	*24.711	*23.775	*8.775	1.039	0.839
7	*0.711	*24.678	*97.757	*10.820	0.252	0.803
8	*0.315	*60.729	*145.147	-2.817	0.418	0.697
9	*2.118	*15.936	*142.673	*28.598	0.112	0.746
10	*0.881	*30.532	*100.656	*8.475	0.303	0.719
Mean	1.556	37.811	97.235	22.399	0.776	**0.836**
SEM	0.269	7.163	22.819	6.355	0.345	**0.030**

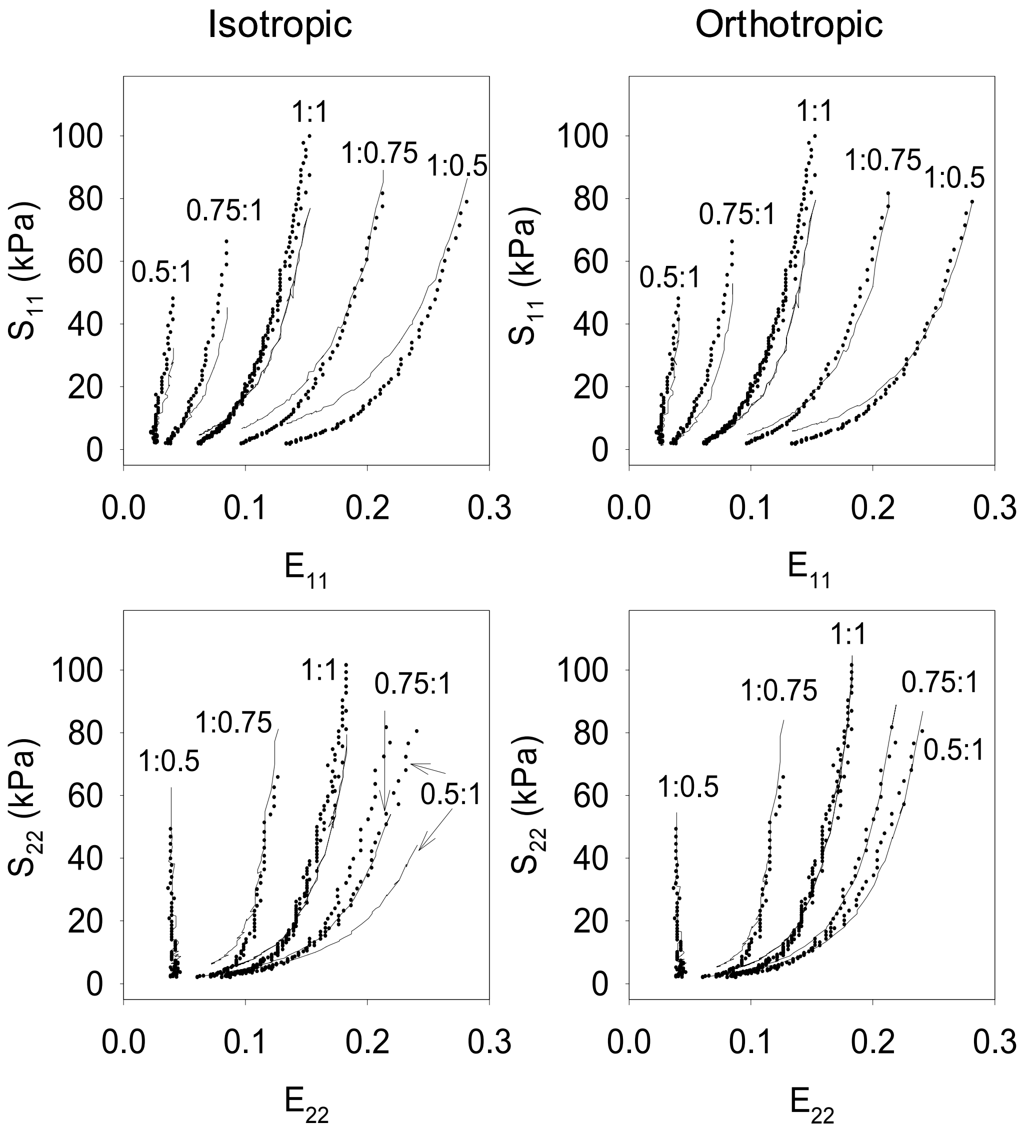

Figure 5-4 Comparison of isotropic and orthotropic functions for a normal bladder specimen (sample number 1 in Table 5-1 and Table 5-2) for all biaxial testing protocols. Equation (5.5) was used for the isotropic fit, and equations (5.6) and (5.7) for the orthotropic fit. Note the discrepancy of the isotropic model was mainly exhibited in the more extreme test protocols. Strain units are length/length.

Since the material direction was along the x_1 axis and high stress gradients in this direction, an additional higher-order term containing E_{11} (e.g. $E_{11}^2\ E_{22}$) was required to better fit the normal group response. An additional modification of equation (5.7) was thus made to test this hypothesis. Further, since the addition of any term would increase the degree of freedom for the model, and thus the quality of the fit without necessarily producing an optimal form, another model containing a $E_{11}\ E_{22}^2$ term was also applied. Thus, the two additional orthotropic models test were

$$Q' = c_1E_{11}^2 + c_2E_{22}^2 + 2c_3E_{11}E_{22} + c_4E_{11}E_{22}^2 \tag{5.8}$$

$$Q'' = c_1E_{11}^2 + c_2E_{22}^2 + 2c_3E_{11}E_{22} + c_5E_{11}^2E_{22} \tag{5.9}$$

As expected, either additional term to the orthotropic fit for the normal specimens increased the goodness of fit over the original equation (5.7) (Table 5-3 and Table 5-4). However, each model resulted in different increases in the quality of fit. The addition of the $E_{11}^2\ E_{22}$ term (mean r^2=0.982) increased the fit substantially as compared to the corresponding $E_{11}\ E_{22}^2$ term (mean r^2=0.920) from an initial mean r^2=0.836 for the 4-parameter model. Hence the $E_{11}^2\ E_{22}$ term resulted in an average fit 7.1% better than the $E_{11}\ E_{22}^2$ term.

Table 5-3 Orthotropic model applied to the normal group plus the separate addition of terms as from equations (5.6) and (5.8). All parameters for all specimens are significantly different from zero with a p-value of less than 0.05 are marked with an asterisk (*).

	Orthotropic+$E_{11}E_{22}^2$ term (Equation (5.8))						
Sample	**c_0**	**c_1**	**c_2**	**c_3**	**c_4**	**c_1/c_2**	**r^2**
1	*0.34	*41.14	*25.9	*14.62	*-109.3	1.59	0.973
2	*0.15	*73.02	*134.8	21.1	*-321.6	0.54	0.969
3	*0.32	*26.37	*92.8	*22.24	*-82.5	0.28	0.964
4	*0.90	*16.35	*145.1	*39.63	*-47.7	0.11	0.962
5	*1.39	*103.4	*23.9	*28.82	*-66.8	4.33	0.917
6	*0.43	*33.29	*95.6	*19.24	*-110.4	0.35	0.922
7	*1.03	*20.10	*35.7	*18.15	*-27.8	0.56	0.897
8	*0.08	*83.75	*169.9	*1.67	*-244.9	0.49	0.847
9	*0.88	*50.36	*107.9	*56.84	*-111.2	0.47	0.879
10	*1.06	*34.23	*251.3	*84.35	*-132.0	0.14	0.870
Mean	0.66	48.21	108.3	30.67	-125.4	0.89	0.920
SEM	0.14	9.24	22.6	7.60	28.7	0.40	0.015

Table 5-4 Orthotropic model applied to the normal group plus the separate addition of terms as from equations (5.6) and (5.9). All parameters for all specimens are significantly different from zero with a p-value of less than 0.05 are marked with an asterisk (*).

	Orthotropic+$E_{22}E_{11}^2$ term (Equation (5.9))						
Sample	c_0	c_1	c_2	c_3	c_5	c_1/c_2	r^2
1	*0.64	*28.90	*38.0	*13.11	*30.5	0.76	0.990
2	0.88	*58.58	*27.1	*71.48	*-262.6	2.17	0.992
3	*1.06	*20.12	*38.7	*15.28	*-25.6	0.52	0.989
4	*0.98	*48.78	*103.7	*43.89	*116.8	0.47	0.989
5	*1.21	*33.68	*253.7	*62.54	*0.6	0.13	0.983
6	*0.25	*17.34	*29.8	*30.51	*-125.2	0.58	0.986
7	*0.40	*24.45	91.2	*6.90	*68.1	0.27	0.975
8	*0.13	*59.33	*154.2	*8.77	*-155.7	0.38	0.975
9	*0.97	*16.38	*138.0	*30.94	*100.0	0.12	0.971
10	*0.49	*30.44	*96.2	*4.89	*53.3	0.32	0.965
Mean	0.70	33.80	97.0	28.83	-20.0	0.57	0.982
SEM	0.12	5.14	22.6	7.51	39.1	0.19	0.003

5.2.4 Normal Bladder Wall Prediction

The prediction abilities of this model were evaluated by fitting the inner three protocols (0.75:1, 1:1, and 1:0.75 stress ratios) to the orthotropic model described by Eqns. (5.6) and (5.7). The resulting parameters were then used to generate the fitted stress values for all five protocols.

The r^2 values were slightly better when the two extreme protocols were removed from the fit (Table 5-2) and the visual match of the fit to the data was almost as good as that obtained from the same fit to all five protocols (Figure 5-5). The c_1/c_2 ratio was closer to one, indicating that the anisotropy is more extreme in the outer two protocols.

Table 5-5 Orthotropic model of Eqns. (5.6) and (5.7) applied to the middle three protocols of all 10 normal samples. Mean and SEM shown.

Parameter	**Five protocols**	**Three protocols**
c_0	1.556 (0.27)	1.655 (0.25)
c_1	37.811 (7.16)	42.825 (10.11)
c_2	97.235 (22.82)	94.475 (23.57)
c_3	22.399 (6.36)	18.729 (5.44)
c_1/c_2	0.776 (0.35)	0.923 (0.44)
r_2	**0.836 (0.03)**	**0.853 (0.027)**

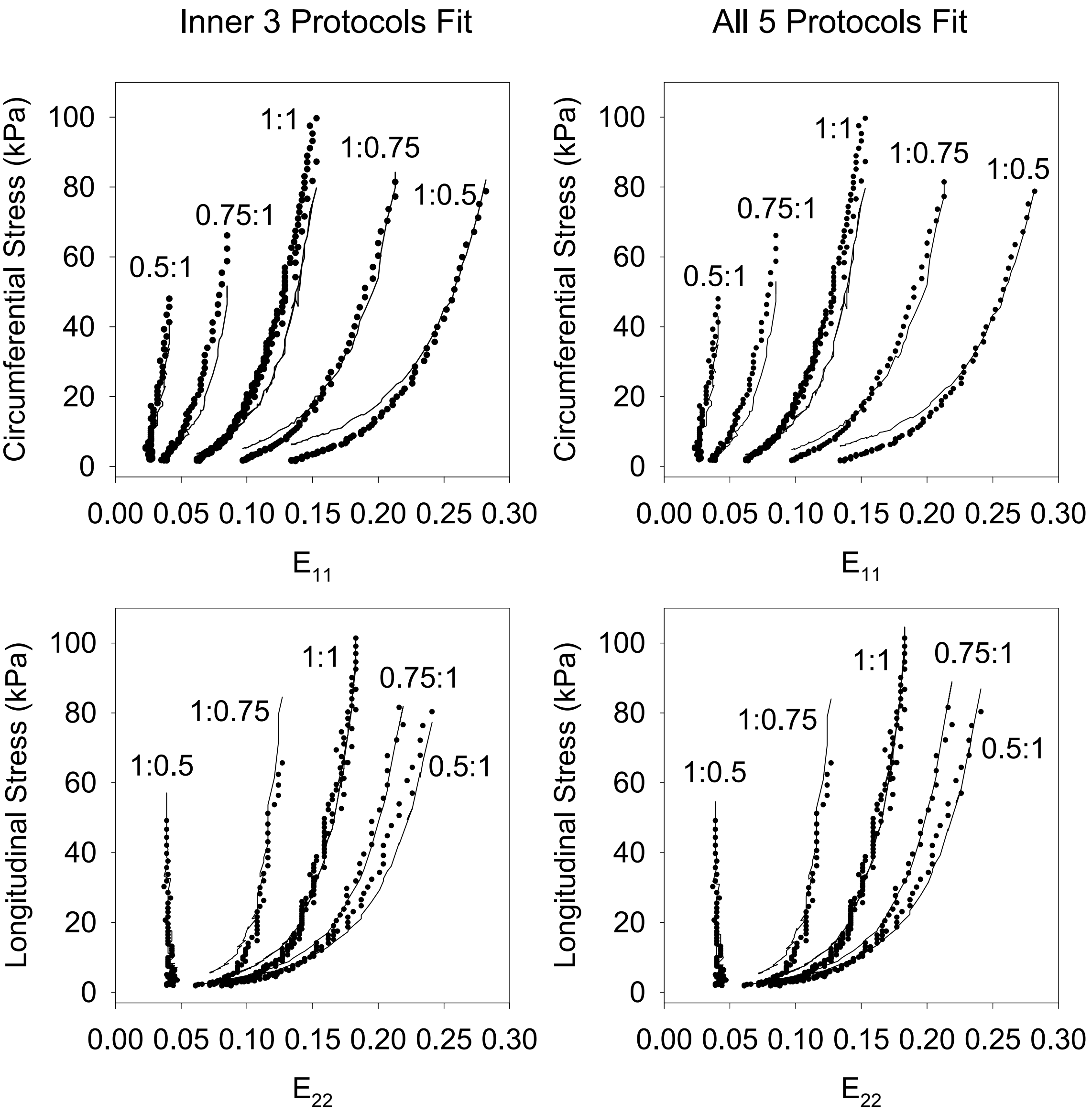

Figure 5-5 Orthotropic fit to normal bladder wall tissue data using inner 3 protocols (left) and all five protocols (right).

5.2.5 SCI Bladder Wall Model Fit

In contrast to the normal tissue response, the SCI bladder tissue was fit well with the isotropic model (Figure 5-6), with a mean of r^2=0.837 (Table 5-6). The two additional parameters in the orthotropic model increased the goodness of fit (mean r^2=0.938). A representative sample shown in Figure 5-6 (sample 6 in Table 5-6) was fit quite well by the isotropic model, though the orthotropic model fit it better since it has more parameters. In addition, all parameters for both models were significant with a p-value below 0.05.

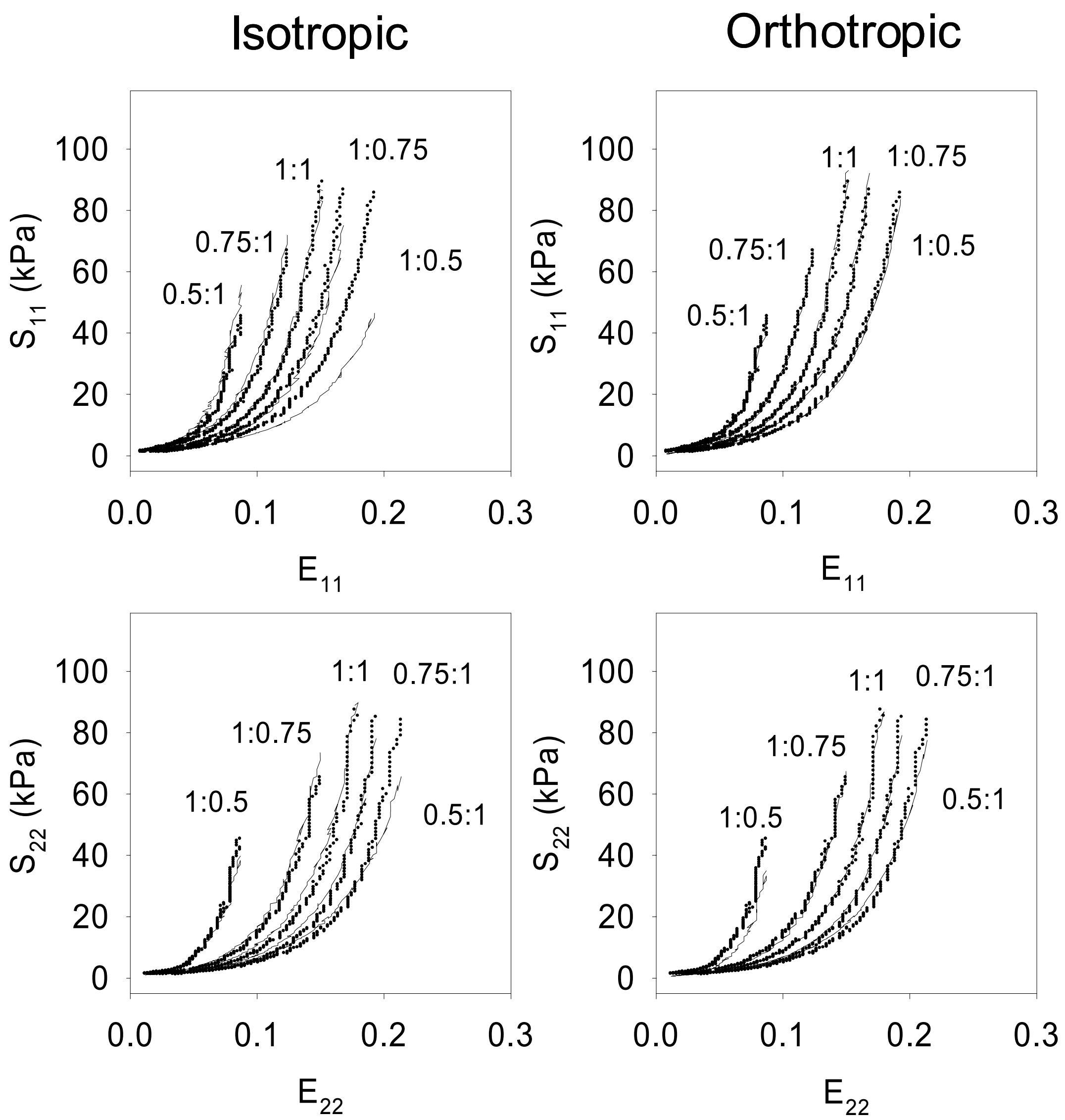

Figure 5-6 Graphical comparison of isotropic and orthotropic strain energy functions for a SCI bladder specimen (sample number 6 in Table 5-6), using all protocols and equation (5.5) for the isotropic function, and equations (5.6) and (5.7) for the orthotropic function. Strain units are length/length.

Table 5-6 Parameters and r^2 values from all data to all SCI samples, showing individual sample fits for the isotropic models. All parameters for all specimens are significantly different from zero with a p-value of less than 0.05.

	Isotropic Fit (Equation (5.5))		
Sample	**c_0**	**c_1**	**r^2**
1	0.059	17.092	0.913
2	0.683	4.786	0.588
3	0.032	11.665	0.865
4	0.100	8.661	0.795
5	0.123	7.673	0.909
6	0.425	12.068	0.928
7	0.347	6.821	0.822
8	0.081	9.386	0.874
Mean	0.231	9.769	**0.837**
SEM	0.082	1.348	**0.039**

Table 5-7 Parameters and r^2 values from all data to all SCI samples, showing individual sample fits for the orthotropic model. All parameters for all specimens are significantly different from zero with a p-value of less than 0.05.

	Orthotropic Fit (Equations (5.6) and (5.7))					
Sample	c_0	c_1	c_2	c_3	c_1/c_2	r^2
1	0.320	99.534	66.187	-16.787	1.504	0.983
2	0.680	15.102	53.103	-1.380	0.284	0.860
3	0.108	60.335	58.823	-17.829	1.026	0.946
4	0.189	32.663	70.708	-11.899	0.462	0.941
5	0.836	27.505	25.979	-4.643	1.059	0.977
6	2.105	46.936	37.138	3.582	1.264	0.989
7	2.020	23.209	20.845	-1.302	1.113	0.878
8	0.568	33.835	30.058	-3.637	1.126	0.926
Mean	0.853	42.390	45.355	-6.737	0.980	**0.938**
SEM	0.278	9.553	6.808	2.769	0.144	**0.017**

As the parameters for c_1 and c_2 were similar for the SCI bladder wall tissue in the orthotropic model, the SCI data were also fit to the following isotropic model with two fit parameters, where

$$Q''' = c_1(E_{11}^2 + E_{22}^2) + 2c_3E_{11}E_{22} \tag{5.10}$$

The fit to this model was slightly better than the strain-invariant isotropic invariant model, with average r^2=0.871 (Table 5-8).

Table 5-8 Parameters and r^2 values from all data to all SCI samples, showing individual sample fits for the 3-parameter orthotropic model. All parameters for all specimens were significantly different from zero with a p-value of less than 0.05.

	Three-parameter Orthotropic Model (Eqn.(5.10)			
Sample	c_0	c_1	c_3	r^2
1	0.517	41.107	15.482	0.919
2	4.714	6.151	7.207	0.594
3	0.108	58.346	-16.599	0.945
4	0.945	12.185	12.086	0.795
5	0.850	26.153	-4.158	0.973
6	2.682	33.855	7.600	0.951
7	1.925	20.309	0.591	0.873
8	0.557	28.110	0.190	0.917
Mean	1.537	28.277	2.800	**0.871**
SEM	0.541	5.850	3.600	**0.044**

The ratio of the parameters c_1/c_2 can be used as an index of anisotropy.(84) In the normal group this ratio was 0.443 (Table 5-1). As discussed previously, the equibiaxial protocol alone results in mean stress-strain curves that are nearly isotropic, as seen in Figure 5-4. In the SCI group, this ratio was close to 1, which is indicative of a material response nearer to isotropic (Table 5-7). This result supports our overall observations that the bladder wall experiences a change in material class, which was not observable by the equibiaxial stress data alone (Figure 3-56).

The three 14-day SCI samples were also fit to the orthotropic function. The fits of these three samples were not as good as the fits to the 10-day samples. Additionally, the c_1/c_2 ratio was further from one in the 14-day samples, indicating more anisotropy in these samples. It is possible that these samples are becoming more anisotropic through time after spinal cord injury. However, as was previously mentioned in section 3.0, these three samples were some of the first tested and the protocol used was not identical. These three samples were tested to a maximum load instead of a strain, and the samples were not sectioned as squares, but were all three rectangles. Therefore, they did not undergo the same stresses and it is likely that some of the differences seen in the results are artifacts of the different testing methods.

Table 5-9 Orthotropic fit to all five protocols of the three 14-day SCI samples. Mean and (SEM) shown.

Parameter	**10 day SCI**	**14-day SCI**
c_0	0.853 (0.28)	0.654 (0.40)
c_1	42.390 (9.55)	11.575 (4.44)
c_2	45.355 (6.81)	16.116 (1.86)
c_3	-6.737 (2.77)	2.410 (2.46)
c_1/c_2	0.980 (0.14)	0.697 (0.24)
r_2	**0.938 (0.02)**	**0.817 (0.05)**

5.2.6 SCI Bladder Wall Model Prediction

As in the normal bladder wall prediction, the prediction abilities of this model were evaluated by fitting the inner three protocols (0.75:1, 1:1, and 1:0.75 stress ratios) to the orthotropic model described by Eqns. (5.6) and (5.7). The resulting parameters were then used to generate the fitted stress values for all five protocols.

The r^2 values were slightly better when the two extreme protocols were removed from the fit (Table 5-10) and the visual match of the fit to the data was almost as good as that obtained from the same fit to all five protocols (Figure 5-7). The parameters and c_1/c_2 ratio are not different between the two groups, indicating that the addition of the two extreme protocols does not introduce much additional information to the model fit.

Table 5-10 Orthotropic model of Eqns. (5.6) and (5.7) applied to the middle three protocols of all 8 SCI samples. Mean and SEM shown.

Parameter	**Five protocols**	**Three protocols**
c_0	0.853 (0.28)	0.856 (0.28)
c_1	42.390 (9.55)	42.565 (9.70)
c_2	45.355 (6.81)	44.713 (7.41)
c_3	-6.737 (2.77)	-6.860 (3.43)
c_1/c_2	0.980 (0.14)	1.008 (0.14)
r_2	**0.938 (0.02)**	**0.953 (0.02)**

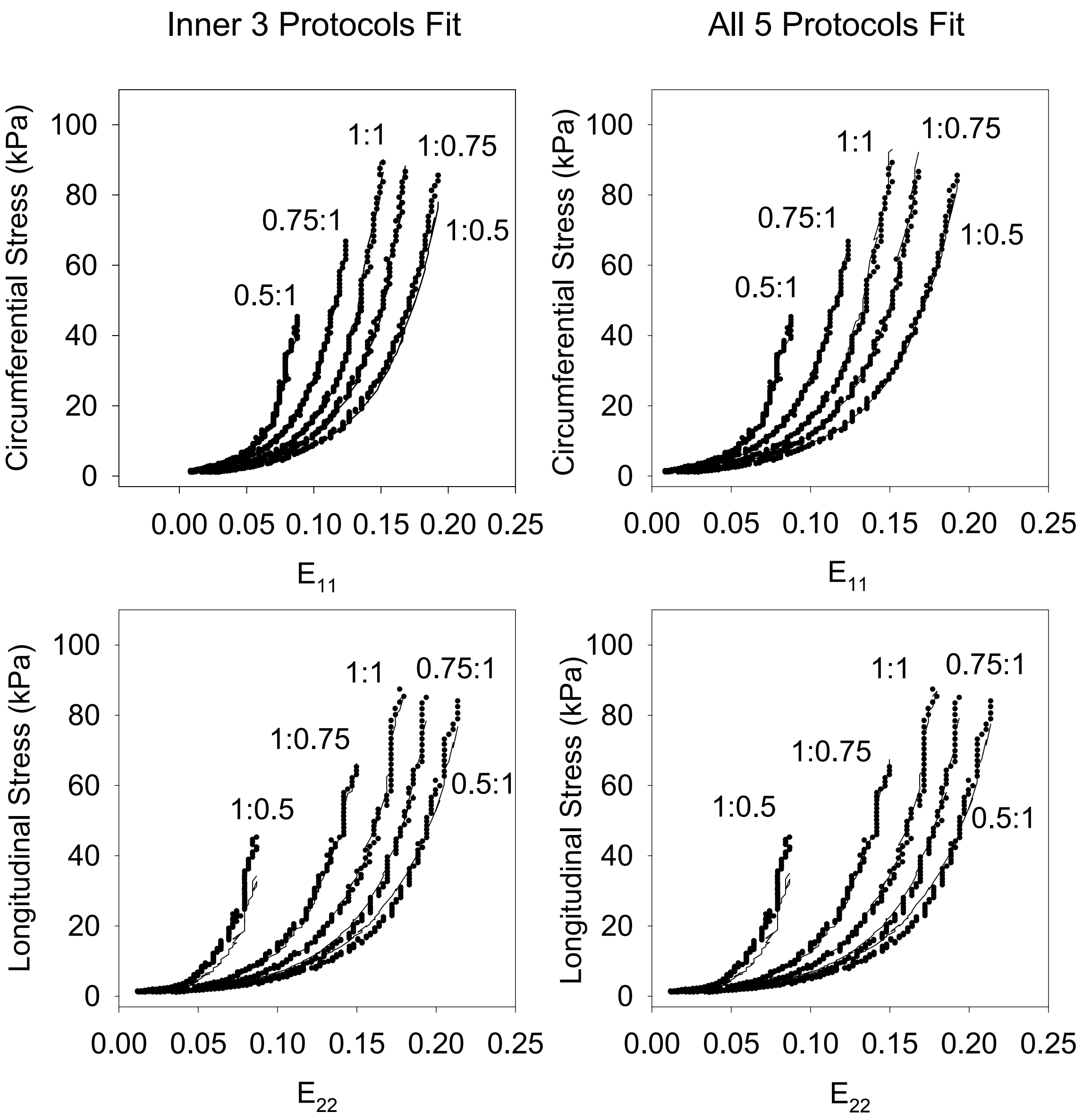

Figure 5-7 Orthotropic fit to inner three protocols (left) and all 5 protocols (right) for a representative SCI sample.

5.2.7 Limitations

In the current work interpolation functions were directly applied to the experimental biaxial mechanical data and were used to identify the material classification independent of the type of test control mode (i.e. stress or strain) or constitutive model choice. However, this method is valid only under the assumption of pseudoelasticity, therefore loading path or time-dependent changes were ignored. Secondly, the approach is dependent on the type of physiological strains experienced by the tissue. For example, the bladder wall experiences very large strains *in vivo* in both directions. In other tissues, a high degree anisotropy (e.g. fasica lata) would produce strains that are extremely low in one direction compared to the other. If the range is too small, additional non-physiologic or strain-controlled tests may be required to obtain sufficient data for the response function analysis.

5.2.8 Summary

To evaluate the mechanical properties of a biological tissue, physiological testing protocols that subject the tissue to realistic *in vivo* forces and deformations should be used. However, the method of analysis to be used often dictates the experimental methods and may require a non-physiological testing regimen. For example, use of a strain energy function of the strain invariants may utilize experimental protocols that directly control the strain invariants.(103) In this study, mechanical data was obtained from biaxial tests based on the physiologic-like loading states, which allowed for a thorough and straightforward experimental investigation of the biaxial mechanical response within the physiological range.

This method in selecting the appropriate constitutive model avoided the choice of misleading models based on incomplete or non-physiological responses obtained under loading conditions that are not possible *in vivo*. For example, most of the samples in the normal group (seven out of nine) and one out of eight in the SCI group demonstrated shortening. This is most likely caused by smooth muscle and collagen fiber rotations, and can be difficult to reproduce in strain control protocols. Although separate stress and strain tests could be conducted, performing only one set of tests is usually preferable because the tissue preparation and test setup is time-consuming.

This study has shown a change in material classification in the biaxial mechanical response of rat bladder wall between normal rats and ten days after SCI rats. The approach used to analyze this data is general and is useful in examining the biaxial mechanical data without assuming a material classification. Moreover, this study demonstrates that accurate characterization of the bladder wall in health and disease requires the quantification of the complete in-plane biaxial mechanical response. Otherwise erroneous modeling conclusions, such as incorrect material classification and choice of constitutive model, can result. The next step is the development of a structure-based constitutive model that can be used to determine the mechanisms and specific structural alterations in bladder wall between the normal and disease states. These mechanisms can then be studied to develop more effective treatment strategies for the bladder dysfunction associated with neurogenic disorders such as spinal cord injury and obstruction.

5.3 Quasi-linear Viscoelasticity

In the past, the modeling of bladder wall viscoelastic behavior was performed primarily with virtual models of several elements using springs and dashpots.(8,9,62) Although this approach has been shown to fit smooth muscle well, there are several drawbacks. First, the choice of the model and the number of elements it contains can drastically affect the fit of the data to the model. Second, the parameters derived from the model, though physical in nature, do not represent meaningful qualities of the material in question. For comparisons between model parameters to be made, the models must be identical. In addition, because these models use a finite number of elements, they predict a strong strain-rate dependence, while in reality soft tissue mechanics are generally strain-rate independent. To obtain strain rate independence in such models requires many elements, which can quickly become complex and cumbersome to manipulate. The quasi-linear viscoelastic (QLV) theory alleviates all these difficulties.

The QLV theory, proposed by Fung in 1972, is a generalized method for obtaining the mechanical response of a material that demonstrates hysteresis and strain history dependence.(104) As it is generally constructed from continuous functions, it is limited to only a few parameters. These parameters are also physically insightful into the tissue properties and can be compared between tissues or treatments. The QLV theory has been used successfully to model many soft tissues, including skeletal muscle, aorta, myocardium, and anterior cruciate ligament.(105-108) No QLV modeling of urinary bladder could be found in the literature, so application of this method is novel.

The QLV model specifies the history of the stress response, called the relaxation function, K(λ,t) as the product of the elastic response T(λ) and a reduced relaxation function (a history of the stress) G(t):

$$K(\lambda,t) = G(t)T(\lambda) \tag{5.11}$$

where λ is the stretch ratio (current length)/(initial length) and t is time. One important note is that this equation assumes that the effects of strain and time are separable into the equations for the elastic response, T and the reduced relaxation function, G. At best this is only an approximation, but has been acceptable for other tissues.(96)

When an infinitesimal change in stretch, δλ(τ) is superimposed on a specimen already under λ stretch in an instant of time τ, for t>τ,

$$\delta K(\lambda,t)=G(t-\tau)\frac{\partial T[\lambda(\tau)]}{\partial\lambda}\delta\lambda(\tau) \tag{5.12}$$

So that when all such small changes in λ are added together (assuming continuity), we have

$$K(\lambda,t)=\int_{-\infty}^{t}G(t-\tau)\frac{\partial T[\lambda(\tau)]}{\partial\lambda}\frac{\partial\lambda(\tau)}{\partial\tau}\partial\tau \tag{5.13}$$

Or, more simply,

$$K(\lambda,t)=\int_{-\infty}^{t}G(t-\tau)\dot{T}(\tau)\partial\tau \tag{5.14}$$

However, the lower limit must begin at experiment time 0, not -∞, so these equations must be rewritten incorporating realistic assumptions of deformation. We assume that the deformation occurs at time 0 and that stress is zero and stretch is unity for all time less than zero ($\sigma_{ij}=0$ and λ=1 for t<0). Then we consider two terms, the first representing the experimental deformation step conducted at time 0, and the second the response that occurs in the tissue from the end of that event to time t.

$$K(\lambda,t)=T(0+)G(t)+\int_{0}^{t}G(t-\tau)\frac{\partial T[\lambda(\tau)]}{\partial\tau}\partial\tau \tag{5.15}$$

If the forms of *T(λ)* and *G(t)* are continuously differentiable over time ∈ [0,∞), then the derivatives and time arguments can be switched in both terms. Further, as *G(time=0)*=1 by definition, the final equation is

$$K(\lambda,t)=T_o(\lambda)+\int_{0}^{t}T[\lambda(t-\tau)]\frac{\partial G(\tau)}{\partial\tau}\partial\tau \tag{5.16}$$

The first term in equation (5.16) is the initial stress generated by the strain step, and the second term, always negative, is the reduction in the total stress through time.

The elastic response, *T(λ)*, is a function of strain only and is time independent after the initial time of stretch. It is defined as the tensile stress generated at the instant when a step function **1**(t) is applied to the tissue. A step function (Figure 5-8a) is instantaneous in time, impossible to achieve experimentally. In practice, the loading curve is a ramp instead of a step (Figure 5-8b). The problem then is what value to take for *T(λ)*. It can be shown that if the time Δt, during which the load is applied is small enough that

$$\Delta t \left| \frac{\partial G}{\partial \tau} \right| \ll 1 \tag{5.17}$$

Then the elastic response equals the response measured at the instant the ramp loading is complete. Since the experimental system often contributes to the elastic response, making this first term erroneous, some experimentalists use the highest stress value, which occurs very quickly after Δt(108) or extrapolate the T(t=Δt) from a linear fit to the next few milliseconds of stress.(90) Generally, Δt is shifted to t=0 during analysis so that the maximum or initial stress, F_o occurs at t=0.

$$T_o(\lambda) \doteq K(\lambda, \Delta t) = F_o \tag{5.18}$$

Therefore, Eq. (5.11) reduces to

$$G(t) = \frac{T(\lambda)}{F_o} \tag{5.19}$$

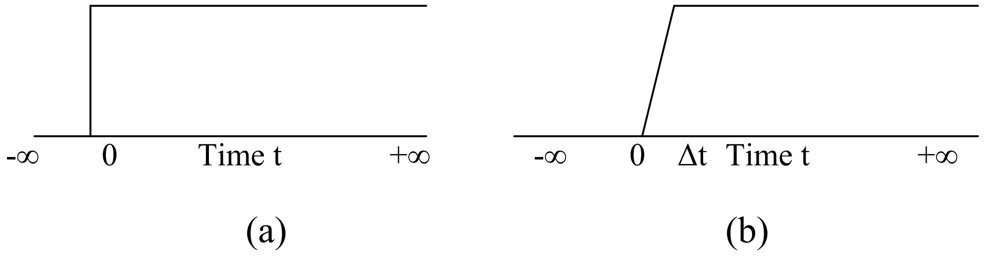

Figure 5-8 Demonstration of the ideal step function **1**(t) (a) as opposed to the experimental, realistic step function (b).

The relaxation function is defined by an appropriate decreasing function. The generalized relaxation function is

$$G(t) = \frac{1 + \int_0^{\infty} S(\tau) e^{-t/\tau} \partial\tau}{1 + \int_0^{\infty} S(\tau) \partial\tau} \tag{5.20}$$

where, S(τ) must be defined, depending on the stress response. It is well known from experimental evidence that the stress in stress relaxation curves decrease with time over most of their length, so, for example

$$S(\tau) = \frac{c}{\tau} \quad \text{for } \tau_1 \leq \tau \leq \tau_2 \tag{5.21}$$

Alternately, S(τ) could be a function of time between τ_1 and τ_2 or other forms may be defined, depending on the experimental data. Now (5.20) becomes the reduced relaxation function, *G(t)*:

$$G(t) = \frac{1 + c\left[X\left(\frac{t}{\tau_2}\right) - X\left(\frac{t}{\tau_1}\right) \right]}{1 + c\ln\left(\frac{\tau_2}{\tau_1}\right)} \tag{5.22}$$

where *X* is the exponential integral function defined as

$$X(z) = \int_0^{\infty} \frac{e^{-t}}{t} dt \quad \text{where } |\arg z| < \pi \tag{5.23}$$

The denominator of (5.22) is a simple normalizing factor obtained by taking the integral over time

$$1 + c\int_{\tau 1}^{\tau 2} \frac{1}{\tau} d\tau = 1 + c\ln\left(\frac{\tau_2}{\tau_1}\right) \tag{5.24}$$

Here c is the decay parameter, τ_1 is the fast time constant (initial slope) and τ_2 is the slow (long-term) time constant. Additionally, the parameter *G(∞)* is often important to approximate and compare between different tissues or treatments. As t approaches infinity (∞), *X(z)* becomes zero and the numerator in (5.22) becomes one so that

$$G(\infty) = \frac{1}{1 + c \ln\left(\frac{\tau_2}{\tau_1}\right)} \tag{5.25}$$

Equation (5.22) was fitted to the data collected as described in section 3.0, utilizing the genetic algorithm minimization routine (section 5.1). Equation (5.25) was used as a constraint on the three parameter values during fitting.

5.3.1 Data Thinning

As previously described, the data was collected at varying rates, with a total of 1400 points for each specimen (Figure 5-9). As the data is concentrated during the highest frequency (low times), the data fit to the QLV model would be biased to minimize the difference at those times, so the data was thinned with an exponential thinning method to end with 73 values of time (Figure 5-10 and Table 5-11). To conserve the integrity of the data, no interpolation was performed between points. That is, every thinned data point chosen is a real data point, not an altered interpolation of the points less than and greater than itself.

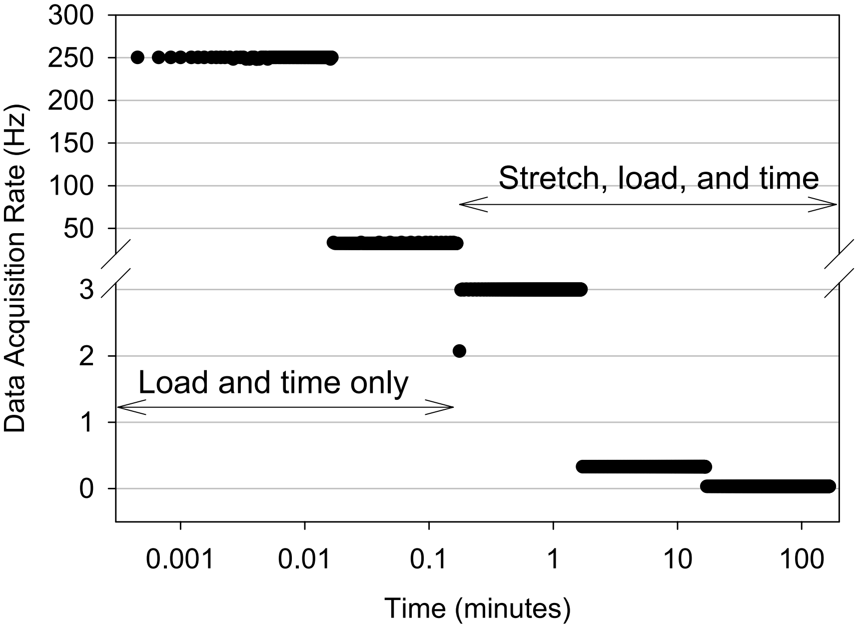

Figure 5-9 Rate of data acquisition for stress relaxation all specimens. Load and time only were recorded until 10 seconds (including loading), at acquisition rates of 250 Hz for 1 second, then at 30 Hz until 10 seconds had elapsed. After 10 seconds, strain was recorded at 3 Hz until 100 seconds, then at 0.3 Hz until 1000 seconds, then at 0.03 Hz until 10,000 seconds. Identical to Figure 3-31.

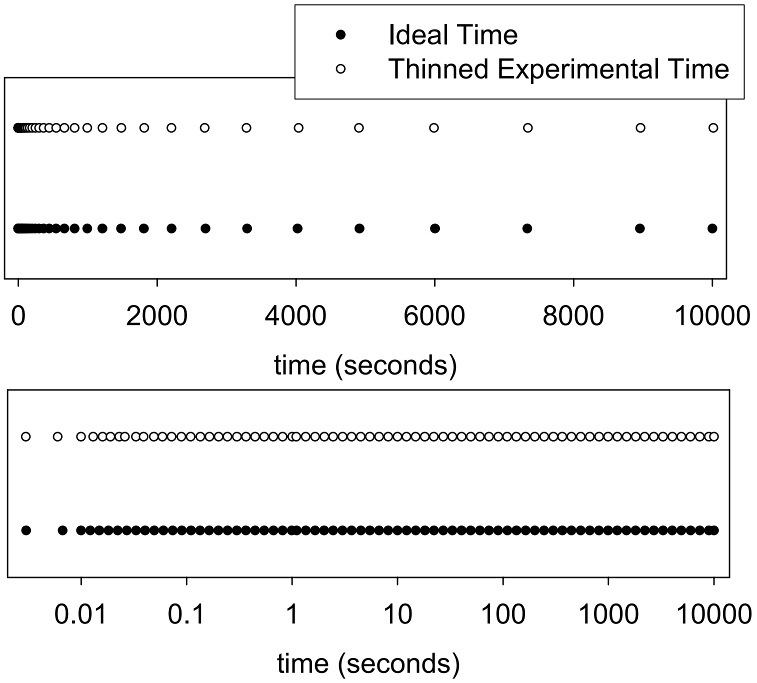

Figure 5-10 Ideal exponential time and exponentially thinned experimental time. The ideal time values are listed in Table 5-11.

Table 5-11 Exponentially spaced time values in seconds used to choose exponentially spaced data points. Comparison to the real thinned exponential time values is shown in Figure 5-10.

3.0042e-3
6.6859e-3
0.0100
0.0122
0.0149
0.0182
0.0222
0.0271
0.0331
0.0404
0.0494
0.0603
0.0737
0.0900
0.1099
0.1343
0.1640
0.2003
0.2447
0.2989
0.3650
0.4459
0.5446
0.6651
0.8124
0.9923
1.1052
1.3499
1.6487
2.0138
2.4596
3.0042
3.6693
4.4817
5.4739
6.6859
8.1662
9.9742
12.1825
14.8797
18.1741
22.1980
27.1126
33.1155
40.4473
49.4024
60.3403
73.6998
90.0171
109.9472
134.2898
164.0219
200.3368
244.6919
298.8674
365.0375
445.8578
544.5719
665.1416
812.4058
992.2747
1211.9671
1480.2999
1808.0424
2208.3480
2697.2823
3294.4681
4023.8724
4914.7688
6002.9122
7331.9735
8955.2927
10000.0000

5.3.2 QLV Model Results

All data sets were fit to the QLV model to very close agreement with r^2 values of 0.98 and higher (Table 5-12, Figure 5-11) and visually good fits (Figure 5-13 through Figure 5-15). As the parameters were different between stress levels, the amount of relaxation is not independent of stress level. Hence, equation (5.11) is not true for the normal urinary bladder wall. Additionally, close analysis of the parameter values reveals that in all samples for both axes τ_2 is actually out of the testing domain, at times three to five times the maximum time recorded. This is a clear indication of incorrect values. In addition, although the r^2 values are high, the fact that the residuals are not normally distributed, but instead have a definite pattern, is further demonstration of the inability of the QLV model to fit these data (Figure 5-12). The reason that the data do not fit the model is as yet unknown, but it is probable that the effects of stretch and time cannot be separated in this manner and that a more complex model is required.

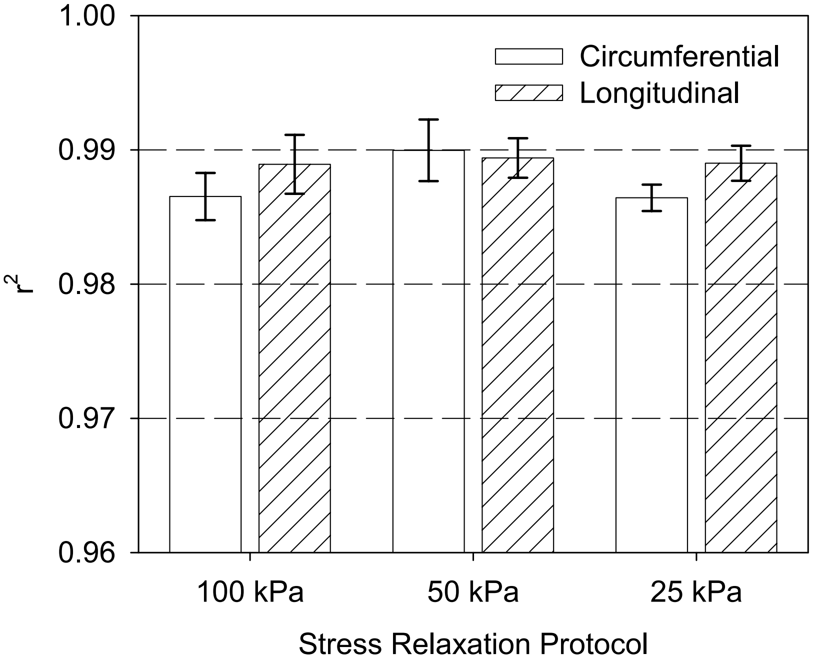

Figure 5-11 R^2 values for all groups. Mean and SEM shown.

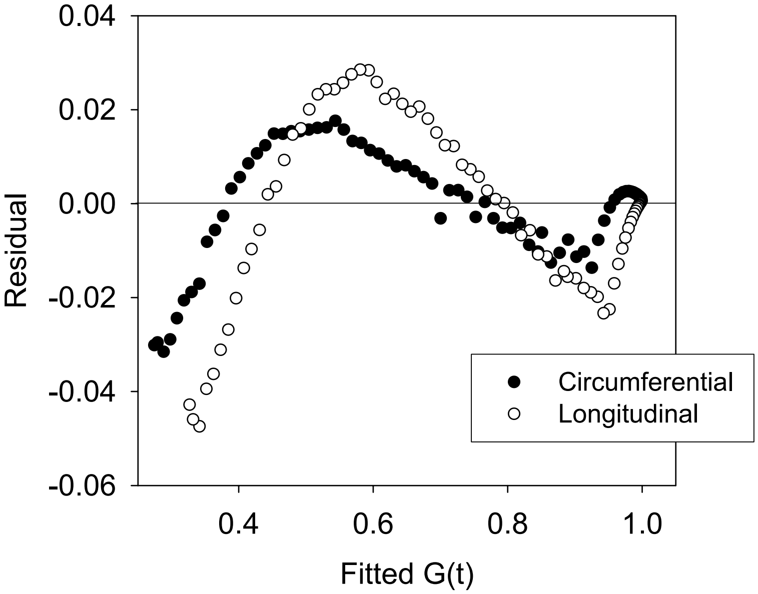

Figure 5-12 Illustration of the residuals for a typical 100 kPa sample. Since the data is not normally distributed, QLV does not model this data well.

Table 5-12 All QLV model parameter results for individual samples.

	Circumferential				Longitudinal			
Sample	c	τ_1 (sec)	τ_2 (sec)	r^2	c	τ_1 (sec)	τ_2 (sec)	r^2
100 kPa								
Bd65	0.195	0.187	39459	0.984	0.183	0.217	55274	0.986
Bd66	0.279	0.183	21516	0.985	0.230	0.311	29745	0.989
Bd67	0.249	0.480	33522	0.992	0.215	0.584	38521	0.996
Bd68	0.157	0.284	50794	0.982	0.171	0.262	49878	0.984
Bd69	0.145	0.310	50939	0.987	0.190	0.259	41406	0.987
Mean	0.205	0.289	39245	0.987	0.198	0.327	42964	0.989
SEM	0.026	0.054	5555	0.002	0.011	0.066	4451	0.002
50 kPa								
Bd70	0.509	0.210	22387	0.987	0.526	0.247	18368	0.988
Bd71	0.402	0.301	17226	0.988	0.393	0.229	16960	0.986
Bd72	0.598	0.267	12018	0.985	0.550	0.328	14985	0.987
Bd73	0.446	0.278	23388	0.990	0.472	0.231	23895	0.989
Bd74	0.349	0.429	28639	0.998	0.428	0.337	20593	0.995
Mean	0.461	0.297	20731	0.990	0.474	0.274	18960	0.989
SEM	0.043	0.036	2833	0.002	0.029	0.024	1535	0.002
25 kPa								
Bd75	0.365	0.101	4163	0.986	0.433	0.134	7138	0.990
Bd76	0.416	0.117	9788	0.984	0.457	0.127	3854	0.990
Bd77	0.354	0.122	7074	0.988	0.352	0.115	4615	0.990
Bd79	0.335	0.121	6526	0.988	0.287	0.159	7317	0.990
Bd80	0.511	0.108	10946	0.984	0.468	0.140	16081	0.983
Mean	0.396	0.114	7699	0.987	0.400	0.135	7800	0.989
SEM	0.032	0.004	1207	0.010	0.035	0.007	2178	0.001

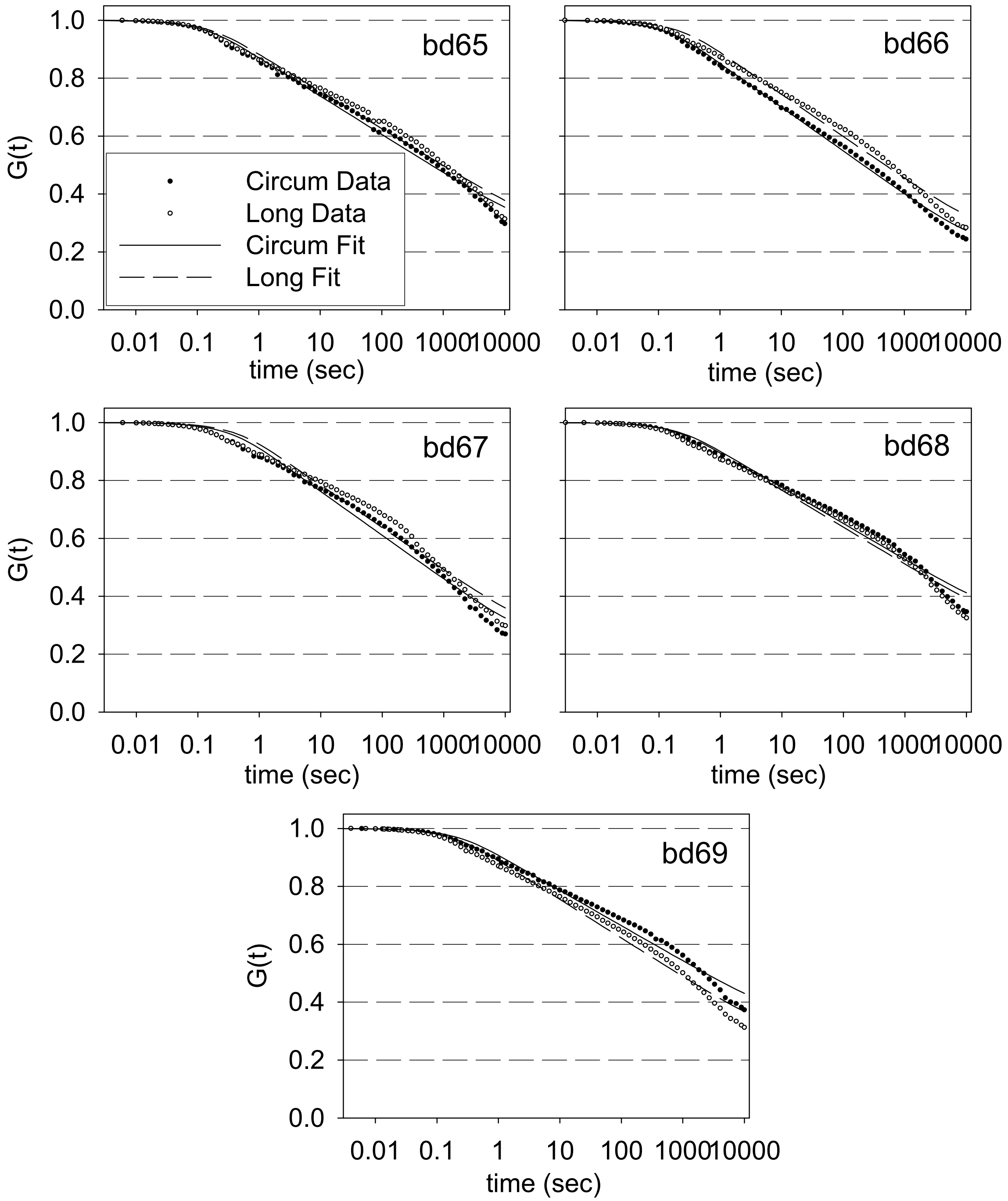

Figure 5-13 Thinned data and fit to the five samples in the 100 kPa stress relaxation protocol. Data are shown as filled and empty circles; fits are lines. All legends are identical to upper left. G(t) is unitless.

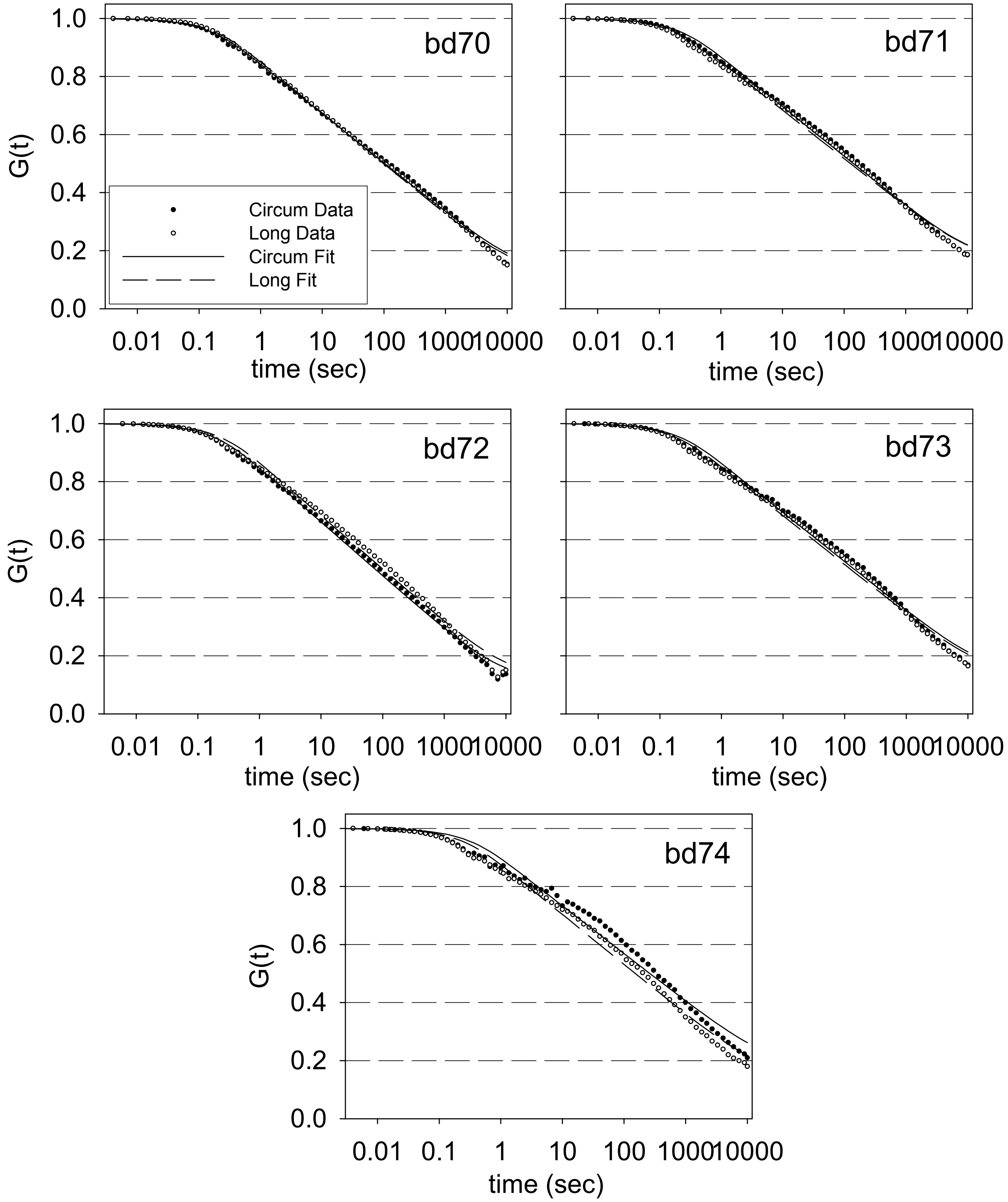

Figure 5-14 Thinned data and fit to the five samples in the 50 kPa stress relaxation protocol. Data are shown as filled and empty circles; fits are lines. All legends are identical to upper left. G(t) is unitless.

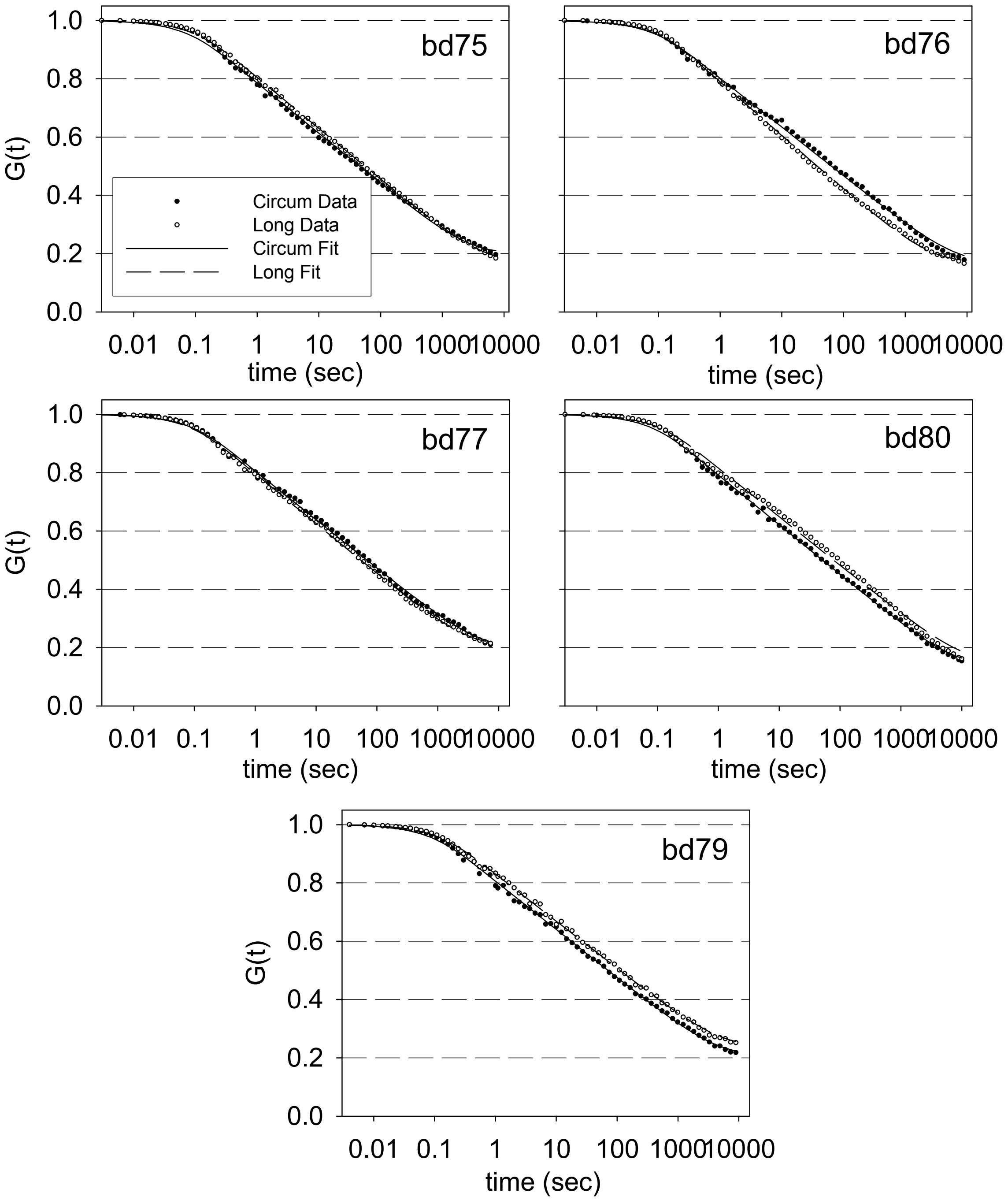

Figure 5-15 Thinned data and fit to the five samples in the 25 kPa stress relaxation protocol. Data are shown as filled and empty circles; fits are lines. All legends are identical to upper left. G(t) is unitless.

In general, the circumferential and longitudinal directions do not differ from each other by more than a standard deviation except for τ_1 in the 25 kPa stress level (Figure 5-16). The c parameter decreased with increasing stress; at 100 kPa it was half of that for the 50 and 25 kPa groups for both axes. Both τ_1 and τ_2 decreased with stress level. The τ_1 parameter was the same for the 100 and 50 kPa stress levels, and less than half that value for 25 kPa. τ_2 decreased in the same proportion as the stress level decreased.

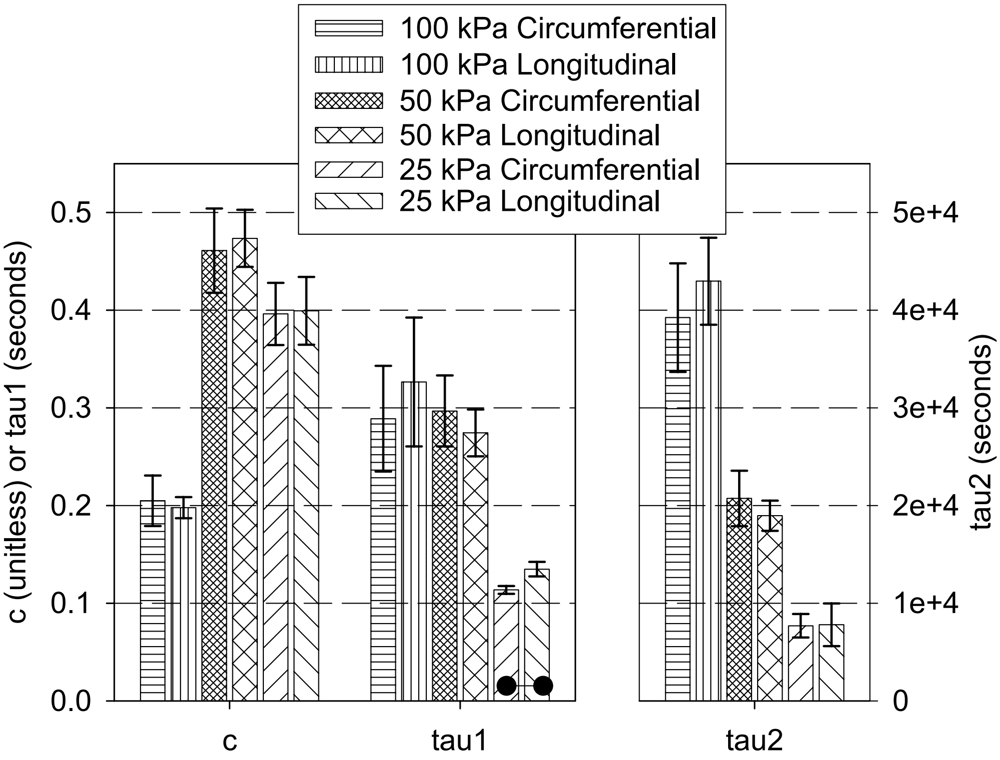

Figure 5-16 Parameter values for each of the three groups. The only significant differences between circumferential and longitudinal directions is in the value of tau1 in the 25 kPa direction, p= 0.0349. Statistical differences between stress levels are shown in Figure 5-17 and Figure 5-18. Mean and SEM shown. The barbell represents statistical difference between the two bars of the graph.

Parameter values between the stress levels were generally the same between the two axes, indicating no directional dependence (Figure 5-17 and Figure 5-18). The decay parameter c was higher in the 50 and 25 kPa protocols, indicating more relaxation in these two protocols, as was demonstrated by Figure 3-51. The initial slope of the G(t) curve, quantified by the fast time constant τ_1, demonstrates that the 100 and 50 kPa groups are similar at early times. As the three slow time constants are all statistically different from each other, the long-term behavior of the three stress levels are different.

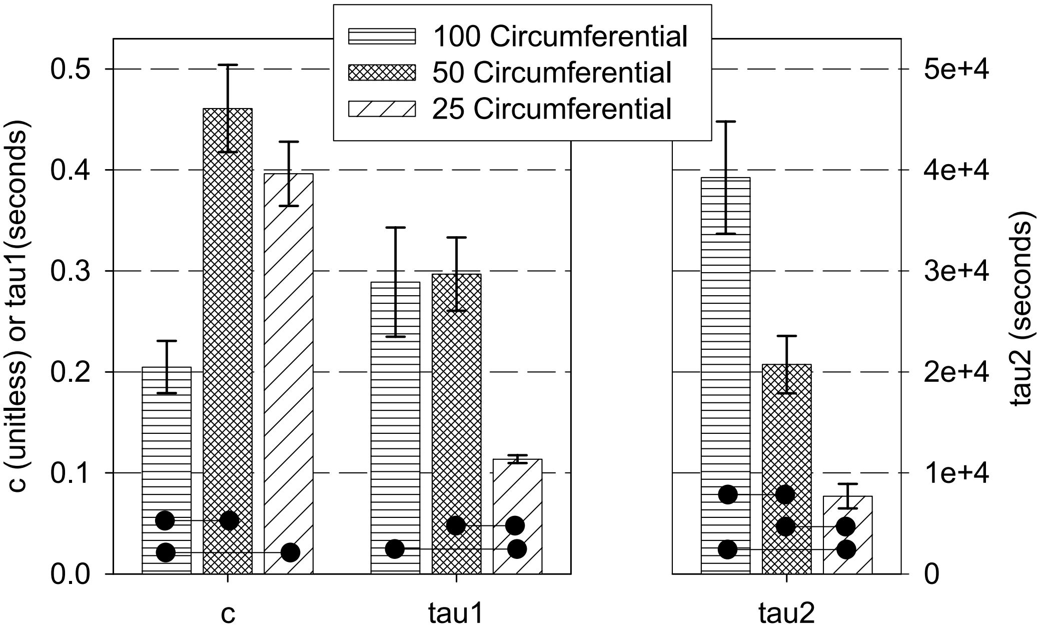

Figure 5-17 Circumferential parameter values for each of the three groups. All the statistically significant groups indicated have p<0.0179. Mean and SEM shown. The barbells represent differences between the bars.

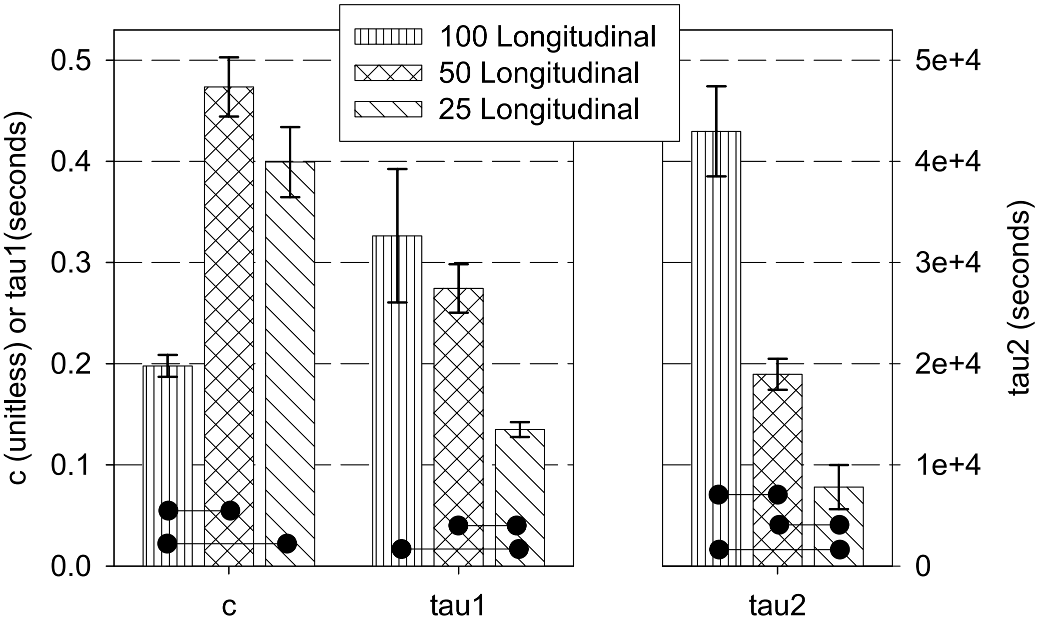

Figure 5-18 Longitudinal parameter values for each of the three groups. All the statistically significant groups indicated have $p<0.0204$. Mean and SEM shown.

5.3.3 Stiffness and Damping

As described previously, the tensile stress at any time t is the sum of the contributions of the product of the elastic response, T(λ), and reduced relaxation function, G(t).

$$K(\lambda,t) = \int_{-\infty}^{t} G(t-\tau)\frac{\partial T[\lambda(\tau)]}{\partial \lambda}\frac{\partial \lambda(\tau)}{\partial \tau}\partial(\tau) \tag{5.26}$$

If a single loading force is applied, that force is of a single frequency and can be substituted as a sinusoidal of the format

$$\begin{aligned} K(\lambda,t) &= T_0 e^{i\omega t} \\ T(\lambda(t)) &= T(\lambda(t))_0 e^{i\omega t} \end{aligned} \tag{5.27}$$

Then the current stress is a fraction of the stress due to the elastic response, a function of the reduced relaxation function. This fraction is called the complex relaxation modulus or complex modulus.(96,109) The form of the complex modulus for reduced relaxation function used here (see Equation (5.22)) is

$$M = \frac{\left[1 + \frac{c}{2}\left(\ln(1+\omega^2\tau_2^2) - \ln(1+\omega^2\tau_1^2)\right) + ic\left(\tan^{-1}(\omega\tau_2) - \tan^{-1}(\omega\tau_1)\right)\right]}{1 + c\ln\frac{\tau_2}{\tau_1}} \tag{5.28}$$

Where ω is the reciprocal of time. The second term in the numerator corresponds to the frequency stiffness and the third, imaginary term corresponds to the frequency damping. From these the stiffness and damping curves were calculated using the mean time constants for both axes and all protocols.

The curves are shown in Figure 5-19 and Figure 5-20. Note that the points indicate the real experimental time values (Figure 5-10). The time values at the two points at the far left, 1,000,000 and 100,000, were added to complete the curves as the stress relaxation was not long enough to collect these points. Little difference between directions was observed in either the stiffness or damping curves. The stiffness curve shifted towards smaller frequencies (larger times) and the slope decreased slightly with increasing stress level (Figure 5-19). This indicates that larger stresses have larger stiffness, resulting in less relaxation. Similarly, the damping curve also shifted down and to smaller frequencies with increasing stress, demonstrating that the maximum damping occurred at over a range of smaller frequencies (Figure 5-20).

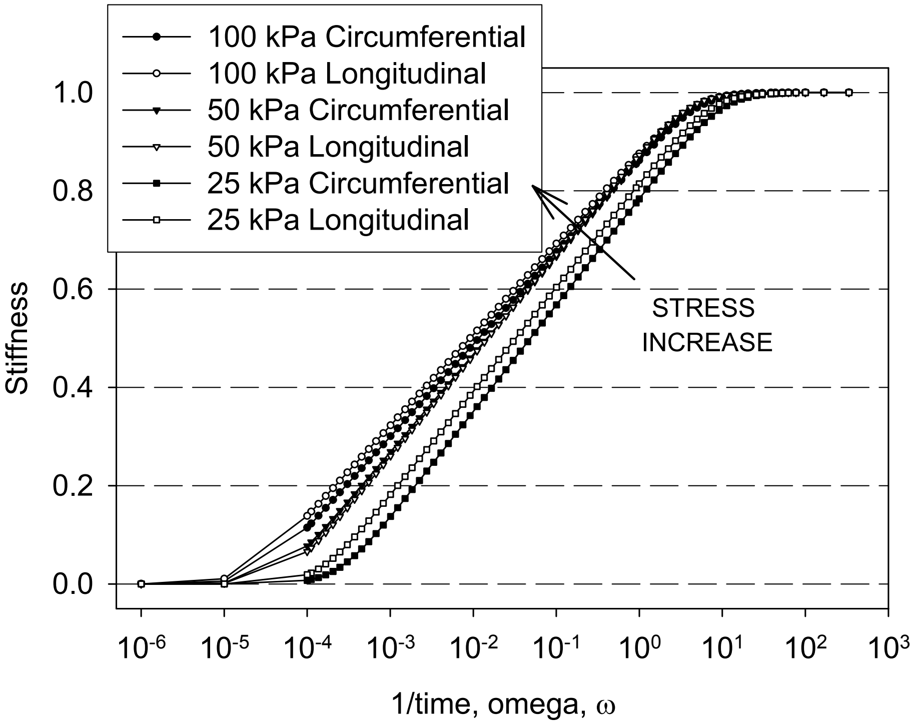

Figure 5-19 Stiffness (unitless) curves for all protocols and both axes.

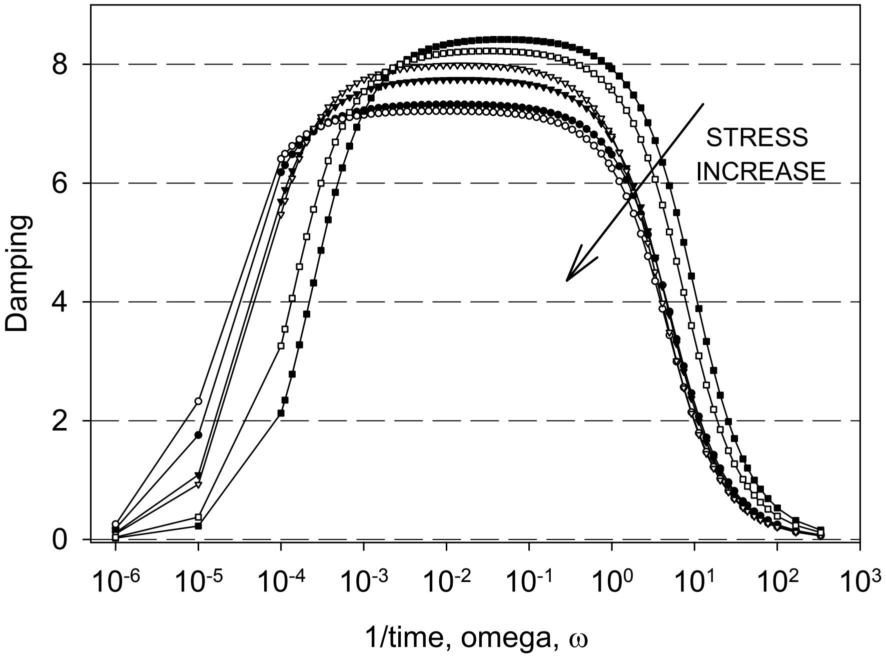

Figure 5-20 Damping (unitless) curves for all protocols and both axes. Legend is identical to that of Figure 5-19 above.

6.0 SUMMARY AND CONCLUSION

In this work, experimental protocols and analysis techniques have been developed to provide a thorough analysis of the urinary bladder wall.

Sections 1.0 and 2.0 described what is currently known about the anatomy, the mechanics, and structure of the bladder. This knowledge does not include rigorous analyses of either the mechanical properties or the structure that are responsible for the behavior of the bladder at a tissue level, so vital to understanding and predicting changes in bladder function after disease.

Section 3.0 detailed the experimental and analytical procedures developed and used to analyze the bladder wall using a rat model. The mechanical response of bladder wall to quasi-static loading was determined, and the bladder wall was found to be insensitive to strain rate over three orders of magnitude. As in other soft tissues, there was a difference in mechanical response in room temperature and under un-oxygenated conditions compared to an oxygenated body temperature environment. Additionally, the behavior of spinal cord injured (SCI) bladder wall was different from that of the normal bladder wall. SCI bladders were much more isotropic and more compliant than the control samples. (Differences in mechanical behavior between normal and SCI rat bladder were published in May of 2002 in *The Journal of Urology*.(86)) Time-dependent testing to three maximum stress levels also showed a significant stress-level dependence on the stress relaxation properties of the bladder wall, and a decrease in total relaxation at higher stresses. (Stress relaxation data and QLV modeling will be presented in a journal article submitted later this year.)

Section 4.0 detailed the development of a MatLAB-based analysis for determining the direction and volume of the connective tissue and cellular components through the thickness of the bladder wall. The stacks of *en face* images were obtained through the use of digital volumetric imaging. Standard histology slides and scanning electron microscopy were also employed for obtaining images. This information forms the basis of a quantitative analysis of the bladder wall.

In section 5.0, the mechanical behavior data were integrated into predictive models. Models developed for the quasi-static data demonstrated that the material classification for the normal and SCI data groups were fundamentally different, underscoring the existence of rapid changes in structure only 10 days after spinal cord injury. (The results of this modeling study were accepted for publication in the *Journal of Biomechanics* in December of 2002.(102)) Additionally, although the quasi-linear viscoelastic (QLV) produced a high r^2 value, the model residuals were a clear indication that QLV does not model rat bladder wall.

6.1 Normal Bladder Mechanical Behavior and Modeling

6.1.1 Directional Differences

In various tests, there was a difference observed between the responses of the circumferential and longitudinal anatomic directions. In both the shorter quasi-static tests (room temperature and physiologic environment), the mechanical response was not statistically different from isotropic during the equibiaxial runs. In the non-equibiaxial runs, the longitudinal direction showed passive contraction, or shortening, in most samples, while the circumferential direction did not demonstrate this response. Additionally, in the slow-loading quasi-static experiment and the intact organ filling experiment, the circumferential response resulted in a significantly higher stretch than the longitudinal direction. The preconditioned stretches in nearly all the tests were higher in the circumferential direction than in the longitudinal direction, and the hysteresis values were lower (Figure 3-21).

A possible explanation for this lies in evidence of three distinct layers in the detrusor muscle layer of the bladder wall.(10) Since the connective tissue is arranged around the cells within these layers, interactions between the layers may affect stretching. The collagen fibers in the circumferential direction may allow more stretch than the longitudinal direction because of the way they are arranged. The anisotropic coupling observed is probably also a result of the difference in interaction between the smooth muscle and connective tissue in the two directions.

6.1.2 Large Changes in Volume with Small Pressure Increase

The bladder is a fascinating organ of study because of its ability to distend to hold large volumes of urine at relatively low pressures, and with little pressure increase until emptying occurs. One of the purposes of this study was to understand what enables such behavior to occur. The evidence found here is that the bladder undergoes slow controlled creep, as is seen in the quasi-static, slow, and, to a lesser extent, the stress relaxation protocols. This creep must be recoverable *in vivo*, however, and this has not been presented here. More complicated studies that involve long patterns of cycling and resting such as those presented recently by Lanir and colleagues may be useful.(110)

6.1.3 Modeling

Although stress control is easier to implement experimentally, control of testing based on the strain components is a better method for constitutive modeling purposes. The preferred method is to keep all but one strain component constant to measure the change in stress with each independent strain component.(103) The use of strain-based protocols designed to guide the choice of the functional form of a strain-energy function dates back to the first studies for rubber materials by Rivlin *et al*.(111) We have found that the use of stress-based protocols facilitate the study of highly anisotropic tissues like the aortic valve.(81,83)

6.2 Changes with Spinal Cord Injury

6.2.1 Increased Compliance After SCI

Researchers have noted again and again that the urinary bladder is stiffer and less compliant after obstruction, including that caused by neurogenic injury. The compliance calculation is based on measurements of the pressure and the volume at the time of voiding. The compliance is equal to the volume divided by the pressure. Yet all the comparison studies here demonstrated an increase in stretch, that is, an increase in compliance. There are several possible explanations to explain this discrepancy.

Firstly, clinical analyses are performed without the ability to measure thickening of the wall. The bladder, after all, cannot be removed for analysis. From past studies it is known that the bladder wall is much thicker after obstruction; it's obvious that the pressure required to distend the obstructed bladder to a normal volume will be greater than the pressure required for the same volume in a normal bladder. All the experiments described in this study are performed to a constant stress, which essentially normalizes the result to the thickness.

Many studies that have considered bladder wall thickness in their calculations do not sufficiently analyze the reference state used. The measurement of the stretch of a uniaxial strip or a ring must be performed with respect to an original length. The definition of this original length is of critical importance. For example, if the length is the resting length of the ring of tissue, strip, or even circumference of the intact bladder, there might be a residual, unmeasured, stress present that differs between control and diseased bladders. Some researchers have concluded that the bladder voiding mechanism is based on tension(112,113) rather than volume (or stretch) and some researchers are undecided as to what affects it.(114) It is reasonable to assume that the control of the bladder micturition reflux impacts the way the bladder responds to disease. Clearly, it is necessary to define the reference used and the motivation for using it, and present some evidence of how a different reference may affect the result, as well.

All the studies found in the literature comparing obstructed and normal bladder wall mechanics at a tissue level have been uniaxial. The uniaxial state is not physiologic as it leaves the edges of the sample stress-free, and the rotation and deformation of the sample will be different from that observed in a constrained tissue sample. Multiaxial testing is required to properly duplicate the forces applied to the bladder *in vivo*.

6.2.2 Quasi-static Testing and Modeling

In this study, the goodness of fit of a normal bladder wall in an orthotropic model was equivalent to that of an isotropic fit to a bladder wall ten days after spinal cord injury (Figure 5-4). This result was also demonstrated graphically, and indicated a change in the material classification from orthotropic in the normal state to isotropic ten days post spinal cord injury (Figure 5-6). This dramatic change in mechanical properties must be induced by an equally dramatic change in structural component types, quantities, or arrangement of the structural components.

It is known that bladder muscle cells hypertrophy after denervation of the bladder.(26) However, the relative amounts of connective tissues and muscle do not change after 10 weeks of obstruction, a condition pathologically similar to SCI.(26,28) In studies of this condition, the increase in amount of collagen has been quantified for the two major types of collagen in the bladder wall. Type I collagen, the type found in tendon and ligament, increases; type III, commonly found in extensible structures such as the uterus, arteries, and intestinal smooth muscle, decreases.(76) We hypothesize that these two types of collagen have different roles in the distribution of mechanical forces in the bladder and that the relative change in quantity of collagen subtypes causes changes in mechanical properties with SCI.

The normally functioning bladder wall must undergo large stretches over several hours to allow for large volumes at low intravesical pressure. In addition, the bladder must quickly return to its original, unstretched configuration within seconds during and immediately after voiding. The structure of the bladder wall must therefore be very specialized. Changes in mechanical response presented by this study suggest an alteration in the structure of the bladder after spinal cord injury. Clinically, the bladder deforms from a spheroid to a elongated "pine tree" shape many years after spinal cord injury.(15) This could indicate preferential directional changes in the deposition or absorption of specific collagen subtypes in various locations in the bladder wall with SCI.

6.2.3 Stress Relaxation

The study of spinal cord injury has continued to include stress relaxation studies. The study is ongoing, but currently 100 kPa and 25 kPa protocols identical to those presented in section 3.0 are utilized to analyze the response of several SCI bladders four weeks after spinal cord transection.(115) The results show that the SCI samples relax less than normal controls; however, the amount of relaxation is not different between 100 kPa and 25 kPa tests. Ongoing analysis of the residuals for the QLV model fits in both the normal and SCI samples will hopefully lead to development of better viscoelastic models. Although the number of samples tested is too low to allow statistical comparisons, the indications are that G(t) may be independent of stress level in the SCI samples.

6.3 Future Studies

6.3.1 Time Course Studies

The experimental and analytical protocols developed and demonstrated in these studies were performed almost exclusively on normal bladder tissue. Although animal tissue is difficult to obtain, normal tissue is much more abundant than diseased tissue. However, the goal of this ongoing study is the comparison of normal to disease and, in particular, spinal cord injury. The condition of the bladder after spinal cord injury changes through time. Although the SCI bladder has been stretched at several different intervals after injury, the data set is incomplete. For example, the areal strain has been observed to increase with time after spinal cord injury. It is not now known when the increase stops. Some preliminary studies not presented here suggest that this may occur around 6 weeks, but the sample numbers are too low for certainty.

Additionally, the effects of different clinical treatments should be studied to analyze changes in behavior. Capsaicin and resiniferatoxin, drugs instilled into the bladder clinically, have been shown to decrease pain due to hyperactive muscle in diseases such as spinal cord injury. Preliminary studies show that capsaicin may not affect mechanical behavior, but the more potent resiniferatoxin may have an effect.

6.3.2 Diversion Studies

The mechanism of the changes seen within the bladder after spinal cord injury is unknown. Diversion studies have been performed in which the bladder is constantly emptied through a urine shunt to another organ, preventing pressure and averting volume overload.(116) Even with the shunt, the bladder develops many of the same problems. This suggests, that overload is not the sole cause of the dysfunction after spinal cord injury. Identifying the factors that cause the smooth muscle hypertrophy and dyssynergia may, in turn, aid in the development of methods to avoid the dysfunction. Mechanical bladder behavior studies on diverted rats and other animals with modified neural stimulation may aid in isolating the causes of the changes in structure and tissue behavior. Without question, the data presented in Figure 3-60 indicate that volume does impact bladder mechanical properties.

6.3.3 Active Properties

The passive studies presented here are simpler to perform than those requiring active tissue response. It is known that the mechanical properties of an actively contracting material are not the same as those of the passive material with a larger stiffness. The fundamental behavior of the material is different and must therefore be studied as a separate material. Stimulation of a large piece of tissue such as the 1 cm square samples, either by electrical or chemical means, is much more difficult to perform than uniaxial strip experiments. Some preliminary studies have been performed in this laboratory, but nothing conclusive has been found.(117) In addition, the mechanical properties will be altered in disease states, necessitating further testing.

6.3.4 Morphology Studies

Knowledge of bladder morphology is required to understand the impact of disease on bladder function. The studies performed here were not exhaustive, and much is left to be learned. To understand the subtle changes in cross-coupling demonstrated by the quasi-static studies, it is necessary to understand how connective tissue and smooth muscle interact, and how the forces in the bladder wall are distributed between them.

One possible method of determining how the tissue-level forces measured in this study relate to the organ-level function may be through the use of computerized tomography or magnetic resonance imaging of the rat bladder before and after disease such as spinal cord injury. The spatial resolution should be adequate to determine thickness variations and other areas of irregularities to aid in a better choice of biaxial sample location.

Additionally, more information is required on the changes in components of the bladder wall. A 30% difference in connective tissue was found between the normal and 4-weeks post-SCI samples in the digital volumetric imaging study. A recent collagen assay of bladder tissue found a 43% decrease in collagen and at the same time a 260% increase in elastin after injury.(115) Unfortunately, no elastin staining is yet available for volumetric imaging that could be used to learn the location of the elastin increase.

On a molecular level, some of the changes observed between diseased and non-diseased bladder wall may be due to active remodeling of the actin protein. There are several types of actin, including, for example, slow and fast actin, which have different properties. As the actin and myosin crossbridges are in series with the forces applied to the tissue, even when the tissue is not contracting and under the relaxing effects of EGTA, any change to the actin molecules will contribute to the differences observed at the tissue level. This may also be an important assay to develop when examining the changes in protein within the bladder wall during disease states.

The phenomenological modeling employed here can quantitatively compare parameter differences between these two groups; however, this type of modeling cannot be used to indicate what structural component or components are responsible for the observed changes. A structural constitutive model approach, such as that suggested by Horowitz, *et al.*(18) for myocardium, in which the muscle fibers connected by collagen fibers were simulated, may be warranted. In this model, both the muscle fibers and collagen fibers have designated direction, distribution, and mechanical properties that were experimentally measured or approximated. We have recently demonstrated how inclusion of morphological tissue data can result in accurate prediction for planar collagenous tissue using a structural approach.(118) However, detailed and accurate quantitative morphological information about the collagen structure between and within muscle bundles in normal and diseased bladder wall is required before this approach can be effectively implemented.

APPENDICES

Appendix A: Genetic Algorithm

See section 5.1 for the use and explanation of this code. This code was modified from the base code publicly available from Dr. Storn's website (www.ICSI.Berkeley.EDU/~storn/code.html). For more details on generalized implementation, see Dr. Storn's website and the work of Kenneth Price and Rainer Storn.(101)

The code is implemented by typing runme at the MatLAB command prompt. The fung4.m or qlv.m and genalgo.m functions are called and the fit is performed on all ascii files contained in the runme.m datafile string vector.

QUASI-STATIC FOUR-PARAMETER FUNG MODEL FIT

runme.m

```
% Script to run the genetic algorithm.
%
% function [bestmem,nfeval] = genalgo(datafile,NP,D,F,CR,itermax,strategy);
% Run DE minimization
% Output arguments (don't need to do anything for these)
% ----------------
% bestmem            : parameter vector with best solution
% nfeval             : number of function evaluations
%
% Input arguments:
% ---------------
% datafile           : datafile to be read in (i.e. 'bd14.txt')
% NP                 : number of population members
%                    should be five to 10 times the number of parameters
% D                  : number of parameters of the objective
%                    function
% F                  : DE-stepsize F ex [0, 1.2]
%                    optimal is between 0.4 to 1
% CR                 : crossover probabililty constant ex [0, 1]
%                    when CR=1, all new vectors are tried
%                    if parameters are correlated, high CR values work better
% itermax            : maximum number of iterations (generations)
% strategy           : 1 --> DE/best/1
%                    2 --> DE/rand/1
%                    3 --> DE/rand-to-best/1  *** THIS WORKS WELL FOR FUNG MODEL ***
%                    4 --> DE/best/2
%                    else  DE/rand/2
```

```
%  First, declare the constants and run the algorithm to determine the best solution.

format long g                          % changes all parameters to long format
number_params=4;                        % These are parameters for genetic algorithm
number_pop=10*number_params;
stepsize_F=0.8;
crossover_prob=1;  %CR
itermax=1000;
strategy=3;

runs=20;    % perform this many fits to each file

%datafile=['bds10.pp';'bds11.pp';'bds12.pp';'bds13.pp'];       % Each file in this list is processed
datafile=['bd13.pp';'bd16.pp'];
%datafile=['bd14.pp';'bd15.pp';'bd17.pp';'bd18.pp';'bd19.pp';'bd20.pp';'bd21.pp';'bd23.pp';'bd24.pp';'bd25.pp';'bds4.pp';'bds5.pp';'b
ds8.pp';'bds9.pp'];%'bds10.pp';'bds11.pp';'bds12.pp';'bds13.pp'];       % Each file in this list is processed
numfiles=size(datafile,1);                              % Number of files to process.
params=zeros(6,runs);

% Now start loop.  Go through each datafile runs times.
for k=1:numfiles

   % For each file, run fit 50 times and record all parameters in a file

   params=zeros(number_params+2,runs);     % zero array for each file
   for j=1:runs
      [bestmem,nfeval]=genalgo(datafile(k,:), number_pop, number_params, stepsize_F, crossover_prob, itermax, strategy);
      params(1,j)=bestmem(1);
      params(2,j)=bestmem(2);
      params(3,j)=bestmem(3);
      params(4,j)=bestmem(4);
      params(5,j)=nfeval;

      % Next, read in the data to determine the r2 value
      [fid,message]=fopen(datafile(k,:),'rt');    % open file for reading ascii
      A=fscanf(fid,'%f %f %f %f %f',[5 inf]);    % read in format of file
      Data=A';                              % transpose array
      clear E11 E22 S11 S22 S11_S S22_S
      E11=Data(:,2);                        % pull out each of the vector values
      E22=Data(:,3);
      S11=Data(:,4);
      S22=Data(:,5);
      S11_S=zeros(size(S22,1));
      S22_S=zeros(size(S22,1));
      fclose(fid);

      %  Now determine the calculated stresses from the computed solution.
      c0=bestmem(1);
      c1=bestmem(2);
      c2=bestmem(3);
      c3=bestmem(4);

      for i=1:size(E11,1)
          S11_S(i)=c0*exp(c1*(E11(i))^2 + c2*(E22(i))^2 + 2*c3*E11(i)*E22(i))*(c1*E11(i) + c3*E22(i));
          S22_S(i)=c0*exp(c1*(E11(i))^2 + c2*(E22(i))^2 + 2*c3*E11(i)*E22(i))*(c2*E22(i) + c3*E11(i));
      end
```

```
      % Determine the R^2 value.  Ref: pg 37 in Myers text, 2nd edition,
      % Classical and Modern Regression with Applications
      % R2= sum all i (fitted stress minus mean real stress)^2/ sum all i (real stress minus mean real stress)^2

      % find mean real stresses
      total=sum(S11,1)+sum(S22,1);
      meanS=total/size(S11,1);
      SSregression=0;
      SStotal=0;
      SSresidual=0;
      for i=1:size(S11,1)
          SStotal=SStotal+(S11(i)+S22(i)-S11_S(i)-S22_S(i))^2+(S11_S(i)+S22_S(i)-meanS)^2
          SSresidual=SSresidual+(S11(i)+S22(i)-S11_S(i)-S22_S(i))^2;
      end
      R2=1-(SSresidual/SStotal);
      fprintf(l,'R-squared value of run %d of file %s is %f\n\n',j,datafile(k,:),R2);
      params(6,j)=R2;

   end   % end of runs

   % Declare filename, open file, and write data
   fprintf(1,'Writing data to disk...\n\n');
   prnfile=[datafile(k,:), '.prn'];
   fid=fopen(prnfile,'wt');    % open new file for writing test
   for i=1:runs
      fprintf(fid,'%f %f %f %f %f %f\n',params(1,i),params(2,i),params(3,i),params(4,i),params(5,i),params(6,i));
   end
   fclose(fid);
end
resultsr2
```

fung4.m

```
function result = fung4(E11, E22, S11, S22, pop);
% Objective function for Differential Evolution
% Fung4 equation, W=a0/2*e^Q where Q=A1*E11^2 + A2*E22^2 + 2*A3*E11*E22
% Input Arguments:
% ---------------
% S11 : kirchoff's stress in x1 direction
% S22 : kirchoff's stress in x2 direction
% E11 : Green's strain in x1 direction
% E22 : Green's strain in x2 direction
% pop     : parameter values, pop(1)=c0, pop(2)=c2, pop(3)=c3, pop(4)=c4
%
% Output Arguments:
% ----------------
% result              : objective function value (cost value)
%
n=length(E11);  % note E11, E22, S11, S22 will all be the same length
pop;
E=zeros(n,2);
S=zeros(n,2);
c0=pop(1);
```

```
c1=pop(2);
c2=pop(3);
c3=pop(4);
sumit=zeros(n,1);
for i = 1:n
   E(1)=E11(i);
   E(2)=E22(i);
   S(1)=S11(i);
   S(2)=S22(i);
   % sum the two squares of the difference between the calculated and measured stresses
    sumit(i)=( (c0*exp(c1*(E(1)^2)+c2*(E(2)^2)+2*c3*E(1)*E(2))*(c1*E(1)+c3*E(2))) -S(1) )^2 +...
            ( (c0*exp(c1*(E(1)^2)+c2*(E(2)^2)+2*c3*E(1)*E(2))*(c2*E(2)+c3*E(1))) -S(2) )^2;
end
result=sum(sumit,1);
```

genalgo.m

```
function [bestmem,nfeval] = genalgo(datafile,NP,D,F,CR,itermax,strategy);
% Run DE minimization
%  For new function, replace functions at lines 82, 91, 183
%                  replace parameter constrains at line 187
%                  initial parameter bounds lines 42-46
%                  datafile contents lines 66-73
% Output arguments:
% ----------------
% bestmem             : parameter vector with best solution
% nfeval              : number of function evaluations
%
% Input arguments:
% ---------------
% datafile            : datafile to be read in (i.e. 'bd14.txt')
% NP                  : number of population members
% D                   : number of parameters of the objective
%                       function
% F                   : DE-stepsize F ex [0, 2]
% CR                  : crossover probabililty constant ex [0, 1]
% itermax             : maximum number of iterations (generations)
% strategy            : 1 --> DE/best/1
%                       2 --> DE/rand/1
%                       3 --> DE/rand-to-best/1
%                       4 --> DE/best/2
%                       else  DE/rand/2

%-----Check input variables---------------------------------------------
if (NP < 5)
   fprintf(1,'Error! NP should be >= 5\n');
end
if ((CR < 0) | (CR > 1))
   fprintf(1,'Error! CR should be ex [0,1]\n');
end
if (itermax < 0)
   fprintf(1,'Error! itermax should be > 0\n');
```

```
end

maxholdit=20;   % stop parameter:  must have the same function value ("cost")
                %  this many times before stop

%-----Initialize population and some arrays------------------------------

pop = zeros(NP,D); %initialize pop to gain speed
lowbound1  = 1;    % Lower bound for c0
highbound1 = 2;    % Upper bound for c0
lowbound2  = 20;    % Lower bound for c1,c2,c3
highbound2 = 100;   % Upper bound for c1,c2,c3

%----pop is a matrix of size NPxD. It will be initialized-------------
%----with random values between highbound and lowbound----------------

for i=1:NP
   pop(i,1) = lowbound1 + rand*(highbound1 - lowbound1);
   pop(i,2) = lowbound2 + rand*(highbound2 - lowbound2);
   pop(i,3) = lowbound2 + rand*(highbound2 - lowbound2);
   pop(i,4) = lowbound2 + rand*(highbound2 - lowbound2);
end

popold    = zeros(size(pop));     % toggle population
val       = zeros(1,NP);          % create and reset the "cost array"
bestmem   = zeros(1,D);           % best population member ever
bestmemit = zeros(1,D);           % best population member in iteration
nfeval    = 0;                    % number of function evaluations

% ---------------- Read in data -------------------------------------

[fid,message]=fopen(datafile,'rt');    % open file for reading ascii
A=fscanf(fid,'%f %f %f %f %f',[5 inf]);   % read in format of file
Data=A';                               % transpose array
E11=Data(:,2);                            % pull out each of the vector values
E22=Data(:,3);
S11=Data(:,4);
S22=Data(:,5);
fclose(fid);                           % close file

%------Evaluate the best member after initialization---------------------

ibest   = 1;                      % start with first population member

%%%%%%%%%%%%%%%%%%
val(1)  = fung4(E11,E22,S11,S22,pop(ibest,:));
%%%%%%%%%%%%%%%%%%

bestval = val(1);                 % best objective function value so far
nfeval  = nfeval + 1;
for i=2:NP                        % check the remaining members

  %%%%%%%%%%%%%%%%%
  val(i)=fung4(E11,E22,S11,S22,pop(i,:));
  %%%%%%%%%%%%%%%%%%%%%
```

```
  nfeval  = nfeval + 1;
  if (val(i) < bestval)           % if member is better
     ibest   = i;                 % save its location
     bestval = val(i);
  end
end
bestmemit = pop(ibest,:);         % best member of current iteration
bestvalit = bestval;              % best value of current iteration

bestmem = bestmemit;              % best member ever

%------DE-Minimization---------------------------------------------
%------popold is the population which has to compete. It is--------
%------static through one iteration. pop is the newly--------------
%------emerging population.----------------------------------------

pm1 = zeros(NP,D);              % initialize population matrix 1
pm2 = zeros(NP,D);              % initialize population matrix 2
pm3 = zeros(NP,D);              % initialize population matrix 3
pm4 = zeros(NP,D);              % initialize population matrix 4
pm5 = zeros(NP,D);              % initialize population matrix 5
bm  = zeros(NP,D);              % initialize bestmember  matrix
ui  = zeros(NP,D);              % intermediate population of perturbed vectors
mui = zeros(NP,D);              % mask for intermediate population
mpo = zeros(NP,D);              % mask for old population
rot = (0:1:NP-1);               % rotating index array
rt  = zeros(NP);                % another rotating index array
a1  = zeros(NP);                % index array
a2  = zeros(NP);                % index array
a3  = zeros(NP);                % index array
a4  = zeros(NP);                % index array
a5  = zeros(NP);                % index array
ind = zeros(4);

iter = 1;
holdit=ones(maxholdit,1);    % use a revolving array to track number changes
                 % first column contains values, second contains percent difference from most recent
holdit(1)=inf;

% Start of loop.  Note that loop will never end before 20 iterations.
while ((iter < itermax) & ( sum(holdit)/holdit(maxholdit) > maxholdit) )
  popold = pop;                   % save the old population

  ind = randperm(4);              % index pointer array

  a1  = randperm(NP);             % shuffle locations of vectors
  rt = rem(rot+ind(1),NP);        % rotate indices by ind(1) positions
  a2  = a1(rt+1);                 % rotate vector locations
  rt = rem(rot+ind(2),NP);
  a3  = a2(rt+1);
  rt = rem(rot+ind(3),NP);
  a4  = a3(rt+1);
  rt = rem(rot+ind(4),NP);
  a5  = a4(rt+1);

  pm1 = popold(a1,:);             % shuffled population 1
```

```
 pm2 = popold(a2,:);             % shuffled population 2
 pm3 = popold(a3,:);             % shuffled population 3
 pm4 = popold(a4,:);             % shuffled population 4
 pm5 = popold(a5,:);             % shuffled population 5

 for i=1:NP                    % population filled with the best member
  bm(i,:) = bestmemit;          % of the last iteration
 end

 mui = rand(NP,D) < CR;          % all random numbers < CR are 1, 0 otherwise
 mpo = mui < 0.5;               % inverse mask to mui

 if (strategy == 1)               % DE/best/1
  ui = bm + F*(pm1 - pm2);        % differential variation
  ui = popold.*mpo + ui.*mui;     % binomial crossover
 elseif (strategy == 2)           % DE/rand/1
  ui = pm3 + F*(pm1 - pm2);       % differential variation
  ui = popold.*mpo + ui.*mui;     % binomial crossover
 elseif (strategy == 3)           % DE/rand-to-best/1
  ui = popold + F*(bm-popold) + F*(pm1 - pm2);
  ui = popold.*mpo + ui.*mui;     % binomial crossover
 elseif (strategy == 4)           % DE/best/2
  ui = bm + F*(pm1 - pm2 + pm3 - pm4);  % differential variation
  ui = popold.*mpo + ui.*mui;           % binomial crossover
 else                            % DE/rand/2
  ui = pm5 + F*(pm1 - pm2 + pm3 - pm4);  % differential variation
  ui = popold.*mpo + ui.*mui;            % binomial crossover
 end

%-----Select which vectors are allowed to enter the new population------------
 for i=1:NP

%%%%%%%%%%%%%
  tempval = fung4(E11,E22,S11,S22,ui(i,:));
%%%%%%%%%%%%%

  nfeval  = nfeval + 1;
  if ((tempval <= val(i)) & (ui(i,1)>0) & (ui(i,2)>0) & (ui(i,3)>0) )  % parameter restrictions here
                                 % if competitor is better than value in "cost array"
                                 %   and the c0, c1, and c2 parameters all >0
    pop(i,:) = ui(i,:);  % replace old vector with new one (for new iteration)
    val(i)   = tempval;  % save value in "cost array"

    %----we update bestval only in case of success to save time-----------
    if (tempval < bestval)     % if competitor better than the best one ever
      bestval = tempval;      % new best value
      bestmem = ui(i,:);      % new best parameter vector ever
    end
  end
 end %---end for imember=1:NP

 bestmemit = bestmem;       % freeze the best member of this iteration for the coming
                       % iteration. This is needed for some of the strategies.

 if (iter < maxholdit+1)
   holdit(iter)=bestval;
```

```
  else
       holdit(rem(iter,maxholdit)+1)=bestval;
  end

%----Output section-----------------------------------------------------------

 if (rem(iter,10) == 0)
     fprintf(1,'Iteration: %d,  Best: %f,  F: %f,  CR: %f, NP: %d\n',iter,bestval,F,CR,NP);
     fprintf(1,'  c0 = %f   c1 = %f   c2 = %f   c3 = %f\n',bestmem(1),bestmem(2),bestmem(3),bestmem(4));
 end

  iter = iter + 1;
end %---end while ((iter < itermax) ...
fprintf(1,'FINAL Iteration: %d,  Best: %f,  F: %f,  CR: %f, NP: %d\n',iter,bestval,F,CR,NP);
fprintf(1,'  c0 = %f   c1 = %f   c2 = %f   c3 = %f\n',bestmem(1),bestmem(2),bestmem(3),bestmem(4));
```

QLV VISCOELASTIC MODEL

runme.m

```
% Script to run the genetic algorithm.
%
% function [bestmem,nfeval] = genalgo(datafile,NP,D,F,CR,itermax,strategy); in separate file
% Run DE minimization
% Output arguments (don't need to do anything for these)
% ----------------
% bestmem             : parameter vector with best solution
% nfeval              : number of function evaluations
% Input arguments:
% ---------------
% datafile            : Datafile to be read in (i.e. 'bd14.txt')
% NP                  : Number of population members
%                     Should be five to 10 times the number of parameters
% D                   : Number of parameters of the objective function
% F                   : DE-stepsize F ex [0, 1.2], optimal is between 0.4 to 1
% CR                  : Crossover probabililty constant ex [0, 1]
%                     When CR=1, all new vectors are tried
%                     If parameters are correlated, high CR values work better
% itermax             : Maximum number of iterations (generations)
% strategy            : 1 --> DE/best/1
%                     2 --> DE/rand/1
%                     3 --> DE/rand-to-best/1  *** THIS WORKS WELL FOR FUNG MODEL ***
%                     4 --> DE/best/2
%                     else  DE/rand/2
%  First, declare the constants and run the algorithm to determine the best solution.

tic
warning off
format long g                          % changes all parameters to long format
number_params=3;                       % These are parameters for genetic algorithm
number_pop=10*number_params;
stepsize_F=0.6;
```

```
crossover_prob=1;  %CR
itermax=1500;
strategy=4;
runs=20;    % perform this many fits to each file

% Each file in this list is processed.
% Note that all filenames must be the same length, or you must run it in two sections.
datafile=['bd65sec.txt';'bd66sec.txt';'bd67sec.txt';'bd68sec.txt';'bd69sec.txt';'bd70sec.txt';'bd71sec.txt';'bd72sec.txt';'bd73sec.txt';'b
d74sec.txt';'bd75sec.txt';'bd76sec.txt';'bd77sec.txt';'bd79sec.txt';'bd80sec.txt'];
numfiles=size(datafile,1);                    % Number of files to process.

% START LOOP.  Go through each datafile runs times.

for k=1:numfiles

   % Initialize parameter arrays for each new datafile
   params1=zeros(number_params+2,runs);     % zero array for each file
   params2=zeros(number_params+2,runs);
   % Open raw data file for r2 calculations here
   fidin=fopen(datafile(k,:),'rt');         % open file for reading ascii
   A=fscanf(fidin,'%f %f %f %f',[4 inf]);   % read in format of file
   Data=A';                                 % transpose array
   ti1=Data(:,1);                           % Save data in appropriate arrays.
   gt1=Data(:,2);
   ti2=Data(:,3);
   gt2=Data(:,4);
   fclose(fidin);

   % For each file, run fit runs number of times and record all parameters in a file
   for j=1:runs

      % AXIS 1: Run genetic algorithm fit and save results in param variable

      fprintf(1,'\nAxis 1 of %s  Run Number %d of %d total runs ',datafile(k,:),j,runs);
      fprintf(1,'using F: %2.1f  CR: %3.2f  NP: %2.0f',stepsize_F,crossover_prob, number_pop);
      [bestmem,nfeval]=genalgo(datafile(k,:), number_pop, number_params, stepsize_F, crossover_prob, itermax,
strategy,ti1,gt1);
      params1(1,j)=bestmem(1);
      params1(2,j)=bestmem(2);
      params1(3,j)=bestmem(3);
      params1(4,j)=nfeval;
      c=bestmem(1);                % Save parameters for r2 calculations below
      tau1=bestmem(2);
      tau2=bestmem(3);

      gt1calc=(1+c*(expint(ti1/tau2)-expint(ti1/tau1)))/(1+c*log(tau2/tau1));

      % Determine the R^2 value.  Ref: pg 37 in Myers text, 2nd edition,
      % Classical and Modern Regression with Applications
      total=sum(gt1,1);                 % easy to sum the real values array
      meanS=total/size(gt1,1);
      SStotal=zeros(size(gt1,1),1);
      SSregression=zeros(size(gt1,1),1);                  % initialize the three sums
      SSresidual=zeros(size(gt1,1),1);

      SSregression=(gt1calc-meanS).^2;
```

```
        SStotal=(gt1-meanS).^2;
        SSresidual=(gt1calc-gt1).^2;
        params1(5,j)=sum(SSregression,1)/sum(SStotal,1);

        %   AXIS 2
        fprintf(1,'\nAxis 2 of %s  Run Number %d of %d total runs ',datafile(k,:),j,runs);
        fprintf(1,'using F: %2.1f  CR: %3.2f  NP: %2.0f',stepsize_F,crossover_prob, number_pop);
        [bestmem,nfeval]=genalgo(datafile(k,:), number_pop, number_params, stepsize_F, crossover_prob, itermax, strategy,
ti2,gt2);
        params2(1,j)=bestmem(1);
        params2(2,j)=bestmem(2);
        params2(3,j)=bestmem(3);
        params2(4,j)=nfeval;

        % Next, read in the data to determine the r2 value
        c=bestmem(1);
        tau1=bestmem(2);
        tau2=bestmem(3);

        % Now determine the calculated g values from the computed solution.
        gt2calc=(1+c*(expint(ti2/tau2)-expint(ti2/tau1)))/(1+c*log(tau2/tau1));

        % calculate r2 again
        total=sum(gt2,1);
        meanS=total/size(gt2,1);
        SSregression=zeros(size(gt1,1),1);                    % initialize the three sums
        SSresidual=zeros(size(gt1,1),1);
        SSregression=(gt2calc-meanS).^2;
        SStotal=(gt2-meanS).^2;
        SSresidual=(gt2calc-gt2).^2;
        R2=sum(SSregression,1)/sum(SStotal,1);
        params2(5,j)=R2;

    end  % end of runs

    % Open two files for writing and write all runs for both axes to separate files
    fprintf(1,'\nWriting data to disk for both axes and all runs for filename %s \n\n',datafile(k,:));
    prnfile1=[datafile(k,:), '1.prn'];            % File for axis1
    fid1=fopen(prnfile1,'wt');                    % open new file for writing test
    prnfile2=[datafile(k,:), '2.prn'];            % File for axis2
    fid2=fopen(prnfile2,'wt');                    % open new file for writing test
    for i=1:runs
        fprintf(fid1,'%f %8.7f %8.7f %f %f\n',params1(1,i),params1(2,i),params1(3,i),params1(4,i),params1(5,i));
        fprintf(fid2,'%f %8.7f %8.7f %f %f\n',params2(1,i),params2(2,i),params2(3,i),params2(4,i),params2(5,i));
    end
    fclose(fid1);
    fclose(fid2);
end  % end of k loop (go through datafiles)

fprintf(1,'Time to Completion, %4.2f hours',toc/3600);
```

qlv.m

```
function result = qlv(gt,ti, pop);
% Objective function for Differential Evolution
% QLV Equation G(t)=(1+c*(expint(tiv/tau2)-expint(tiv/tau2)))/(1+c*log(tau1/tau2))
% Input Arguments:
% ---------------
% gtv : G(t)
% tiv : time (seconds)
% pop     : parameter values, pop(1)=c, pop(2)=tau1, pop(3)=tau2
%
% Output Arguments:
% ----------------
% result              : objective function value (cost value)
%
n=size(gt,1);
c=pop(1);   % c
tau1=pop(2);   % tau1
tau2=pop(3);   % tau2
sumit=0;
denom= (1+c*(log(tau2/tau1)));
sumit=(((1+c*(expint(ti/tau2)-expint(ti/tau1))) /denom) -gt).^2;
result=sum(sumit,1);
```

genalgo.m

```
function [bestmem,nfeval] = genalgo(datafile,NP,D,F,CR,itermax,strategy,ti,gt);
% Run DE minimization
%  For new function, replace functions at lines 82, 91, 183
%                  replace parameter constrains at line 187
%                  initial parameter bounds lines 42-46
%                  datafile contents lines 66-73
% Output arguments:
% ----------------
% bestmem              : parameter vector with best solution
% nfeval               : number of function evaluations
%
% Input arguments:
% ---------------
% datafile             : datafile to be read in (i.e. 'bd14.txt')
% NP                   : number of population members
% D                    : number of parameters of the objective
%                        function
% F                    : DE-stepsize F ex [0, 2]
% CR                   : crossover probabililty constant ex [0, 1]
% itermax              : maximum number of iterations (generations)
% strategy             : 1 --> DE/best/1
%                        2 --> DE/rand/1
%                        3 --> DE/rand-to-best/1
%                        4 --> DE/best/2
%                        else  DE/rand/2

%-----Check input variables---------------------------------------------
if (NP < 5)
```

```
  fprintf(1,'Error! NP should be >= 5\n');
end
if ((CR < 0) | (CR > 1))
  fprintf(1,'Error! CR should be ex [0,1]\n');
end
if (itermax < 0)
  fprintf(1,'Error! itermax should be > 0\n');
end

maxholdit=100;   % stop parameter:  must have the same function value ("cost")
              %  this many times before stop
%-----Initialize population and some arrays-------------------------------

pop = zeros(NP,D); %initialize pop to gain speed
lowbound1  = 1;    % Lower bound for c
highbound1 = 100;    % Upper bound for c
lowbound2  = 0.001;    % Lower bound for tau1
highbound2 = 0.1;   % Upper bound for tau1
lowbound3  = 50;
highbound3 = 1000;

%----pop is a matrix of size NPxD. It will be initialized-------------
%----with random values between highbound and lowbound----------------
ginf=gt(size(gt,1));
for i=1:NP
  %pop(i,1) = lowbound1 + rand*(highbound1 - lowbound1);
  pop(i,2) = lowbound2 + rand*(highbound2 - lowbound2);
  pop(i,3) = lowbound3 + rand*(highbound3 - lowbound3);
  if (pop(i,3)<pop(i,2)) pop(i,3)=pop(i,2)+rand*(lowbound2); end
  pop(i,1) = (1-ginf)/(ginf*log(pop(i,3)/pop(i,2)));
end

popold    = zeros(size(pop));     % toggle population
val       = zeros(1,NP);          % create and reset the "cost array"
bestmem   = zeros(1,D);           % best population member ever
bestmemit = zeros(1,D);           % best population member in iteration
nfeval    = 0;                    % number of function evaluations

%------Evaluate the best member after initialization----------------------

ibest   = 1;                      % start with first population member
%%%%%%%%%%%%%%%%%%
val(1)  = qlv(gt,ti, pop(ibest,:));
%%%%%%%%%%%%%%%%%%
bestval = val(1);                 % best objective function value so far
nfeval  = nfeval + 1;
for i=2:NP                        % check the remaining members
 %%%%%%%%%%%%%%%%%%
 val(i)=qlv(gt,ti,pop(i,:));
 %%%%%%%%%%%%%%%%%%%%%%

 nfeval  = nfeval + 1;
 if (val(i) < bestval)           % if member is better
    ibest   = i;                 % save its location
    bestval = val(i);
 end
```

```
end
bestmemit = pop(ibest,:);         % best member of current iteration
bestvalit = bestval;              % best value of current iteration

bestmem = bestmemit;              % best member ever

%------DE-Minimization--------------------------------------------
%------popold is the population which has to compete. It is--------
%------static through one iteration. pop is the newly-------------
%------emerging population.--------------------------------------

pm1 = zeros(NP,D);            % initialize population matrix 1
pm2 = zeros(NP,D);            % initialize population matrix 2
pm3 = zeros(NP,D);            % initialize population matrix 3
pm4 = zeros(NP,D);            % initialize population matrix 4
pm5 = zeros(NP,D);            % initialize population matrix 5
bm  = zeros(NP,D);            % initialize bestmember  matrix
ui  = zeros(NP,D);            % intermediate population of perturbed vectors
mui = zeros(NP,D);            % mask for intermediate population
mpo = zeros(NP,D);            % mask for old population
rot = (0:1:NP-1);             % rotating index array
rt  = zeros(NP);              % another rotating index array
a1  = zeros(NP);              % index array
a2  = zeros(NP);              % index array
a3  = zeros(NP);              % index array
a4  = zeros(NP);              % index array
a5  = zeros(NP);              % index array
ind = zeros(4);

iter = 1;
holdit=ones(maxholdit,1);    % use a revolving array to track number changes
                  % first column contains values, second contains percent difference from most recent
holdit(maxholdit-1)=inf;

% Start of loop.  Note that loop will never end before 20 iterations.
while ((iter < itermax) & (  floor(100000*(sum(holdit)/holdit(maxholdit))) ~= maxholdit*100000) )

  popold = pop;                  % save the old population

  ind = randperm(4);             % index pointer array

  a1  = randperm(NP);            % shuffle locations of vectors
  rt = rem(rot+ind(1),NP);       % rotate indices by ind(1) positions
  a2  = a1(rt+1);                % rotate vector locations
  rt = rem(rot+ind(2),NP);
  a3  = a2(rt+1);
  rt = rem(rot+ind(3),NP);
  a4  = a3(rt+1);
  rt = rem(rot+ind(4),NP);
  a5  = a4(rt+1);

  pm1 = popold(a1,:);            % shuffled population 1
  pm2 = popold(a2,:);            % shuffled population 2
  pm3 = popold(a3,:);            % shuffled population 3
  pm4 = popold(a4,:);            % shuffled population 4
  pm5 = popold(a5,:);            % shuffled population 5
```

```
  for i=1:NP                    % population filled with the best member
    bm(i,:) = bestmemit;          % of the last iteration
  end

  mui = rand(NP,D) < CR;          % all random numbers < CR are 1, 0 otherwise
  mpo = mui < 0.5;               % inverse mask to mui

  if (strategy == 1)               % DE/best/1
    ui = bm + F*(pm1 - pm2);        % differential variation
    ui = popold.*mpo + ui.*mui;     % binomial crossover
  elseif (strategy == 2)           % DE/rand/1
    ui = pm3 + F*(pm1 - pm2);       % differential variation
    ui = popold.*mpo + ui.*mui;     % binomial crossover
  elseif (strategy == 3)           % DE/rand-to-best/1
    ui = popold + F*(bm-popold) + F*(pm1 - pm2);
    ui = popold.*mpo + ui.*mui;     % binomial crossover
  elseif (strategy == 4)           % DE/best/2
    ui = bm + F*(pm1 - pm2 + pm3 - pm4);  % differential variation
    ui = popold.*mpo + ui.*mui;          % binomial crossover
  else                           % DE/rand/2
    ui = pm5 + F*(pm1 - pm2 + pm3 - pm4);  % differential variation
    ui = popold.*mpo + ui.*mui;           % binomial crossover
  end

%-----Select which vectors are allowed to enter the new population------------
  for i=1:NP

%%%%%%%%%%%%%%
    tempval = qlv(gt,ti, ui(i,:));
%%%%%%%%%%%%%%

    nfeval  = nfeval + 1;
    if ((tempval <= val(i)) & (ui(i,3) > ui(i,2)) & (ui(i,1)>0) & (ui(i,2)>0) & (ui(i,3)>0) &
(round(ginf*100)==round(100/(1+ui(i,1)*log(ui(i,3)/ui(i,2))))) )  % parameter restrictions here
                                 % if competitor is better than value in "cost array"
                                 %   and the c>0 tau2>tau1
      pop(i,:) = ui(i,:);  % replace old vector with new one (for new iteration)
      val(i)   = tempval;  % save value in "cost array"

      %----we update bestval only in case of success to save time-----------
      if (tempval < bestval)     % if competitor better than the best one ever
        bestval = tempval;      % new best value
        bestmem = ui(i,:);      % new best parameter vector ever
      end
    end
  end %---end for imember=1:NP

  bestmemit = bestmem;       % freeze the best member of this iteration for the coming
                        % iteration. This is needed for some of the strategies.

  if (iter < maxholdit+1)
     holdit(iter)=bestval;
  else
      holdit(rem(iter,maxholdit)+1)=bestval;
  end
```

```
%----Output section---------------------------------------------------------
 if (rem(iter,10) == 0)
     fprintf(1,'\nIter: %d  Best: %f',iter,bestval);
     fprintf(1,'  c: %6.4f  tau1: %8.7f  tau2: %8.7f',bestmem(1),bestmem(2),bestmem(3));
 end

  iter = iter + 1;
end %---end while ((iter < itermax) ...
fprintf(1,'\nFINAL Iteration: %d,  Best: %f, ',iter, bestval);
fprintf(1,'  c:%4.3f   tau1:%8.7f  tau2:%8.7f  \n',bestmem(1), bestmem(2), bestmem(3));
```

Appendix B: Fiber Orientation Analysis

See section 4.2 for detailed explanation. The fiber direction analysis is performed with four code segments. The code is implemented by typing fibor at the MatLAB command prompt. This function calls imagefiber, which actually runs the analysis. For convenience, imagefiber calls drawline, which creates an image the same size as the source image with a series of lines showing the fiber alignment direction. Imagefiber further outputs a large ASCII file for each image that contains the coordinates of each subimage followed by the 180 intensity values. The function preferreddirection is then called to determine the mean and error of all of the subimage orientations in each image.

fibor.m

```
function f=FIBOR(filebase,number,step)
% FIBOR  Reads in images in sequence and runs imagefiber.m on each
%  Filebase is the base filename and number is the number of images.
%   Created to analyze ResVIEW tiff stacks.

for frame=1:step:number
   if frame<10
      zer='000';
   elseif (frame<100 & frame>9)
     zer='00';
  elseif (frame<1000 & frame>99)
      zer='0';
   elseif frame>999
      zer='';
   end
   filename=[filebase,zer,int2str(frame)];
   disp(filename);    % display current working file
   filenamered=['r',filebase,zer,int2str(frame)];
   imagefiber(filenamered,'tif',1,70);   % muscle bundles 50-120 micron diameter
   fprintf(1,'G... ');
   filenamegreen=['g',filebase,zer,int2str(frame)];
   imagefiber(filenamegreen,'tif',1,10);    % collagen fibers are 0-2 microns
end % end for frame
```

imagefiber.m

```
function f=imagefiber(filename,type,color,boxsize)
%IMAGEFIBER (filename, type, color boxsize).
%     Takes an image and performs Chaudhuri type filtering (see
%     Pattern Recognition Letters, v 14(2) p 148) on the entire image.
%     filename: string with prefix of filename (no extension)
%     type: type of file (either tiff, bmp, or gif)
%     color: color of vectors to draw on image (0-black or 1-white)
%     boxsize: size of box for final filtering (10-30)

%     Notes:
%                         Filter dimensions are s+1 x s+1
%     Current 9/06/01 by DCG.

tic                          % starts timer going

%% FIRST INITIALIZATION SECTION
sigma=10;                                                            % picked sigma from article, default is 2
sigma2=sigma^2;
s=3;                          % array size - must be ODD, default is 5
conver=pi/180;                                                  % conversion factor from degrees to radians
warning off;                                                    % turned off warnings - they're annoying
Hx=zeros(s*2+1:s*2+1);        % zero both convolution arrays
Hy=zeros(s*2+1:s*2+1);

Cval=zeros(boxsize,boxsize);
I_G=zeros(boxsize,boxsize);
I_psi=zeros(boxsize,boxsize);
testnum=0;

for i=-s:s
  for j=-s:s            % Note index change +n+1
    Hy(i+s+1,j+s+1)=(2*i/sigma2)*exp(-(i^2+j^2)/sigma2);
    Hx(i+s+1,j+s+1)=(2*j/sigma2)*exp(-(i^2+j^2)/sigma2);
  end
end

if type=='bmp'
   startimage=[filename, '.bmp'];
elseif type=='tif'
   startimage=[filename, '.tif'];
end

% Read in image, convert to grayscale, and plot to screen for verification

I=imread(startimage);                                 % READ IN image (24-bit)
I2=histeq(I);
clear I

% SECOND INIALIZATION SECTION
xsize=size(I2,2);                          % size of image in x direction
ysize=size(I2,1);                          % size of image in y direction

totaltestnum=round(ysize/boxsize)*round(xsize/boxsize);

startval=round(s/2);    % need to step in s/2 (rounded up)
```

```
mag=fix(s/2);                                          % rounded down

E_G=zeros(ysize,xsize);                                % edge image declaration
E_psi=zeros(ysize,xsize);                  % gradient angle matrix

% Make edge and gradient images.
% Apply convolution array above to sxs subimages.  Take the center pixel of
%  the resultant array as the final result - use center pixels to make final
%  edge and gradient images.
% NOTES: image pixel counting based on center point.
%   Start at pixel that is s from edge (rounded up)
fprintf(1,'Convolving...  ');
for row=startval : ysize-mag,  % start rows
  for col=startval : xsize-mag, % start cols, put 50 here!
    I4=imcrop(I2,[(col-mag) (row-mag) s-1 s-1]);   % crop a piece nxn centered on (row,col)
            Gx=conv2(I4,Hx);               % convolve subimage
            Gy=conv2(I4,Hy);
    G=(Gx.^2+Gy.^2);                                   % get gradient
    center=round(size(G,1)/2);  % find center of matrix
    psi=atan(Gy./Gx);     % get psi for this point
    E_G(row,col)=G(center,center);      % write data at center to
    E_psi(row,col)=psi(center,center);  % matrix at point
  end
end
clear I4 G Gx Gy psi Hx Hy

% Find all values out of 0 to 360 range and zero them
[r,s]=find(E_psi<1.5709 & E_psi>1.5707);
for row2=1:size(r)
  E_psi(r(row2),s(row2))=0;
end
clear r s

% Next section:  Accumulator bins of angular distributions
% Note, A is configured this way:
%   Sizes:
%   first dimension is # rows (y direction) of image
%   second dimension is # columns (x direction) of image
%   third dimension is 180 (for 0-179 degrees)
%   Data is stored as y,x positions of start of box, then angle
%   Therefore, most of A will be empty, but there will be data only
%     in the third dimension of startval+boxsize*i in each axis

I_G=zeros(boxsize,boxsize);
I_psi=zeros(boxsize,boxsize);

% Prepare to write the fiber distribution information to file row by row
x=0;
prnfile=[filename, '.prn'];
fid=fopen(prnfile,'wt');    % open new file for writing test
testnum=0;
A=zeros(mod((ysize-1),boxsize)*mod((xsize-1),boxsize),182);  % zero distribution array

fprintf(1,'Binning...  ');
for row=1 : boxsize : ysize-boxsize+1
  for col = 1 : boxsize : xsize-boxsize+1  % here startval
```

```
      testnum=testnum+1;
      I_G= imcrop(E_G,[col row boxsize-1 boxsize-1]);
      I_psi= imcrop(E_psi,[col row boxsize-1 boxsize-1]);
      A(testnum,1)=row;
      A(testnum,2)=col;
      for theta=1 :180                                        % Note that I need theta=0, so I subtract one below
         argument=2*( ((theta-1)*conver)-I_psi);  % note conversion to radians.
         tempit=exp(2*cos(argument))/exp(2);
         Cval=I_G.*tempit;

         [r,s]=find(isinf(Cval));
         for row2=1:size(r)
           Cval(r(row2),s(row2))=0;
         end
         clear r s

         [r,s]=find(isnan(Cval));
         for row2=1:size(r)
           Cval(r(row2),s(row2))=0;
         end
         clear r s

         A(testnum,theta+2)=sum((sum(Cval))');
       end
       %     end  % end of if mod == 20
  end
end
clear E_psi E_G Cval I_G I_psi

% Now write the fiber distribution information to file

fprintf(1,'Writing prn...  ');
prnfile=[filename, '.prn'];
fid=fopen(prnfile,'wt');    % open new file for writing test
for row=1 : testnum,               % same dimensions as above (number of rows)
  for col = 1 : 182
      fprintf(fid, '%f ',A(row,col));             % print each value of theta
   end
   fprintf(fid,'\n');  % put a new line after each point
end
fclose(fid);

% Now overlay the fiber direction on the image and display it

fprintf(1,'Creating tiff...  ');
overlaid=drawline(I2,testnum,prnfile,boxsize,color);
fiberfile=[filename, '_fiber.tif'];
imwrite(overlaid,fiberfile,'tiff');

%Notes: How to set up a figure
%h=figure;
%set(h,'Name','Grayscale of whole image','NumberTitle','off');

fprintf(1,'%f minutes. \n',toc/60);             %outputs time in seconds from tic
```

drawline.m

```
function C=drawline(B,x,filename,boxsize,color);
%    function C=drawline(B,x,filename,boxsize);
%       B is the image
%       x is number of lines in A file (points at which lines are drawn)
%       A is a 3d matrix that contains the direction data
%                          boxsize is the size of the box used for computation
%       color is either 1 (black) or 0 (white) lines

%compute conversion factor - radians-degrees
conver=pi/180;
center=boxsize/2;
%Copy B into C so C will be altered with lines added
C=zeros(size(B,1),size(B,2));

fid=fopen(filename,'rt');
A=zeros(182,x);
[A,count] = fscanf(fid,'%lf ',[182,x]);
fclose(fid);

for k=1:x
   B=A(3:182,k);    %extract last 180 points as distribution curve
   [B,degree]=max(B,[],1); %extract largest degree for P.D.
   maxval=max(B(1,:),[],2); % extract largest value (not index) in angle histogram
   xcenter=A(2,k);      %center of box in y direction (NOTE REVERSAL)
   ycenter=A(1,k);      %center of box in x direction
   deg=degree(1)-90;
   for i=1 : center
      x=round(cos(deg*conver)*i);
      y=round(sin(deg*conver)*i);
      if (x>=center) x=x-1; end
      if (y>=center) y=y-1; end
      C(center-y+ycenter,center-x+xcenter)=color;
      C(center-y+ycenter+1,center-x+xcenter)=color;
      if(x-1<=-center) x=x+1; end
              if (y-1<=-center) y=y+1; end
      C(y+center+ycenter,x+center+xcenter)=color;
      C(y+center+ycenter+1,x+center+xcenter)=color;
   end
   C(center+ycenter,center+xcenter)=color;
   C(center+ycenter+1,center+xcenter)=color;
End
```

preferreddirection.m

```
function f=preferreddirection(filebase,number,step)
%% function preferreddirection
%%  Takes in the results from imagefiber and
%%  calculates the prefered direction.

sizeit=ceil(number/step)+1;
all=zeros(sizeit,3);
tiff=0;
for frame=1:step:number
    tiff=tiff+1;
```

```
   if frame<10
      zer='000';
   elseif (frame<100 & frame>9)
      zer='00';
   elseif (frame<1000 & frame>99)
      zer='0';
   elseif frame>999
      zer='';
   end

   filename=[filebase,int2str(frame),'m.prn'];
   disp(filename);
   fprintf(1,'M...  ');
   filenamered=['m',filename];
   imagefiber(filenamered,'tif',1,70);   % muscle bundles 50-120 micron diameter
   filename=[filebase,zer,int2str(frame),'.prn'];
   disp(filename);
   fid=fopen(filename,'rt');
   it=fscanf(fid,'%f',[182,inf]);
   fclose(fid);
   pref=zeros(1,size(it,2));
   for i=1:size(it,2)
      if sum(it(3:182,i),1)>0.001
        [value,index]=max(it(3:182,i));
        pref(i)=index-1;
     end
   end
   k2=pref(1,1:size(it,2));
   k=find(k2>0);
   all(tiff,1)=sum(k2(k))/size(k,2);
   all(tiff,2)=std(k2(k));
   all(tiff,3)=size(k,2);
   fprintf(1,'%f %f %f %f\n',frame,all(tiff,1),all(tiff,2),all(tiff,3));

end % end for frame

filename=[filebase,'prefdirec.txt'];
fid= fopen(filename,'wt');
for tiff=1:size(all,1)
   fprintf(fid,'%f %f %f %f\n', tiff,all(tiff,1),all(tiff,2),all(tiff,3));
end
fclose(fid);
```

Appendix C: Volume Component Analysis

Details are found in section 4.3.

volumize.m

```
function [all,reds,greens,equal]=volumize(filebase,number)
%% SCRIPT volumeize
%%  Takes a file base of characters, ex: 'sci' and
%%   and tacks on number increments from 1 to number
%%   and a .tif extension. Reads in all images and calculates:
%%  Nuumber of non-zero pixels (one or more RGB channels non-zero)
%%  Number pixels where red channel is greater than green
%%  Number pixels where green channel is greater than red
%%  Number pixels where red=green (just to double check)

tic
all=zeros(1,number);
reds=zeros(1,number);
greens=zeros(1,number);
equal=zeros(1,number);
for frame=1:number
   switch(frame)
     case {1,9}, zer='000';
     case {10,99}, zer='00';
     case {100,999}, zer='0';
     case {1000,inf}, zer='';
   end
   filename=[filebase,zer,int2str(frame),'.tif'];
   disp(filename);
   im=imread(filename);
   if frame==1
      rows=size(im,1);
      cols=size(im,2);
   end

   for r=1:rows
      for c=1:cols
         if ( (double(im(r,c,1)) >0 ) | (double(im(r,c,2))>0) | (double(im(r,c,3))>0) )
            all(frame)=all(frame)+1;
            val=double(im(r,c,1)) - double(im(r,c,2));
            if (val>0) reds(frame)=reds(frame)+1;
            elseif (val<0) greens(frame)=greens(frame)+1;
            elseif (val==0) equal(frame)=equal(frame)+1;
            end
         end  % end if
      end   % end for cols
   end   % end for rows
end % end for frame
```

```
[fid,message]=fopen('output.txt','w');
fprintf(fid,'file\t all\t equal\t reds\t greens\t redvol\t greenvol\n');
for frame=1:number
  fprintf(fid,'%d\t %d\t %d\t %d\t %d\t %d\t %d\t\n',frame,all(frame),equal(frame), reds(frame),greens(frame),...
     reds(frame)/(all(frame)-equal(frame)),greens(frame)/(all(frame)-equal(frame)));
end
fprintf(fid,'Red Volume: %f\n', sum(reds)/(sum(all)-sum(equal)));
fprintf(fid,'Green Volume: %f\n',sum(greens)/(sum(all)-sum(equal)));
fclose(fid);

fprintf(1,'\nVolume fractions\n');
fprintf(1,'Red: %f\n',sum(reds)/(sum(all)-sum(equal)));
fprintf(1,'Green: %f\n',sum(greens)/(sum(all)-sum(equal)));
fprintf(1,'Green: %d,   Red: %d,   Equal: %d,   All: %d',sum(greens), sum(reds), sum(equal), sum(all));
fprintf(1,'\nMinutes to Completion: %f',toc/60);
```

BIBLIOGRAPHY

BIBLIOGRAPHY

1. Damaser, M.S., et al., "The concept of bladder work: work and power in bladder emptying". *Scand J Urol Nephrol Suppl*, 1997. **184**: p. 35-41.

2. van Mastrigt, R., B.L.R.A. Coolsaet, and W.A. van Duyl, "First results of stepwise straining of the human urinary bladder and human bladder strips". *Investigative Urology*, 1981. **19**(1): p. 58-61.

3. Tözeren, A., "Assessment of fiber strength in a urinary bladder by using experimental pressure volume curves: an analytical method". *Journal of Biomechanical Engineering*, 1986. **108**: p. 301-305.

4. Alexander, R.S., "Series elasticity of urinary bladder smooth muscle". *American Journal of Physiology*, 1976. **231**(5 Pt. 1): p. 1337-42.

5. Finkbeiner, A.E., "In vitro responses of detrusor smooth muscle to stretch and relaxation". *Scand J Urol Nephrol Suppl*, 1999. **201**: p. 5-11.

6. Ghoniem, G.M., et al., "Effect of vesical outlet obstruction on detrusor contractility and passive properties in rabbits". *J Urol*, 1986. **135**(6): p. 1284-9.

7. Coolsaet, B.L.R.A., et al., "Viscoelastic properties of bladder wall strips at constant elongation". *Investigative Urology*, 1976. **13**(6): p. 435-440.

8. Kondo, A., J.G. Susset, and J. Lefaivre, "Viscoelastic properties of bladder I. Mechanical model and its mathematical analysis". *Investigative Urology*, 1972. **10**(2): p. 154-163.

9. Andersson, S., A. Kronström, and P. Bjerle, "Viscoelastic properties of the normal human bladder". *Scandanavian Journal of Urological Nephrology*, 1989. **23**: p. 115-120.

10. Gray, H. and W.H. Lewis, *Anatomy of the Human Body*. 2000, Philadelphia: Lea & Febiger, 1918. 1396.

11. Netter, F.H., *Atlas of Human Anatomy*. 2nd ed. 1997, East Hanover: Navartis. 525.

12. German, K., et al., "An assessment of the contribution of visco-elastic factors in the aetiology of poor compliance in the human neuropathic bladder". *Br J Urol*, 1994. **74**(6): p. 744-8.

13. Watanabe, T., D.A. Rivas, and M.B. Chancellor, "Urodynamics of spinal cord injury". *Urol Clin North Am*, 1996. **23**(3): p. 459-73.

14. Kruse, M.N., L.A. Bray, and W.C. de Groat, "Influence of spinal cord injury on the morphology of bladder afferent and efferent neurons". *J Auton Nerv Syst*, 1995. **54**(3): p. 215-24.

15. Ogawa, T., T. Yoshida, and T. Fujinaga, "[Bladder deformity in traumatic spinal cord injury patients]". *Hinyokika Kiyo*, 1988. **34**(7): p. 1173-8.

16. Chang, S.L., et al., "Roles of the lamina propria and the detrusor in tension transfer during bladder filling". *Scand J Urol Nephrol Suppl*, 1999. **201**: p. 38-45.

17. Damaser, M.S., K. Brzezinski, and P.A. Longhurst, "Filling mechanics of obstructed and de-obstructed rat urinary bladders". *Neurourol Urodyn*, 1999. **18**(6): p. 659-71.

18. Horowitz, A., et al., "Structural three-dimensional constitutive law for the passive myocardium". *J Biomech Eng*, 1988. **110**(3): p. 200-7.

19. Chang, S.L., et al., "Role of type III collagen in bladder filling". *Neurourol Urodyn*, 1998. **17**(2): p. 135-45.

20. Deveaud, C.M., et al., "Molecular analysis of collagens in bladder fibrosis". *J Urol*, 1998. **160**(4): p. 1518-27.

21. Koenig, F., et al., "Near-infrared confocal laser scanning microscopy of bladder tissue in vivo". *Urology*, 1999. **53**(4): p. 853-7.

22. Murakumo, M., et al., "Three-dimensional arrangement of collagen and elastin fibers in the human urinary bladder: a scanning electron microscopic study". *J Urol*, 1995. **154**(1): p. 251-6.

23. Cartwright, P.C. and B.W. Snow, "Bladder autoaugmentation: partial detrusor excision to augment the bladder without use of bowel". *J Urol*, 1989. **142**(4): p. 1050-3.

24. Macarak, E.J., et al., "The collagens and their urologic implications". *Adv Exp Med Biol*, 1995. **385**: p. 173-7; discussion 179-84.

25. Yoo, J.J., et al., "Bladder augmentation using allogenic bladder submucosa seeded with cells". *Urology*, 1998. **51**(2): p. 221-5.

26. Gabella, G. and B. Uvelius, "Urinary bladder of rat: fine structure of normal and hypertrophic musculature". *Cell Tissue Res*, 1990. **262**(1): p. 67-79.

27. Cortivo, R., et al., "Elastin and collagen in the normal and obstructed urinary bladder". *Br J Urol*, 1981. **53**(2): p. 134-7.

28. Kim, K.M., et al., "Collagen and elastin in the normal fetal bladder". *J Urol*, 1991. **146**(2 (Pt 2)): p. 524-7.

29. Susset, J.G., et al., "Collagen in 155 human bladders". *Invest Urol*, 1978. **16**(3): p. 204-6.

30. Burgeson, R.E. and M.E. Nimni, "Collagen types. Molecular structure and tissue distribution". *Clin Orthop*, 1992(282): p. 250-72.

31. Macarak, E.J. and P.S. Howard, "The collagens and their urologic significance". *Scand J Urol Nephrol Suppl*, 1997. **184**: p. 25-33.

32. Macarak, E.J. and P.S. Howard, "The role of collagen in bladder filling". *Adv Exp Med Biol*, 1999. **462**: p. 215-23; discussion 225-33.

33. Ewalt, D.H., et al., "Is lamina propria matrix responsible for normal bladder compliance?" *J Urol*, 1992. **148**(2 Pt 2): p. 544-9.

34. Koo, H.P., et al., "Developmental expression of interstitial collagen genes in fetal bladders". *J Urol*, 1997. **158**(3 Pt 1): p. 954-61.

35. Strauss, L., et al., "Distribution of collagen XII and XIV in the bladder wall of the male rat with outlet obstruction". *J Urol*, 2000. **163**(4): p. 1304-8.

36. Rosenbloom, J., et al., "Elastic fibers and their role in bladder extracellular matrix". *Adv Exp Med Biol*, 1995. **385**: p. 161-72; discussion 179-84.

37. Cleary, E.G., *The microfibrillar component of the elastic fibers*, in *Connective Tissue Disease. Modelular Pathology of the Extracellular Matrix*, U. Uitto and A.J. Perejda, Editors. 1987, Marcel Dekker: New York.

38. Koo, H.P., et al., "Temporal expression of elastic fiber components in bladder development". *Connect Tissue Res*, 1998. **37**(1-2): p. 1-11.

39. Ushiki, T. and M. Murakumo, "Scanning electron microscopic studies of tissue elastin components exposed by a KOH-collagenase or simple KOH digestion method". *Arch Histol Cytol*, 1991. **54**(4): p. 427-36.

40. Baskin, L.S., et al., "Type III collagen decreases in normal fetal bovine bladder development". *J Urol*, 1994. **152**(2 Pt 2): p. 688-91.

41. Coplen, D.E., et al., "Characterization of a fibroblast cell from the urinary bladder wall". *In Vitro Cell Dev Biol Anim*, 1994. **30A**(9): p. 604-8.

42. Baskin, L., et al., "Bovine bladder compliance increases with normal fetal development". *J Urol*, 1994. **152**(2 Pt 2): p. 692-5; discussion 696-7.

43. Davidson, J.M. and M.G. Giro, *Control of elastin synthesis: molecular and cellular aspects*, in *Regulation of matrix accumulation*, R.P. Mecham, Editor. 1986, Academic Press: Orlando. p. 177-216.

44. Dahms, S.E., et al., "Composition and biomechanical properties of the bladder acellular matrix graft: comparative analysis in rat, pig and human". *Br J Urol*, 1998. **82**(3): p. 411-9.

45. Watanabe, H., et al., "A finite deformation theory of intravesical pressure and mural stress of the urinary bladder". *Journal of Experimental Medicine*, 1981. **135**: p. 301-307.

46. Alexander, R.S., "Mechanical properties of urinary bladder". *American Journal of Physiology*, 1971. **220**(5): p. 1413-1421.

47. Coplen, D.E., E.J. Macarak, and R.M. Levin, "Developmental changes in normal fetal bovine whole bladder physiology". *J Urol*, 1994. **151**(5): p. 1391-5.

48. Levin, R.M., P. Horan, and S.P. Liu, "Metabolic aspects of urinary bladder filling". *Scand J Urol Nephrol Suppl*, 1999. **201**: p. 59-66.

49. Coolsaet, B.L.R.A., et al., "Viscoelastic properties of bladder wall strips". *Investigative Urology*, 1975. **12**(5): p. 351-355.

50. van Mastrigt, R., B.L.R.A. Coolsaet, and W.A. van Duyl, "The passive properties of the urinary bladder in the collection phase". *Urologia Internationali*, 1978. **33**: p. 14-21.

51. Damaser, M.S., "Whole bladder mechanics during filling". *Scand J Urol Nephrol Suppl*, 1999. **201**: p. 51-8.

52. Klevmark, B., "Natural pressure-volume curves and conventional cystometry". *Scand J Urol Nephrol Suppl*, 1999. **201**: p. 1-4.

53. Zermann, D.H., et al., "Diagnostic value of natural fill cystometry in neurogenic bladder in children". *Eur Urol*, 1997. **32**(2): p. 223-8.

54. van Mastrigt, R. and J.C. Nagtegaal, "Dependence of the viscoelastic response of the urinary bladder wall on strain rate". *Med Biol Eng Comput*, 1981. **19**(3): p. 291-6.

55. Salinas, J., et al., "A study on the viscoelastic properties of the urinary bladder in dogs". *Urol Int*, 1992. **49**(4): p. 185-90.

56. Bross, S., et al., "Combined evaluation of detrusor pressure and bladder wall thickness as a parameter for the assessment of detrusor function: an experimental in vivo study". *J Urol*, 2001. **166**(3): p. 1130-5.

57. Kim, K.J., et al., "Principles of urodynamics pressure measurement and its implication to female continence function". *J Biomech*, 1998. **31**(9): p. 861-5.

58. Abbey, J.C. and L. Close, "Electrical impedance measurement of urinary bladder fullness". *Journal of Microwave Power*, 1983. **18**(3): p. 305-9.

59. Simmons, A., et al., "Dynamic multi-planar EPI of the urinary bladder during voiding with simultaneous detrusor pressure measurement". *Magn Reson Imaging*, 1997. **15**(3): p. 295-300.

60. Ozawa, H., et al., "Development of noninvasive velocity flow video urodynamics using Doppler sonography. Part I: Experimental urethra". *J Urol*, 1998. **160**(5): p. 1787-91.

61. Ozawa, H., et al., "Development of noninvasive velocity flow video urodynamics using Doppler sonography. Part II: clinical application in bladder outlet obstruction". *J Urol*, 1998. **160**(5): p. 1792-6.

62. Coolsaet, B.L.R.A., et al., "Visco-elastic properties of the bladder wall". *Urologia Internationali*, 1975. **30**: p. 16-26.

63. Koo, H.P., et al., "The ontogeny of bladder function in the fetal calf". *J Urol*, 1995. **154**(1): p. 283-7.

64. Alexander, R.S., "Viscoplasticity of smooth muscle of urinary bladder". *American Journal of Physiology*, 1973. **224**(3): p. 618-22.

65. Dean, G.E., et al., "Active and passive compliance of the fetal bovine bladder". *J Urol*, 1997. **158**(3 Pt 2): p. 1094-9.

66. Stover, S.L. and P.R. Fine, "The epidemiology and economics of spinal cord injury". *Paraplegia*, 1987. **25**(3): p. 225-8.

67. Stover, S.L., et al., "Iatrogenic dilatation of the upper urinary tract during radiographic evaluation of patients with spinal cord injury". *J Urol*, 1986. **135**(1): p. 78-82.

68. de Groat, W.C., et al., "A study of synaptic transmission and neuropeptide function in extramural colonic ganglia of the cat". *Nippon Heikatsukin Gakkai Zasshi*, 1985. **21 (suppliment)**: p. 95.

69. Palmtag, H., G. Gullich, and H. Heering, "Bladder neck hypertrophy and wide bladder neck anomaly (WBNA)". *Urol Int*, 1978. **33**(5): p. 285-92.

70. Tekgul, S., et al., "Collagen types I and III localization by in situ hybridization and immunohistochemistry in the partially obstructed young rabbit bladder". *J Urol*, 1996. **156**(2 Pt 2): p. 582-6.

71. Kim, J.C., et al., "Effects of partial bladder outlet obstruction and its relief on types I and III collagen and detrusor contractility in the rat". *Neurourol Urodyn*, 2000. **19**(1): p. 29-42.

72. Ji, P., et al., "Elastin morphology in normal and obstructed guinea-pig bladders. Localization of elastin to the trigone". *World J Urol*, 1995. **13**(3): p. 191-4.

73. Mimata, H., et al., "Changes of rat urinary bladder during acute phase of spinal cord injury". *Urol Int*, 1993. **51**(2): p. 89-93.

74. Anderson, G.F., P.M. Goellner, and J.M. Pierce, "The electrical properties of isolated detrusor muscle as studied with the sucrose gap". *Investigative Urology*, 1972. **9**: p. 470.

75. Charlton, R.G., et al., "Focal changes in nerve, muscle and connective tissue in normal and unstable human bladder". *BJU Int*, 1999. **84**(9): p. 953-60.

76. Kim, K.M., et al., "Collagen and elastin in the obstructed fetal bladder". *J Urol*, 1991. **146**(2 (Pt 2)): p. 528-31.

77. Yokoyama, O., et al., "Morphological and functional factors predicting bladder deterioration after spinal cord injury [see comments]". *J Urol*, 1996. **155**(1): p. 271-4.

78. Weld, K.J., M.J. Graney, and R.R. Dmochowski, "Differences in bladder compliance with time and associations of bladder management with compliance in spinal cord injured patients". *J Urol*, 2000. **163**(4): p. 1228-33.

79. Wagg, A. and C.H. Fry, "Visco-elastic properties of isolated detrusor smooth muscle". *Scand J Urol Nephrol Suppl*, 1999. **201**: p. 12-8.

80. Billiar, K.L. and M.S. Sacks, "Biaxial mechanical properties of the native and glutaraldehyde-treated aortic valve cusp: Part II--A structural constitutive model". *J Biomech Eng*, 2000. **122**(4): p. 327-35.

81. Sacks, M.S., "Biaxial mechanical evaluation of planar biological materials". *Journal of Elasticity*, 2000. **61**: p. 199-246.

82. Fung, Y.C., *Biomechanics: Mechanical Properties of Living Tissues*. 2nd ed. 1993, New York: Springer Verlag. 568.

83. Billiar, K.L. and M.S. Sacks, "Biaxial mechanical properties of the natural and glutaraldehyde treated aortic valve cusp--Part I: Experimental results". *J Biomech Eng*, 2000. **122**(1): p. 23-30.

84. Sacks, M.S. and C.J. Chuong, "Orthotropic mechanical properties of chemically treated bovine pericardium". *Ann Biomed Eng*, 1998. **26**(5): p. 892-902.

85. Sacks, M.S., "A method for planar biaxial mechanical testing that includes in-plane shear". *J Biomech Eng*, 1999. **121**(5): p. 551-5.

86. Gloeckner, D.C., et al., "Passive biaxial mechanical properties of the rat bladder wall after spinal cord injury". *Journal of urology*, 2002. **167**(5): p. 2247-2252.

87. Berggren, T. and B. Uvelius, "Cystometrical evaluation of acute and chronic overdistension in the rat urinary bladder". *Urol Res*, 1998. **26**(5): p. 325-30.

88. Chancellor, M.B., et al., "Micturition patterns after spinal trauma as a measure of autonomic functional recovery". *J Urol*, 1994. **151**(1): p. 250-4.

89. Funk, J.R., et al., "Linear and quasi-linear viscoelastic characterization of ankle ligaments". *J Biomech Eng*, 2000. **122**(1): p. 15-22.

90. Myers, B.S., J.H. McElhaney, and B.J. Doherty, "The viscoelastic responses of the human cervical spine in torsion: experimental limitations of quasi-linear theory, and a method for reducing these effects". *J Biomech*, 1991. **24**(9): p. 811-7.

91. Lanir, Y., "Biaxial stress-relaxation in skin". *Ann Biomed Eng*, 1976. **4**(3): p. 250-70.

92. Byrne, D.S., et al., "Effect of intravesical capsaicin and vehicle on bladder integrity control and spinal cord injured rats". *J Urol*, 1998. **159**(3): p. 1074-8.

93. Yoshiyama, M., W.C. de Groat, and M.O. Fraser, "Influences of external urethral sphincter relaxation induced by alpha-bungarotoxin, a neuromuscular junction blocking agent, on voiding dysfunction in the rat with spinal cord injury". *Urology*, 2000. **55**(6): p. 956-60.

94. Fung, Y.C. and S.Q. Liu, "Change of residual strains in arteries due to hypertrophy caused by aortic constriction". *Circ Res*, 1989. **65**(5): p. 1340-9.

95. Gao, C. and H. Gregersen, "Biomechanical and morphological properties in rat large intestine". *J Biomech*, 2000. **33**(9): p. 1089-97.

96. Fung, Y.C., *Biomechanics: Mechanical Properties of Living Tissues*. 1981, New York: Springer-Verlag.

97. Chaudhuri, B.B., P. Kundu, and N. Sarkar, "Detection and Gradation of Oriented Texture". *Pattern Recognition Letters*, 1993. **14**(2): p. 147-153.

98. Karlon, W.J., et al., "Automated measurement of myofiber disarray in transgenic mice with ventricular expression of ras". *Anat Rec*, 1998. **252**(4): p. 612-25.

99. Kass, M. and A. Witkin, "Analyzing oriented patterns". *Computer Vision, Graphics, and Image Processing*, 1987. **37**: p. 362-385.

100. Kershmann, R., *personal communication*. Jan 2, 2003: CEO and President of Resolution Sciences Corporation.

101. Price, K. and R. Storn, "Differential evolution". *Dr Dobbs Journal*, 1997. **22**(4): p. 18-+.

102. Gloeckner, D.C., M.B. Chancellor, and M.S. Sacks, "Changes in material classification of hte urinary bladder wall after spinal cord injury". *Journal of Biomechanics*, 2003, accepted pending revision.

103. Humphrey, J.D., R.K. Strumpf, and F.C. Yin, "Determination of a constitutive relation for passive myocardium: I. A new functional form". *J Biomech Eng*, 1990. **112**(3): p. 333-9.

104. Fung, Y.C., *Stress-strain-history relations of soft tissue in simple elongation*, in *Biomechanics: Its Foundations and Objective*, Y.C. Fung, P. N., and M. Anliker, Editors. 1972, pretice-Hall: New Jersey. p. 181-208.

105. Best, T.M., et al., "Characterization of the passive responses of live skeletal muscle using the quasi-linear theory of viscoelasticity". *J Biomech*, 1994. **27**(4): p. 413-9.

106. Tanaka, T.T. and Y.C. Fung, "Elastic and inelastic properties of the canine aorta and their variation along the aortic tree". *J Biomech*, 1974. **7**(4): p. 357-70.

107. Kwan, M.K., T.H. Lin, and S.L. Woo, "On the viscoelastic properties of the anteromedial bundle of the anterior cruciate ligament". *J Biomech*, 1993. **26**(4-5): p. 447-52.

108. Miller, C.E., M.A. Vanni, and B.B. Keller, "Characterization of passive embryonic myocardium by quasi-linear viscoelasticity theory". *J Biomech*, 1997. **30**(9): p. 985-8.

109. Findley, W.N., J.S. Lai, and K. Onaran, *Creep and Relaxation of Nonlinear Viscoelastic Materials: With an Introduction to Linear Viscoelasticity*. 1989, New York: Dover Publications.

110. Sverdlik, A. and Y. Lanir, "Time-dependent mechanical behavior of sheep digital tendons, including the effects of preconditioning". *J Biomech Eng*, 2002. **124**(1): p. 78-84.

111. Rivlin, R.S. and D.W. Saunders, "Large Elastic Deformations of Isotropic Materials .7. Experiments on the Deformation of Rubber". *Philosophical Transactions of the Royal Society of London Series a-Mathematical and Physical Sciences*, 1951. **243**(865): p. 251-288.

112. Iggo, A., "Tension receptors in the stomach and urinary bladder". *Journal of Physiology, London*, 1955. **128**: p. 593-607.

113. Talaat, M., "Afferent impulses in the nerves supplying the urinary bladder". *Journal of Physiology, London*, 1937. **89**: p. 1-13.

114. Phillips, R.J. and T.L. Powley, "Tension and stretch receptors in gastrointestinal smooth muscle: re-evaluating vagal mechanoreceptor electrophysiology". *Brain Res Brain Res Rev*, 2000. **34**(1-2): p. 1-26.

115. Nagatomi, J., et al. *Passive-state viscoelastic properties of normal vs. neurogenic bladder wall tissue*. in *2003 Summer Bioengineering ASME*. 2003, submitted. Key Biscayne, FL.

116. Kruse, M.N., B. Bennett, and W.C. De Groat, "Effect of urinary diversion on the recovery of micturition reflexes after spinal cord injury in the rat". *J Urol*, 1994. **151**(4): p. 1088-91.

117. Gloeckner, D.C., et al. *Active biaxial mechanical response of the urinary bladder wall*. in *American Society of Mechanical Engineering Summer Bioengineering Conference*. 2001. Snowbird, Utah.

118. Sacks, M.S., "A structural constitutive model for planar collagenous tissues that integrates SALS-derived fiber orientation data". *Journal of Biomechanial Engineering*, accepted.